08400

BULK SEMICONDUCTOR MATERIALS FOR MILLIMETER- AND SUBMILLIMETER-WAVE DETECTION

TECHNICAL REPORT NO. 118

By

I. I. ELDUMIATI

December 1970

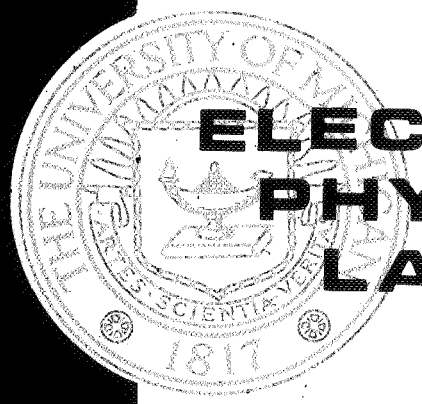

ELECTRON PHYSICS LABORATORY

DEPARTMENT OF ELECTRICAL ENGINEERING
THE UNIVERSITY OF MICHIGAN, ANN ARBOR

CONTRACT WITH:
OFFICE OF SPACE SCIENCE AND APPLICATIONS,
NATIONAL AERONAUTICS AND SPACE ADMINISTRATION,
WASHINGTON, D.C. RESEARCH GRANT NO. NGL 23-005-183.

This report has also been submitted as a dissertation in partial fulfillment of the requirements for the degree of Doctor of Philosophy in The University of Michigan, 1970.

THE UNIVERSITY OF MICHIGAN
ANN ARBOR, MICHIGAN

BULK SEMICONDUCTOR MATERIALS FOR MILLIMETER- AND SUBMILLIMETER-WAVE DETECTION

Technical Report No. 118

Electron Physics Laboratory
Department of Electrical Engineering

By

I. I. Eldumiati

Approved by: 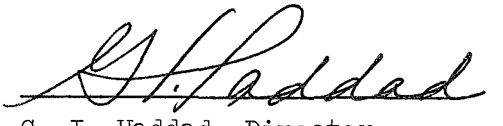

G. I. Haddad, Director
Electron Physics Laboratory

Project 08400

RESEARCH GRANT NO. NGL 23-005-183
OFFICE OF SPACE SCIENCE AND APPLICATIONS
NATIONAL AERONAUTICS AND SPACE ADMINISTRATION
WASHINGTON, D. C. 20546

December, 1970

ABSTRACT

The purpose of this study is to investigate the properties of bulk semiconductor materials for application as millimeter- and submillimeter-wave detectors using a downconversion process. The hot-electron effect serves as the process responsible for the detection mechanism. Power applied at the millimeter-wave frequency causes a change in the material conductivity, which in turn causes a change in the microwave power absorption. Millimeter- and submillimeter-wave detection can be achieved by monitoring the corresponding change in the microwave power absorption.

In order to determine the characteristics of the downconverter, a thorough study of the properties of shallow-type impurity semiconductors in the presence of microwave and dc magnetic fields was carried out as a function of temperature (4.2 to 300°K). Measurements using cavity perturbation techniques were used to determine the properties of the material and the theoretical and experimental results were compared. The hot-electron effect was found to be insignificant above liquid nitrogen temperature and the scattering mechanisms were dominated by acoustic and polar modes over the same temperature range.

The results on the material study are utilized to develop the physical properties of the detection scheme using an equivalent circuit approach. Expressions for the conversion loss, noise equivalent power and response time are given. The dependence of the downconverter's performance on the material and circuit parameters is studied and the optimum values for these parameters are given.

An experimental program was carried out to demonstrate the feasibility of the detection scheme. A high-purity n-type indium antimonide sample mounted in a reentrant cavity and cooled to 4.2°K was successfully operated as a millimeter- and submillimeter-wave detector. The device was tested between 35 and 150 GHz with no long or short cutoff wavelength observed. A minimum terminal-to-terminal conversion loss and NEP of 11.5 dB and 6.8×10^{-11} W per unit bandwidth was measured. No marked improvement was observed by introducing the magnetic field. The conversion loss and NEP can be improved by as much as 10 dB through proper choice of material.

In brief, the scheme offers a fast, highly sensitive and rugged detector with low conversion loss. It excels over bulk mixers by eliminating the need for the local oscillator at the millimeter-wave frequency, and over Putley detectors (dc biased) with regard to the speed of response and the elimination of flicker noise.

ACKNOWLEDGMENT

The author wishes to express his gratitude to his doctoral committee and especially his chairman, Professor G. I. Haddad, for suggesting the problem and for his continued guidance and encouragement throughout the course of this work. The author would like to thank Professor Walter R. Curtice for the many discussions concerning the experimental measurements. The efforts of the laboratory staff are greatly appreciated. Special thanks are due to Mr. M. Gene Robinson and Mr. Edmund Kayser for helping with the test device, to Mrs. Wanita Rasey for typing the manuscript, to Miss Betty Cummings for editing it and to Mr. Leslie Shive for preparing the figures. The author also wishes to thank his wife for her kind support and vast encouragement. Finally, the author wishes to extend special thanks to his parents for their support and encouragement over a long period of time.

TABLE OF CONTENTS

LIST OF ILLUSTRATIONS

LIST OF TABLES

CHAPTER I. INTRODUCTION

1.1 Uses and Potential Applications for Millimeter and Submillimeter Waves

The usefulness of millimeter and submillimeter waves in the fields of spectroscopy,[1] radio astronomy[2] and atomic and molecular physics are well known. Moreover, it has been shown[3] that the potential for communication systems in this wavelength range excels in comparison with microwave and optical systems. The applications include high-resolution radar, navigation aids, sensing devices and space communications. The advantages of using millimeter waves compared to microwaves include lightweight miniature components, increased bandwidth and higher resolution, and when compared to optical waves the millimeter-wave systems experience less atmospheric and background noise and also have a higher reliability.

The slow progress and lack of thrust in such a vital area of the spectrum can be attributed to the relative lack of availability of signal sources and sensitive, fast and reliable detectors.[4] Recently there has been substantial progress in the field of signal generation. Klystrons are available at frequencies up to 170 GHz, while carcinotrons have been operated CW at frequencies up to 600 GHz, giving 10 mW of power. Harmonic generators using point contact diodes are used as signal sources above 600 GHz. However, the output power of these harmonic generators is limited by the high conversion loss involved together with the low burnout signal level. Current research on available avalanche diodes shows that these devices will be useful as signal sources in the millimeter-wave range.

1.2 Evaluation of Available Detectors

1.2.1 Basis of Comparison of Different Detectors. It is difficult to develop a systematic scheme for comparing the performance of millimeter- and submillimeter-wave detectors, although several attempts have been made in this direction. These include the work by Jones,[5,6] Putley[7] and Krumm.[8] Jones' treatment is phenomenological in nature. Putley surveys the best available detectors and compares their performance. On the other hand Krumm pursues the analysis developed by McLean and Putley[9] to determine the theoretical sensitivity limits for various detectors. The difficulty in setting universal criteria for comparing millimeter- and submillimeter-wave detectors can be summarized as follows. First, the suitability of a detector depends on the intended application. For example, a detector very suitable for radio astronomy might be considered inferior for communication purposes. Second, the mechanisms and modes of operation of each group of detectors are basically different. This indicates that it is more meaningful to consider the "usefulness" of a detector. In evaluating such "usefulness," the following parameters are considered valuable:

1. The noise equivalent power (NEP), which is defined as the power input to the detector which will give rise to a mean-square output equal to the mean-square value of the output noise. When normalized to a 1 Hz bandwidth it gives a good measure of the detection capability of the detector, a practice which will be followed throughout.

2. The response time, which measures the capability of the detector to respond to modulated signals at sufficiently rapid rates.

3. The bandwidth, which is defined as the frequency range over which the detector's response does not deteriorate appreciably.

4. The dynamic range, which is the ratio of the maximum to the minimum detectable signal levels. This character is of importance whenever the signal level to be detected varies appreciably.

5. The ease of operation, realization and maintenance of the device.

With the above criteria of usefulness of millimeter- and submillimeter-wave detectors in mind a review of the best available ones is presented next.

1.2.2 Thermal Detectors. In this class of detectors the incident radiation causes a change in the temperature of the sensitive element of the detector which in turn will change its electrical properties. This change can be used to monitor the incident radiation. Bolometers, thermocouples and the Golay cell are the most prominent examples. The inherent thermal inertia involved in the detection mechanism causes the response time to be large. The Golay cell works at room temperature and can be used for power monitoring purposes when the speed of response is not important. The best available Golay cell has an NEP of 10^{-10} W over 1 Hz bandwidth and a time constant around 15 ms.

The performance of superconducting and cooled bolometers surpasses the Golay cell, however they need cooling to cryogenic temperatures (1.5 to 2.5°K). Martin and Bloor[10] reported a superconducting detector whose NEP is 3×10^{-12} W over 1 Hz bandwidth and a time constant of

1.25 s at the operating temperature of 3.7°K. Germanium bolometers[11,12] cooled to 2.15°K and 4.2°K have an NEP of 5 x 10^{-13} W per unit bandwidth with a time constant of 0.3 ms for the first detector.

1.2.3 Point-Contact and Junction Diodes. Point-contact diodes mounted in waveguide sections have been used as video or superheterodyne detectors in the frequency range from 30 to 220 GHz.[13] The main advantage of this type of detector is that it does not need cooling. However above 30 GHz the performance of these detectors starts falling due to the shunting effect of the junction capacity. To reduce the contact capacity, extremely fine points are used for the contact. The small-size contacts impose severe burnout restrictions dictated by the failure of the junction to dissipate high-level absorbed power. Straight video detectors at 140 GHz were reported[14] to have an NEP of 1.6 x 10^{-12} W per unit bandwidth. However these detectors are expected to have a time constant around 10 μs. Point-contact superheterodyne receivers surpass the video detectors in achieving better sensitivity and lower response time. It has been indicated by Dees[4] that an NEP of 10^{-15} W and a response time as small as 10^{-9} s could be achieved. The disadvantages of this class of detectors are the burnout limitations together with the scarcity of high-level, low-noise, local oscillator sources at these frequencies. It is also worth noting that the response of these detectors falls off as the IF increases which imposes further demands on the stability and tunability of the local oscillator source.

1.2.4 Narrow-Band Quantum Detectors. A narrow-band quantum detector utilizes the quantum transitions between discrete energy levels to monitor the incident radiation. The bandwidth of this detector is

limited by the resonance absorption linewidth, and its time constant is limited by the relaxation rates of the excited states involved. The main advantages of this kind of detector are the narrow bandwidth and tuning ability. This makes them good candidates for applications in spectroscopy and radio astronomy. Narrow-band tunable quantum detectors have been treated by Krumm and Haddad[15] and by Krumm.[8] An NEP of 0.5×10^{-10} W per unit bandwidth with a time constant of 4 ms were achieved at 4.2°K. However the sensitivity can be traded for a higher speed of response by working at liquid nitrogen temperature.

1.2.5 Detectors Using Bulk Semiconductor Materials. In 1961 Rollin[16] indicated the feasibility of detecting millimeter- and submillimeter-wave radiation by free-carrier absorption in indium antimonide. Dc biased indium antimonide photoconductive detectors have been developed and incorporated in millimeter- and submillimeter-wave systems by Putley[17,18] Kinch and Rollin[19] and Giggey et al.[20] These detectors are referred to as Putley detectors.

Putley detectors can be operated as wideband or narrow-band tunable ones in the presence of small or high magnetic fields, respectively. The best known Putley detector[17] has an NEP of 5×10^{-12} W over 1 Hz and a time constant of 2×10^{-7} s in the presence of a magnetic field and at a temperature of 1.5°K. Another detector[17] has been operated at 4.2°K with no magnetic field; its NEP and time constant are 10^{-13} W over 1 Hz bandwidth and 10^{-3} s, respectively. Giggey et al.[20] reported an NEP per unit bandwidth of 10^{-12} W and a time constant of 0.25 μs at liquid helium temperature.

The feasibility of superheterodyne receivers using mixing in bulk indium antimonide was first demonstrated by Arams et al.[21] and recently by Whalen and Westgate.[22] Arams and his co-workers measured a conversion loss of 22.6 and 25.7 dB at 1.8 and 4.2°K, respectively, in the frequency range between 30 and 40 GHz. Whalen and Westgate reported a conversion loss at 69 GHz that varied from 9 to 28 dB as the operating temperature was changed between 1.5 and 22°K. There is no information available on the NEP of this class of detectors. The dc bias current required to optimize the detection will contribute to the low-frequency noise generated within the mixer. However the main disadvantage of these detectors is that the intermediate frequency is restricted to about 1 MHz. The limit on the intermediate frequency is set by the long energy relaxation time of the carriers. This fact is an added inconvenience to the presence of a local oscillator at such a high frequency. It will also hinder the tuning capability of such detectors.

1.3 Microwave-Biased Bulk Semiconductor Detectors

The previous section indicates that detectors employing bulk semiconductor material as their sensitive element are superior concerning their speed of response and NEP. They are the most promising in the fields of communications, spectroscopy and many other applications. In a Putley detector the incident radiation changes the conductivity of the dc biased bulk material. This change is monitored through a sampling resistance and amplified using a low-noise amplifier. Ohmic contacts are required which add to the complexity of sample manufacture.

The response time is limited by the circuit resistance and distributed capacitance, which is at least one order of magnitude larger than the carrier relaxation time and four orders of magnitude larger than the dielectric relaxation time. Moreover the NEP is degraded by the low-frequency flicker noise due to the dc bias and is essentially limited by the relatively low-input impedance postamplifier. This indicates that the dc bias is the main factor toward degrading the performance of this class of detectors.

It has been shown[23-25] that a photoconductor with high-frequency bias outperforms one with dc bias for all practical signal levels. The improvement is due to the fact that the bias signal changes polarity many times during a photocarrier lifetime which effectively localizes the carriers within the material and increases their lifetime. Moreover the sensitivity, NEP and time constant will not be degraded by the low-input impedance amplifier since high-resistance samples can be capacitively coupled to a microwave cavity or a waveguide.

1.3.1 A Summary of the Detection Scheme Investigated Here. The basic elements of the detection scheme are shown in Fig. 1.1 and consist of the following:

1. A cavity containing the semiconductor sample, which is placed in the highest field region to ensure the greatest interaction between the material and the incident radiation.

2. A local oscillator (at a microwave frequency) which is coupled to the cavity through a circulator.

3. A low-noise amplifier and conventional detector. The low-noise amplifier may not be needed if the responsivity of the system is high enough.

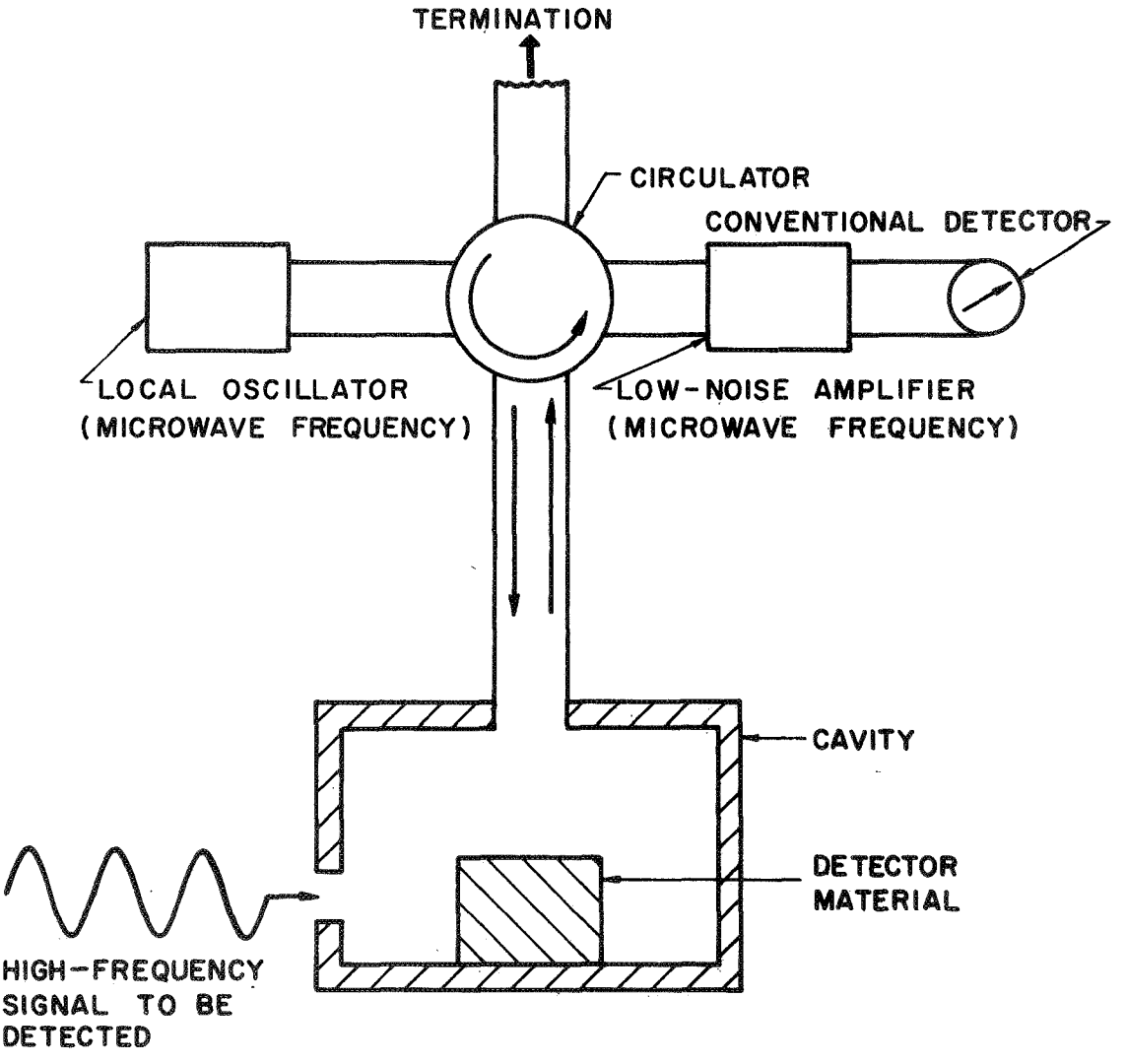

FIG. 1.1 PROPOSED HIGH-FREQUENCY DETECTION SCHEME.

4. A coupling hole for the high-frequency signal to be detected.

The scheme could work either on a photoconductive basis if the carriers are bound to the impurity band, or by free-carrier absorption if the impurity and conduction bands overlap. In both cases the scheme is similar to a downconverter where the high-frequency signal to be detected causes a change in the material properties, which can be monitored at the microwave frequency.

To illustrate the principle of the detection scheme on a photoconductive basis, assume that the semiconductor material has an energy-band picture as shown in Fig. 1.2.

If all the electrons are residing in the valence and impurity bands and the frequency of the local oscillator is such that $f_{lo} < \Delta E/h$ (h is Planck's constant), the material then will behave as a dielectric and the coupling coefficient of the local oscillator to the cavity can be adjusted to a desired value of reflected power. However, if the signal frequency to be detected is such that $f_s > \Delta E/h$ then illuminating the material will change its resistivity and, in turn, the reflection coefficient between the local oscillator and the cavity; thus changing the power arriving at the conventional detector. The change in the reflected power is a measure of the signal power to be detected.

On the other hand if the carriers are not bound to the impurity band the radiation incident on the semiconductor sample will be absorbed by the free carriers. As a result the energy of the free carriers will increase above the value corresponding to the lattice temperature.[26] The increase in the carriers' energy due to the absorption of the incident radiation will cause a change in the mobility of the sample and, in turn,

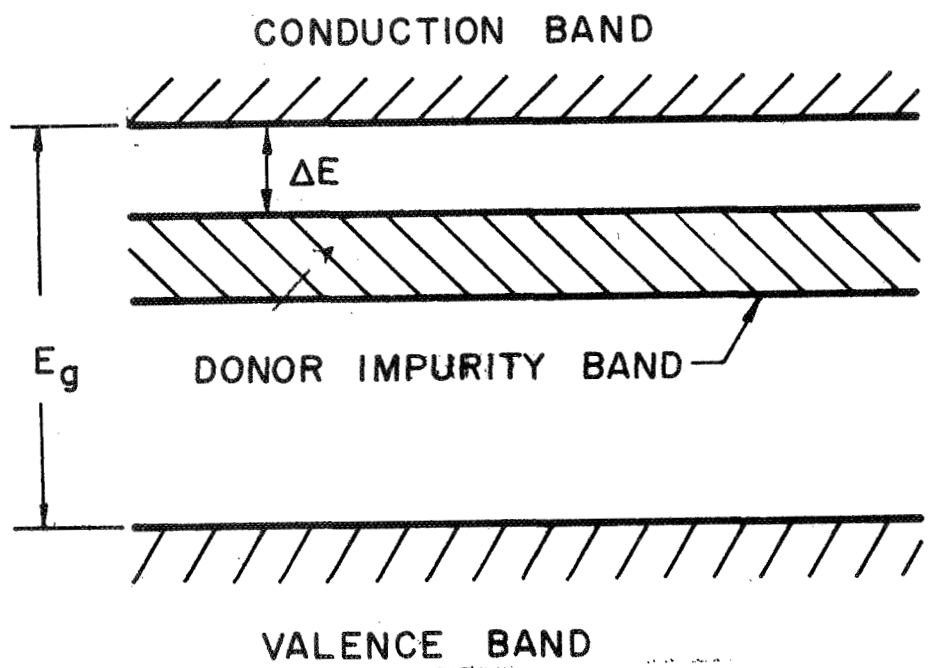

FIG. 1.2 ENERGY-BAND PICTURE OF A SEMICONDUCTOR MATERIAL FOR USE IN THE PROPOSED DETECTION SCHEME.

its conductivity will change with the incident radiation. The signal to be detected can be monitored, as indicated previously, by monitoring the reflected microwave power.

This scheme combines all the attractive features of detectors using bulk semiconductor materials. These include ruggedness, simplicity and ease of manufacture and no burnout limitations. When compared to the Putley detector, the scheme makes it possible to use high-purity samples thus reducing the trapping effects which seriously degrade the performance of an insulating semiconductor.[27] It eliminates the need for ohmic contacts since the sample can be capacitively coupled to the cavity. These factors will introduce a higher gain bandwidth, faster speed of response and lower NEP.

It will be shown that microwave-biased and heterodyne detectors using bulk semiconductors will have a similar conversion loss. Most important, the need for a stable local oscillator at the millimeter-wave frequency can be eliminated. This is a very important feature which makes microwave-biased semiconductor detectors highly desirable for applications above 100 GHz where tunable and stable local oscillators are scarce, and where the performance of most detectors starts to deteriorate. The only inconvenience in using these detectors is the operation at cryogenic temperatures, however, this is quite feasible with the use of closed refrigeration systems.

1.3.2 Outline of the Present Study. The main purpose of this study is a thorough evaluation of microwave-biased bulk semiconductor detectors for the millimeter- and submillimeter-wave region of the spectrum. Theoretical and experimental investigations were carried out for this purpose.

Chapter II deals with the properties of a shallow donor impurity semiconductor as a function of temperature in the presence of electric and magnetic fields. A two-band conduction model is used to determine the material conductivity and dielectric constant in the presence of these fields. Measurements to compare the theoretical and experimental results are carried out using cavity perturbation techniques.

In Chapter III a derivation of the equivalent circuit of a semiconductor sample placed in a cavity is given. The equations relating the change in the power absorbed by the cavity and the shift in its resonant frequency to the conductivity and the dielectric constant of the sample are derived. This chapter will also include a theoretical analysis of the coupling problem.

Chapter IV is devoted to a theoretical derivation of the detector parameters. Expressions for the NEP, conversion loss and an evaluation of the response time are given. The experimental results on the detection scheme are presented in Chapter V. These results will be compared with the theoretical limits and currently available detectors.

Finally, Chapter VI includes a discussion of the basic conclusions and the suggestions for future work.

CHAPTER II. THEORY OF CONDUCTION IN INDIUM ANTIMONIDE

2.1 Introduction

This chapter is devoted to the study of bulk semiconductor materials suitable for millimeter- and submillimeter-wave detection. It was indicated in Chapter I that detectors using bulk semiconductor materials can be operated in a photoconductive mode, or by free-carrier absorption. The mechanism of photoconductive detectors depends on the existence of bound carriers which can be excited into a conduction state by the incident electromagnetic radiation. In the case of a semiconductor, the incident radiation excites carriers from either the valence or impurity band into the conduction band. These detectors are characterized by a long wavelength cutoff. For the photoconductive effect to be observed, the electromagnetic radiation should provide at least the minimum energy required to free the bound carriers, i.e.,

$$hf_s \geq \Delta E \quad , \tag{2.1}$$

where f_s = the frequency of the signal to be detected,

h = Planck's constant and

ΔE = the energy gap.

At the same time the lattice thermal energy should be smaller than ΔE:

$$kT < \Delta E \quad , \tag{2.2}$$

where k = Boltzmann's constant and

T = the lattice temperature in °K.

Equations 2.1 and 2.2 show that in order to detect electromagnetic radiation of 1 mm wavelength, the energy gap should be less than 1.2×10^{-3} eV and the semiconductor material should be cooled below 14°K. Such a small energy gap is impossible to achieve with intrinsic semiconductor materials since most of them have an energy gap which is two to three orders of magnitude greater than the required one. Therefore shallow-type impurity semiconductors are most suitable for this purpose.

On the other hand if a discrete energy-band picture as shown in Fig. 1.2 does not exist, the detector can operate by free-carrier absorption if the proper material is chosen. It has been shown by Rollin[16] that the sensitivity of detectors operating on this principle is inversely proportional to the free-carriers' effective mass.

Assuming that, for low concentrations, the impurities in type III and V semiconductors are fairly well approximated by a hydrogen-like model, the ionization energy ΔE and the orbital radius r_n^* are given by

$$\Delta E_n = \frac{e^2}{2\epsilon_r r_n^*} \qquad (2.3a)$$

and

$$r_n^* = \frac{\epsilon_r n^2 h^2}{4\pi^2 e^2 m^*} , \qquad (2.3b)$$

where e = the electronic charge,

ϵ_r = the relative dielectric constant of the material,

n = the principal quantum number and

m^* = the effective mass of the charge carriers in the material.

Applying Eqs. 2.3 to n-type InSb, which has an effective mass of 0.0133 times the free electron mass and an ϵ_r of 16, it is found that the ionization energy for impurities is approximately 0.7 meV. This value for the ionization energy, together with the small effective mass, makes n-type InSb one of the most appropriate media for millimeter- and submillimeter-wave detection.

2.2 Two-Band Conduction in Indium Antimonide

Due to the small effective mass and the relatively large dielectric constant of n-type InSb, the donor electron wave functions overlap even at liquid helium temperature and reasonably low concentrations. This will cause the impurity and conduction bands to merge together. This effect has been demonstrated by many authors.[28-30] Following Conwell's analysis,[31] the carrier concentration N_c at which the impurity band merges completely with the conduction band and that required for band formation N_b can be estimated. In this analysis the impurity ions are assumed to be arranged on a regular uniform lattice and the atomic polyhedra surrounding each impurity ion are approximated by spheres of radius r_s such that,

$$\frac{4}{3}\pi r_s^3 = \frac{1}{N_I} , \tag{2.4}$$

where N_I = the net impurity concentration. The concentration at which the impurity and conduction bands merge together should occur approximately at $r_s = r_1^*$, and that required for band formation should be about $r_s = 5r_1^*$, where r_1^* is the first Bohr radius of the impurity atom. Applying these conditions yields:

$$N_c \geq \frac{3}{4\pi(r_1^*)^3} \tag{2.5}$$

and

$$N_b \leq \frac{3}{4\pi(5r_1^*)^3} \quad . \tag{2.6}$$

Using an effective mass of 0.0133 m_o in Eqs. 2.5 and 2.6, the impurity and conduction bands merge together at a concentration of approximately 0.92×10^{15} cm^{-3} and a concentration of at most 0.74×10^{13} cm^{-3} is required for the familiar band picture to prevail. It is also worth noting that if the randomness of the impurity centers is taken into account the cited number would be lower. Between these two values of concentrations the two-band conduction model, first introduced by Hung,[32] is most suited for studying the properties of these materials. In this model different values for the mobility and effective mass are assigned to the carriers in each band.

Although the purest available InSb has a concentration greater than 10^{13} cm^{-3}, energy bands can be achieved in the presence of a magnetic field. Magnetically induced banding in InSb was discussed theoretically by Yafet et al.[33] and investigated experimentally by many authors, among them are Keyes and Sladek;[34] Sladek;[35] Brown and Kimmit[36] and recently by Apel et al.[37] The effect depends on the electron motion being quantized in the plane perpendicular to the magnetic field and was intended to explain Hall-effect measurements and photoconductive effects in InSb. In all cases dc bias was applied to the samples under test which caused the electrons to be heated considerably.

The two-band conduction model will be used to study the microwave properties of the bulk material as a function of temperature and magnetic field.

2.2.1 Calculations of the Freeze-Out Magnetic Field. In the presence of a magnetic field the motion of the impurity electrons become quantized in the direction perpendicular to the magnetic field. The conduction band will be split into Landau levels with an energy difference of $\hbar\omega_c$, where ω_c is the angular cyclotron frequency. However, it was shown by Putley[38] that the number of states in the lowest Landau level is greater than the number of available electrons for all impurity concentrations of interest here. The quantization in the plane normal to the magnetic field tends to cause the electrons to become strongly tied to their impurity ions as the magnetic field is increased. At a certain value of the magnetic field B_F, essentially all the carriers become bound to their impurity ions and the overlap between the impurity and conduction bands is reduced to a minimum. The criterion for band formation is that the average cyclotron radius $\langle r_c \rangle$ equals the separation between the donor ions r_s. The cyclotron radius corresponding to a magnetic field intensity B is given by

$$r_c = \frac{m^* v}{qB} \quad , \tag{2.7}$$

where v is the velocity of the charge carriers in the plane perpendicular to B and q is the carrier's charge.

As a first-order approximation for determining $\langle r_c \rangle$, a Maxwellian distribution is assumed. The energy of the carriers $\mathcal{E}$ will be given by:

$$\mathcal{E} \cong kT_e + hf_{lo} \quad , \tag{2.8}$$

where T_e is the electrons' temperature, which might be different from the lattice temperature as a result of the heating effect of the monitoring microwave radiation, whose frequency is f_{lo}. At 10 GHz, hf_{lo} corresponds to 4.135×10^{-2} meV, which is too small compared to the thermal energy, down to liquid helium temperature. Therefore hf_{lo} can be safely neglected in Eq. 2.8. In addition, hf_{lo} is smaller than the $\hbar\omega_c$ values of interest, which implies that the carriers will only be limited to the first Landau level.

From Eq. 2.7,

$$\langle r_c \rangle = \frac{m^*}{qB} \langle v \rangle \quad ,$$

and the freeze-out magnetic field B_F can be obtained by equating r_s, defined in Eq. 2.5, to $\langle r_c \rangle$ giving:

$$B_F = \frac{m^* \langle v \rangle}{q} \left(\frac{4\pi N_I}{3} \right)^{1/3} \quad . \tag{2.9}$$

If the magnetic field is oriented along the z-axis, the average value of v will be given by

$$\langle v \rangle = \frac{\int_{-\infty}^{\infty} e^{-a^2 v_z^2} \, dv_z \cdot 2\pi \int_0^{\infty} v^2 \, e^{-a^2 v^2} \, dv}{\int_{-\infty}^{\infty} \exp[-a^2(v_x^2 + v_y^2 + v_z^2)] \, dv_x \, dv_y \, dv_z} \quad , \tag{2.10}$$

where $v^2 = v_x^2 + v_y^2$ and $a^2 = m^*/2kT_e$. Carrying out the integration and substituting the value of $\langle v \rangle$ in Eq. 2.9 yields,

$$B_F = \left(\frac{4\pi N_I}{3}\right)^{1/3} \left(\frac{\pi m^* kT_e}{2q^2}\right)^{1/2} . \qquad (2.11)$$

The value of q will depend on the nature of the chemical bond between the indium and antimony atoms,[39,40] and can be expressed by the following relation

$$q = ee^* , \qquad (2.12)$$

where e^* is the effective charge ratio of the carriers. In InSb the indium atom has three valence electrons and the antimony atom has five. If no charge transfer occurs between the indium and the antimony (In^0Sb^0), the binding is neutral. However, if each indium atom acquires an electron ($In^{+1}Sb^{-1}$), the binding is purely covalent. On the other hand if each antimony atom acquires all three valence electrons of an indium atom ($In^{-3}Sb^{+3}$), the binding becomes purely ionic. The previous argument is an oversimplification and could be conclusive in determining e^* if the charge distribution near the ions is intense and a definite boundary exists between the neighboring ions, which is the case only for ionic crystals. Since the binding in InSb is likely to be a mixture of all three bonds, a more rigorous means to determine e^* is necessary. It was indicated by Cochran[41] that the effective ionic charge depends on the difference between the electronic polarizabilities of the two ions concerned and the parameters describing the short-range interaction. This idea was pursued by Hass and Henvis[42] by studying the infrared lattice reflectivity of InSb at liquid helium temperature.

Expressions for the polarizability derived by Born and Huang[43] which assume a tetrahedral symmetry were used and resulted in a value of 0.42 for e^* in the case of InSb. This value agrees fairly well with the 0.45 value obtained by x-ray diffraction.[44,45] The value 0.42 will be used in the following calculation, since Hass and Henvis carried out their experiment using a spectrometer converted to grating operation. This reduces the effect of electron heating and consequently the contribution of the free-carrier absorption to the dielectric constant to a minimum.

The value obtained from Eq. 2.11 is expected to be on the lower side, since 46 percent of the carriers have velocities larger than $\langle v \rangle$, and in turn will have a larger cyclotron radius. The magnetic field B_{Fh} required to cause 90 percent of the impurity electrons to have an r_c smaller than or equal to r_s is 1.72 times B_F. Figure 2.1 shows the values of B_F and B_{Fh} as a function of temperature for an InSb sample with a net carrier concentration of 5×10^{13} cm^{-3} and assuming the lattice and carrier temperatures to be the same. It should be noted that in obtaining Fig. 2.1 the carrier concentration was assumed to be independent of temperature.

2.2.2 The Conductivity of a Semiconductor Material in Crossed dc-Magnetic and Microwave Fields. This section deals with the dependence of the material's conductivity and dielectric constant on crossed electric and magnetic fields whose orientation is shown in Fig. 2.2. Both carriers in the conduction and impurity bands contribute to these parameters. Therefore,

$$\sigma = q(\mu_c n_c + \mu_i n_i) \quad , \tag{2.13}$$

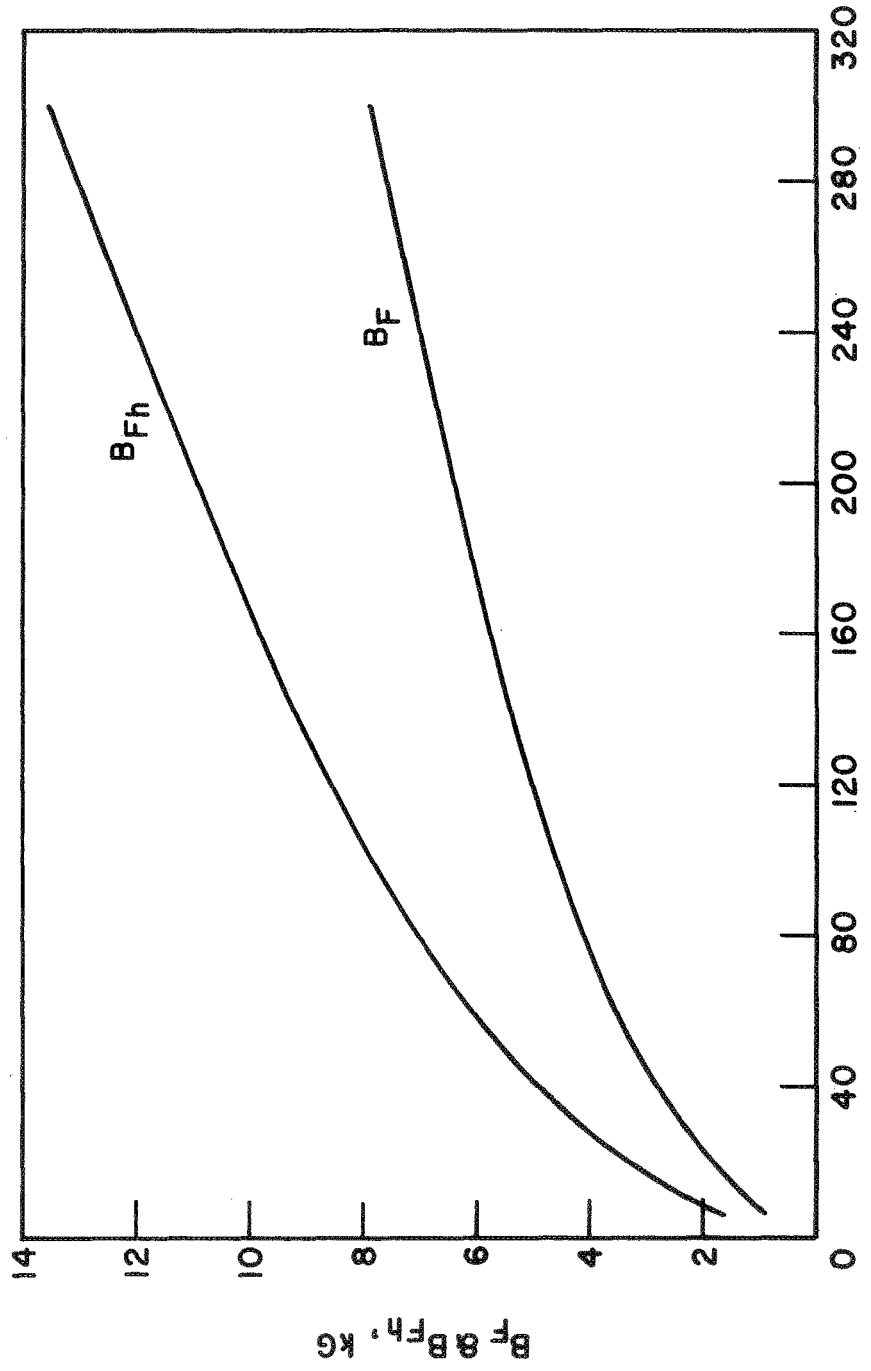

FIG. 2.1 B_F AND B_{Fh} VS. TEMPERATURE. ($N_I = 5 \times 10^{13}$ cm^{-3}, $e^* = 0.42$)

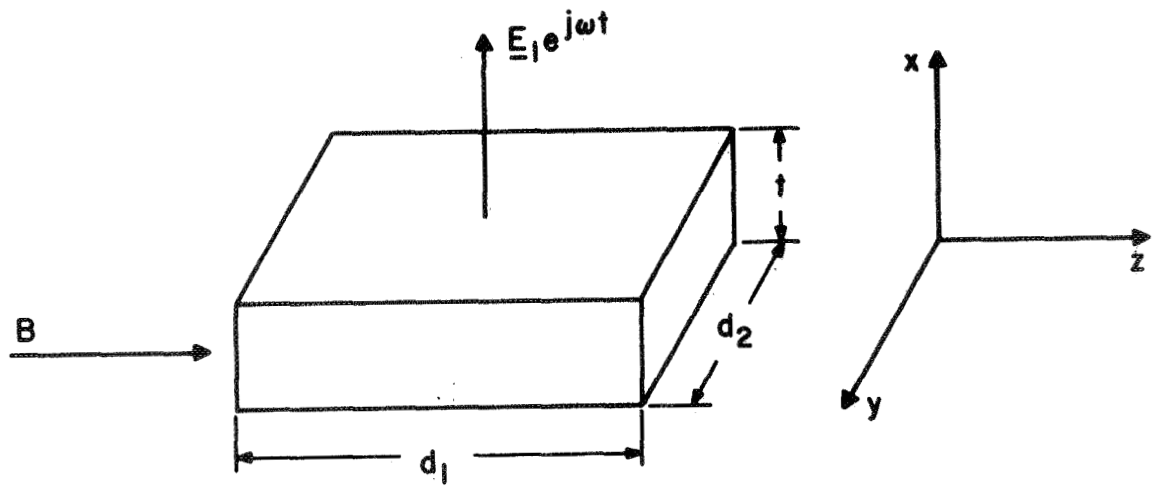

FIG. 2.2 ORIENTATION OF THE FIELDS APPLIED TO THE BULK SEMICONDUCTOR.

where μ_c and n_c are the mobility and the number of carriers, respectively, in the conduction band and μ_i and n_i are those in the impurity band. n_c and n_i are related to the net carrier concentration as follows

$$n_c + n_i = N_I \tag{2.14}$$

and the division of the carriers between the two bands will depend on the values of the electric and magnetic fields as well as the temperature. It is adequate to study the contribution of either kind of carrier to the conductivity and then combine the effect of both of them using Eq. 2.13. The equation of motion for the carriers in the presence of a steady magnetic induction $\underline{B}$ and a microwave field $\underline{E}$ is expressed as

$$q\underline{E} + q\underline{v} \times \underline{B} = m^* \frac{d\underline{v}}{dt} + \frac{m^*}{\tau} \underline{v} \quad , \tag{2.15}$$

where $\underline{v}$ = the average particle velocity and

τ = the carrier relaxation time.

For a quasi-steady state

$$\underline{E} = \underline{E}_1 e^{j\omega t} \tag{2.16}$$

and

$$\underline{v} = \underline{v}_1 e^{j\omega t} \quad . \tag{2.17}$$

Substituting Eqs. 2.16 and 2.17 into 2.15 results in

$$q\underline{E}_1 + q\underline{v}_1 \times \underline{B} = \frac{m^*}{\tau} (1 + j\omega\tau) \underline{v}_1 \quad . \tag{2.18}$$

Assuming $\underline{B}$ to be along the z-axis and expanding Eq. 2.18 in three Cartesian components yields,

$$qE_{1x} = \frac{m^*}{\tau}(1 + j\omega\tau)v_{1x} - qv_{1y}B \quad , \tag{2.19}$$

$$qE_{1y} = \frac{m^*}{\tau}(1 + j\omega\tau)v_{1y} + qv_{1x}B \tag{2.20}$$

and

$$qE_{1z} = \frac{m^*}{\tau}(1 + j\omega\tau)v_{1z} \quad . \tag{2.21}$$

Equation 2.21 can be reduced to

$$v_{1z} = \mu_\omega E_{1z} \quad , \tag{2.22}$$

where μ_ω is defined as

$$\mu_\omega = \frac{\mu_o}{1 + j\omega\tau} \tag{2.23}$$

and $\mu_o = (q/m^*)\tau$. Solving Eq. 2.20 for v_{1y} and substituting its value into Eq. 2.19 yields,

$$E_{1x} = \frac{1 + j\omega\tau}{\mu_o}\left(1 + \frac{\mu_o^2B^2}{(1 + j\omega\tau)^2}\right)v_{1x} - \frac{\mu_o B}{1 + j\omega\tau}E_{1y} \quad .$$

Arranging terms and substituting from Eq. 2.23 gives

$$v_{1x} = \frac{\mu_\omega}{1 + \mu_\omega^2B^2}E_{1x} + \frac{\mu_\omega^2B^2}{1 + \mu_\omega^2B^2}E_{1y} \quad . \tag{2.24}$$

Similarly,

$$v_{1y} = \frac{\mu_\omega}{1 + \mu_\omega^2B^2}E_{1y} - \frac{\mu_\omega^2B^2}{1 + \mu_\omega^2B^2}E_{1x} \quad . \tag{2.25}$$

If n is the number of carriers per unit volume in the band under consideration, then $\underline{J}$, the contribution of this band to the current density, is given by

$$\underline{J} = nq\underline{v} \quad .$$

Using the values of $\underline{v}$ obtained in Eqs. 2.22, 2.24 and 2.25,

$$\underline{J} = qn\mu_\omega \begin{bmatrix} \frac{1}{1+\mu_\omega^2 B^2} & \frac{\mu_\omega B}{1+\mu_\omega^2 B^2} & 0 \\ \frac{-\mu_\omega B}{1+\mu_\omega^2 B^2} & \frac{1}{1+\mu_\omega^2 B^2} & 0 \\ 0 & 0 & 1 \end{bmatrix} \begin{bmatrix} E_{1x} \\ E_{1y} \\ E_{1z} \end{bmatrix}$$

which yields the following expression for the conductivity,

$$\underline{\sigma}_c = qn\mu_\omega \begin{bmatrix} \frac{1}{1+\mu_\omega^2 B^2} & \frac{\mu_\omega B}{1+\mu_\omega^2 B^2} & 0 \\ \frac{-\mu_\omega B}{1+\mu_\omega^2 B^2} & \frac{1}{1+\mu_\omega^2 B^2} & 0 \\ 0 & 0 & 1 \end{bmatrix} \tag{2.26}$$

Examining the different terms of $\underline{\sigma}$ it can be shown that

$$\frac{\mu_\omega^2}{1 + \mu_\omega^2 B^2} = \frac{\mu_o^2(1 + \mu_o^2 B^2 - \omega^2\tau^2) - 2j\omega\tau\mu_o^2}{(1 + \mu_o^2 B^2 - \omega^2\tau^2)^2 + 4\omega^2\tau^2} \tag{2.27}$$

and

$$\frac{\mu_\omega}{1 + \mu_\omega^2 B^2} = \mu_o \left[\frac{1 + \mu_o^2 B^2 + \omega^2\tau^2}{(1 + \mu_o^2 B^2 - \omega^2\tau^2)^2 + 4\omega^2\tau^2} + j\omega\tau \frac{\mu_o^2 B^2 - \omega^2\tau^2 - 1}{(1 + \mu_o^2 B^2 - \omega^2\tau^2)^2 + 4\omega^2\tau^2} \right.$$

(2.28)

The real part of $\underline{\underline{\sigma}}_c$ will contribute to the conduction process within the bulk material and will be denoted by $\underline{\underline{\sigma}}$, while the imaginary part will be responsible for the change in the material's dielectric constant. This change is given by the imaginary part of $\underline{\underline{\sigma}}_c$ divided by the product of the angular frequency and the permittivity of free space κ_o. Therefore,

$$\underline{\underline{\sigma}} = \mathrm{Re}(\underline{\underline{\sigma}}_c) \tag{2.29}$$

and

$$\epsilon_r = \epsilon_\ell + \mathrm{Im}(\underline{\underline{\sigma}}_c)/(\omega\kappa_o) \quad , \tag{2.30}$$

where κ_o is the permittivity of free space and ϵ_ℓ is the lattice dielectric constant of the material.

Since InSb is isotropic, the functional dependence of the conductivity and dielectric constant can be written by substituting Eqs. 2.26 through 2.30 into 2.13 which yields

$$\sigma = q\left[n_c\mu_{co}\frac{1+\mu_{co}^2B^2+\omega^2\tau_c^2}{(1+\mu_{co}^2B^2-\omega^2\tau_c^2)^2+4\omega^2\tau_c^2}\right.$$

$$\left.+\,n_i\mu_{io}\frac{1+\mu_{io}^2B^2+\omega^2\tau_i^2}{(1+\mu_{io}^2B^2-\omega^2\tau_i^2)^2+4\omega^2\tau_i^2}\right] \quad (2.31)$$

and

$$\epsilon_r = \epsilon_\ell + \frac{q^2}{\omega^2\kappa_o}\left[\frac{n_{co}}{m_c^*}\,\frac{(\mu_{co}^2B^2-\omega^2\tau_c^2-1)\omega^2\tau_c^2}{(1+\mu_{co}^2B^2-\omega^2\tau_c^2)^2+4\omega^2\tau_c^2}\right.$$

$$\left.+\,\frac{n_{io}}{m_i^*}\,\frac{(\mu_{io}^2B^2-\omega^2\tau_i^2-1)\omega^2\tau_i^2}{(1+\mu_{io}^2B^2-\omega^2\tau_i^2)^2+4\omega^2\tau_i^2}\right] \quad , \quad (2.32)$$

where μ_{co} and μ_{io} are the dc mobilities in the conduction and impurity bands. In order to determine the dependence of n_c and n_i on the magnetic field, the cyclotron radius of the individual carriers is compared with r_s. A carrier will belong to the conduction band if r_c is greater than r_s, and to the impurity band if the opposite is true. The average speed v_o at which the cyclotron radius equals the occupancy radius r_s is given by

$$v_o = \frac{qr_s}{m^*}B \quad .$$

Substituting the value of r_s as defined in Eq. 2.5 yields*

---

* In obtaining this value of v_o, all the carriers are assumed to be in the conduction band in the absence of a magnetic field.

$$v_o = \frac{q}{m^*}\left(\frac{3}{4\pi N_I}\right)^{1/3} B \quad . \tag{2.33}$$

Therefore, in the presence of magnetic induction B, those electrons whose speed in the plane normal to B is greater than v_o will belong to the conduction band, while the rest will be in the impurity band. Among N_I particles having a Maxwellian distribution and an effective temperature T_e, the number of particles n'_{v_o} whose speed in an arbitrary plane is greater than v_o is given by

$$n'_{v_o} = N_I \exp\left(-\frac{m^* v_o^2}{2kT_e}\right) \quad . \tag{2.34}$$

Combining Eqs. 2.34, 2.33 and 2.14 yields

$$n_c = N_I e^{-bB^2} \tag{2.35}$$

and

$$n_i = N_I(1 - e^{-bB^2}) \quad , \tag{2.36}$$

where

$$b = \frac{q^2}{2m^* kT_e}\left(\frac{3}{4\pi N_I}\right)^{2/3} \quad . \tag{2.37}$$

Substituting the values of n_c and n_i, as obtained in Eqs. 2.35 and 2.36, into Eqs. 2.31 and 2.32, the following expressions for ϵ_r and σ are obtained

$$\sigma = qN_I \left(\mu_{co} \frac{1 + \mu_{co}^2 B^2 + \omega^2\tau_c^2}{(1 + \mu_{co}^2 B^2 - \omega^2\tau_c^2)^2 + 4\omega^2\tau^2} e^{-bB^2} \right.$$

$$\left. + \mu_{io} \frac{1 + \mu_{io}^2 B^2 + \omega^2\tau_i^2}{(1 + \mu_{io}^2 B^2 - \omega^2\tau_i^2)^2 + 4\omega^2\tau_i^2} (1 - e^{-bB^2}) \right) \qquad (2.38)$$

and

$$\epsilon_r = \epsilon_\ell + \frac{qN_I}{\omega^2\kappa_o} \left(\frac{1}{m_c^*} \frac{(\mu_{co}^2 B^2 - \omega^2\tau_c^2 - 1)\omega^2\tau_c^2}{(1 + \mu_{co}^2 B^2 - \omega^2\tau_c^2)^2 + 4\omega^2\tau^2} e^{-bB^2} \right.$$

$$\left. + \frac{1}{m_i^*} \frac{(\mu_{io}^2 B^2 - \omega^2\tau_i^2 - 1)\omega^2\tau_i^2}{(1 + \mu_{io}^2 B^2 - \omega^2\tau_i^2)^2 + 4\omega^2\tau_i^2} (1 - e^{-bB^2}) \right) . \qquad (2.39)$$

Taking the limits of Eq. 2.38 for zero and large values of the magnetic field yields,

$$\sigma_o = \frac{qN_I\mu_{co}}{1 + \omega^2\tau^2} \qquad (2.40)$$

and

$$\sigma_{B+} = qN_I\mu_{io} \left(\frac{1 + \mu_{io}^2 B^2 + \omega^2\tau_i^2}{(1 + \mu_{io}^2 B^2 - \omega^2\tau^2)^2 + 4\omega^2\tau_i^2} \right) . \qquad (2.41)$$

The corresponding values for the dielectric constant are

$$\epsilon_o = \epsilon_\ell - \frac{q^2 N_I}{\omega^2 \kappa_o m_c^*} \left(\frac{\omega^2 \tau_c^2}{1 + \omega^2 \tau_c^2} \right) \tag{2.42}$$

and

$$(\epsilon_r)_{B^+} = \epsilon_\ell + \frac{q^2 N_I}{\omega^2 m_i^* \kappa_o} \left(\frac{(\mu_{io}^2 B^2 - \omega^2 \tau_i^2 - 1)\omega^2 \tau_i^2}{(1 + \mu_{io}^2 B^2 - \omega^2 \tau_i^2)^2 + 4\omega^2 \tau_i^2} \right) . \tag{2.43}$$

It is quite instructive to investigate the functional dependence of σ and ϵ_r in the presence of a small magnetic field; this investigation will prove useful when comparing the theory to the experiment. Figure 2.3 shows the relative number of carriers in the impurity and conduction bands at 77°K as described by Eqs. 2.35 and 2.36 for an impurity concentration of 5×10^{13} cm^{-3} as a function of the applied magnetic field. This figure shows that for a magnetic field less than 1.5 kG essentially all the carriers are in the conduction band. This factor, added to the fact that the carrier's mobility in the impurity band is much less than that in the conduction band, will cause the contribution of the carriers in the impurity band to the conductivity and the change in the dielectric constant to be negligible. Therefore for small values of the magnetic field σ and ϵ_r are approximately given by

$$\sigma = qN_I \mu_{co} \left(\frac{1 + \mu_{co}^2 B^2 + \omega^2 \tau_o^2}{(1 + \mu_{co}^2 B^2 - \omega^2 \tau_c^2)^2 + 4\omega^2 \tau^2} e^{-bB^2} \right) \tag{2.44}$$

and

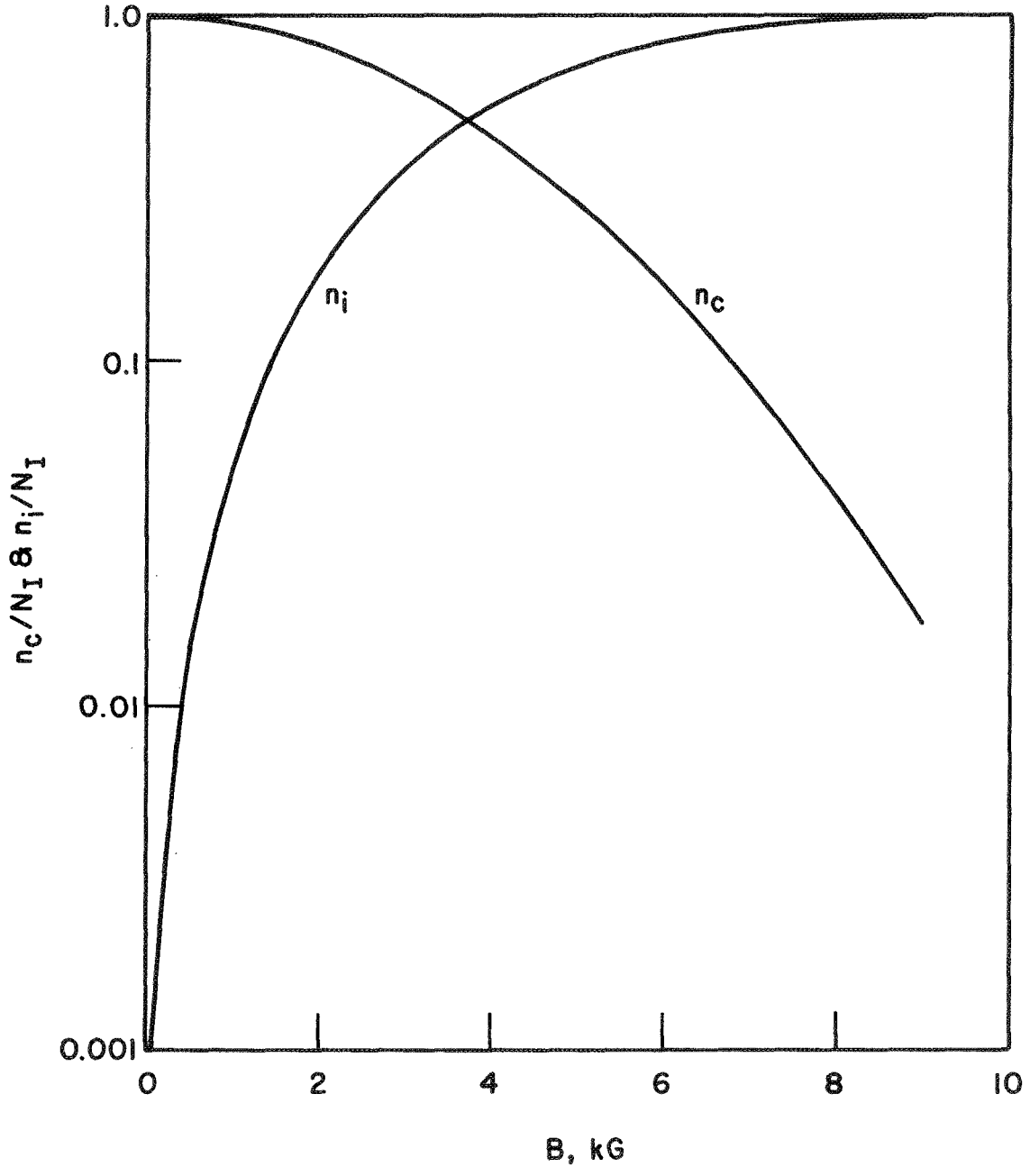

FIG. 2.3 RELATIVE CARRIER CONCENTRATIONS IN THE IMPURITY AND CONDUCTION BANDS VS. B AT 77°K. ($n = 5 \times 10^{13}$ cm^{-3}, $e^* = 0.42$)

$$\epsilon_r = \epsilon_\ell + \frac{qN_I}{\omega^2 \kappa_o m_c^*} \left(\frac{(\mu_{co}^2 B^2 - \omega^2\tau_c^2 - 1)\omega^2\tau_c^2}{(1 + \mu_{co}^2 B^2 - \omega^2\tau_c^2)^2 + 4\omega^2\tau_c^2} e^{-bB^2} \right) . \quad (2.45)$$

Differentiating Eq. 2.44 with respect to B^2 and equating the results to zero gives

$$ay^3 + [1 + a(3 - z)]y^2 + [2(1 + z) + a(3 + 2z - z^2)]y$$

$$+ [1 - 2z - 3z^2 + a(1 + 3z + 3z^2 + z^3)] = 0 \quad , \quad (2.46)$$

where $a = b/\mu_{co}^2$, $y = \mu_{co}^2 B^2$ and $z = \omega^2\tau_c^2$. If a real positive root exists for Eq. 2.46 the σ-B characteristic will have a critical point at some value of the magnetic field B_o. To investigate this case further it is worth noting that, for all materials of interest (samples with high mobilities) and values of magnetic fields below 1.5 kG, both a and (a·y) are small compared to one. This reduces Eq. 2.46 to the following form

$$y^2 + 2(1 + z)y + (1 - 2z - 3z^2) = 0 \quad , \quad (2.47)$$

which gives the following value of y

$$y = -(1 + z) \pm 2\sqrt{z(1 + z)} \quad .$$

Since y is a positive semidefinite quantity, the solution with the negative sign is insignificant. Therefore

$$y = -(1 + z) + 2\sqrt{z(1 + z)} \quad , \quad (2.48)$$

and the σ-B characteristic has a critical point for a real value of B if y > 0 which implies,

$$\omega\tau_c \geq \frac{1}{\sqrt{3}} \quad . \tag{2.49}$$

The second derivative of σ with respect to y was investigated and turned out to be negative irrespective of the value of z. This shows that if the condition defined by Eq. 2.49 is fulfilled σ will assume a maximum. The value of the magnetic field B_o at which the maximum value of σ occurs is given by

$$B_o = \frac{1}{\mu_{co}} \left[2\omega\tau_c \sqrt{1 + \omega^2\tau_c^2} - (1 + \omega^2\tau_c^2) \right]^{1/2} \quad . \tag{2.50}$$

Solving Eq. 2.46 for z yields

$$\omega^2\tau_c^2 = \frac{1}{3} \left[(\mu_{co}^2 B_o^2 - 1) \pm \sqrt{2(\mu_{co}^2 B_o^2 - 1)^2 + 4\mu_{co}^2 B_o^2} \right] \quad .$$

The solution with the negative sign can be disregarded as being physically insignificant. Therefore

$$\omega^2\tau_c^2 = \frac{1}{3} \left[(\mu_{co}^2 B_o^2 - 1) + \sqrt{2(\mu_{co}^2 B_o^2 - 1)^2 + 4\mu_{co}^2 B_o^2} \right] \quad . \tag{2.51}$$

The equation expresses the carrier relaxation time τ_c as a function of the dc mobility μ_{co} and the magnetic field B_o. This suggests an indirect meansfor the measurement of the carrier relaxation time if the frequency of the monitoring microwave signal is chosen to satisfy Eq. 2.49.

2.3 Experimental Investigation

Experiments were carried out at five temperatures between liquid nitrogen and room temperature to verify the previous analysis. In all the experiments samples were cut from lapped slices of high purity n-type single crystal InSb. The samples were cut with a wire saw using a slurry consisting of equal weights of glycerine and 240 mesh silicon carbide abrasive. Five-mil wire and light pressure were used and the samples were cleaned using chemically pure grade benzene. To provide protection for the samples, the unused ones were kept in a container filled with paraffin oil. The sample had dimensions of 1 x 2 x 4 mm and the manufacturer* supplied the data shown in Table 2.1.

Table 2.1

Manufacturer's Data for the InSb Samples at 77°K

Resistivity = 0.26 to 0.28 Ω-cm

Hall mobility = 6.1 to 6.2 x 10^5 cm^2 $V\text{-}s^{-1}$

Net carrier concentration ≅ 4 x 10^{13} cm^{-3}

The sample was placed under the central post of a reentrant-type cavity system as shown in Fig. 2.4. The cavity system was sealed in vacuum in order to overcome the problems arising from liquid nitrogen cooling and eliminate the effect of humidity on the resonance frequency shift and the change in the coupling factor measurements. The cavity setup with the vacuum-tight jacket was placed in a stainless steel dewar

---

* Cominco American Incorporated.

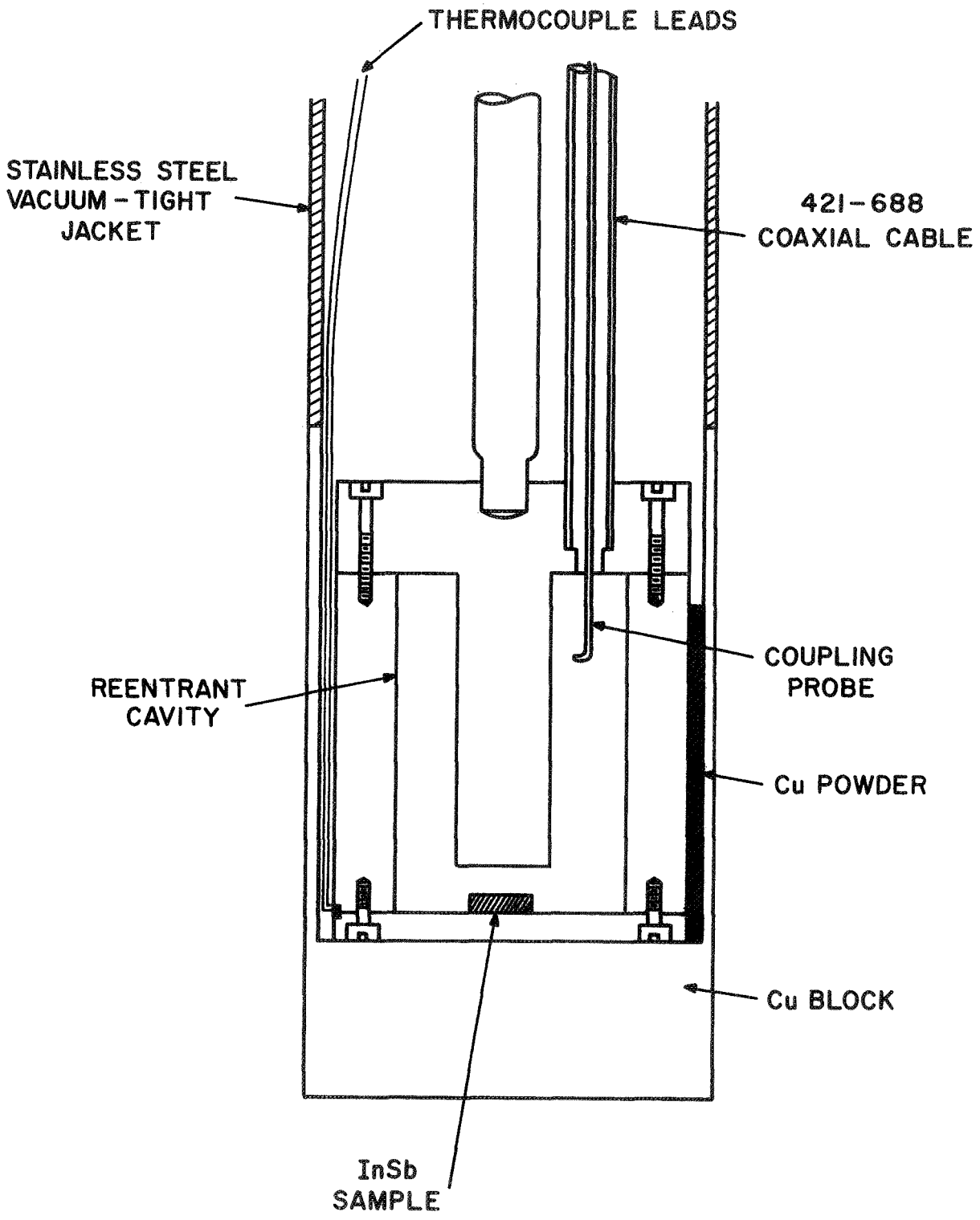

FIG. 2.4 CAVITY SYSTEM FOR TESTING THE MATERIAL PROPERTIES.

mounted between the pole pieces of an electromagnet. Thermal contact between the liquid nitrogen bath and the cavity was achieved by filling the space between the cavity walls and the vacuum jacket with copper powder. A copper-constantan thermocouple was used to monitor the temperature of the sample. Intermediate temperatures between liquid nitrogen and room temperature were investigated by contacting the cavity to a large copper block to provide a thermal load. The temperature of the evacuated cavity system was monitored as it warmed up very slowly to room temperature.

Expressions relating the change in the reflected power and resonance frequency shift of the cavity system to the conductivity and dielectric constant of the material will be derived in Chapter III. Figure 2.5 shows the microwave circuit used to measure these quantities. In carrying out the measurements any mismatch loss must be reduced to a minimum especially between the circulator and the cavity or the calibrated crystal detector. The loss due to the cavity is comprised of two parts, a mismatch loss at the coupling hole and an insertion loss introduced by the attenuation in the coaxial line. These losses are separable and each can be accounted for when analyzing the experimental results. The slide-screw tuner No. 2 is used to match the 1N23C calibrated crystal detector to the circulator. On the other hand, the isolator and the attenuating pad at the input port reduce the effect of any mismatch loss that may be present in the line. At each operating temperature the cavity Q and coupling factor and the line loss were measured. A knowledge of these parameters is necessary for obtaining the desired data as will be shown in Chapter III. Figure 2.6 shows typical cavity

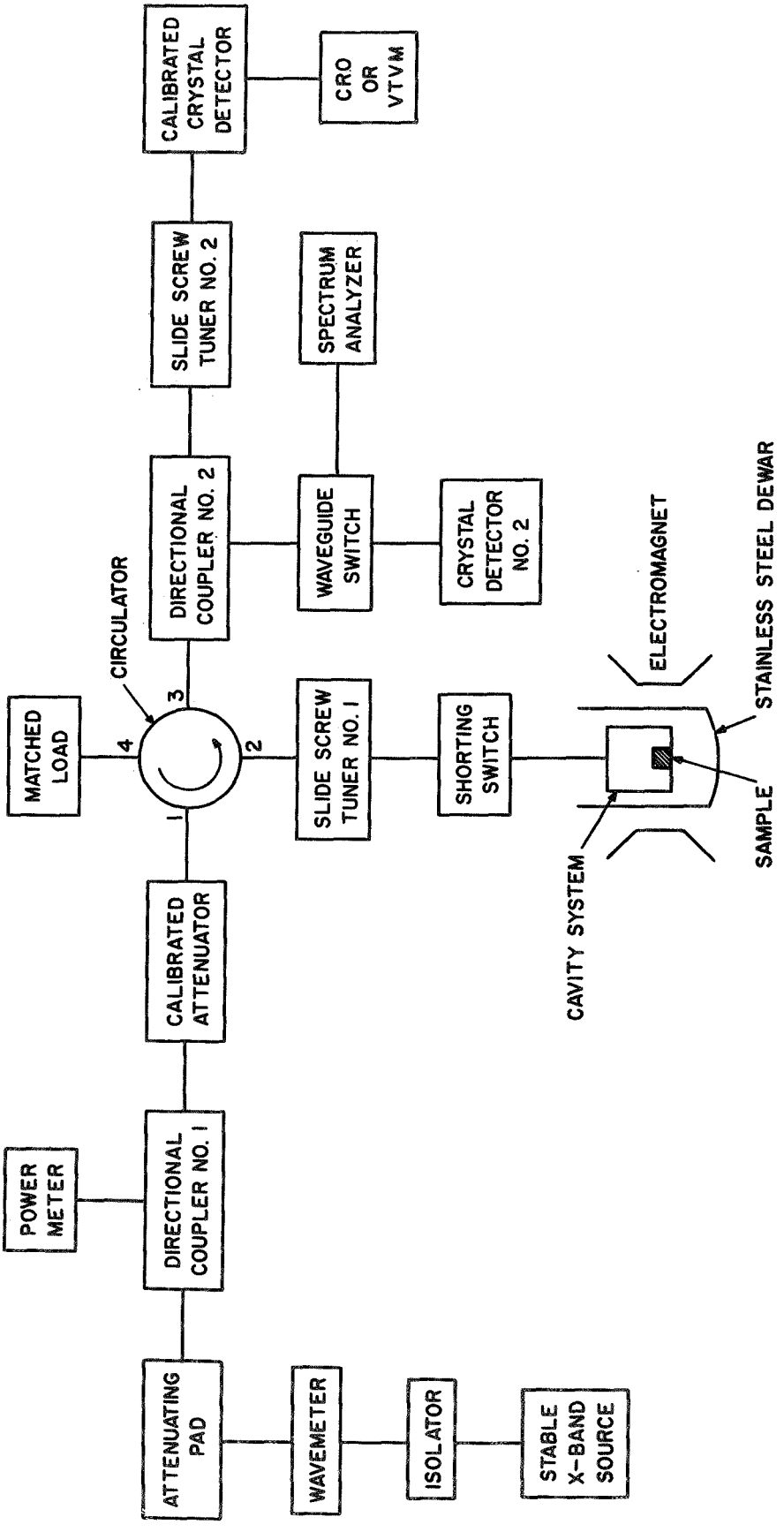

FIG. 2.5 MICROWAVE CIRCUIT FOR INVESTIGATION OF THE MATERIAL PROPERTIES.

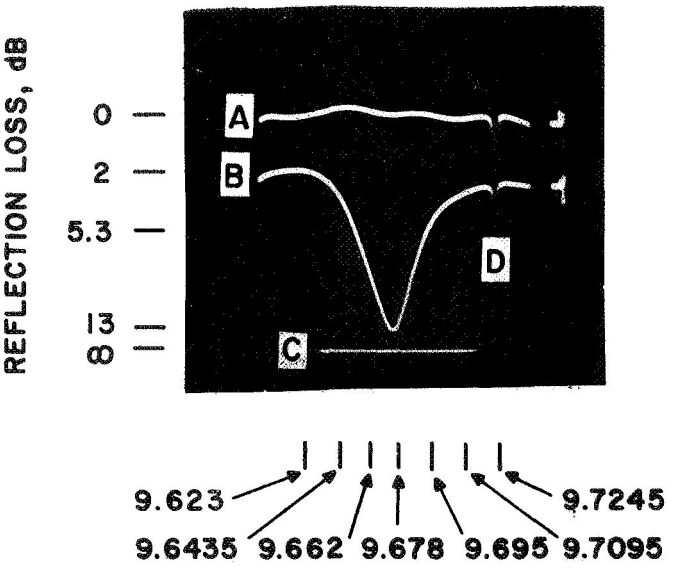

FIG. 2.6 MICROWAVE CAVITY CHARACTERISTICS.

characteristics as displayed on an oscilloscope. Such a display is utilized to determine the cavity Q and the coupling factor by using a modification on the reflectometer method described by Sucher.[46] All the experiments at liquid nitrogen temperature and above were carried out under vacuum seal and corrections were made to compensate for the shift in resonance frequency and coupling factor as a result of the temperature change. These factors will be discussed in more detail in Chapter III. In all cases the experiments were carried out for three different orientations of the magnetic field with respect to the (110)-crystal plane.

2.4 Analysis of the Results

This section deals with the experimental results concerning the change in the conductivity and dielectric constant of InSb as a function of the magnetic field at different temperatures. The test signal was supplied by an ultrastable oscillator which was stabilized at the cavity resonance frequency of 9.675 GHz, and the signal level was varied between -2 and -11 dBm. The experiments were carried out at temperatures of 4.2, 77, 170, 200 and 300°K. In each case the change of the detected power was monitored as the magnetic field was varied between zero and 8.8 kG.

Figure 2.7 shows the relative change in the detected power with respect to the power available from the source vs. B at 77°K when the magnetic field is parallel to the (110)-plane. This set of curves serves two purposes; namely, it will be used to illustrate how to determine the relative change of conductivity from the experimentally

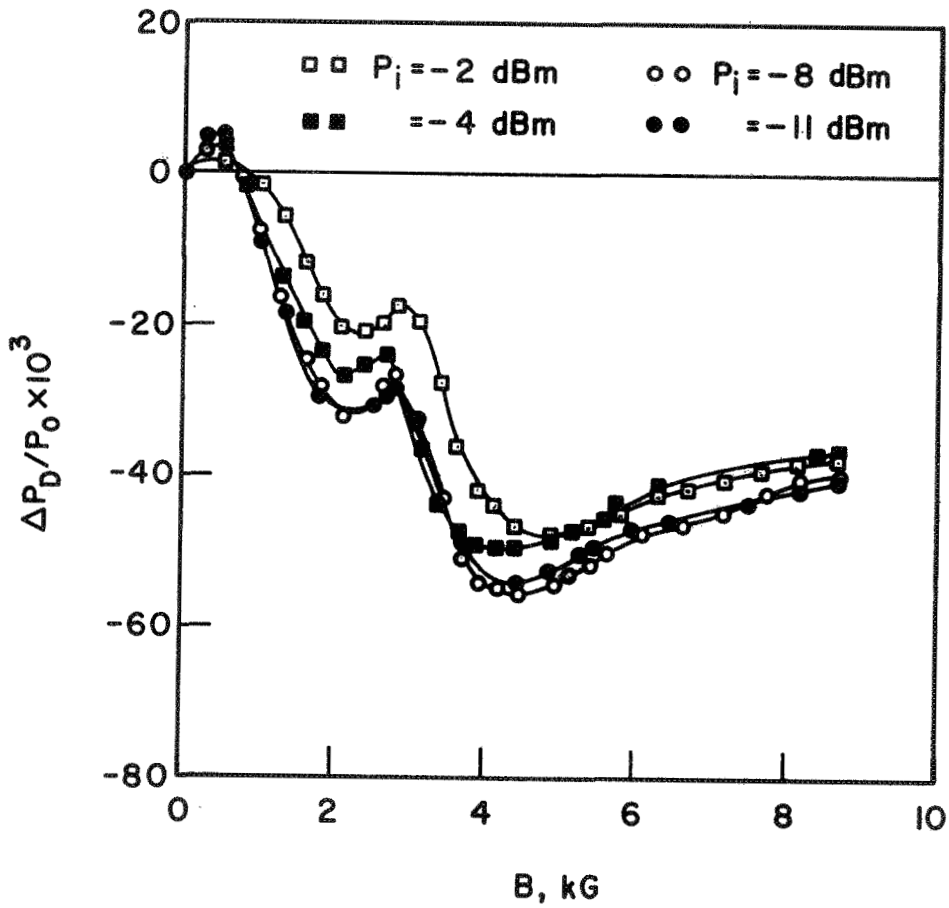

FIG. 2.7 THE MEASURED RELATIVE CHANGE IN THE DETECTED POWER AT 77°K [B IS PARALLEL TO THE (110)-CRYSTAL PLANE].

measured quantities and also as a check on the measurement theory presented in Chapter III. The curves indicate a cyclotron resonance absorption whose peak occurs at a magnetic field B_c of approximately 2.9 kG. Assuming the material to be compensated, this resonance could be due to carriers in the impurity, valence or conduction bands. The effective mass corresponding to this peak can be obtained by equating the cyclotron resonance frequency to the frequency of the incident radiation, i.e.,

$$\omega = \frac{q}{m} B_c \quad , \tag{2.52}$$

where ω is the angular frequency of the incident radiation. Substituting the values for ω, q and B_c gives a value for m which equals 0.78 times the electronic mass. The effective mass of the electrons at the edge of the conduction band was determined a long time ago and was confirmed recently[47,48] as having a value of 0.0139 m. On the other hand, the effective mass of the holes in InSb was shown[49,50] to be 0.4 m. This leads to the conclusion that the resonance is due to carriers in the impurity band. Therefore m_i^*, the effective mass of the carriers in the impurity band, equals 0.78 m. The ratio of the effective mass in the impurity band to that in the conduction band at liquid nitrogen temperature is therefore approximately equal to 58.8. The scattering mechanisms for this temperature and above are dominated by either acoustic or polar modes which lead to a mobility proportional to $(m^*)^{-5/2}$ in the first case and $(m^*)^{-3/2}$ in the latter case. Therefore the ratio of the mobility

of the carriers in the impurity band to that in the conduction band is at most 0.0025; this justifies neglecting the contribution of the carriers in the impurity band to the conduction process for temperatures equal to or above liquid nitrogen temperature.

Figure 2.7 can also be used to check the accuracy of the experimental results and how they compare to the theoretical analysis. It is seen from this figure that above a magnetic field of 3 kG the change in the detected power from the undercoupled cavity decreases with increasing magnetic field until it reaches a minimum where it starts increasing again. The cavity becomes critically coupled at the point of minimum detectable power and changes to an overcoupled one as it passes through it. Table 2.2 shows the theoretical and experimental values of the relative change in the detected power at the critical points for the power levels and coupling factors used in the experimental investigation. The agreement between theory and experiment is excellent.

Table 2.2

The Relative Change in the Detected Power at the Critical Points

Incident Power (dBm)	β_o †	Measured $\Delta P_D/P_o$ ††	Calculated $\Delta P_D/P_o$ ††
-2	0.64	48×10^{-3}	48.16×10^{-3}
-4	0.64	49.5×10^{-3}	48.16×10^{-3}
-8	0.60	55.5×10^{-3}	62.5×10^{-3}
-11	0.60	54.5×10^{-3}	62.5×10^{-3}

† β_o is the cavity coupling factor at zero magnetic field.

†† Both columns are normalized to the case of lossless coupling.

2.4.1 Behavior of the Conductivity at Liquid Nitrogen Temperature. Figures 2.8 through 2.10 display the relative change (relative to σ at $B = 0$) in the conductivity of the InSb sample as a function of the magnetic field, measured at 77°K. In comparing these results to the theory derived earlier, the contribution of the carriers in the impurity band to the conductivity will be neglected. This was shown to be the case in the previous section. Since the graphs exhibit peaks at a magnetic field B_o whose value is 1.25 kG, Eq. 2.50 can be used in conjunction with Eq. 2.44 to compare the experimental and theoretical results. The relative change in the conductivity can be obtained from Eq. 2.44 and is given by

$$\frac{\sigma - \sigma_o}{\sigma_o} = \frac{(1 + \mu_{co}^2 B^2 + \omega^2\tau_c^2)(1 + \omega^2\tau_c^2)}{(1 + \mu_{co}^2 B^2 - \omega^2\tau_c^2) + 4\omega^2\tau_c^2} e^{-bB^2} - 1 \quad . \tag{2.53}$$

The mobility is related to the magnetic field B_o and $\omega\tau_c$ by Eq. 2.50 and can be written as

$$\mu_{co} = \frac{1}{B_o}\left[2\omega\tau_c\sqrt{1 + \omega^2\tau_c^2} - (1 + \omega^2\tau_c^2)\right]^{1/2} \quad . \tag{2.54}$$

The net carrier concentration N_I was determined by carrying out a set of Hall measurements on the sample which gave a value of 5×10^{13} cm^{-3}, which is in fair agreement with the data supplied by the manufacturer. This value was substituted in Eq. 2.37 to determine the value of b. Equations 2.53 and 2.54 were numerically programmed using

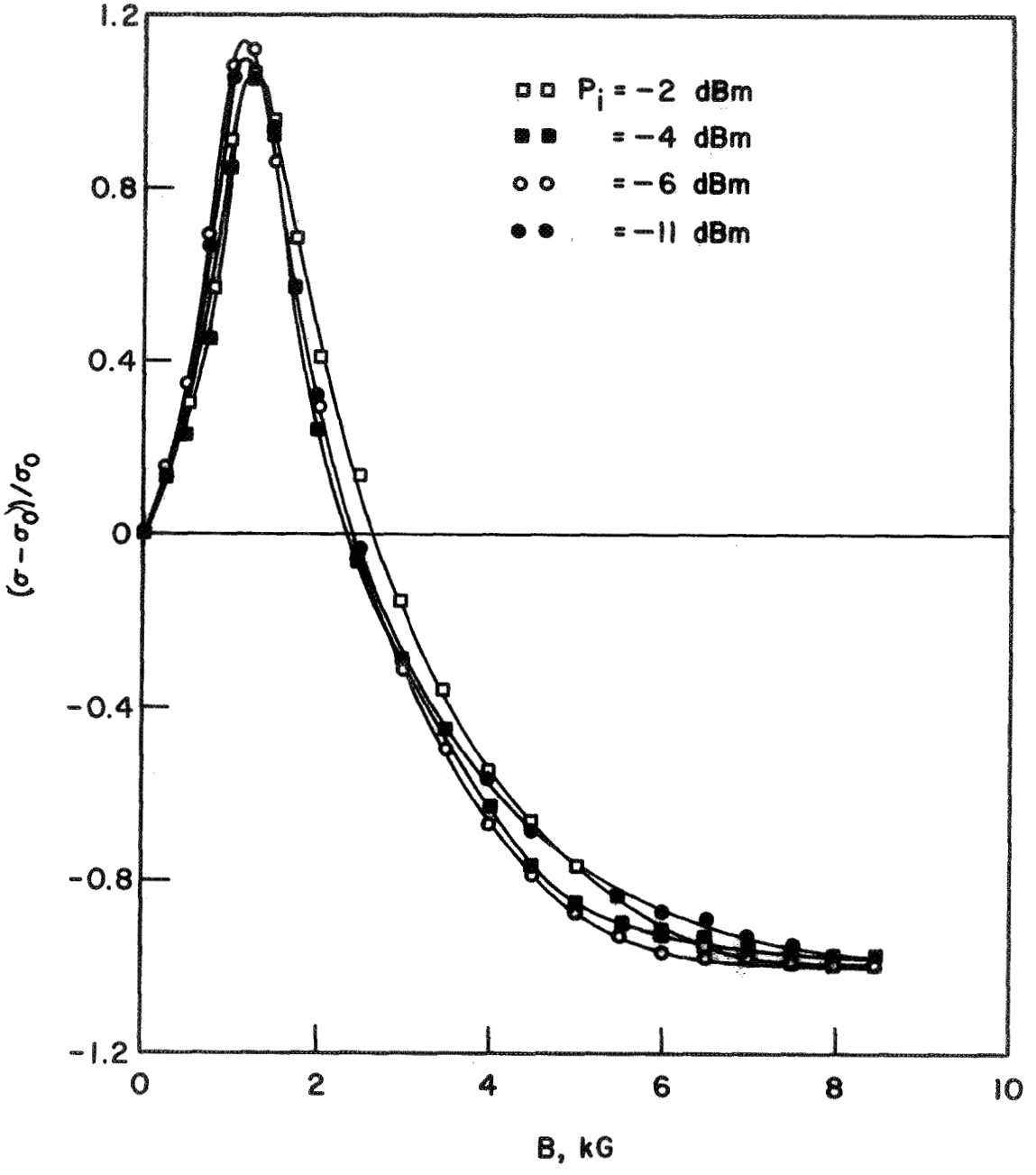

FIG. 2.8 $(\sigma-\sigma_o)/\sigma_o$ VS. B AT 77°K [B IS PARALLEL TO THE (110)-CRYSTAL PLANE].

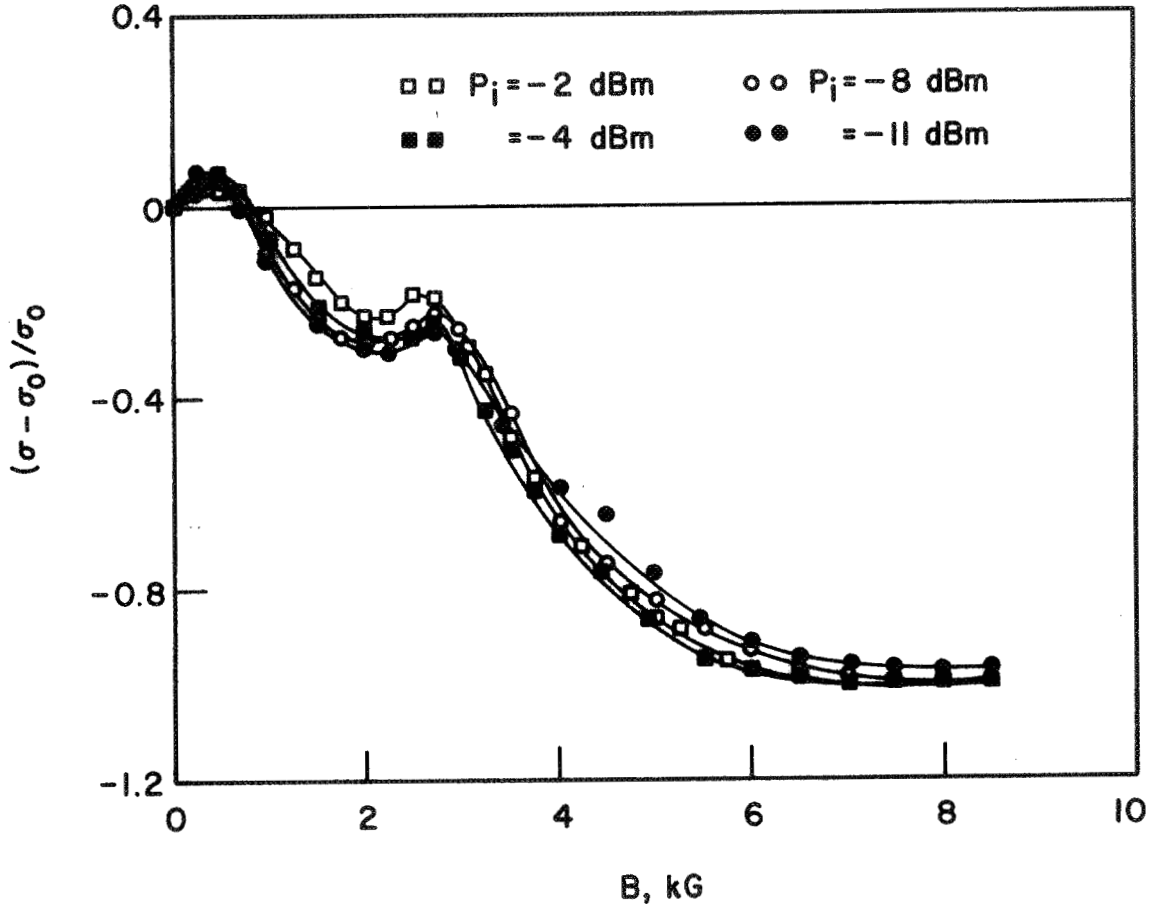

FIG. 2.9 $(\sigma - \sigma_o)/\sigma_o$ VS. B AT 77°K [B IS NORMAL TO THE (110)-CRYSTAL PLANE].

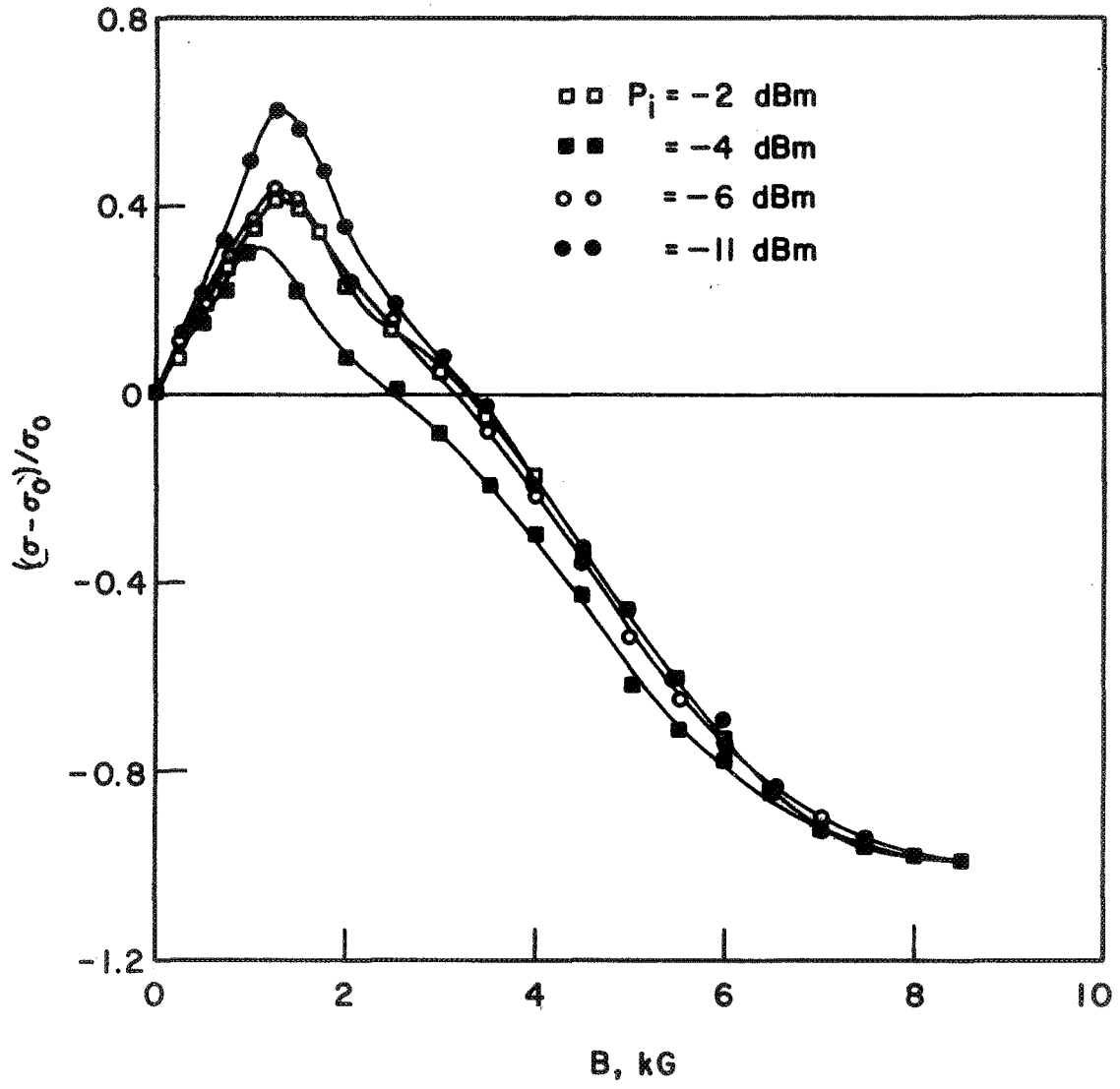

FIG. 2.10 $(\sigma - \sigma_o)/\sigma_o$ VS. B AT 77°K [B IS 45 DEGREES TO THE (110)-CRYSTAL PLANE].

the determined values of B_o and b and taking $\omega\tau_c$ as a variable parameter until the best fit to the experimental results was obtained. Figure 2.11 shows a comparison between the theoretical and experimental results. The deviation of the experimental results from the theoretical ones between 2.0 and 4.5 kG can be attributed to the cyclotron resonance absorption which has not been taken into account in the theoretical analysis. The relative change in the conductivity due to resonance absorption $\Delta\sigma_{cr}/\sigma_o$ vs. B can be obtained by subtracting the theoretical results expressed by Eq. 2.53 from the experimental results. A plot of $\Delta\sigma_{cr}/\sigma_o$ was included in Fig. 2.11 which shows a peak at 2.9 kG which is in agreement with the results obtained earlier for the other orientation of the magnetic field.

The value of the magnetic field B_{Fh} at which 90 percent of the carriers are in the impurity band was found to be 5.75 kG. This value compares very favorably with the theoretical value of 6.5 kG obtained from Fig. 2.1. Figures 2.8 through 2.10 also show that the relative change of the material's conductivity at liquid nitrogen and higher temperatures is independent of the incident power level. This indicates that the mobility of the free carriers is independent of the electric field intensity within the sample. Therefore, the free-carrier absorption contribution to the conductivity change is negligible for this temperature range.

2.4.2 Results at Temperatures Above Liquid Nitrogen. This section deals with the behavior of the sample's conductivity at temperatures above liquid nitrogen as a function of the magnetic field and the incident

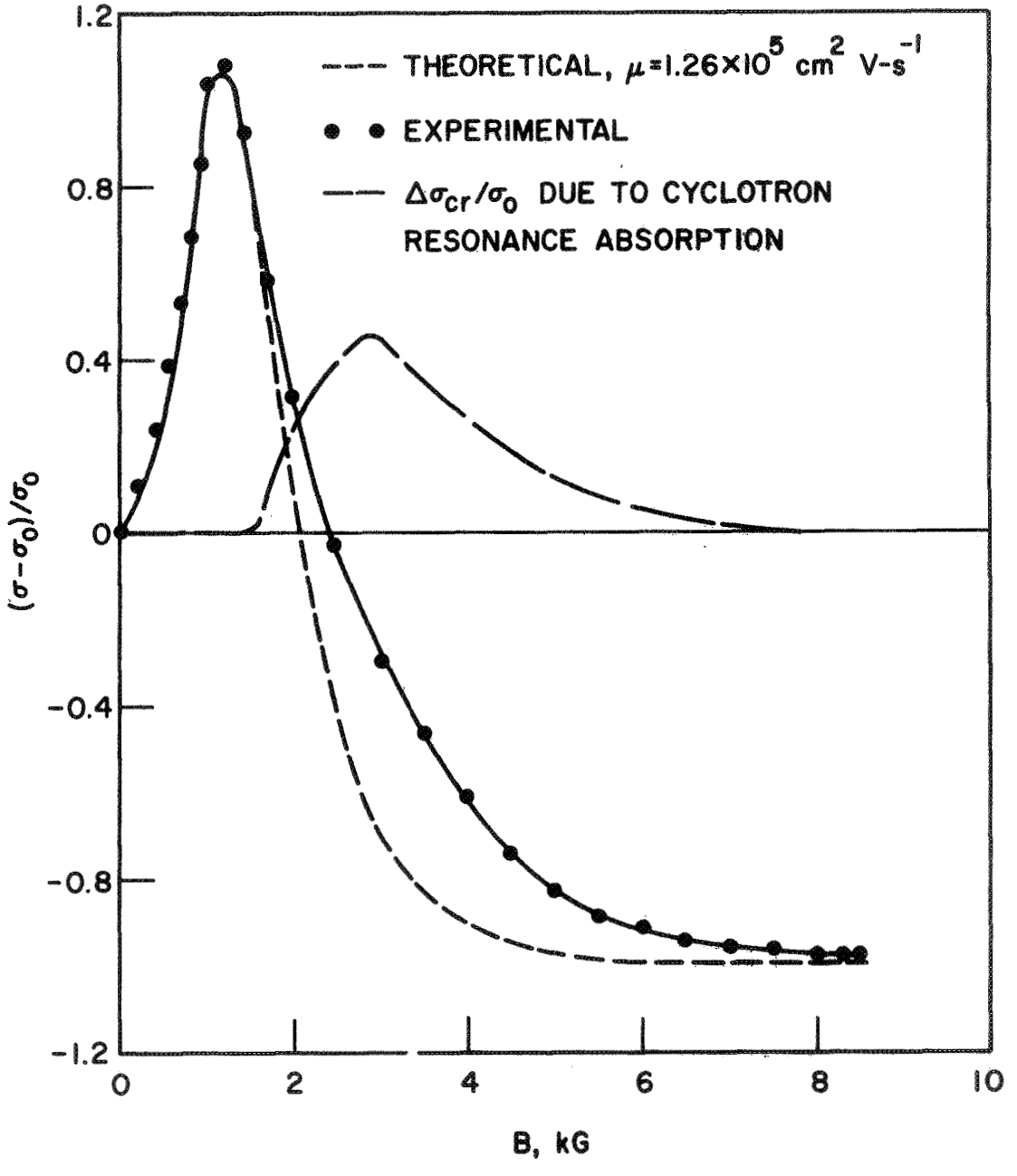

FIG. 2.11 COMPARISON OF THE THEORETICAL AND EXPERIMENTAL RESULTS OF $(\sigma - \sigma_o)/\sigma_o$ AT 77°K [B IS PARALLEL TO THE (110)-CRYSTAL PLANE].

microwave radiation. The experimental procedure is the same at all temperatures except at room temperature. At this temperature the change in the detected voltage as a result of the perturbation is very small, and in order to improve the accuracy of the measurements the change in the detected signal was amplified using a differential amplifier. In comparing the experimental and theoretical results the value of the intrinsic concentration was used in place of N_I in Eq. 2.53, since the material is essentially intrinsic at these temperatures and the hole mobility is much smaller than the electron mobility. Table 2.3 shows the intrinsic carrier concentration of InSb at the temperature of interest. It is clear from the table that the intrinsic concentration above 175°K is much higher than the net carrier concentration measured at 77°K (5×10^{13} cm^{-3}). Moreover the values cited in the table agree with those obtained by Hall measurements at 290°K.

Table 2.3

Intrinsic Carrier Concentration in InSb

Temperature (°K)	Intrinsic Concentration (cm^{-3})
77	2.5×10^{9}
175	3.5×10^{14}
200	1.13×10^{15}
295	2.15×10^{16}

Figures 2.12 through 2.19 show the experimental results for the relative change in the conductivity vs. magnetic field. The main conclusions from these plots are:

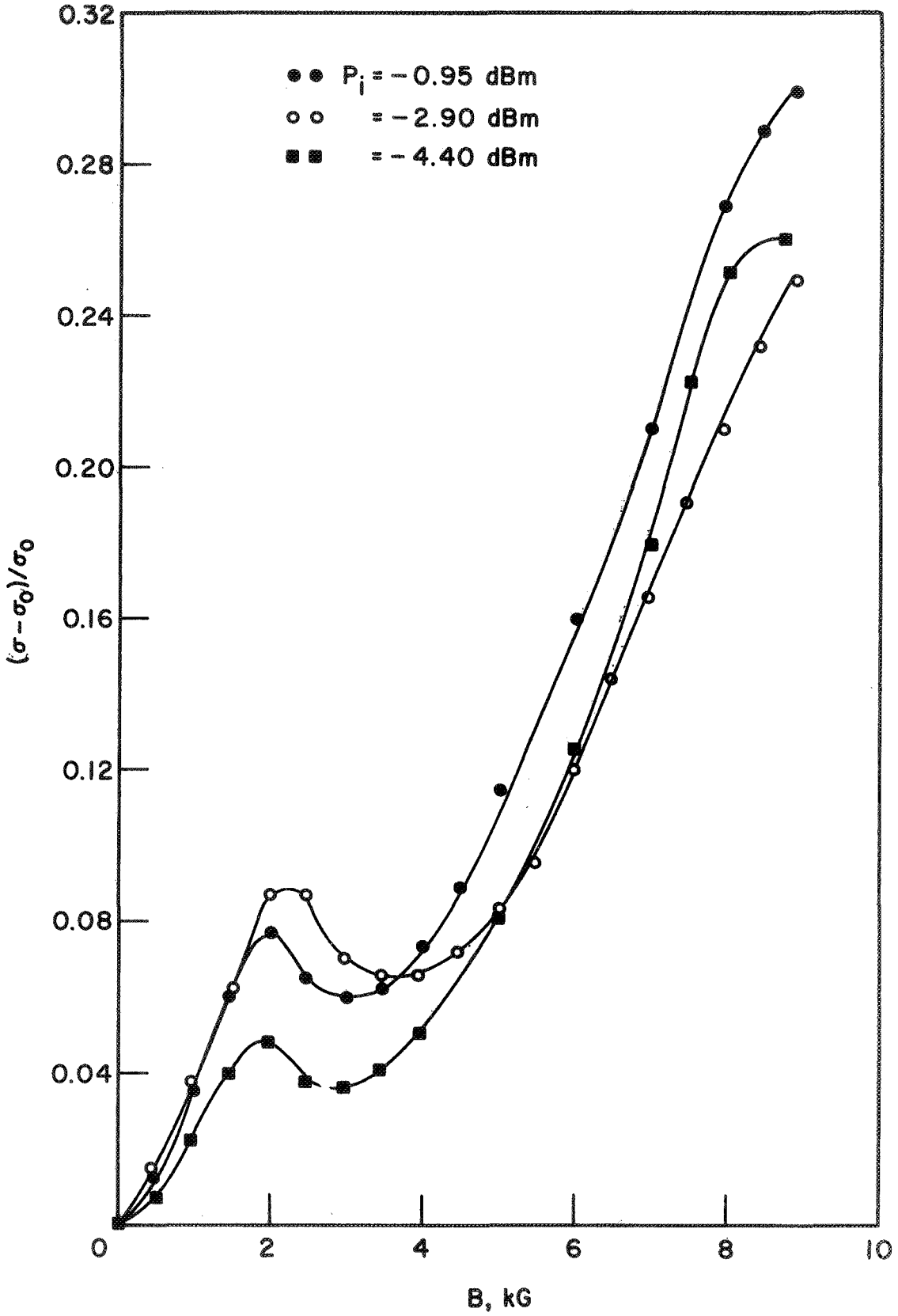

FIG. 2.12 $(\sigma - \sigma_o)/\sigma_o$ VS B AT 175°K [B IS PARALLEL TO THE (110)-CRYSTAL PLANE].

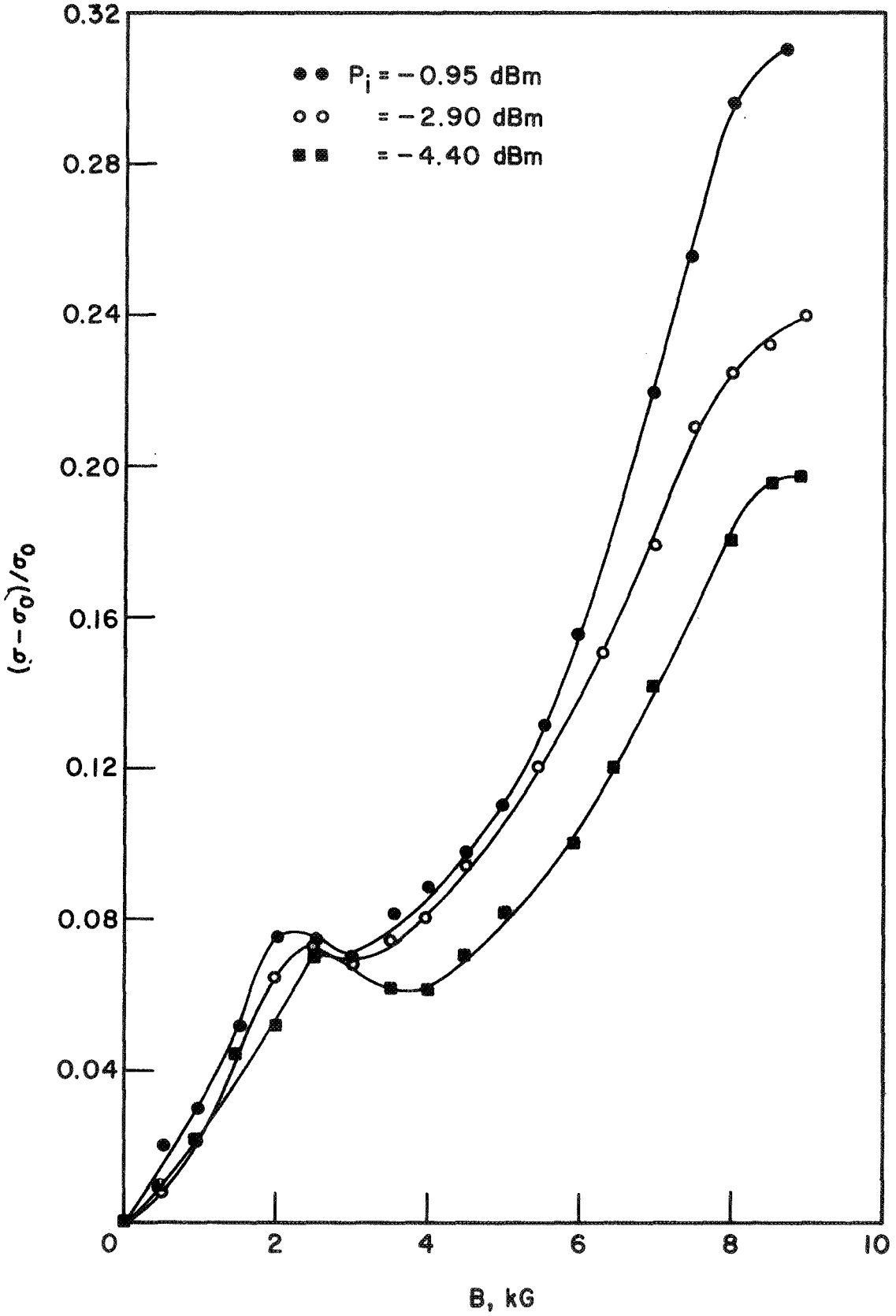

FIG. 2.13 $(\sigma - \sigma_o)/\sigma_o$ VS. B AT 175°K [B IS 45 DEGREES TO THE (110)-CRYSTAL PLANE].

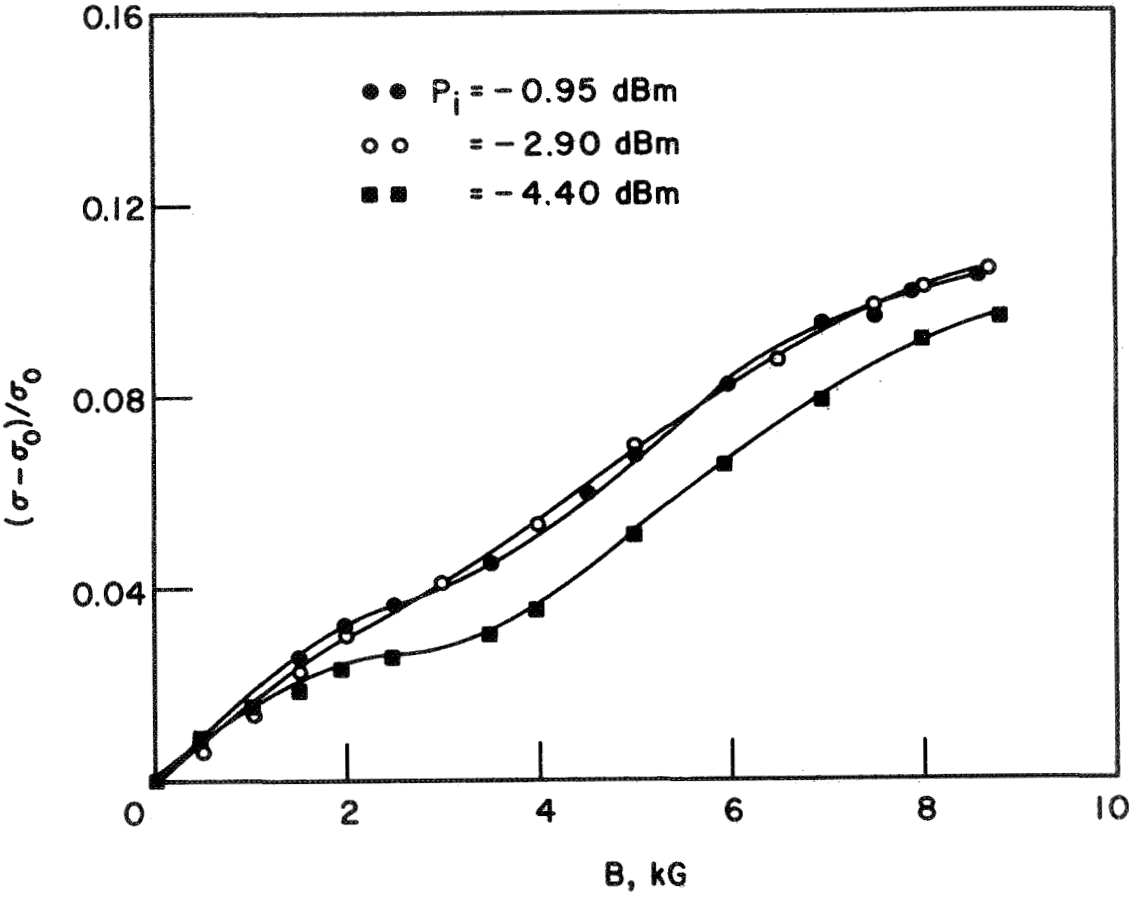

FIG. 2.14 $(\sigma - \sigma_o)/\sigma_o$ VS. B AT 175°K [B IS NORMAL TO THE (110)-CRYSTAL PLANE].

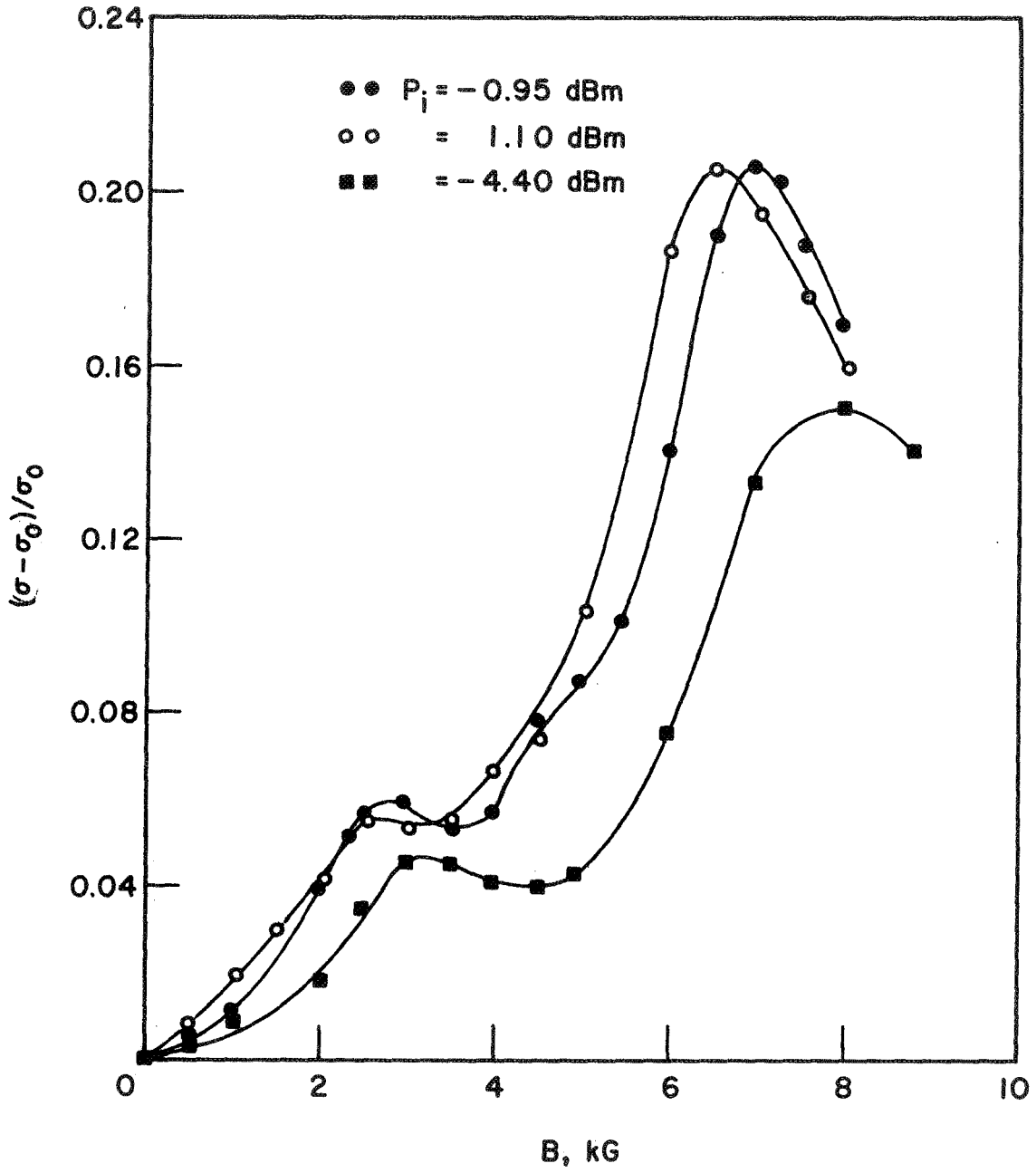

FIG. 2.15 $(\sigma - \sigma_o)/\sigma_o$ VS. B AT 200°K [B IS PARALLEL TO THE (110)-CRYSTAL PLANE].

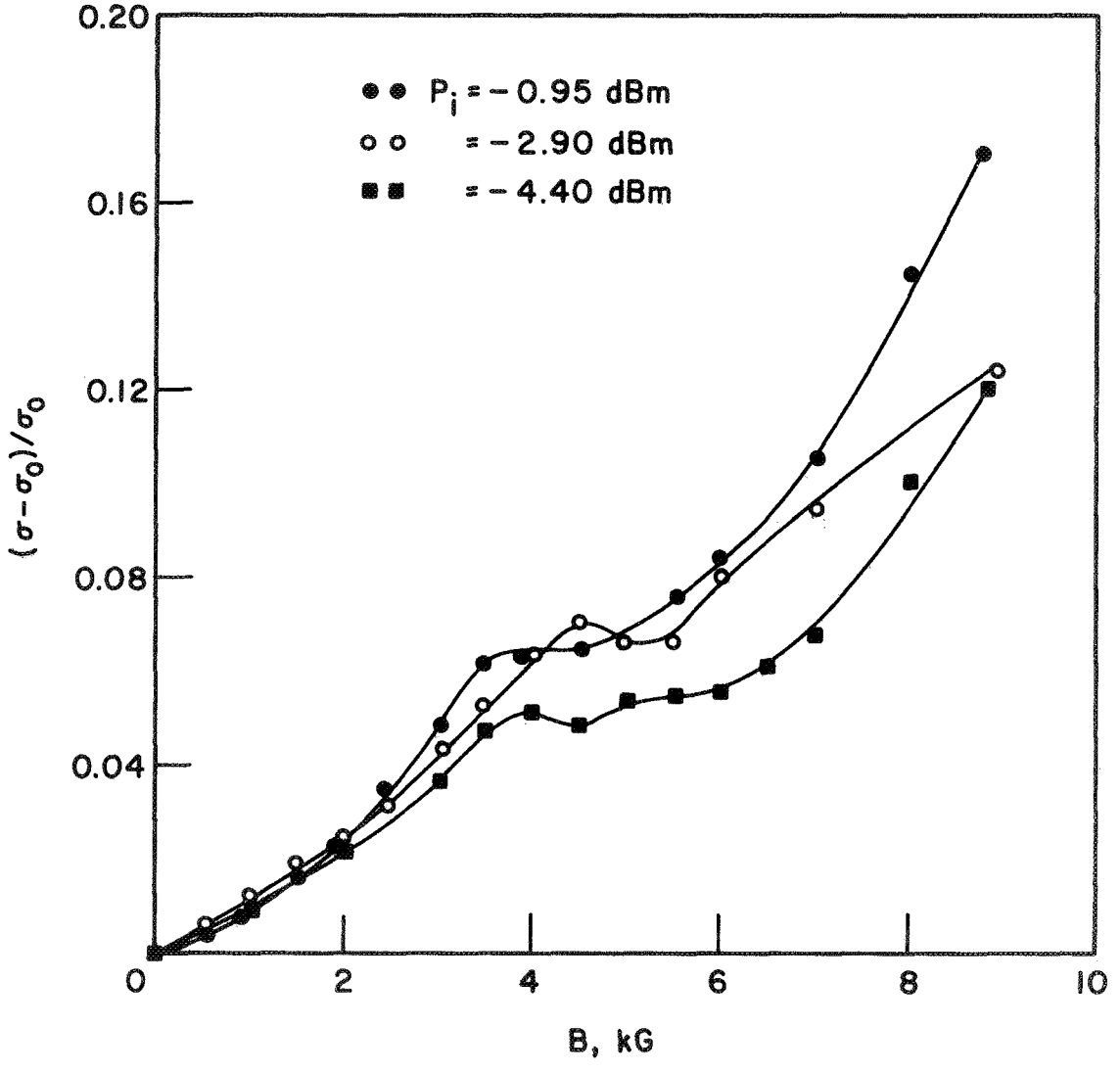

– FIG. 2.16 $(\sigma - \sigma_o)/\sigma_o$ VS. B AT 200°K [B IS 45 DEGREES TO THE (110)-CRYSTAL PLANE].

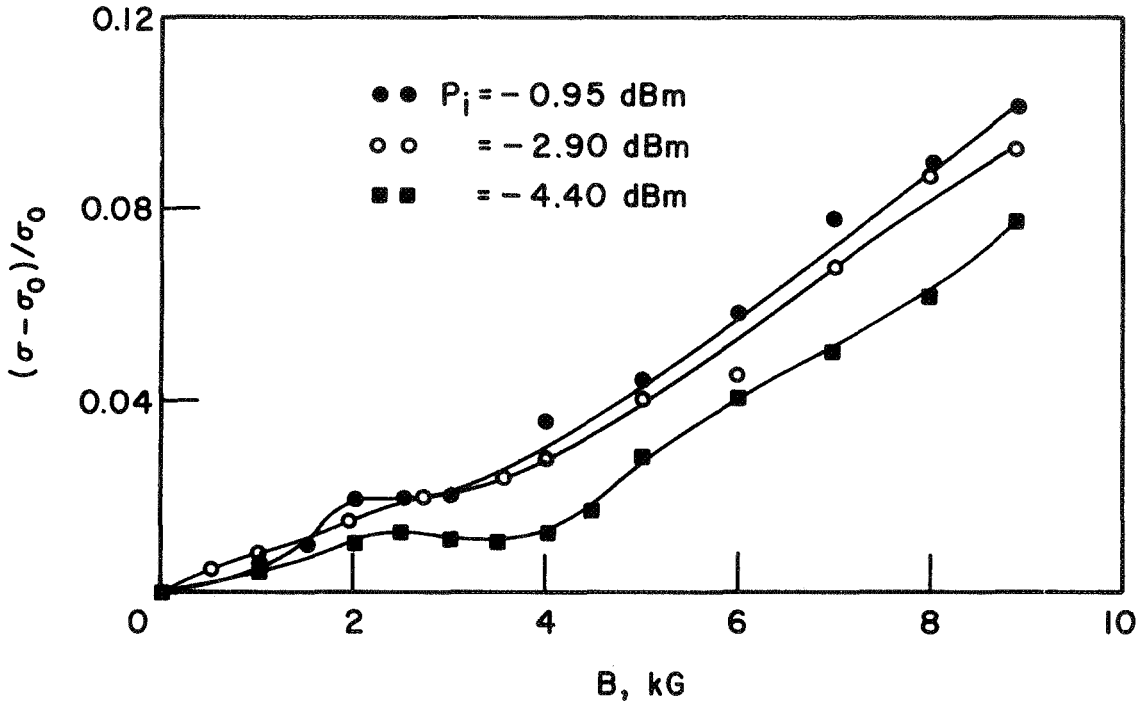

FIG. 2.17 $(\sigma - \sigma_o)/\sigma_o$ VS. B AT 200°K [B IS NORMAL TO THE (110)-CRYSTAL PLANE].

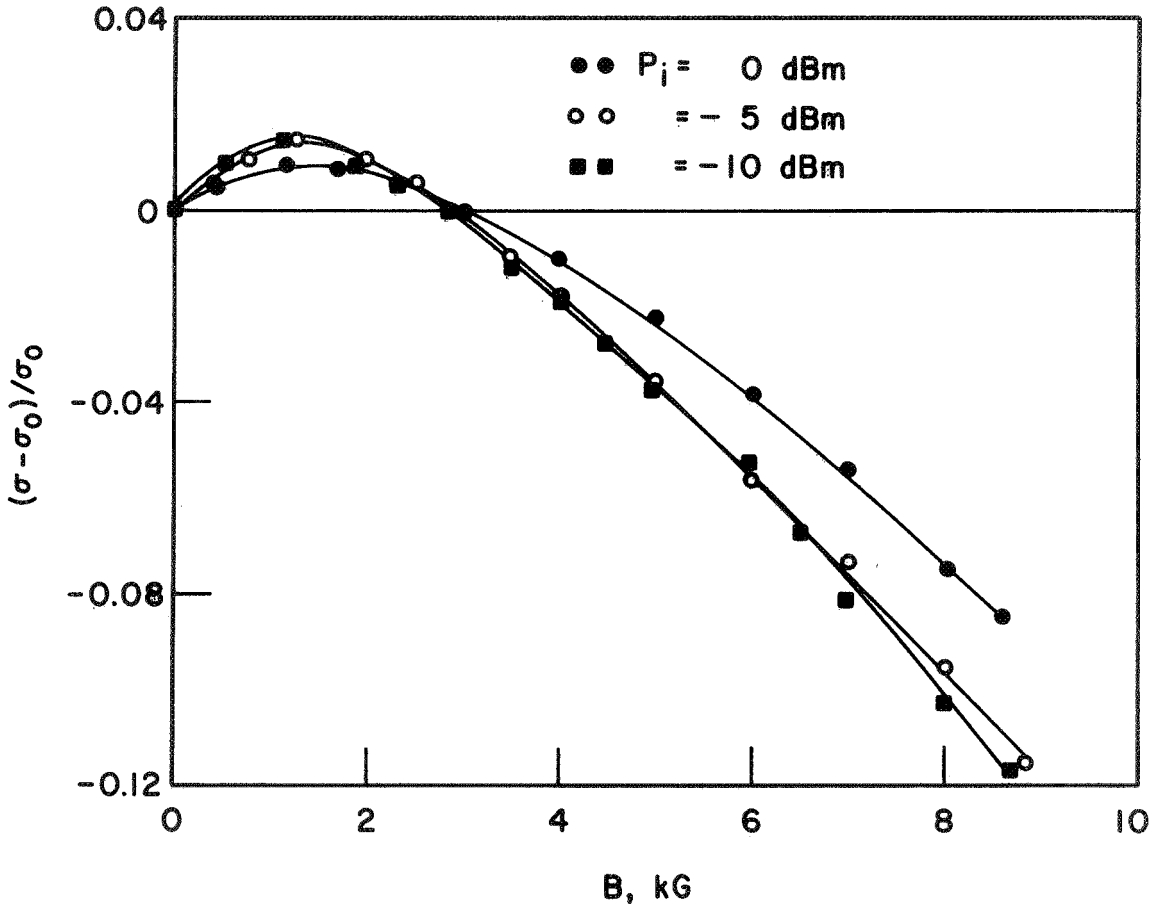

FIG. 2.18 $(\sigma - \sigma_o)/\sigma_o$ VS. B AT 295°K [B IS PARALLEL TO THE (110)-CRYSTAL PLANE].

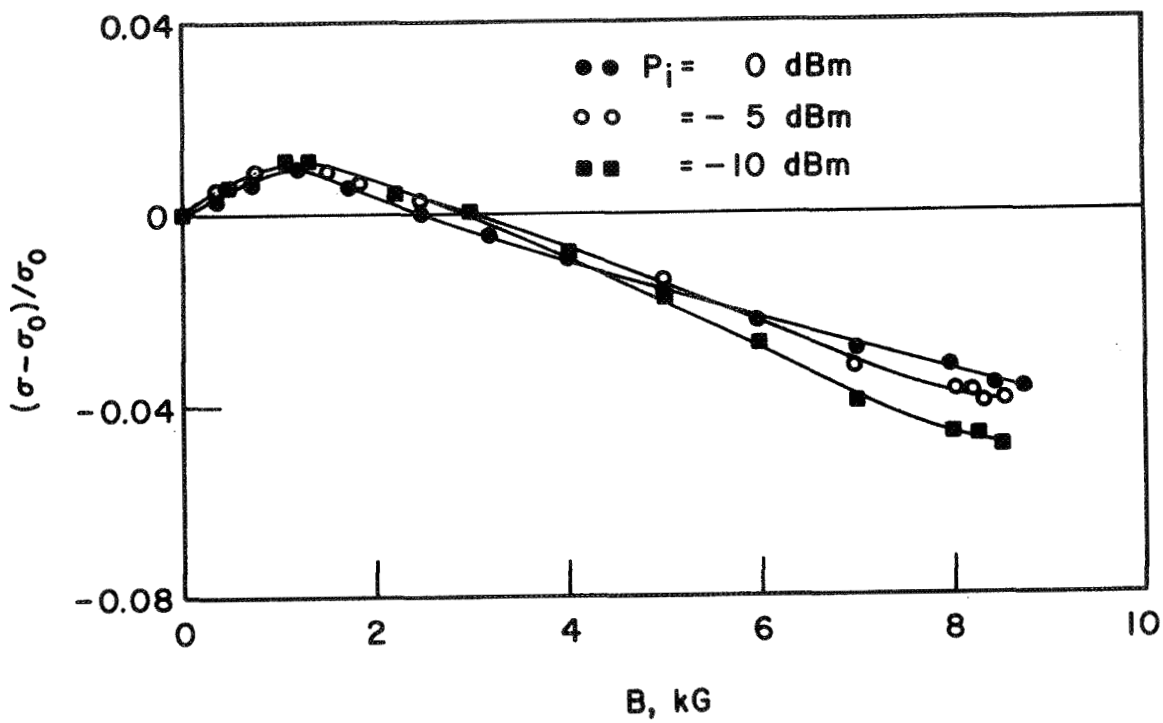

FIG. 2.19 $(\sigma - \sigma_o)/\sigma_o$ VS. B AT 295°K [B IS NORMAL TO THE (110)-CRYSTAL PLANE].

1. The magnitude of the relative change in conductivity decreases as the temperature is increased and is much smaller than that at liquid nitrogen temperature. This is due to the fact that the mobility decreases with temperature.

2. The freeze-out effect has not been observed at 175, 200 and 290°K for magnetic fields as high as 8.8 kG; this is to be expected since the theoretical results obtained from Eq. 2.11 give a value of B_{Fh} of approximately 19, 30 and 41 kG at 175, 200 and 295°K, respectively.

3. The peak of the absorption occurs at about 3 kG for both measurements at 175 and 200°K which indicates that m_i^* is independent of the temperature.

Figures 2.20 through 2.22 show the comparison between the experimental and theoretical results for $(\sigma-\sigma_o)/\sigma_o$ vs. B for temperatures of 175, 200 and 295°K. The values of the mobilities deduced from these figures together with Fig. 2.11 can be used to study the temperature dependence of the mobility. The results can be used to check the scattering mechanisms involved.

A plot of mobility (normalized to the value at liquid nitrogen temperature) vs. the temperature is shown in Fig. 2.23. The dependence of the mobility on temperature can be represented by the expression

$$\mu = \mu_1 \left(\frac{T}{77}\right)^{-2.07} , \qquad (2.55)$$

where μ_1 is the mobility at 77°K and has a value of 1.26×10^5 cm^2 $V\text{-}s^{-1}$. This indicates that the scattering mechanism is a combination of acoustic and polar lattice scattering. The lower value of the mobility at 77°K is obviously due to the fact that the sample is compensated.

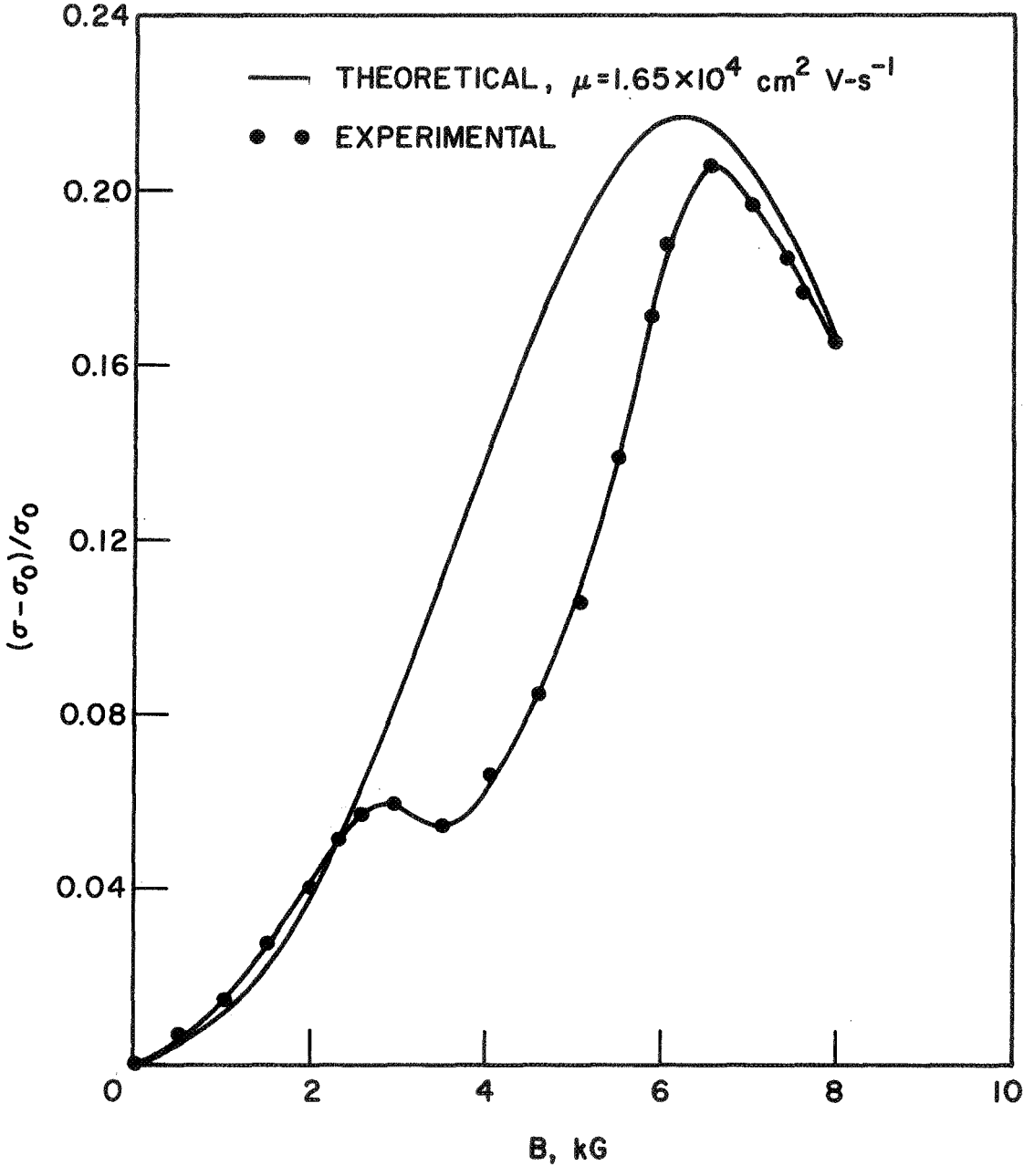

FIG. 2.20 COMPARISON BETWEEN THE EXPERIMENTAL AND THEORETICAL RESULTS OF $(\sigma - \sigma_o)/\sigma_o$ VS. B AT 200°K [B IS PARALLEL TO THE (110)-CRYSTAL PLANE].

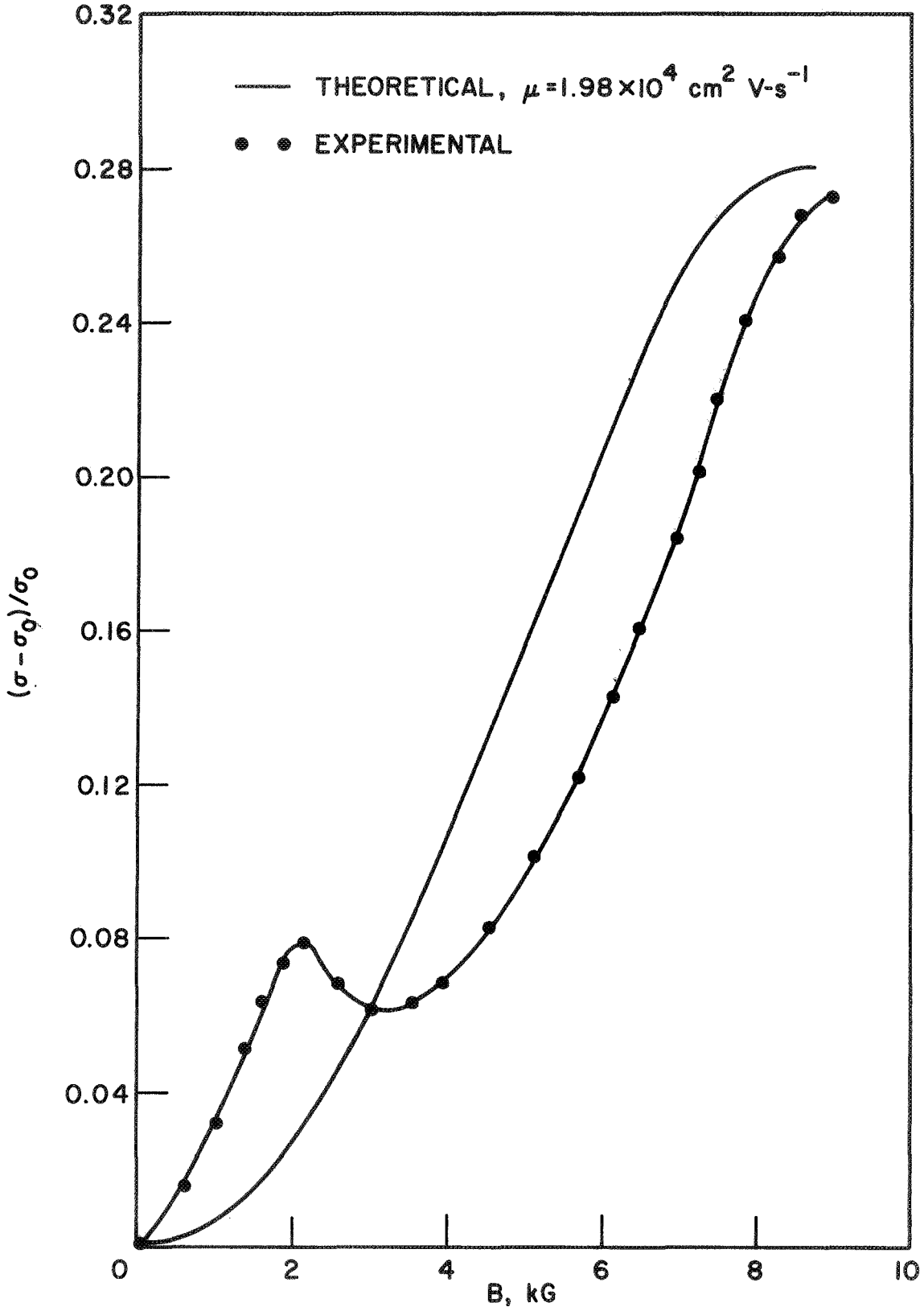

FIG. 2.21 COMPARISON BETWEEN THE THEORETICAL AND EXPERIMENTAL RESULTS OF $(\sigma - \sigma_o)/\sigma_o$ VS. B AT 175°K [B IS PARALLEL TO THE (110)-CRYSTAL PLANE].

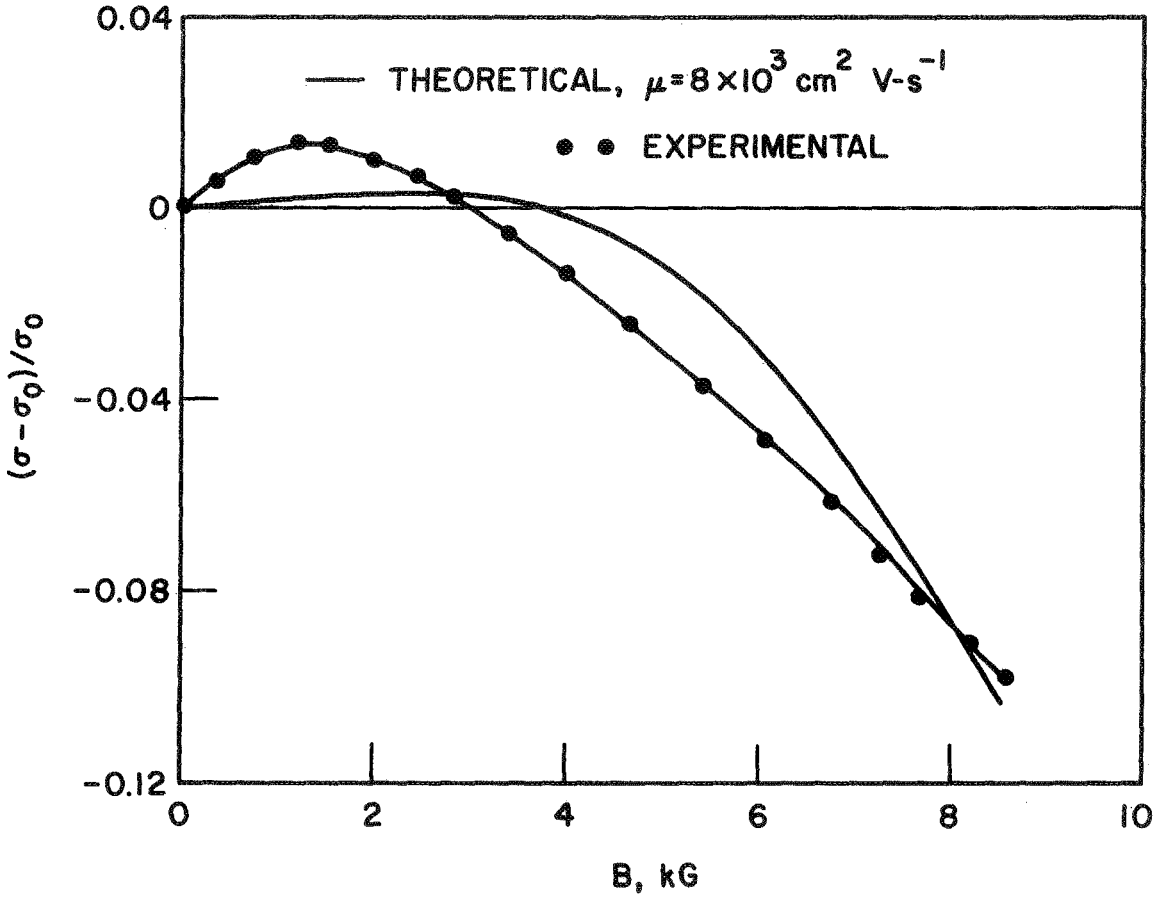

FIG. 2.22 COMPARISON BETWEEN THE THEORETICAL AND EXPERIMENTAL RESULTS OF $(\sigma - \sigma_o)/\sigma_o$ VS. B AT 290°K [B IS PARALLEL TO THE (110)-CRYSTAL PLANE].

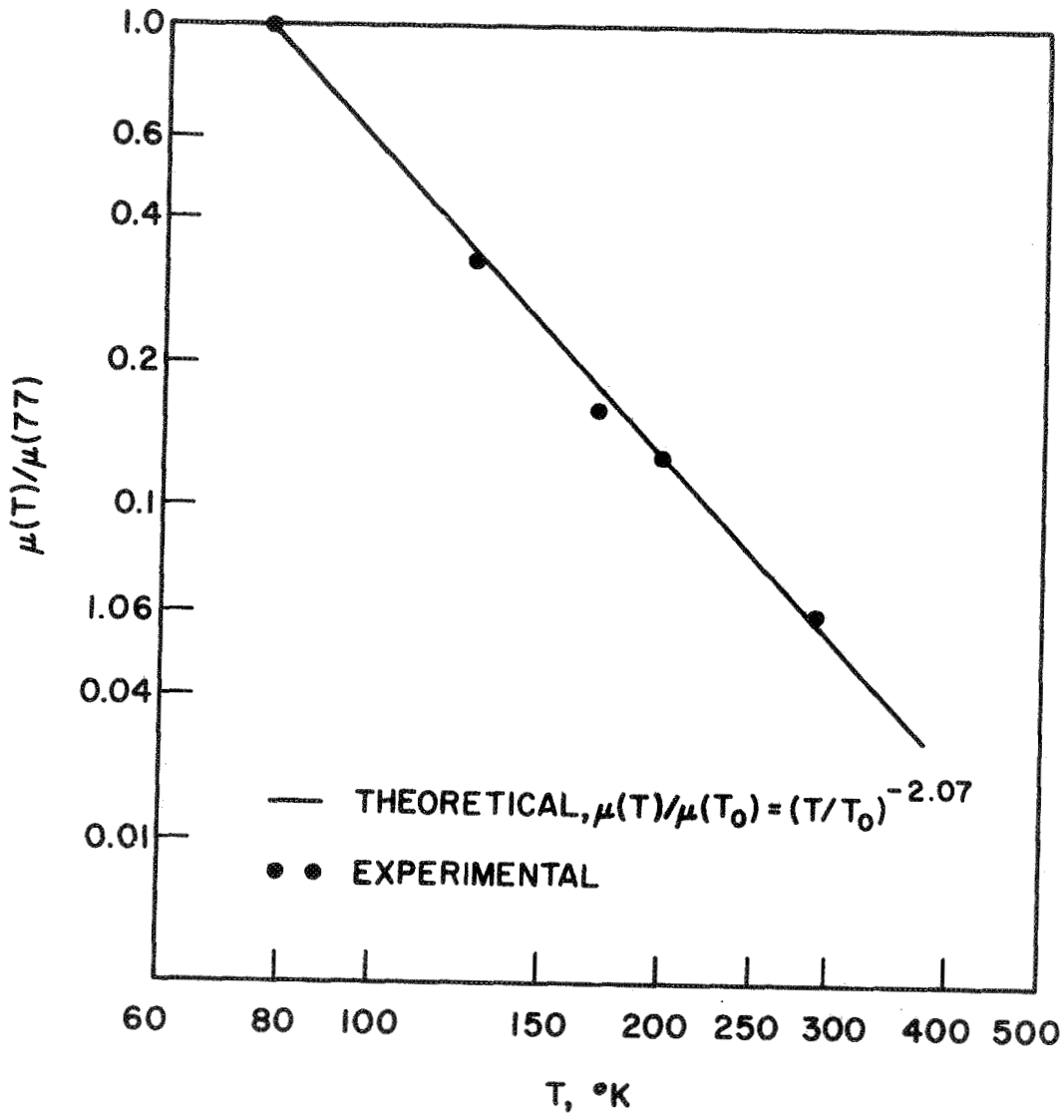

FIG. 2.23 TEMPERATURE DEPENDENCE OF THE MOBILITY IN InSb.

2.4.3 Behavior of the Conductivity at Liquid Helium Temperature. Figures 2.24 through 2.26 are plots of the relative change of the conductivity vs. magnetic field for several X-band signal levels at 4.2°K. The figures show a marked dependence of conductivity on the incident power level. The results are in contrast with the behavior at liquid nitrogen temperature and above, where the conductivity is independent of the signal level. The change in the conductivity is due to free-carrier absorption which gives rise to an increase in the carrier temperature above that of the lattice thermal equilibrium, and in turn will change the carrier mobility. This means that the hot electron effect in InSb is not significant at liquid nitrogen temperature or above for signal levels of interest (1 mW or lower). On the other hand it is very pronounced at liquid helium temperature. The results of measuring the dependence of the conductivity on the incident power level are presented in Fig. 2.27. The conductivity saturates for power levels above -2 dBm and exhibits a linear dependence on the incident power for signal levels below -3 dBm. The hot-electron effect in InSb was discussed by several authors among them are Kogan[48] and Putley,[17] where it was shown that for small steady electric fields the conductivity varies quadratically with the electric field intensity. This agrees favorably with the results presented in Fig. 2.27 since the square of the electric field intensity under the central post is proportional to the incident power.

A knowledge of the effective carrier temperature is necessary to compare the theoretical and experimental results. The effective temperature can be determined by studying the temperature dependence of the

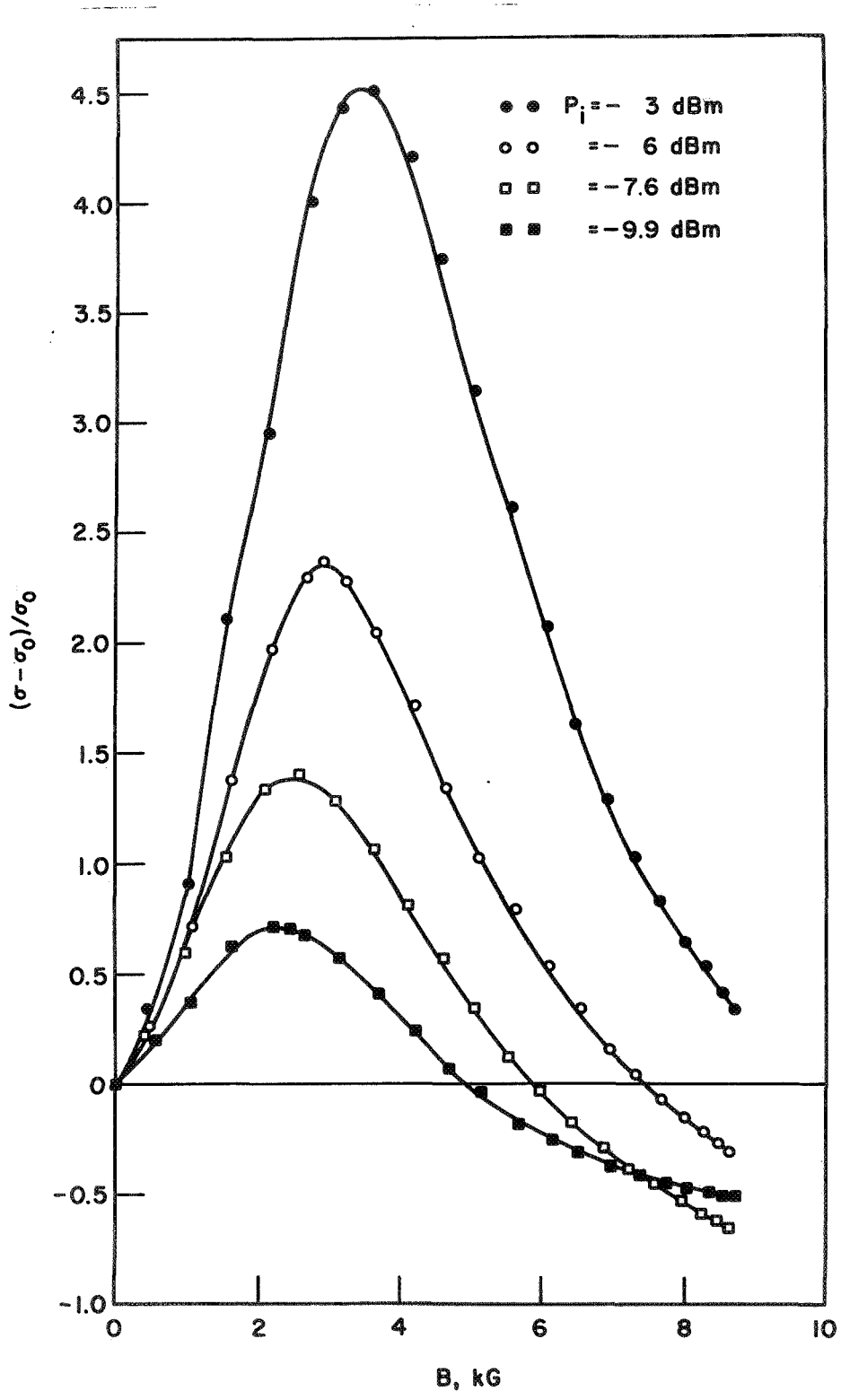

FIG. 2.24 $(\sigma - \sigma_o)/\sigma_o$ VS. B AT 4.2°K [B IS PARALLEL TO THE (110)-CRYSTAL PLANE].

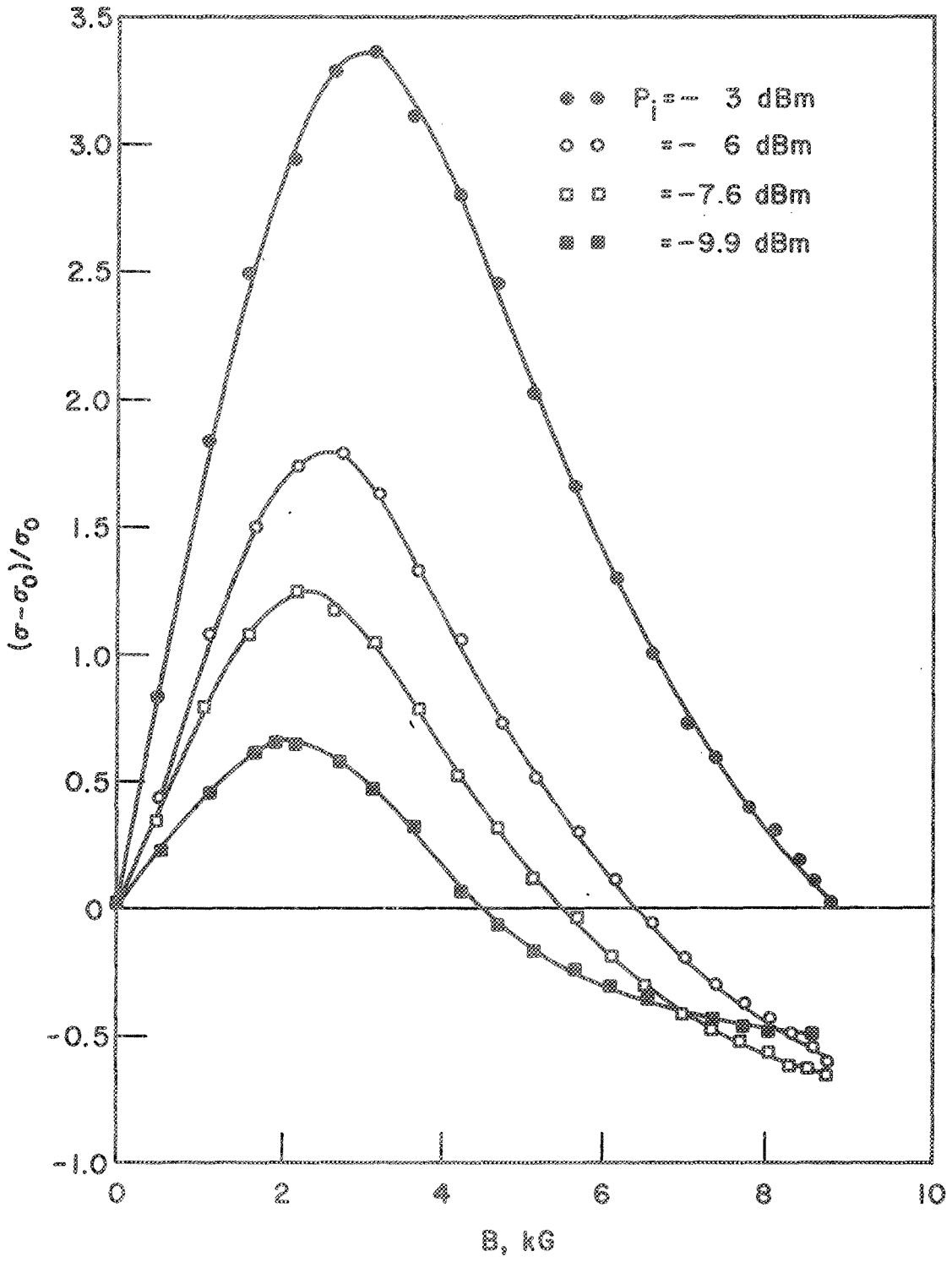

FIG. 2.25 $(\sigma - \sigma_o)/\sigma_o$ VS. B AT 4.2°K [B IS NORMAL TO THE (110)-CRYSTAL PLANE].

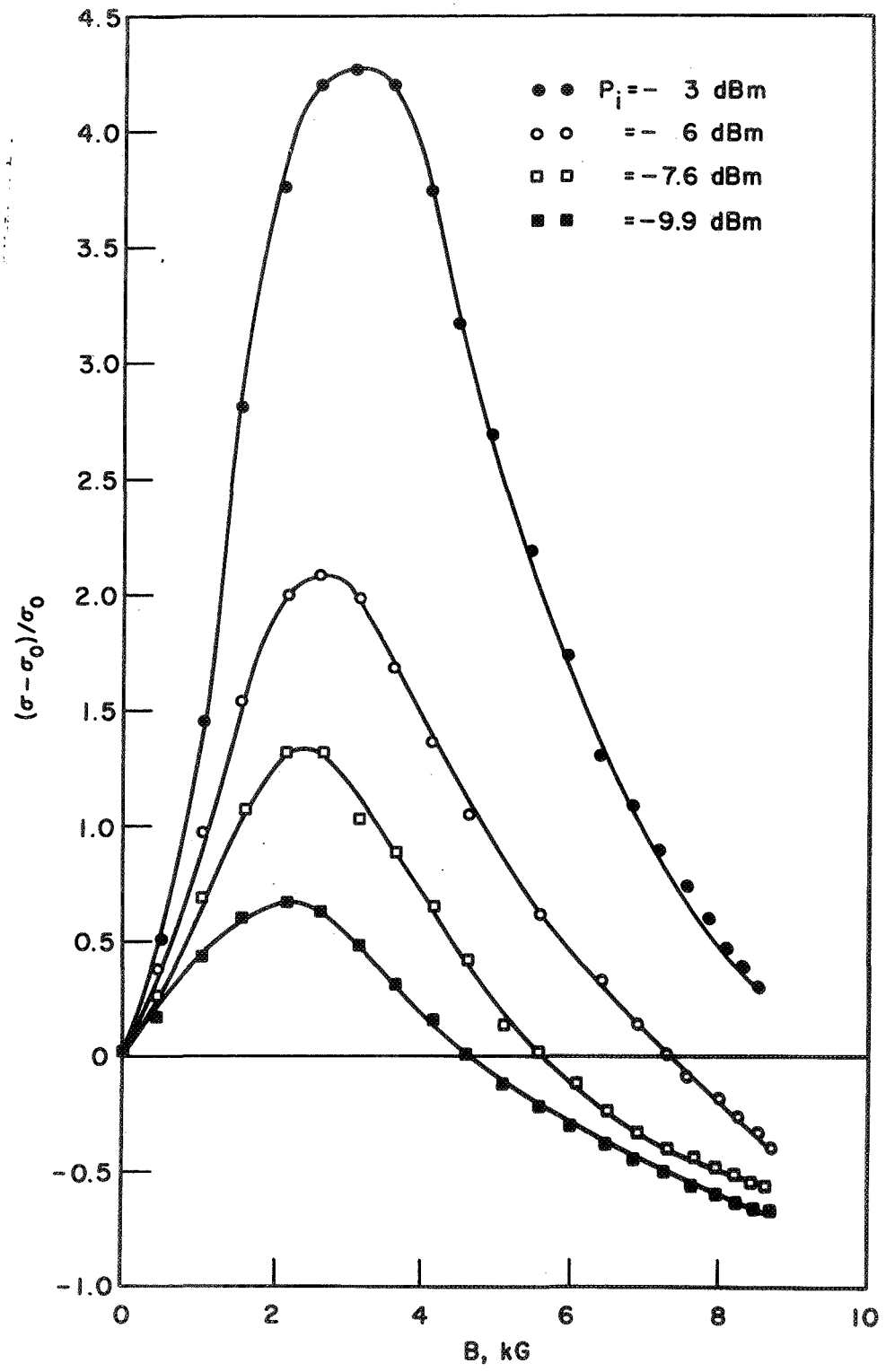

FIG. 2.26 $(\sigma - \sigma_o)/\sigma_o$ VS. B AT 4.2°K [B IS 45 DEGREES TO THE (110)-CRYSTAL PLANE].

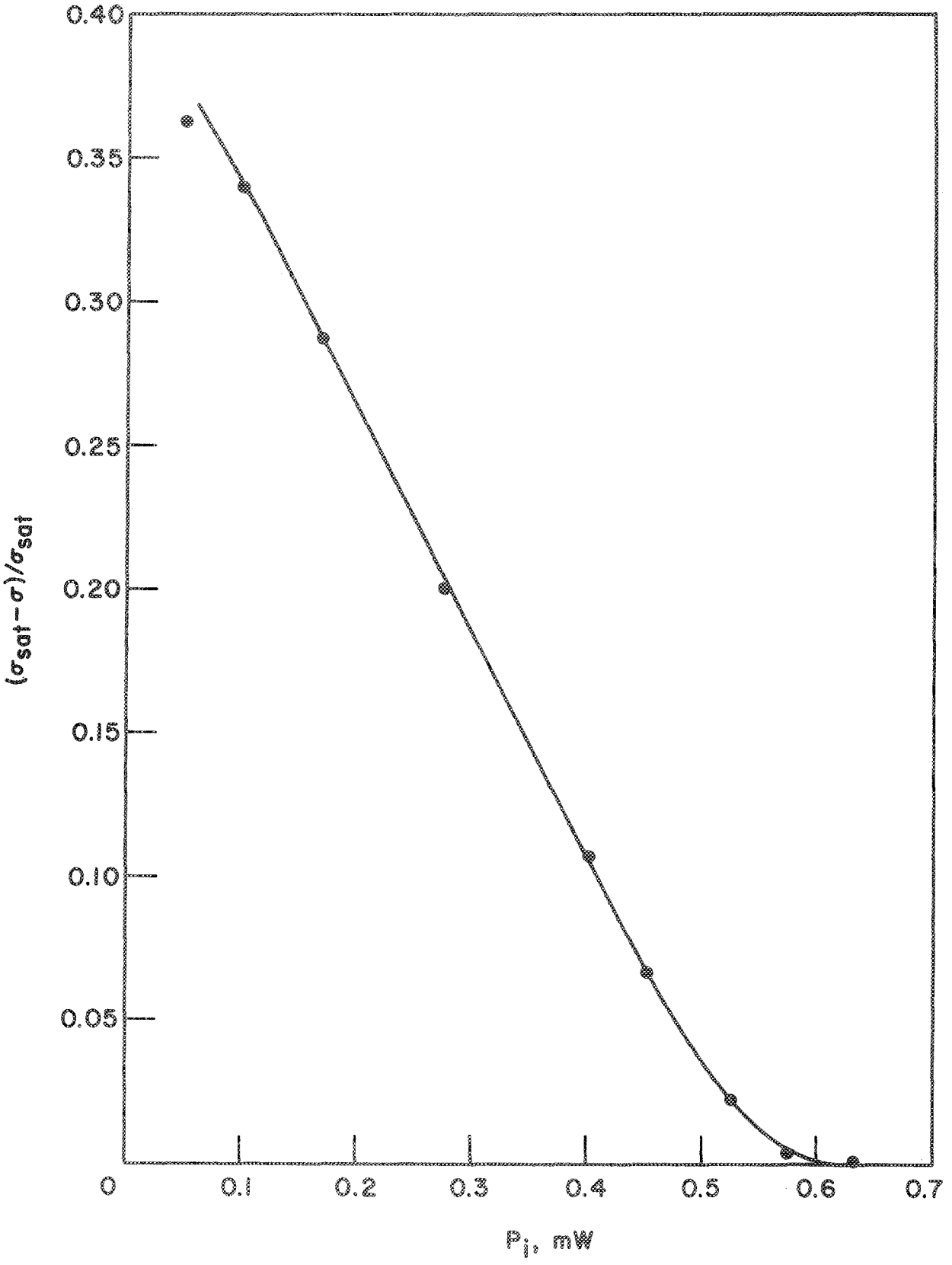

FIG. 2.27 DEPENDENCE OF THE SAMPLE CONDUCTIVITY ON THE INCIDENT POWER LEVEL AT 4.2°K. (B = 0)

mobility as a function of temperature at approximately 4.2°K, which could not be achieved with the available experimental facilities. However, as far as the detection scheme is concerned, the relative change in the conductivity as presented in Fig. 2.27 is adequate. This makes it unnecessary to pursue any further study on the material conductivity.

2.4.4 Measurement of the Relative Dielectric Constant. The dependence of the material dielectric constant on electric and magnetic fields was investigated at temperatures between 4.2 and 290°K. It will be shown in Chapter III that measurement of the cavity filling factor η and its resonance frequency shift is adequate for this purpose. The circuit shown in Fig. 2.5 was used to measure the cavity resonance frequency shift as a result of perturbing the sample. On the other hand, η was measured in a separate experiment to be discussed later and was found to have a value of 0.006. Measurements were carried out for two cases. In the first case the material dielectric constant was investigated as a function of the temperature for different signal levels at zero magnetic field. The resonance frequency shift arises from two effects, namely, the change in the material parameters and the thermal expansion of the cavity walls. The experimentally measured values for the resonance frequency shift as a result of varying the sample temperature between 77 and 290°K are shown in F g. 2.28. A plot of the theoretical values of the resonance frequency shift for the empty cavity as described by Eq. 3.64 is also included. It is seen from this figure that the net frequency shift due to variation of the sample temperature between 77 and 290°K is essentially zero. Therefore the material dielectric constant is independent of the temperature over the range of 77 to 290°K.

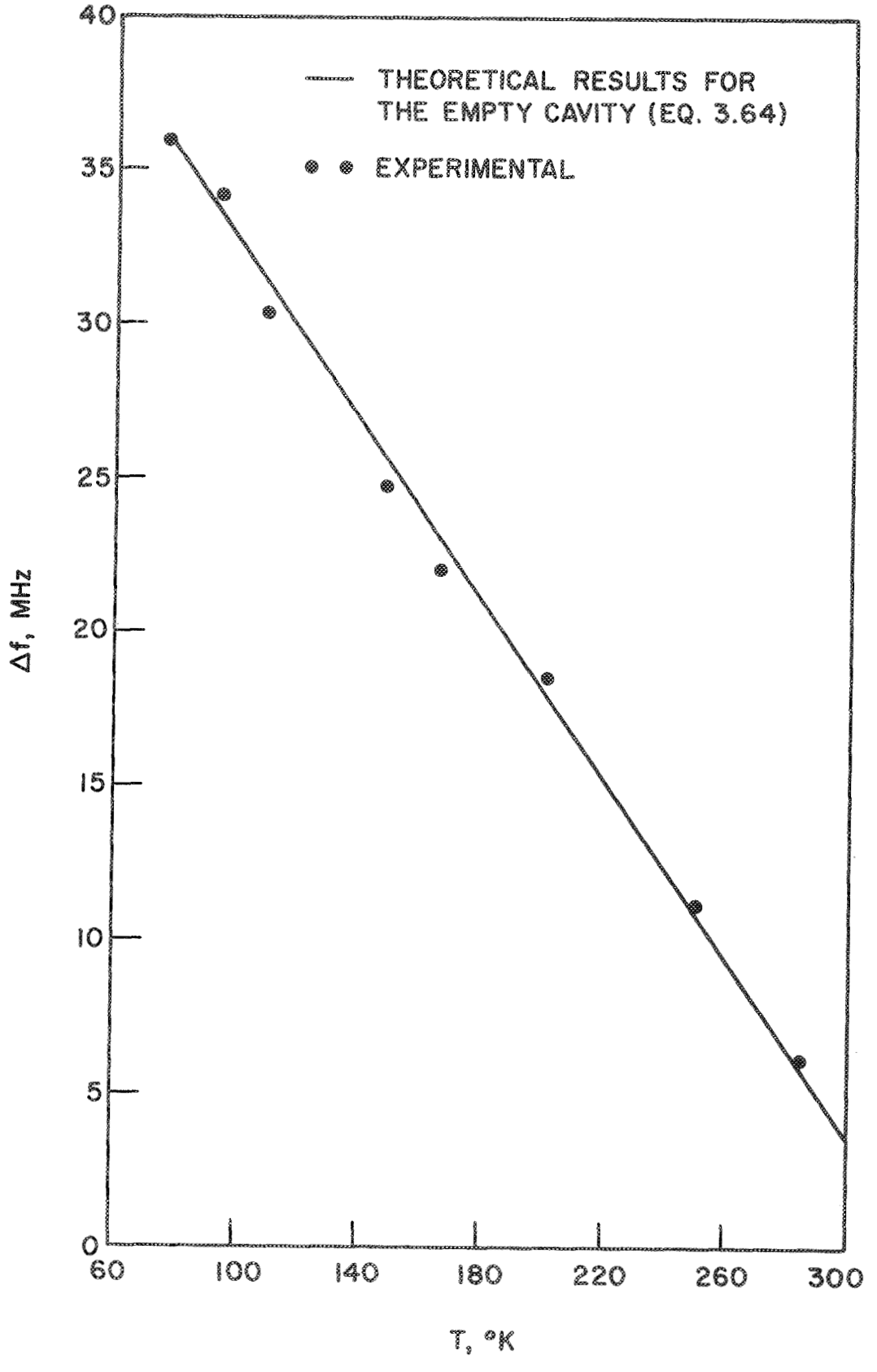

FIG. 2.28 CAVITY RESONANCE FREQUENCY SHIFT VS. T. (B = 0)

Moreover the dielectric constant was found to be independent of the X-band signal level over the same temperature range. This shows that between 77 and 290°K, all charge carriers are in the conduction band in the absence of a magnetic field. This is in agreement with the discussion presented earlier in Section 2.1.

The second set of measurements deals with the dependence of ϵ_r on magnetic field. Experiments were carried out for temperatures between 4.2 and 290°K. The resonance frequency shift at 175°K and above was found to be of the same order as the experimental uncertainties (10 kHz when using a spectrum analyzer). These results will not be presented here. Figure 2.29 shows the experimental results of the frequency shift and the dielectric constant of the sample at 4.2°K. On the other hand, Figs. 2.30 through 2.32 show similar results at 77°K for different orientations of the magnetic field with respect to the (110)-crystal plane. The figures exhibit the same resonance absorption effects as those for the conductivity presented earlier in the chapter.

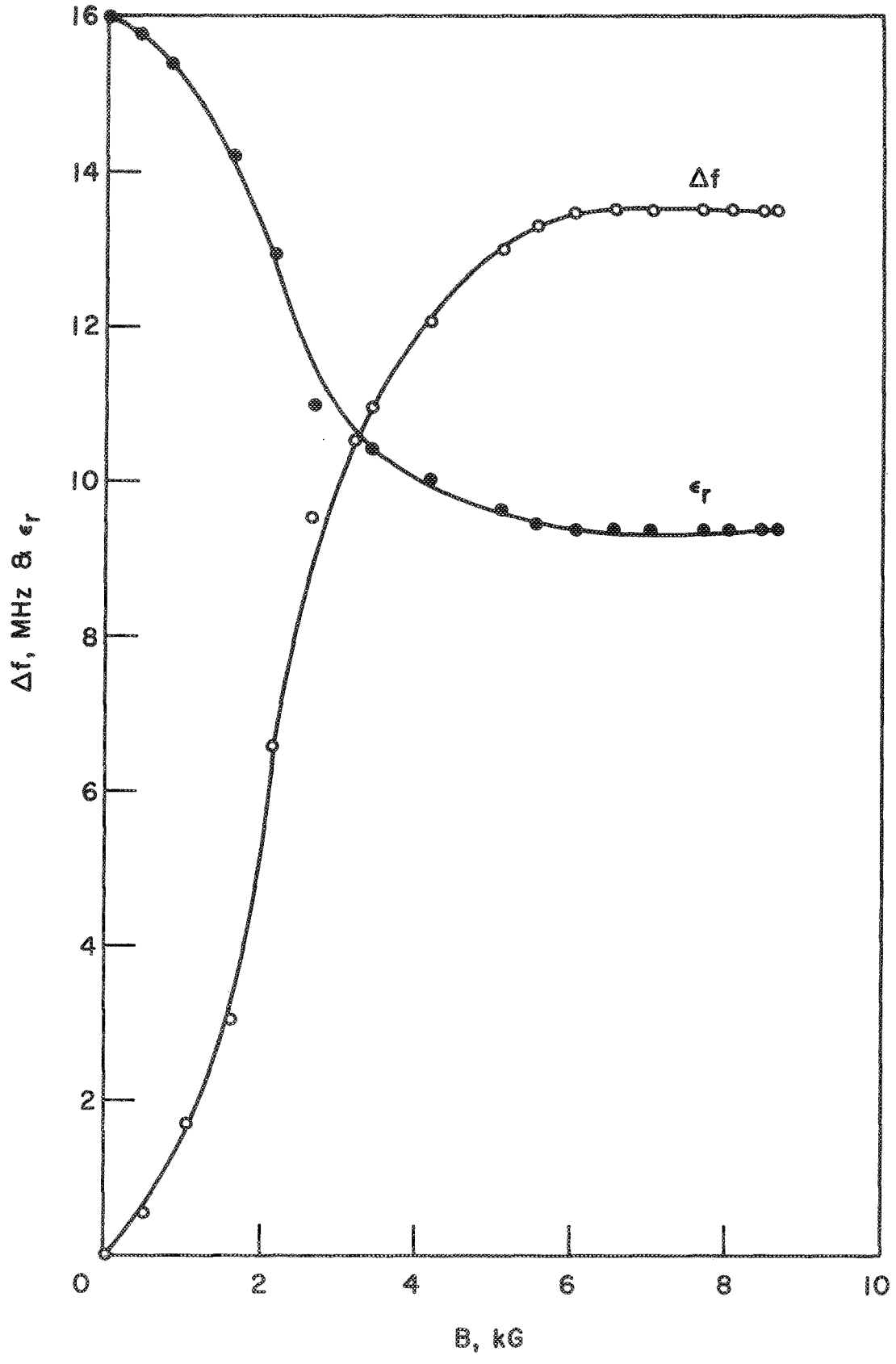

FIG. 2.29 CAVITY RESONANCE FREQUENCY SHIFT AND DIELECTRIC CONSTANT VS. MAGNETIC FIELD AT 4.2°K.

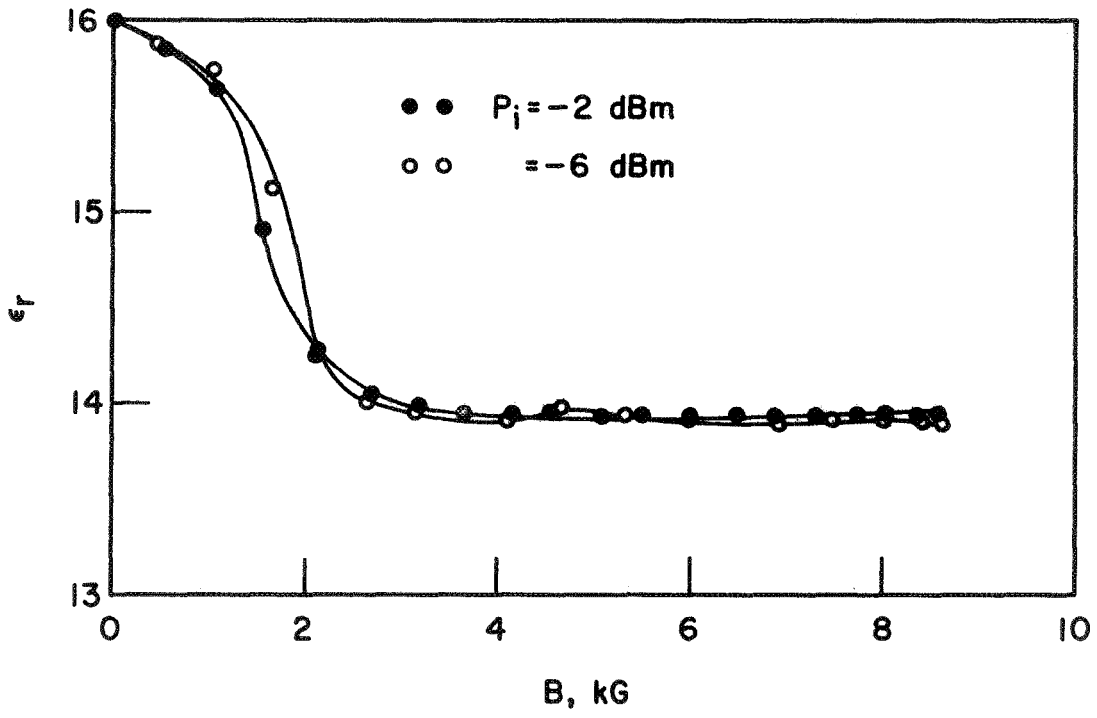

FIG. 2.30 DIELECTRIC CONSTANT VS. B AT 77°K [MAGNETIC FIELD IS PARALLEL TO THE (110)-CRYSTAL PLANE].

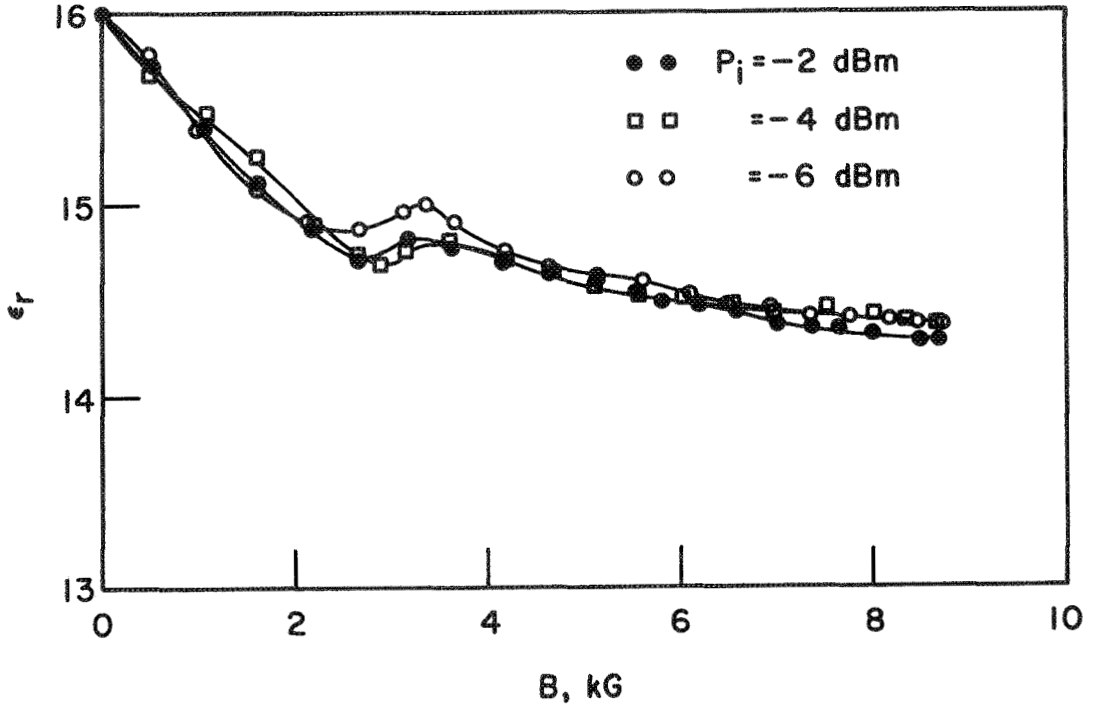

FIG. 2.31 DIELECTRIC CONSTANT VS. B AT 77°K [MAGNETIC FIELD IS NORMAL TO THE (110)-CRYSTAL PLANE].

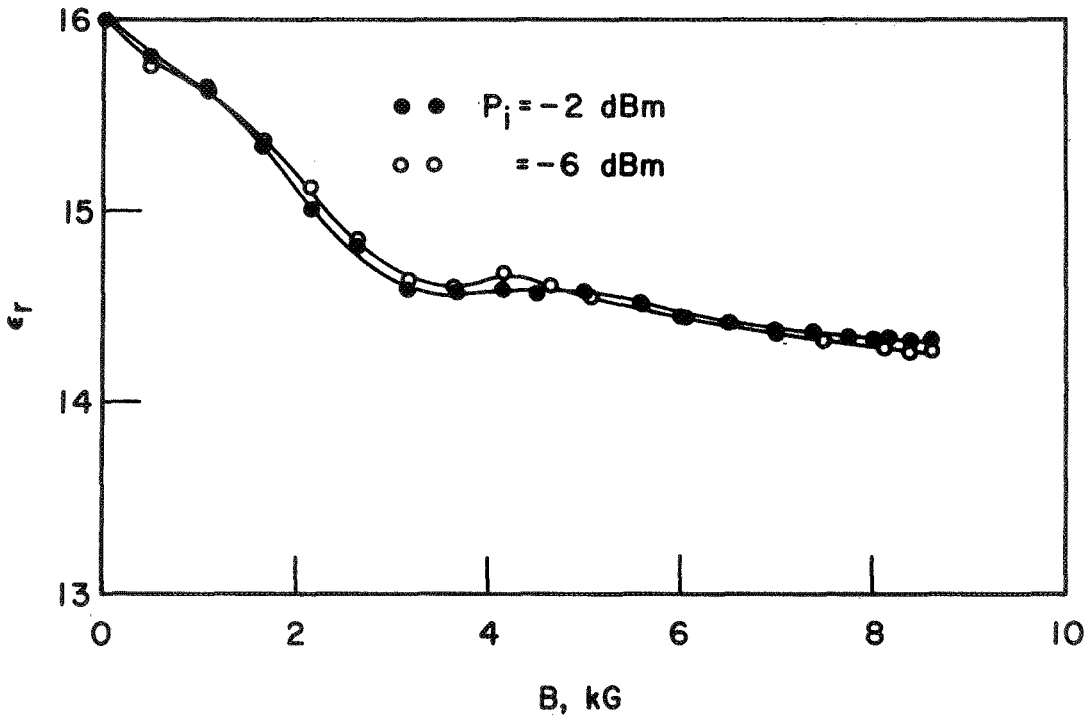

FIG. 2.32 DIELECTRIC CONSTANT VS. B AT 77°K [B IS 45 DEGREES TO THE (110)-CRYSTAL PLANE].

CHAPTER III. CAVITY PERTURBATION TECHNIQUES FOR MEASUREMENT OF THE PERMITTIVITY AND DIELECTRIC CONSTANT OF A BULK SEMICONDUCTOR

3.1 Introduction

The complex microwave conductivity of a semiconductor material has been measured using two different methods. In the first one a semiconductor slab completely fills a waveguide section and measurements are made to determine the complex reflection or transmission coefficients. This method has been reported by many authors[51-53] and has been reviewed recently by Datta and Nag.[54] The accuracy achieved with the reflection method is not very precise, especially with high conductivity materials since the VSWR to be measured is very high (nearly 20 dB) and the phase angle is very small. On the other hand, when this method is used in a transmission mode the accuracy is degraded further due to available commercial standards for attenuators and phase shifters. The fact that the sample should completely fill the transverse cross section of the waveguide poses two serious problems. First, in many cases it is very hard to get large enough samples to fill the waveguide cross section; this problem becomes more serious when the sample is a single crystal. Second, there is always a small air gap between the sample and waveguide walls even with tight fitting, this effect was shown to give erroneous results.[55] Recently, Holm[56] suggested a mode transducer to overcome this "gap effect." Holm's idea takes advantage of the fact that the contact problem is important when the electric field is normal to the sample surface and by converting the TE_{10} mode of the rectangular guide into a TE_{10} mode of a circular

guide, the electric field is tangential to the surface of the sample at the boundary. This scheme may be difficult to realize with a brittle material like indium antimonide.

The second method for measuring the microwave conductivity is by using cavity perturbation techniques. The strong interaction between the fields in the cavity and the sample makes this method very sensitive and highly versatile. Small size samples are adequate when using cavity perturbation techniques and the measurement procedures require very stable signal sources and accurate frequency measurements. Highly stable microwave sources are available, and frequency shifts as small as 1 kHz can be resolved using spectrum analyzers.

The complex angular frequency associated with a lossy cavity can be written as[57]

$$\Omega = \omega + j\omega_i \quad , \tag{3.1}$$

where ω is related to the real frequency f by the relation $\omega = 2\pi f$, while the imaginary part which represents the cavity losses is related to its loaded Q by the following equation,

$$\omega_i = \frac{\omega}{2Q_L} \quad , \tag{3.2}$$

where Q_L is the loaded Q of the cavity. It was shown[58] that the relative shift in the cavity resonance frequency due to cavity perturbation is given by

$$\frac{f - f_o}{f} + \frac{1}{2Q_L}\left(\frac{1}{Q_L} - \frac{1}{Q_{Lo}}\right) + \frac{1}{2} j \left(\frac{1}{Q_L} - \frac{1}{Q_{Lo}}\right) =$$

$$\frac{\int_{V_s} [(\mu - \mu_o)\underline{H} \cdot \underline{H}_o - (\epsilon - \epsilon_o)\underline{E} \cdot \underline{E}_o] \, dV}{\int_{V_c} (\epsilon \underline{E} \cdot \underline{E}_o - \mu \underline{H} \cdot \underline{H}_o) \, dV} \quad , \quad (3.3)$$

where V_c and V_s are the cavity and the sample volumes, respectively; f is the cavity resonance frequency and μ and ϵ are the permeability and dielectric constant of the medium. The subscript zero denotes quantities in the absence of perturbation. If the sample is placed under the central post of a reentrant cavity and the size of the sample is chosen such that the energy stored within the sample is smaller than the energy stored in the cavity, the following relations will hold over the size of the sample

$$\underline{E} = \frac{\kappa_o}{\epsilon} \underline{E}_o$$

$$\underline{H} = \mu_r \underline{H}_o \quad , \quad (3.4)$$

where κ_o is the permittivity of free space and μ_r is the relative permeability of the sample. Hence Eq. 3.3 becomes

$$\frac{f - f_o}{f_o} + \frac{1}{2Q_L}\left(\frac{1}{Q_L} - \frac{1}{Q_{Lo}}\right) + j \frac{1}{2}\left(\frac{1}{Q_L} - \frac{1}{Q_{Lo}}\right) =$$

$$\frac{\left(\mu_o - \frac{\mu_o^2}{\mu}\right) \int_{V_s} |H_o|^2 \, dV - \frac{\epsilon - \epsilon_o}{\epsilon} \int_{V_s} \kappa_o |E_o|^2 \, dV}{\int_{V_c} \left(\kappa_o |E_o|^2 - \mu_o |H_o|^2\right) dV} \quad . \quad (3.5)$$

If $\mu = \mu_o$, which is true for the case under consideration, then Eq. 3.5 reduces to,

$$\frac{f - f_o}{f_o} + \frac{1}{2Q_L}\left(\frac{1}{Q_L} - \frac{1}{Q_{Lo}}\right) + j\left(\frac{1}{Q_L} - \frac{1}{Q_{Lo}}\right) = -\frac{1}{2}\left(\frac{\epsilon - \epsilon_o}{\epsilon}\right)\frac{\int_{V_s} |E_o|^2 \, dV}{\int_{V_c} |E_o|^2 \, dV} \quad . \tag{3.6}$$

Substituting,

$$\epsilon = \kappa_o\left(\epsilon_r + \frac{\sigma}{j\omega\kappa_o}\right) = \kappa_o\epsilon_r - j\epsilon_i \quad , \tag{3.7}$$

where ϵ_r is the relative dielectric constant of the sample and σ is its conductivity, yields,

$$\frac{f - f_o}{f_o} + \frac{1}{2Q_L}\left(\frac{1}{Q_L} - \frac{1}{Q_{Lo}}\right) = \frac{\epsilon_i(\epsilon_{io} - \epsilon_i) + \kappa_o^2\epsilon_r(\epsilon_{ro} - \epsilon_r)}{\kappa_o^2\epsilon_r^2 + \epsilon_i^2}(\eta) \tag{3.8}$$

and

$$\frac{1}{Q_L} - \frac{1}{Q_{Lo}} = \frac{\epsilon_i\epsilon_{ro} - \epsilon_r\epsilon_{io}}{\kappa_o^2\epsilon_r^2 + \epsilon_i^2}(\kappa_o\eta) \quad , \tag{3.9}$$

where

$$\eta = \frac{1}{2}\,\frac{\int_{V_s} |E_o|^2 \, dV}{\int_{V_c} |E_o|^2 \, dV} \quad .$$

However for the samples of interest and at a frequency of 10 GHz $\kappa_o\epsilon_r \gg \epsilon_i$, also it is quite reasonable to neglect $(1/2)(1/Q_L)[(1/Q_L) - (1/Q_{Lo})]$ with respect to $(f-f_o)/f_o$, which allows simplification of Eqs. 3.8 and 3.9 to the following forms,

$$\frac{f - f_o}{f} = -\eta \frac{(\epsilon_r - \epsilon_{ro})}{\epsilon_r} \tag{3.10}$$

and

$$\frac{1}{Q_L} - \frac{1}{Q_{Lo}} = \frac{\eta}{\kappa_o \omega}\left(\sigma \frac{\epsilon_{ro}}{\epsilon_r} - \sigma_o\right) \tag{3.11}$$

or

$$\frac{1}{Q_L} - \frac{1}{Q_{Lo}} = \frac{\eta}{\kappa_o \omega}\left((\sigma - \sigma_o) + \frac{\sigma(f - f_o)}{\eta f_o}\right) . \tag{3.12}$$

Equations 3.9 and 3.11 relate the change in the conductivity and dielectric constant of the sample to the experimentally measurable quantities. The parameter η is thought of as a filling factor depending on the geometry of the sample and the cavity. This parameter can be determined either experimentally by using a sample with known parameters, or theoretically by studying the fields within the cavity. Equation 3.10 will be used to study the change in the dielectric constant of the sample due to electric and magnetic fields. However, Eq. 3.11 will not be used in the analysis of the experimental results due to the fact that the values of Q_L and Q_{Lo} are very close to each other. Instead, the more accurate method of power measurement will be used. In the following analysis it will be shown that a knowledge of the coupling factor in the absence of perturbation together with the change in reflected power and resonance frequency shift as a result of the perturbation is adequate for the determination of the material conductivity. This eliminates the need to follow the Q-factor change as a function of the perturbation which might lead to appreciable error in the presence of mismatch loss.

3.2 Cavity Analysis: An Equivalent Circuit Approach

In this analysis the power is coupled to the cavity through a circulator and a lossy line with attenuation α as shown in Fig. 3.1. It is intended here to derive the dependence of the detected power on the change of the material conductivity. For simplicity the circulator is assumed to be matched to both the line and the crystal detector, however if any mismatch is present it can be very easily accounted for. The various measurable power levels can be defined as follows:

P_o = the power available from the source which is the power delivered to a matched load through a lossless coupling,

P_r = the power reflected from the cavity,

P_c = the power absorbed in the cavity and

P_D = the detected power.

Therefore, $P_r = \alpha P_o - P_c$ and $P_D = \alpha P_r = \alpha^2 P_o - \alpha P_c$. The change in the detected power ΔP_D due to the introduction of perturbation can be expressed as

$$\Delta P_D = -\alpha(P_c - P_{co}) \quad , \tag{3.13}$$

where the subscript zero denotes quantities in the absence of perturbation.

The cavity equivalent circuit at resonance shown in Figs. 3.2 can be used to express ΔP_D in terms of the circuit parameters. These circuit parameters are defined as Y_o = the line conductance reflected into the cavity, G_o = the cavity conductance, σ is the real part of the material conductivity and K is a geometrical factor to be determined later. The power absorbed by the cavity in the presence and absence of perturbation are given, respectively, by

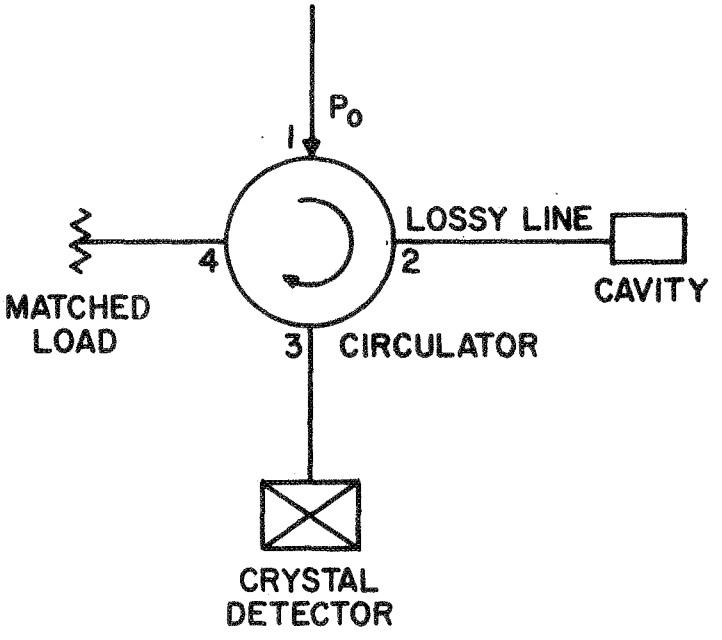

FIG. 3.1 CAVITY MEASUREMENT SYSTEM.

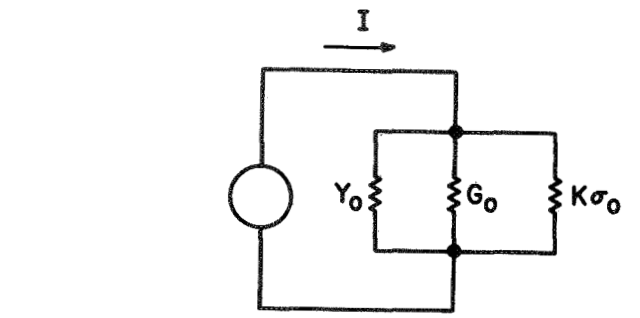

(a) WITHOUT PERTURBATION

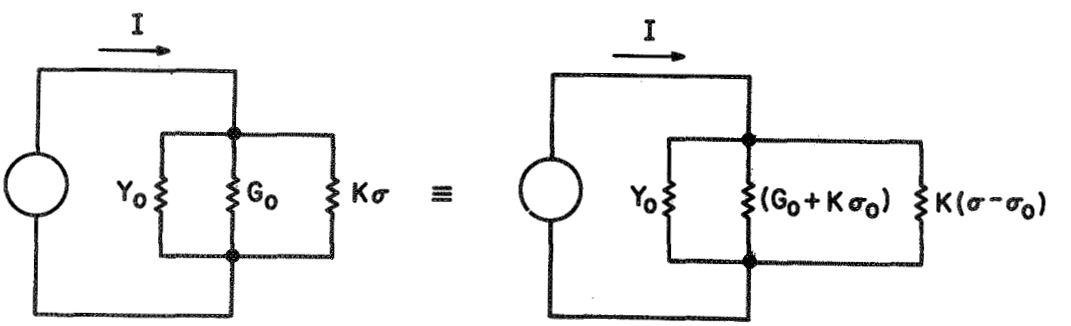

(b) WITH PERTURBATION

FIG. 3.2 CAVITY EQUIVALENT CIRCUIT.

$$P_c = I^2 \frac{K\sigma + G_o}{(K\sigma + G_o + Y_o)^2} \tag{3.14}$$

and

$$P_{co} = I^2 \frac{K\sigma_o + G_o}{(K\sigma_o + G_o + Y_o)^2} \quad . \tag{3.15}$$

From Eqs. 3.14 and 3.15 the change in the power absorbed by the cavity as a result of the perturbation will be,

$$P_c - P_{co} = I^2 \left(\frac{K\sigma + G_o}{(K\sigma + G_o + Y_o)^2} - \frac{K\sigma_o + G_o}{(K\sigma_o + G_o + Y_o)^2} \right) \quad . \tag{3.16}$$

But,

$$P_o = \frac{I^2}{4Y_o} \quad . \tag{3.17}$$

Using Eqs. 3.13, 3.16 and 3.17, the change in the detected power as a result of a change in the material conductivity from σ_o to σ can therefore be written as,

$$\frac{\Delta P_D}{P_o} = -4\alpha \left[\left(\frac{K\sigma + G_o}{K\sigma + G_o + Y_o} \right) \left(\frac{Y_o}{K\sigma + G_o + Y_o} \right) - \left(\frac{K\sigma_o + G_o}{K\sigma_o + G_o + Y_o} \right) \cdot \left(\frac{Y_o}{K\sigma_o + G_o + Y_o} \right) \right] \quad . \tag{3.18}$$

Defining the quantities Q_L, Q_U, Q_{Lo} and Q_{Uo} as the cavity loaded and unloaded Q-factors, respectively, in the presence and absence of perturbation, then

$$\frac{Q_L}{Q_U} = \frac{K\sigma + G_o}{K\sigma + G_o + Y_o} \tag{3.19}$$

and

$$\frac{Q_{Lo}}{Q_{Uo}} = \frac{K\sigma_o + G_o}{K\sigma_o + G_o + Y_o} \quad . \tag{3.20}$$

Substituting Eqs. 3.19 and 3.20 into 3.18 yields

$$\frac{\Delta P_D}{P_o} = -4\alpha \left[\frac{Q_L}{Q_U} \left(1 - \frac{Q_L}{Q_U} \right) - \frac{Q_{Lo}}{Q_{Uo}} \left(1 - \frac{Q_{Lo}}{Q_{Uo}} \right) \right] \tag{3.21}$$

which gives the change in the detected power as a function of the Q-factors of the cavity with and without perturbation. However, it is more convenient for experimental purposes to express $\Delta P_D/P_o$ as a function of the material conductivity and the cavity coupling factor with no perturbation β_o. The coupling factor β_o is related to the circuit parameters as follows,

$$\beta_o = \frac{Y_o}{G_o + k\sigma_o} \quad . \tag{3.22}$$

This approach will make it easier to analyze the experimental results, in addition to the fact that the coupling factor can be measured to a much higher degree of accuracy when compared to the Q-factor, especially in the presence of mismatch or insertion loss. With this in mind, Eq. 3.18 can be written as

$$\frac{\Delta P_D}{P_o} = -4\alpha \left(\frac{(1 + x)\beta_o}{(1 + x + \beta_o)^2} - \frac{\beta_o}{(1 + \beta_o)^2} \right) , \tag{3.23}$$

where $x = F\,\Delta\sigma/\sigma_o$,

$F = K\sigma_o/(G_o+K\sigma_o)$ and

β_o = the cavity coupling factor with no perturbation.

This equation gives the change in the detected power as a function of the material conductivity, the cavity parameters with no perturbation and the power available from the source. Referring to Fig. 2.4, P_o can be measured by closing the shorting switch, therefore all the power incident on circulator port No. 1 will be transmitted to port No. 3. If the VSWR and the detected power at port No. 3 are Γ_3 and P_{D3}, respectively, then

$$P_o = \frac{P_{D3}}{\alpha_{23}(1 - \Gamma_3^2)} , \tag{3.24}$$

where α_{23} is the insertion loss of the circulator between Ports 2 and 3.

3.2.1 The Optimum Coupling Coefficient. Once P_o and β_o are known it is a straightforward process to determine the change in the real part of the conductivity as a function of the change of the detected power. However, there exists an optimum coupling factor which results in the largest value of $\Delta P_D/P_o$ for a certain value of x. The knowledge of such a coupling factor will improve the accuracy of the experimental results. To determine this optimum coupling factor, the first derivative with respect to β_o of the left-hand side of Eq. 3.23 is equated to zero which results in,

$$\left(\beta_{op}^4 - (x+2)\beta_{op}^3 - 6(x+1)\beta_{op}^2 - (x+1)(x+2)\beta_{op} + (x+1)^2\right) x = 0 , \tag{3.25}$$

where β_{op} is the optimum coupling factor. Figures 3.3 and 3.4 give plots of the optimum coupling factor vs. x for overcoupled and undercoupled cavities, respectively. It is worthwhile to investigate the case when $x \ll 1$ in order to get more insight from these graphs. In such a case, Eq. 3.25 reduces to the following,

$$\beta_{op}^4 - 2\beta_{op}^3 - 6\beta_{op}^2 - 2\beta_{op} + 1 = 0 \quad . \tag{3.26}$$

The four roots of the above equation are -1, -1, $(2 + \sqrt{3})$ and $(2 - \sqrt{3})$. The two roots having the value of -1 have no physical significance and will be disregarded. The remaining two roots indicate that either an undercoupled or overcoupled cavity can be designed for optimum test conditions. The criterion to choose between an overcoupled or an undercoupled cavity is determined by the fact that the cavity should not change from one kind of coupling to the other as a result of the perturbation. This requirement will cause the detected power to be either monotonically increasing or decreasing as a result of perturbing the sample. Therefore, any confusion due to a change in the kind of coupling is totally eliminated.

The change in the cavity coupling factor as a result of the perturbation for various values of β_o is shown in Figs. 3.5 and 3.6 for positive and negative values of x, respectively. Figure 3.5 shows that the cavity coupling factor always decreases as a result of the perturbation. Therefore if the perturbation increases the conductivity of the material under test (x is positive), the cavity should be undercoupled. On the other hand, Fig. 3.6 shows the opposite case which indicates that the cavity

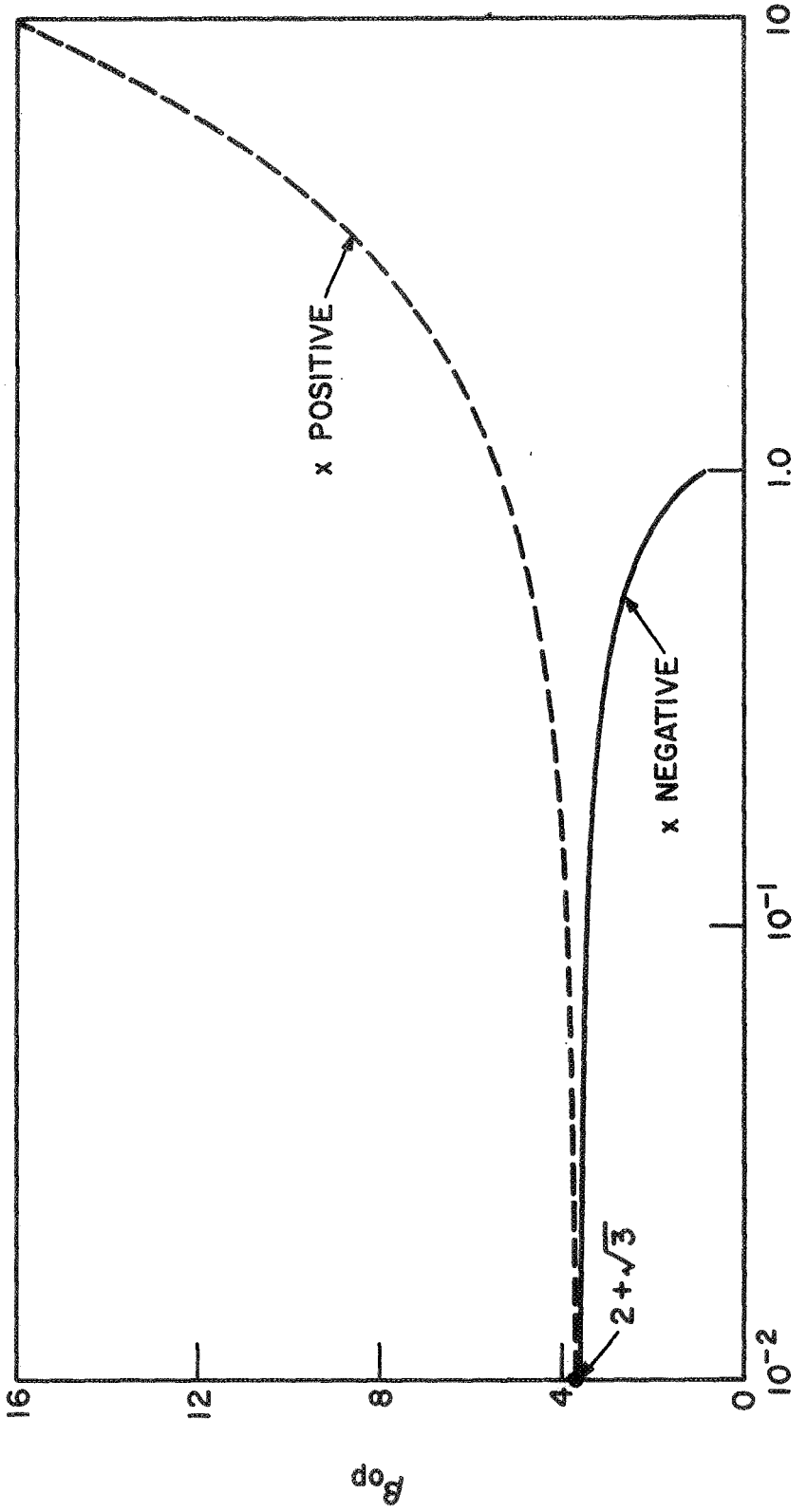

FIG. 3.3 OPTIMUM COUPLING FACTOR FOR OVERCOUPLED CAVITIES.

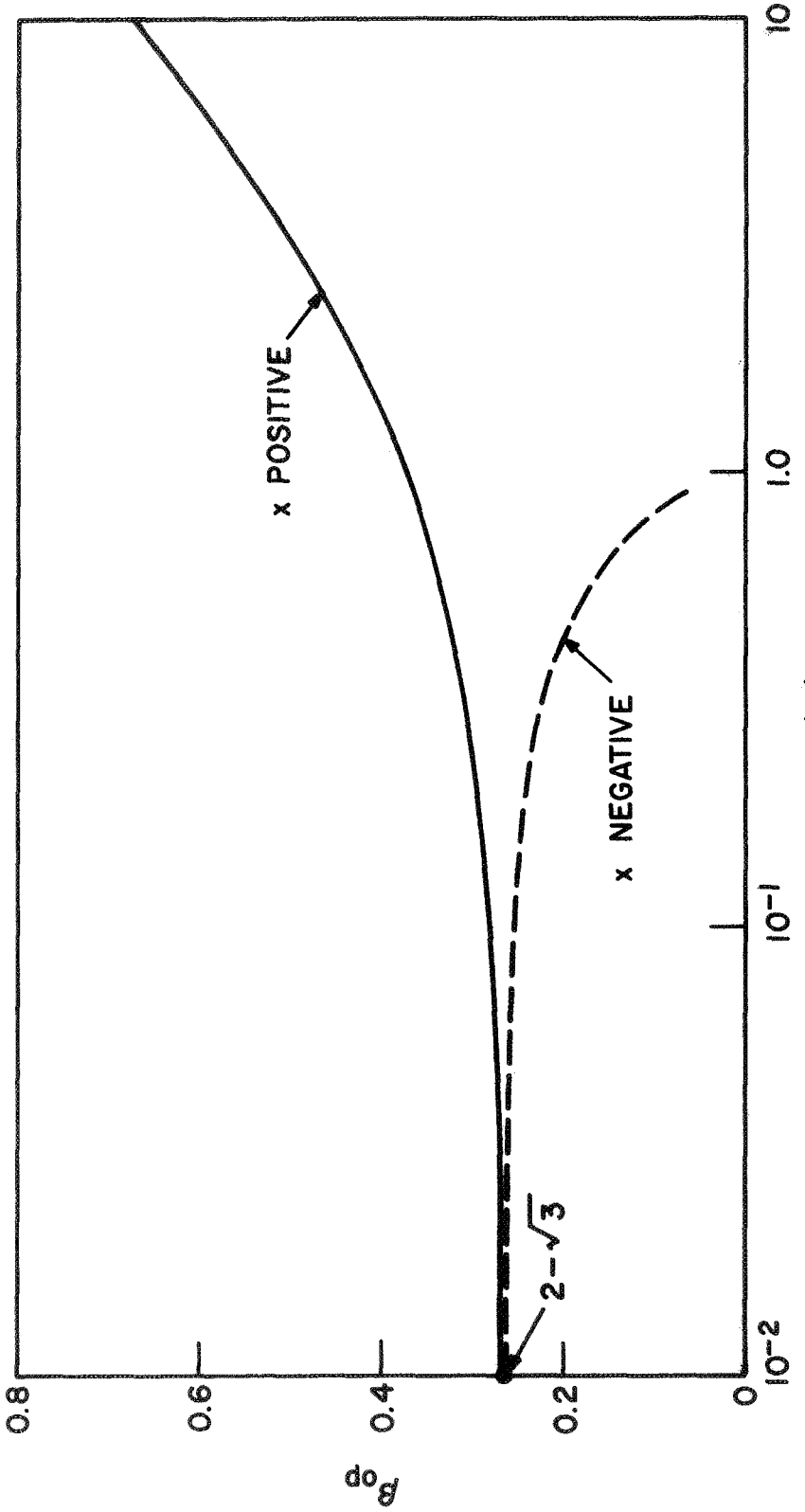

FIG. 3.4 OPTIMUM COUPLING FACTOR FOR UNDERCOUPLED CAVITIES.

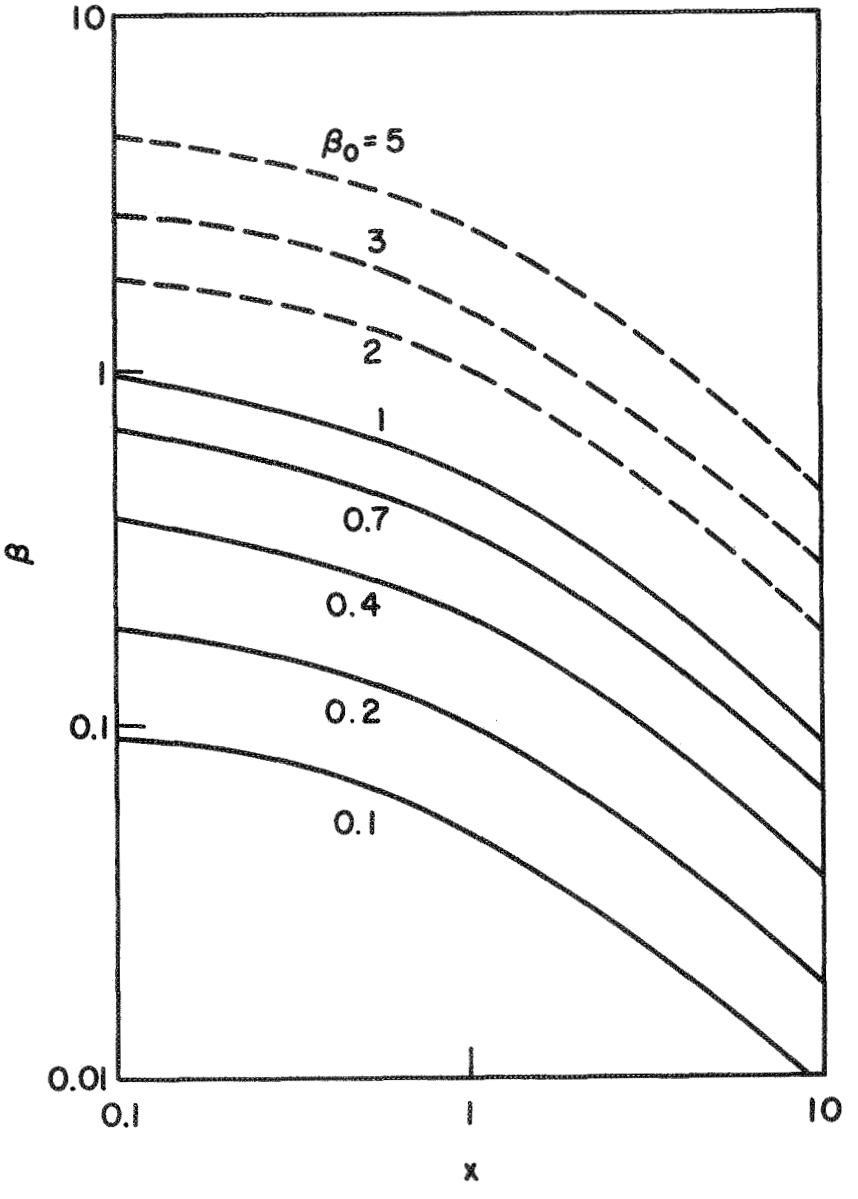

FIG. 3.5 THE CHANGE IN THE COUPLING FACTOR FOR POSITIVE VALUES OF x.

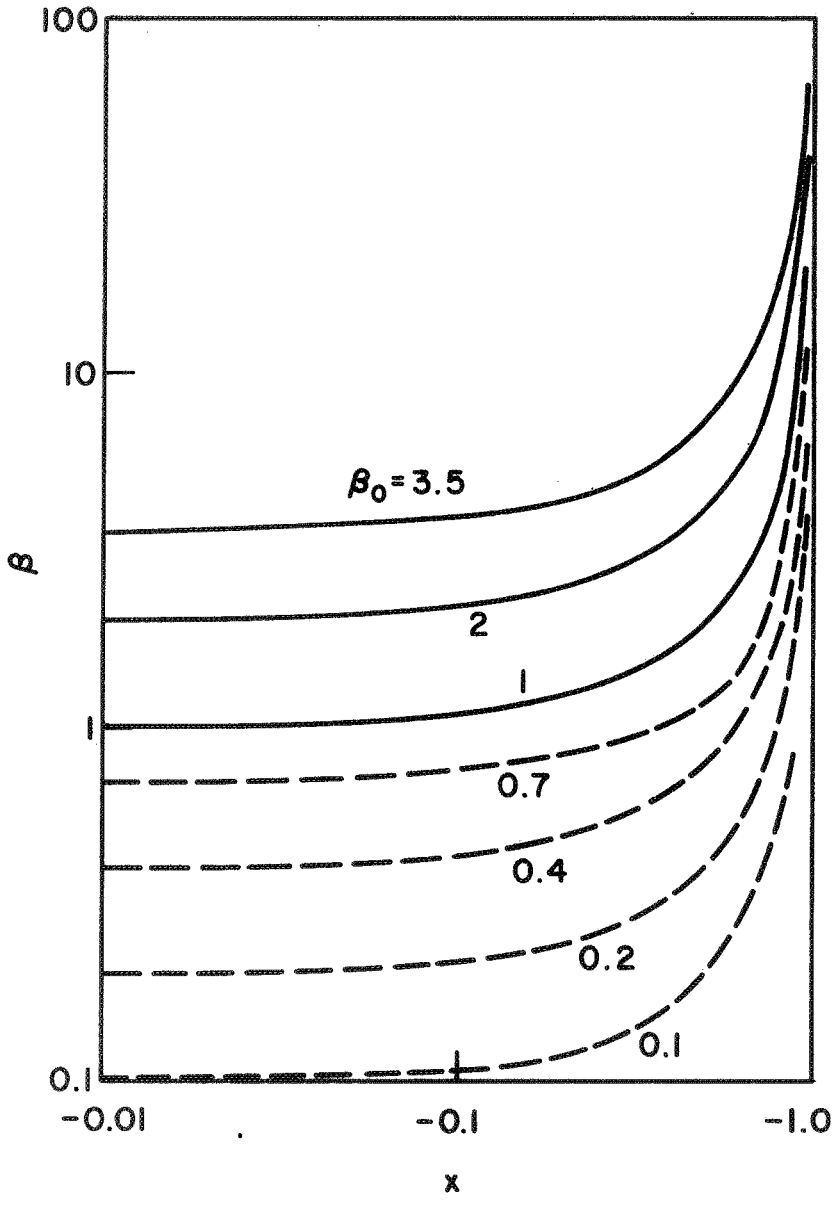

FIG. 3.6 THE CHANGE IN THE COUPLING FACTOR FOR NEGATIVE VALUES OF x.

should be overcoupled if the perturbation causes the conductivity of the sample to decrease. Therefore the solid lines in Figs. 3.3 and 3.4 will serve to give the optimum coupling factor according to the anticipated change in the material's conductivity.

3.2.2 Calculation of the Change in the Detected Power. Figures 3.7 through 3.10 show the change in the detected power relative to the power available from the source for various coupling factors. The plots are numerically generated from Eq. 3.23 with α assumed unity (lossless coupling). The programming is done through iterative steps where each step corresponds to an absolute change in x of 0.001 and after each step the new coupling factor, the conductance and the incremental change in the detected power are determined. The results obtained after each iteration serve as initial conditions for the subsequent one. This makes the analysis suitable for small as well as large values of perturbation. The following observations are worth mentioning.

1. The change in the detected power is monotonically increasing for an overcoupled cavity if x is monotonically decreasing or for an undercoupled cavity with x monotonically increasing as shown in Figs. 3.7 and 3.8, respectively.

2. If the cavity is overcoupled and x is increased the detected power will decrease until it reaches zero and the cavity becomes critically coupled. If x is increased further the detected power starts increasing again as shown in Fig. 3.9. The same effect will occur for an undercoupled cavity if x is decreased monotonically as shown in Fig. 3.10.

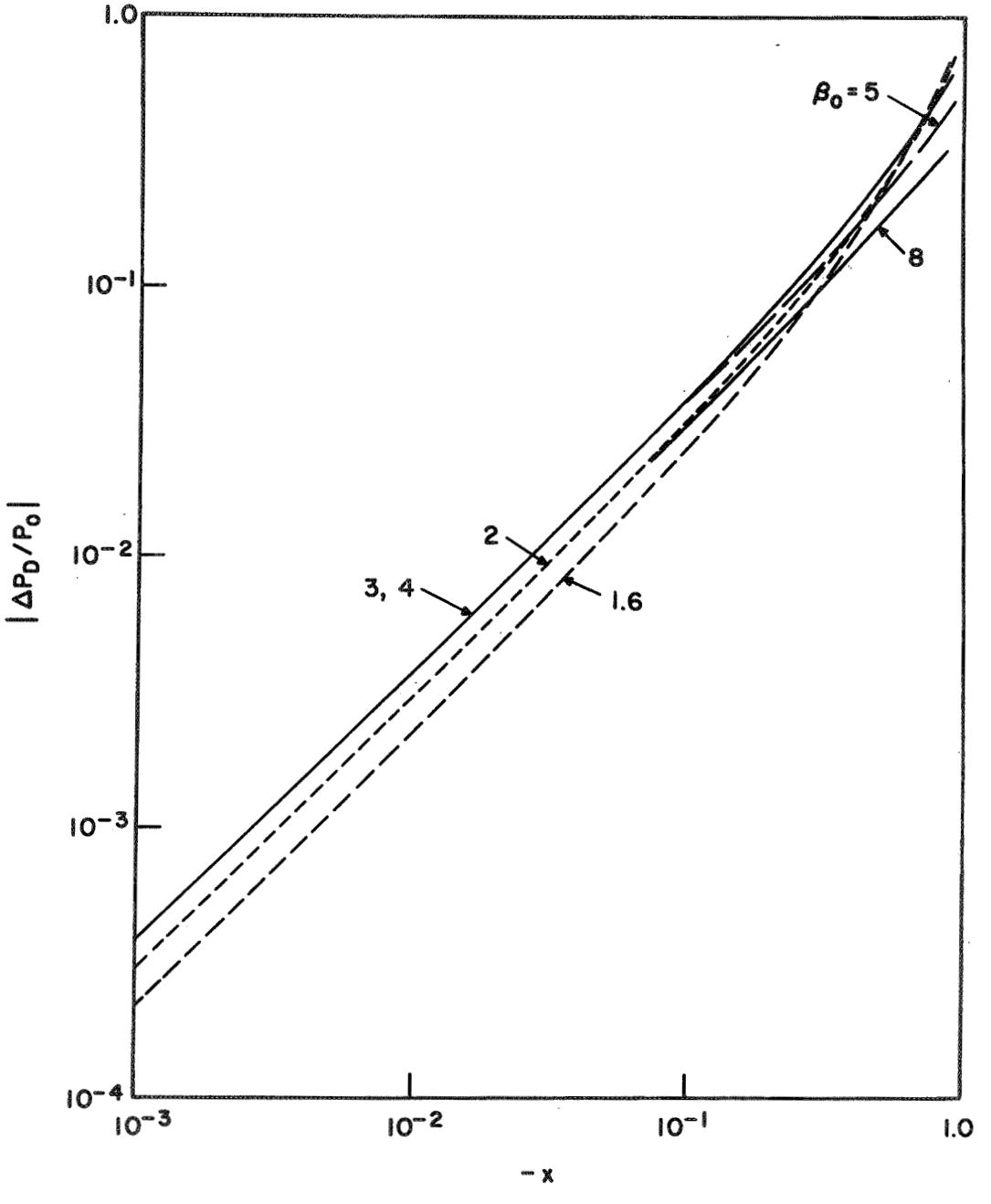

FIG. 3.7 THE RELATIVE CHANGE IN THE DETECTED POWER VS. NEGATIVE VALUES OF x FOR OVERCOUPLED CAVITIES.

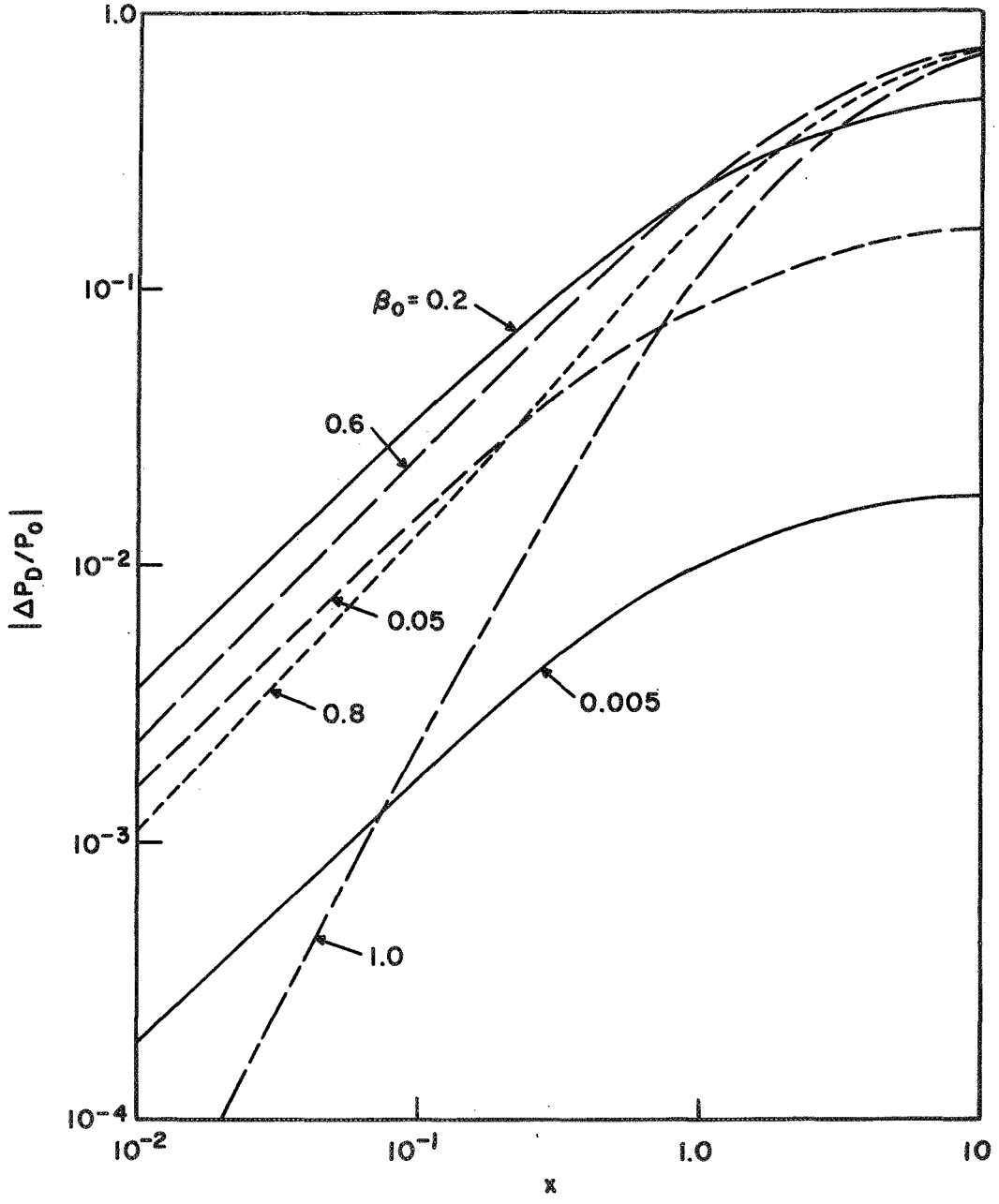

FIG. 3.8 THE RELATIVE CHANGE IN THE DETECTED POWER VS. POSITIVE VALUES OF x FOR UNDERCOUPLED CAVITIES.

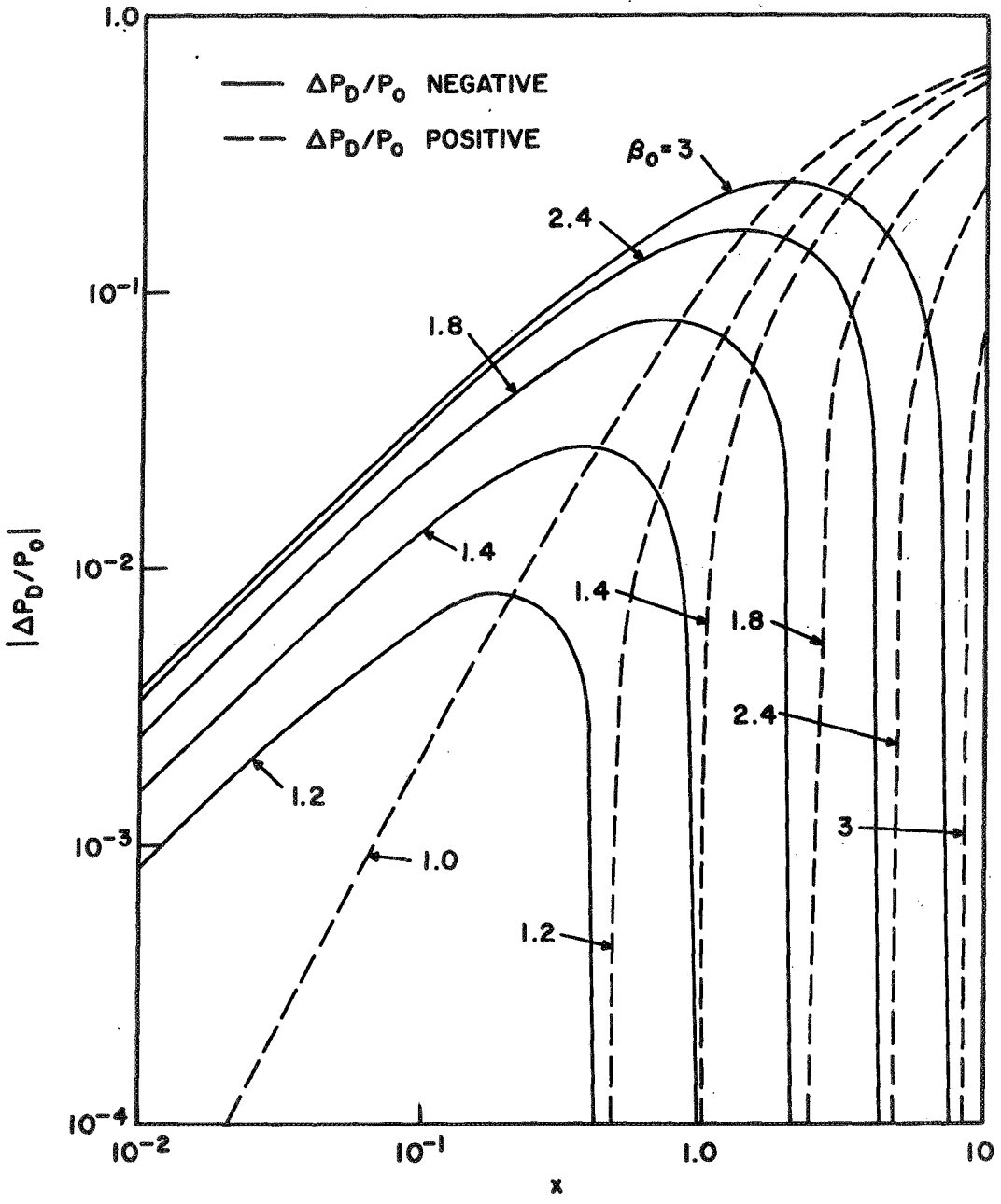

FIG. 3.9 THE RELATIVE CHANGE IN THE DETECTED POWER VS. POSITIVE VALUES OF x FOR OVERCOUPLED CAVITIES.

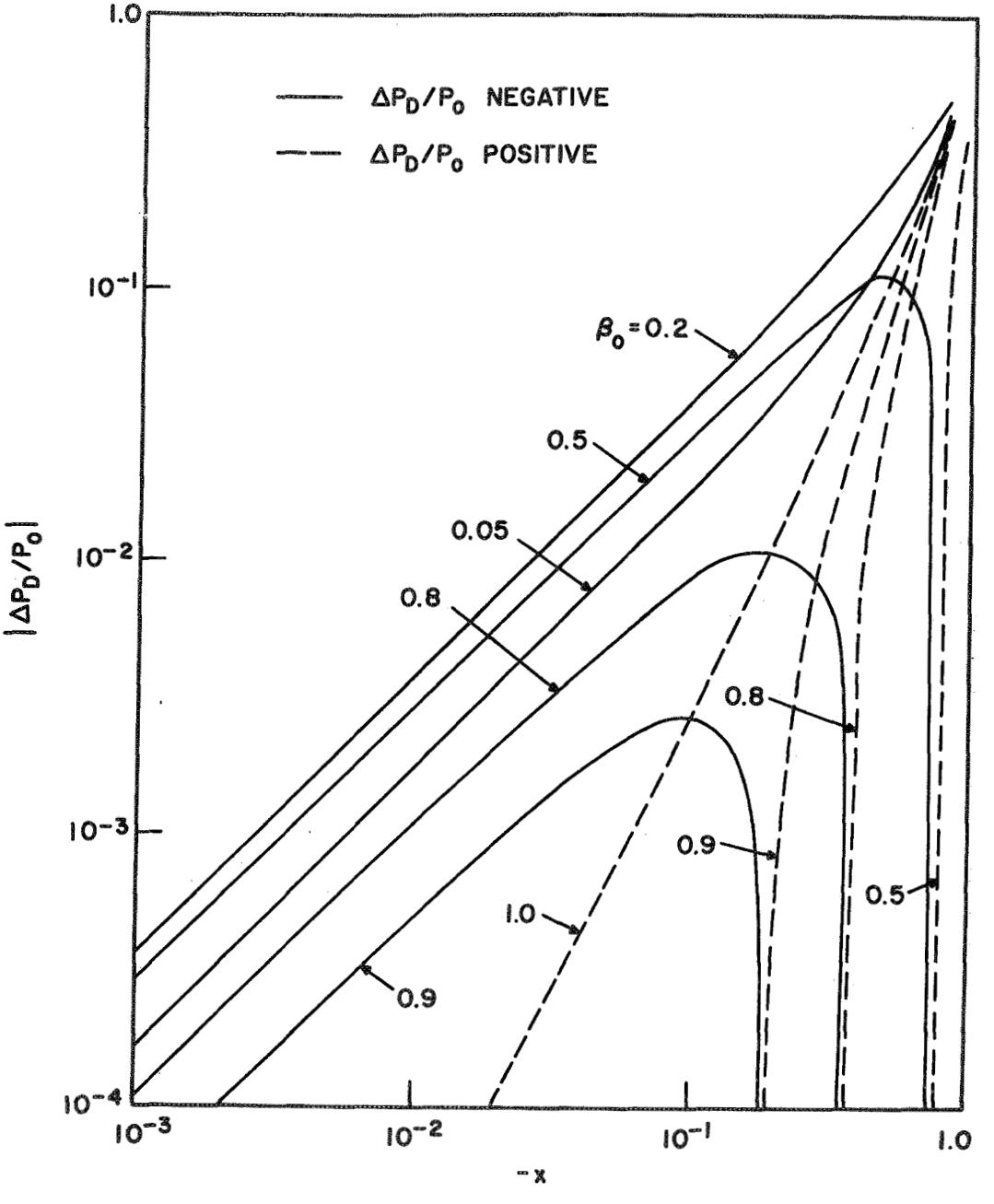

FIG. 3.10 THE RELATIVE CHANGE IN THE DETECTED POWER VS. NEGATIVE VALUES OF x FOR UNDERCOUPLED CAVITIES.

3. Concerning the two cases mentioned in the previous paragraph, there is a value for x at which the change in the detected power is zero. This value is given by

$$x_o = \beta_o^2 - 1 \quad . \tag{3.27}$$

It is clear that x_o is positive if the cavity is overcoupled and negative otherwise. This fact supports the previous discussion for choosing the optimum coupling factor.

4. The curve corresponding to $\beta_o = 1$ passes through all the relative maxima and minima of Figs. 3.9 and 3.10 since these are the points at which the instantaneous coupling factor assumes a value of one.

3.3 Equivalent Circuit of a Semiconductor Material in a Reentrant Cavity in the Presence of an External Magnetic Field

In this treatment, the sample is placed under the central post of the cavity as shown in Fig. 2.3 and the field orientations are assumed to be as indicated in Fig. 2.1. Placing the sample in that region has the following advantages.

1. The electric field is maximum in this region which results in a greater interaction between the sample and the signal.

2. The field is essentially uniform, which simplifies the analysis considerably.

The sample will carry both conduction and displacement currents, i.e.,

$$\underline{J} = \underline{\underline{\sigma}}\,\underline{E} + \frac{\partial \underline{D}}{\partial t} \quad , \tag{3.28}$$

where $\underline{D}$ is the electric displacement vector; the rest of the symbols were defined earlier. Since the microwave field due to the dominant TEM mode is parallel to the x-axis and varies as $e^{j\omega t}$, Eq. 3.28 can be written as

$$\underline{J} = \underline{\underline{\sigma}}\,\underline{E} + j\omega\epsilon\underline{E} \quad . \tag{3.29}$$

It was shown in Chapter II that the conductivity tensor of a material in the presence of a magnetic field along the z-axis can be written as

$$\underline{\underline{\sigma}} = \begin{bmatrix} \sigma_{xx} & \sigma_{xy} & 0 \\ \sigma_{yx} & \sigma_{yy} & 0 \\ 0 & 0 & \sigma_{zz} \end{bmatrix} \quad . \tag{3.30}$$

Therefore by substituting Eq. 3.30 into 3.29, the x- and y-components of the current density can be written as follows

$$J_x = (\sigma_{xx} + j\omega\epsilon_{xx})E_x + (\sigma_{yx} + j\omega\epsilon_{yx})E_y \tag{3.31}$$

and

$$J_y = (\sigma_{xy}E_x + j\omega\epsilon_{xy})E_x + (\sigma_{yy} + j\omega\epsilon_{yy})E_y \quad . \tag{3.32}$$

The continuity of current at the sample surface normal to the y-axis implies that the displacement current outside the sample should be equal to the total current within the sample. And since the electric field is uniform and along the x-axis, $J_y = 0$. Therefore

$$E_y = -\frac{\sigma_{xy} + j\omega\epsilon_{xy}}{\sigma_{yy} + j\omega\epsilon_{yy}} E_x \quad . \tag{3.33}$$

Substituting Eq. 3.33 into Eq. 3.31 we get,

$$J_x = \left((\sigma_{xx} + j\omega\epsilon_{xx}) - \frac{(\sigma_{xy} + j\omega\epsilon_{xy})(\sigma_{yx} + j\omega\epsilon_{yx})}{\sigma_{yy} + j\omega\epsilon_{yy}} \right) E_x \quad . \tag{3.34}$$

Therefore the equivalent admittance of a sample of thickness t and an area A follows immediately from Eq. 3.34,

$$Y_m = \frac{A}{t}\left(\sigma_{xx} + j\omega t_{xx}\right) + Y_{ani} \quad , \tag{3.35}$$

where Y_m is the equivalent conductance of the material and Y_{ani} is the contribution to Y_m due to the anisotropy of the material and is given by

$$Y_{ani} = - \frac{(\sigma_{xy} + j\omega\epsilon_{xy})(\sigma_{yx} + j\omega\epsilon_{yx})}{\sigma_{yy} + j\omega\epsilon_{yy}} \frac{A}{t} \quad . \tag{3.36}$$

However, it has been shown that[59] $\sigma_{xy} = -\sigma_{yx}$ and $\epsilon_{xy} = -\epsilon_{yx}$, and thus Y_{ani} reduces to

$$Y_{ani} = \left(\frac{\sigma_{yy}(\sigma_{12}^2 - \omega^2\epsilon_{12}^2) + 2\omega^2\epsilon_{12}\sigma_{12}\epsilon_{yy}}{\sigma_{yy}^2 + \omega^2\epsilon_{yy}^2} + j\omega \frac{2\epsilon_{12}\sigma_{12}\sigma_{yy} + \epsilon_{yy}(\omega^2\epsilon_{12}^2 - \sigma_{12}^2)}{\sigma_{yy}^2 + \omega^2\epsilon_{yy}^2} \right) \frac{A}{t} \quad , \tag{3.37}$$

where $\epsilon_{xy} = -\epsilon_{yx} = \epsilon_{12}$ and $\sigma_{xy} = -\sigma_{yx} = \sigma_{12}$. If σ_{12} is much greater then $\omega\epsilon_{12}$ then the equivalent admittance of the sample becomes

$$Y_m = \frac{A}{t}\left(\sigma_{xx} + j\omega\epsilon_{xx} + \frac{\sigma_{12}^2}{\sigma_{yy} + j\omega\epsilon_{yy}} \right) \quad . \tag{3.38}$$

On the other hand, if the material is isotropic, the expression for the equivalent admittance of the sample becomes

$$(Y_m)_{iso} = \frac{A}{t}(\sigma + j\omega\epsilon) \quad . \tag{3.39}$$

Figures 3.11 show the equivalent circuit of the sample under consideration.

3.3.1 Equivalent Circuit of the Cavity Including the Sample. Figures 3.12 shows the material orientation within the cavity together with the sample dimensions. The cavity is divided into two parts by the plane A-A. The section above this plane can be represented by a transmission line terminated in a short circuit. This part is equivalent to a parallel R, L and C circuit. The value of these elements (L_o, R_o and C_o) are functions of the dimensions a_1, a_2, L and the conductivity of the cavity walls. The section below the plane A-A adds an extra shunt impedance Z which will depend on the sample parameters. It is fairly reasonable to assume that most of the contribution of this section to Z comes from the region underneath the central post. With this in mind the impedance Z could be divided into three components, namely

1. The reactance of a capacitance C_1 due to the air gap between the two planes A-A and B-B under the central post which is given by

$$C_1 = \frac{\kappa_o \pi a_1^2}{\ell - t} \quad . \tag{3.40}$$

2. An impedance Z_m due to the presence of the sample whose value was derived in the previous section.

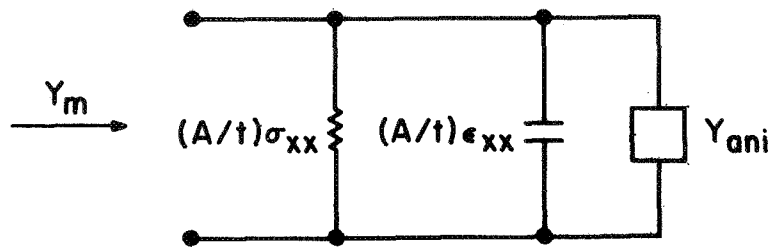

(a) ANISOTROPIC MATERIAL

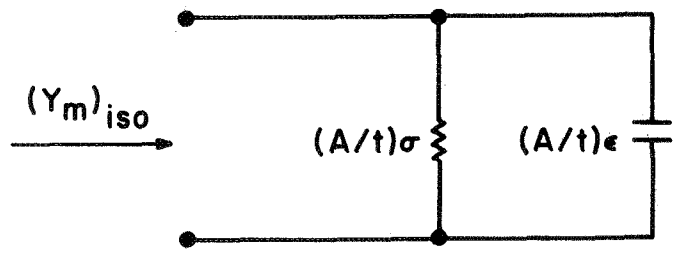

(b) ISOTROPIC MATERIAL

FIG. 3.11 EQUIVALENT CIRCUIT OF THE SAMPLE.

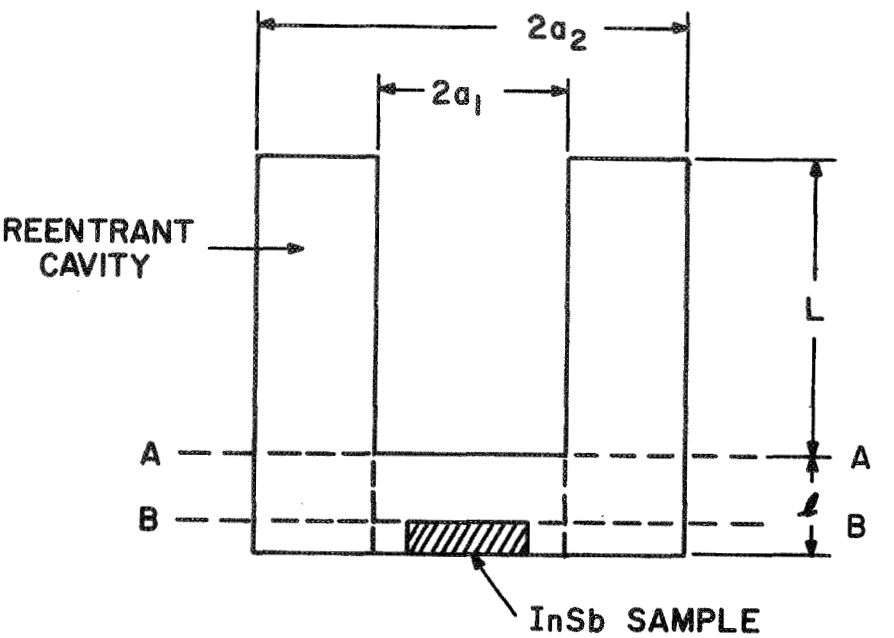

(a) SAMPLE ORIENTATION WITHIN THE CAVITY

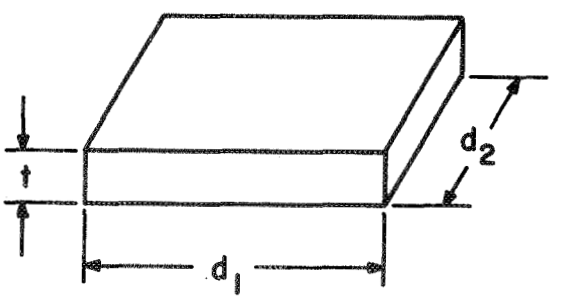

(b) SAMPLE DIMENSIONS

FIG. 3.12 ORIENTATION AND DIMENSIONS OF THE CAVITY AND SAMPLE.

3. The reactance of a second capacitance C_2 due to the air gap under the plane B-B that is not occupied by the sample and is given by

$$C_2 = \frac{\kappa_o(\pi a_1^2 - d_1 d_2)}{t} \quad . \tag{3.41}$$

The impedance Z will be composed of the impedance due to C_1 in series with the shunt combination of C_2 and Z_m and is therefore given by

$$Z = \frac{1}{j\omega C_1} + \frac{Z_m}{1 + j\omega Z_m C_2} \quad . \tag{3.42}$$

Substituting the value of Y_m as obtained from Eq. 3.38 into Eq. 3.42 yields

$$Z = \frac{1}{j\omega C_1} + \frac{1}{G' + j\omega C'} \quad , \tag{3.43}$$

where

$$G' = K_1 \left(\sigma_{xx} + \frac{\sigma_{12}^2}{\sigma_{yy}^2 + \omega^2 \epsilon^2} \sigma_{yy} \right) \quad , \tag{3.44}$$

$$C' = K_1 \left(\epsilon_{xx} - \epsilon_{yy} \frac{\sigma_{12}^2}{\sigma_{yy}^2 + \omega^2 \epsilon^2} \right) + C_2 \tag{3.45}$$

and

$$K_1 = \frac{d_1 d_2}{t} \quad . \tag{3.46}$$

The equivalent admittance of the cavity section below plane A-A can be obtained by inverting Z which yields

$$Y = G_{eff} + j\omega C_{eff} \quad , \tag{3.47}$$

where

$$G_{eff} = \frac{G'}{\frac{G'^2}{\omega^2 C_1^2} + \left(1 + \frac{C'}{C_1}\right)^2} \tag{3.48}$$

and

$$C_{eff} = C_1 \frac{1 + \frac{\omega^2 C_1 C'}{G'^2}\left(1 + \frac{C'}{C_1}\right)}{1 + \frac{\omega^2 C_1^2}{G'^2}\left(1 + \frac{C'}{G}\right)^2} . \tag{3.49}$$

Figures 3.13a and c show the cavity equivalent circuit in the absence and presence of the sample, respectively. The capacitance C_a is the gap capacitance in the absence of the material and equals approximately $(\kappa_o \pi a_1^2/\ell)$. Figure 3.13b shows the equivalent circuit of the cavity section under the central post where Z_m, the sample equivalent circuit, was derived earlier.

If the material is isotropic both σ_{12} and ϵ_{12} become zero and the expressions for G_{eff} and C_{eff} become

$$G_{eff} = \frac{K_1 \sigma}{\frac{K_1^2 \sigma^2}{\omega^2 C_1^2} + \left(1 + \frac{C}{C_1}\right)^2} \tag{3.50}$$

and

$$C_{eff} = C_1 \frac{1 + \frac{\omega^2 C^2}{K_1^2 \sigma^2}\left(1 + \frac{C_1}{C}\right)}{1 + \frac{\omega^2 C^2}{K_1^2 \sigma^2}\left(1 + \frac{C_1}{C}\right)^2} , \tag{3.51}$$

where $C = C_1 + K_1 \epsilon$. The values of C_1, C_2 and $K_1 \epsilon$ for the cavity used for testing the material are 0.11, 0.21 and 1.31 pF, respectively, where the

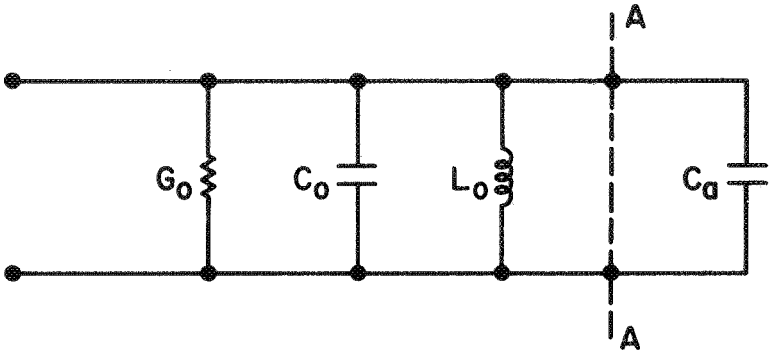

(a) EMPTY CAVITY

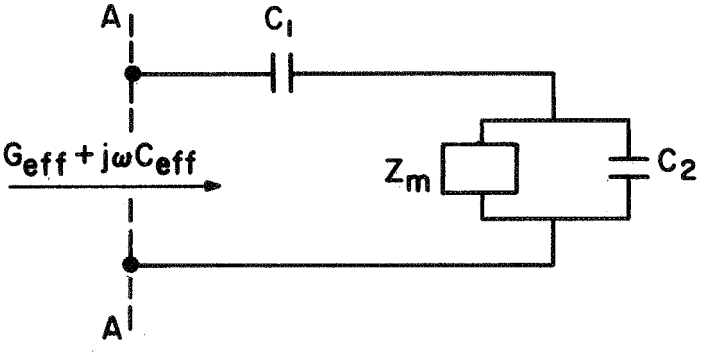

(b) SECTION UNDER THE CENTRAL POST WITH THE SAMPLE PRESENT

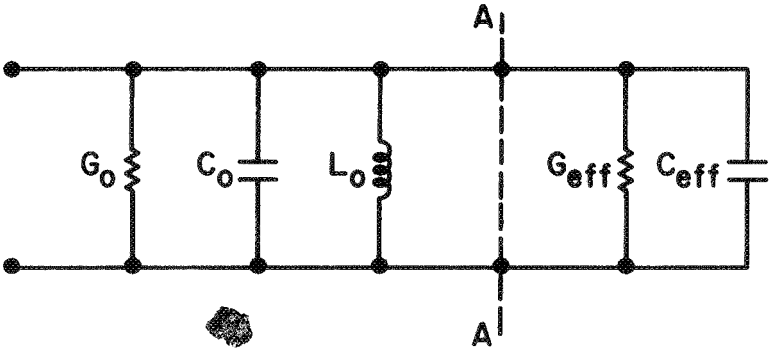

(c) CAVITY IN THE PRESENCE OF THE SAMPLE

FIG. 3.13 CAVITY EQUIVALENT CIRCUIT.

lattice dielectric constant was substituted for ϵ. Thus for the indium antimonide samples of interest here both $(\omega C/K_1\sigma)^2$ and $(\omega C_1/K_1\sigma)^2$ are much greater than one. This simplifies Eqs. 3.50 and 3.51 to the following form:

$$G_{eff} = K\sigma \tag{3.52}$$

and

$$C_{eff} = \frac{C_1 C}{C_1 + C} , \tag{3.53}$$

where $K = [K_1/(1 + C/C_1)^2]$.

It is worth noting that this K is the geometrical factor presented earlier in Chapter II. Therefore the change in the conductivity of the material will change the equivalent conductance of the test cavity and can be measured by monitoring the change in the detected power as presented in Section 3.2. On the other hand, the change in the material dielectric constant will in turn change C_{eff}, and as a result the resonance frequency of the cavity will shift slightly. The cavity equivalent circuit shown in Figs. 3.13 can be used to relate the change in the sample dielectric constant to the resonance frequency shift. The cavity resonance frequency is given by

$$f = \frac{1}{2\pi \sqrt{L_o(C_o + C_{eff})}} . \tag{3.54}$$

For a small shift in the resonance frequency as a result of the perturbation, Eq. 3.54 can be written as follows:

$$f_o + \Delta f = \frac{1}{2\pi \sqrt{L_o(C_o + C_{effo} + \Delta C_{eff})}} \quad . \tag{3.55}$$

The relative shift in the resonance frequency can be expressed as

$$\frac{\Delta f}{f_o} = \frac{1}{\sqrt{1 + \dfrac{\Delta C_{eff}}{C_o + C_{effo}}}} - 1 \quad . \tag{3.56}$$

Equation 3.56 can be utilized to study the incremental change in the material dielectric constant as a function of the resonance frequency shift. Substituting Eq. 3.53 in the Taylor expansion of Eq. 3.56 yields

$$\frac{\Delta f}{f_o} = -\frac{1}{2} A(K_1 \Delta\epsilon) + \frac{3}{8} A^2 (K_1 \Delta\epsilon)^2 + \ldots \quad , \tag{3.57}$$

where

$$A = \frac{C_1}{(C_1 + C_2 + K_1 \epsilon_o)(C_o + C_{effo})} \quad . \tag{3.58}$$

Since we are dealing with incremental changes in ϵ, it becomes quite reasonable to neglect higher-order terms in $\Delta\epsilon$ which results in

$$\frac{\Delta f}{f_o} = -\frac{1}{2} \frac{C_1}{(C_1 + C_2 + K_1 \epsilon_o)\left(C_o + \dfrac{C_1 (C_2 + K_1 \epsilon_o)}{C_1 + C_2 + K_1 \epsilon_o}\right)} K_1 \Delta\epsilon \quad . \tag{3.59}$$

Therefore the change in the relative dielectric constant of the material is given by

$$\Delta\epsilon_r = -\eta_1 \frac{\Delta f}{f_o} \quad , \tag{3.60}$$

where

$$\eta_1 = \frac{2}{\kappa_o K_1} \left(1 + \frac{C_2}{C_1} + \frac{K_1 \epsilon_o}{C_1}\right)\left(C_o + \frac{C_1 (C_2 + K_1 \epsilon_o)}{C_1 + C_2 + K_1 \epsilon_o}\right) \quad . \tag{3.61}$$

Equation 3.60 is similar to Eq. 3.10 where both η and η_1 depend on the geometry of the cavity system. Either formula can be used to study the

change of the dielectric constant as a result of the perturbation if the geometrical filling factor is known.

3.4 Calibration of the Cavity System

In order to study the change in the material conductivity and dielectric constant as a result of the perturbing signal the parameter F and either η or η_1 should be determined. Moreover, it is necessary to investigate the dependence of these parameters together with β_o on the temperature.

The geometrical factor η can be determined by studying the field configuration within the cavity system. However, this is a very lengthy and involved process, especially if higher-order modes are excited. This factor can be determined experimentally by studying the frequency shift due to samples of known dielectric constant. Samples of glass and single crystal silicon and germanium having the same dimensions as the indium antimonide samples under test were used for this purpose. The shift in the resonance frequency from that of the empty cavity was measured in each case and was used in conjunction with Fig. 3.14 or 3.15 to determine η. Figures 3.14 and 3.15 are plots of the sample ϵ_r and $\Delta\epsilon_r$, respectively, vs. the normalized frequency shift Δf_N, which is given by the relation

$$\Delta f_N = \frac{f - f_o}{\eta f_o} \quad . \tag{3.62}$$

The plots are generated from Eq. 3.10 assuming ϵ_{ro} equals one which corresponds to the empty cavity. The plots are extended to large values of $\Delta\epsilon_r$ and ϵ_r by using an iteration process; this improves the accuracy of calibration.

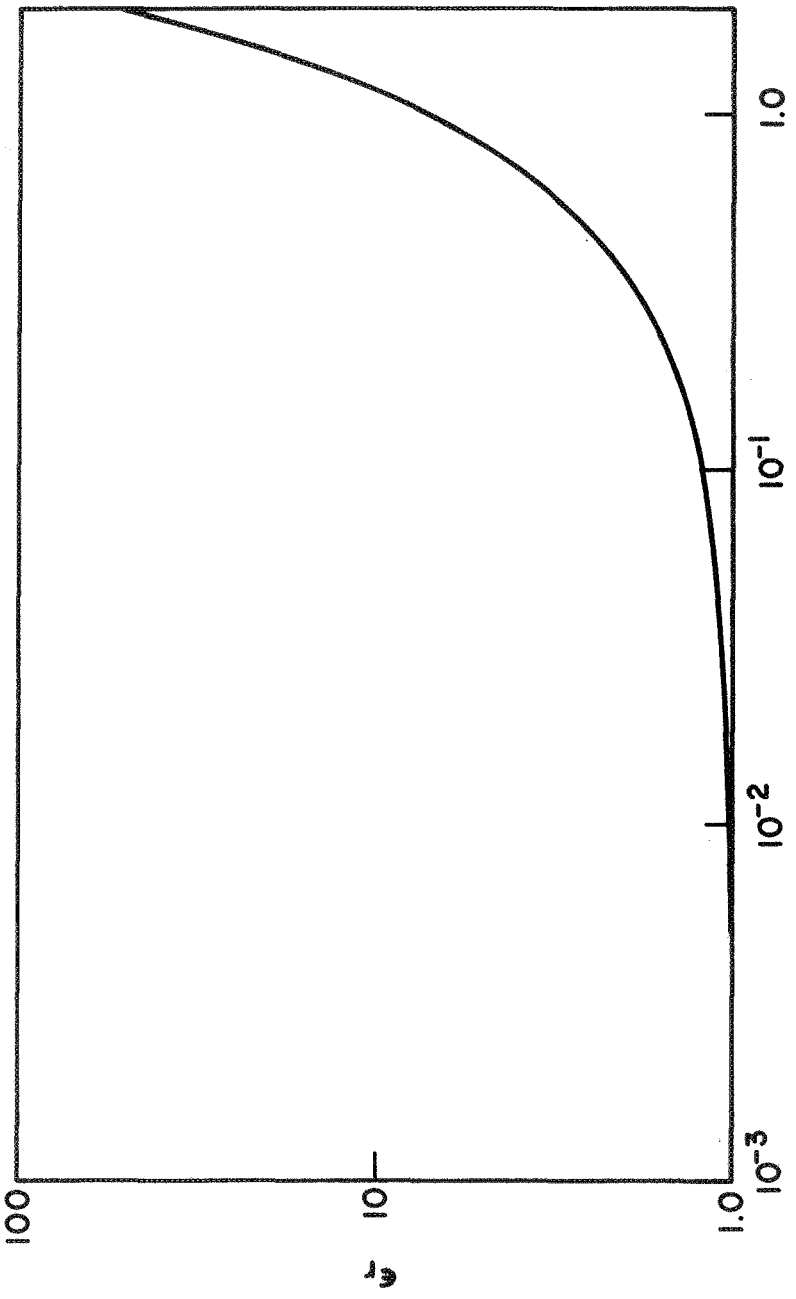

FIG. 3.14 THE DIELECTRIC CONSTANT OF THE SAMPLE VS. Δf_N. ($\epsilon_{ro} = 1$)

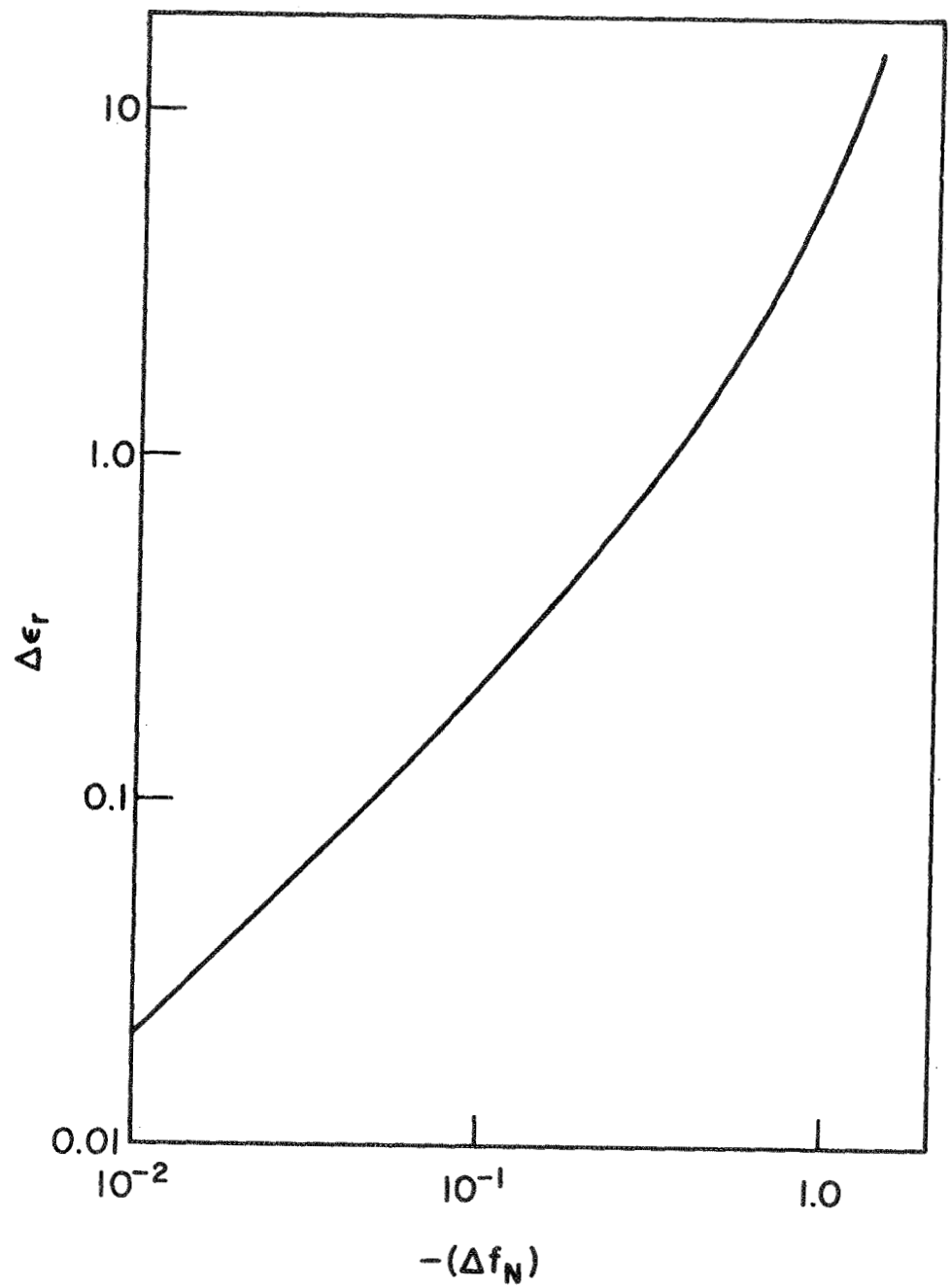

FIG. 3.15 CHANGE IN THE RELATIVE DIELECTRIC CONSTANT OF THE SAMPLE VS. Δf_N. ($\epsilon_{ro} = 1$)

In order to study the sample dielectric constant as a function of temperature, the contribution to the frequency shift due to the change in the cavity dimensions should be accounted for. The net frequency shift due to the change in the sample dielectric constant as a result of temperature change is given by

$$\Delta f = \Delta f_m - \Delta f_e \quad , \tag{3.63}$$

where Δf_m = the measured frequency shift and

Δf_e = the frequency shift as a result of the thermal expansion of the cavity walls.

It was shown by Montgomery[60] that Δf_e is given by

$$\Delta f_e = -\alpha_T f_o (\Delta T) \quad , \tag{3.64}$$

where ΔT = the change in cavity temperature and

α_T = the coefficient of thermal expansion of the cavity walls.

The coefficient of thermal expansion of the cavity walls (commercial brass) is given by the following[61]

$$\alpha_T = 14.916 \times 10^{-6} + 1.25 \times 10^{-8}\, T \quad ; \text{ per } ^\circ K \quad . \tag{3.65}$$

Equations 3.64 and 3.65 were used to determine Δf_e as the cavity temperature was changed from liquid nitrogen temperature (77°K), assuming that the resonance frequency at this temperature is 9.675 GHz (the cavity resonance frequency at 77°K in the presence of the sample), the result is shown in Fig. 3.16.

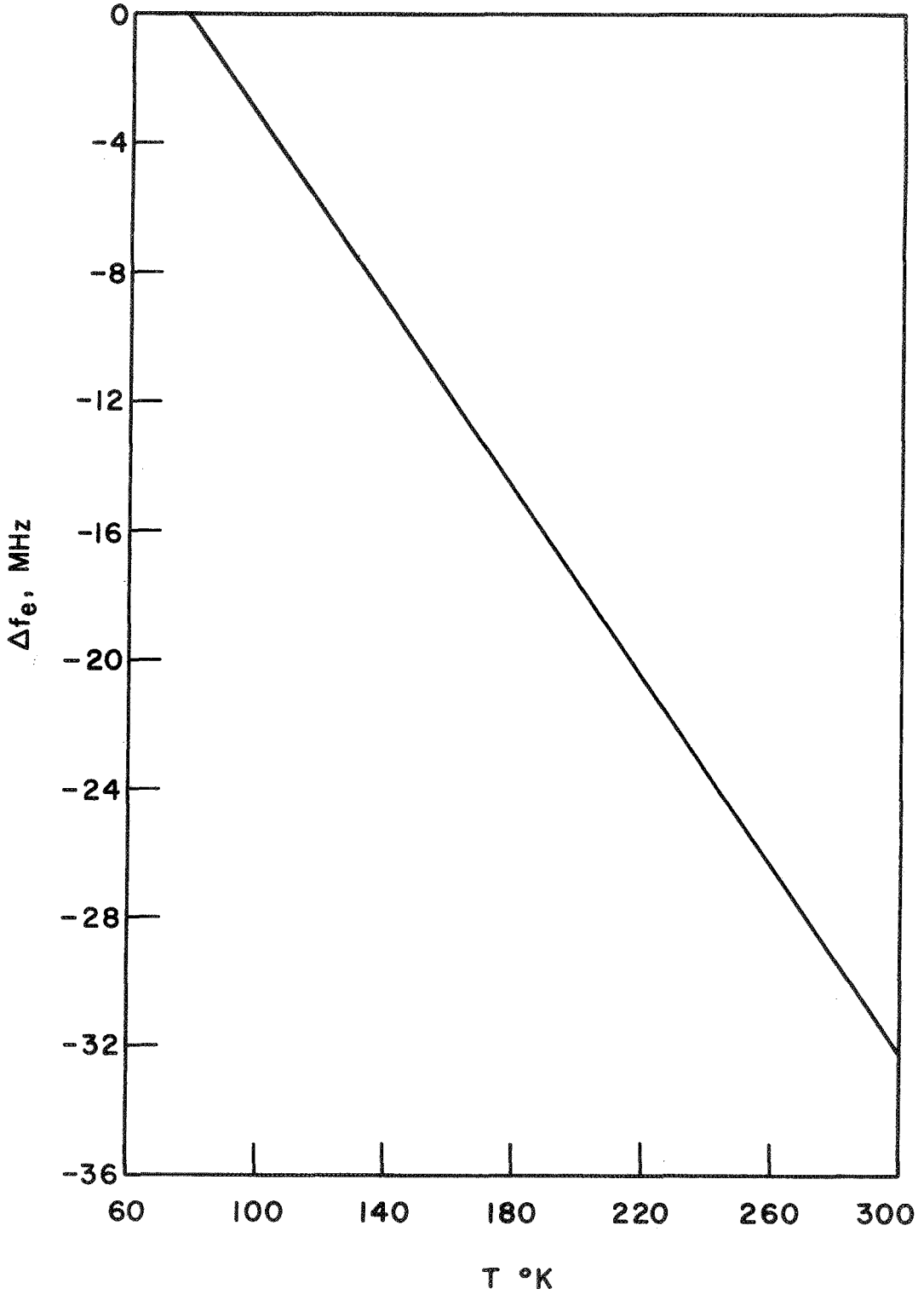

FIG. 3.16 FREQUENCY SHIFT DUE TO THERMAL EXPANSION OF THE CAVITY WALLS.

In order to conclude the analysis for calibration of the cavity system, a discussion concerning the determination of the parameter F and its temperature dependence is in order. It can be shown that F can be determined by measuring the cavity coupling factor without the sample β_{oo} and with the sample present at zero magnetic field. From Eq. 3.23,

$$F = \frac{K\sigma_o}{K\sigma_o + G_o} \tag{3.66}$$

which can be written as

$$F = \frac{K}{K + \frac{G_o}{\sigma_o}} \quad . \tag{3.67}$$

Since β_o and β_{oo} are given by the following equations,

$$\beta_{oo} = \frac{Y_o}{G_o} \tag{3.68}$$

and

$$\beta_o = \frac{Y_o}{K_o\sigma_o + G_o} \quad , \tag{3.69}$$

combining these two equations yields

$$\frac{G_o}{\sigma_o} = \frac{K_o\beta_o}{\beta_{oo} - \beta_o} \quad . \tag{3.70}$$

Substituting Eq. 3.70 into 3.67 yields

$$F = \frac{\beta_{oo} - \beta_o}{\beta_{oo} - \beta_o\left(1 - \frac{K_o}{K}\right)} \quad , \tag{3.71}$$

where K was defined earlier as

$$K = K_1/(1 + C/C_1)^2 \quad . \tag{3.72}$$

Equation 3.71 is used to determine the factor F and its temperature dependence by measuring K, β_{oo} and β_o as a function of temperature. The factor F was measured between 77°K and 300°K. No resonance frequency shift due to the presence of the sample was observed as the temperature was varied between liquid nitrogen and room temperatures. This implies that K_o equals K over this temperature range. Thus for temperatures above liquid nitrogen, F will be given by

$$F = \left(1 - \frac{\beta_o}{\beta_{oo}}\right) \quad . \tag{3.73}$$

Figure 3.17 shows the measured values of β_o, β_{oo} and the corresponding F as given by Eq. 3.73 for temperature values above liquid nitrogen. On the other hand, if the sample dielectric constant is a function of the perturbation, then K/K_o must be evaluated and Eq. 3.71 will be used to determine F.

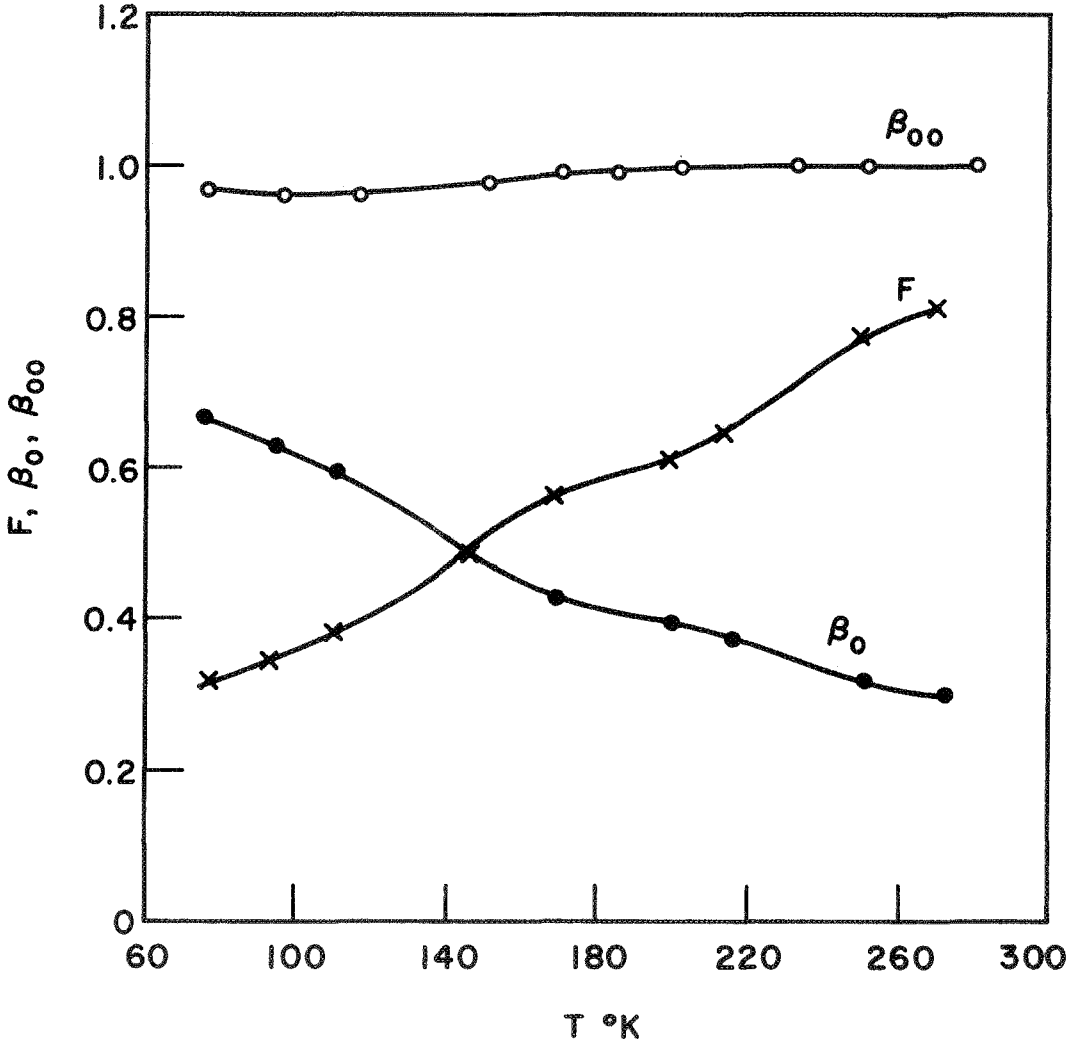

FIG. 3.17 MEASURED VALUES OF β_o, β_{oo} AND F VS. T FOR A CONSTANT VALUE OF $K = K_o$.

CHAPTER IV. PHYSICAL PROPERTIES OF THE DETECTION SCHEME

4.1 Introduction

In this chapter the parameters characterizing the performance of the detection scheme are derived. An equivalent circuit approach making use of the results obtained earlier in Chapters II and III is utilized for this purpose.

The terminal-to-terminal conversion loss of the downconversion scheme is evaluated and the dependence of the conversion loss on the external circuit parameters and the bulk material parameters is presented. This approach is very advantageous for optimizing the detection scheme.

The noise sources in the detection scheme are discussed and the minimum detectable power and noise equivalent power of the downconverter are determined and the theoretical and experimental results are compared.

Finally, an estimate of the time constant of the detector is given and its dependence on the material and circuit parameters is discussed. The last section deals with the detector performance as a function of the magnetic field.

4.2 Study of the Conversion Loss

4.2.1 Introduction. In order to develop the concept of conversion loss it is necessary to understand how the signal detection is accomplished. Figure 4.1 together with Fig. 1.1 explain the principle of operation of the detection scheme. For a certain microwave bias power P_{ix}, the coupling to the cavity can be adjusted to result in a

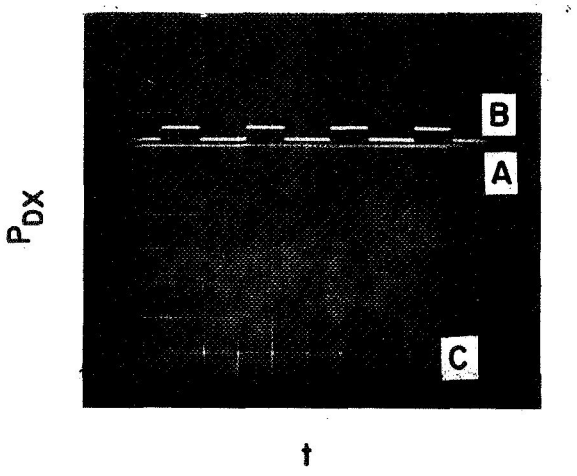

A. P_{DX} IN THE ABSENCE OF THE MILLIMETER-WAVE SIGNAL

B. P_{DX} IN THE PRESENCE OF A SQUARE-WAVE MODULATED MILLIMETER-WAVE SIGNAL

C. ZERO SIGNAL LEVEL

FIG. 4.1 PRINCIPLE OF OPERATION OF THE DETECTION SCHEME.

detected signal P_{Dx} in the absence of the millimeter-wave signal to be detected. As a result of applying the millimeter-wave power P_i the detected signal will change by ΔP_D. The terminal-to-terminal conversion loss will therefore be given by

$$L_T = \frac{\Delta P_D}{P_i} \quad , \tag{4.1}$$

where L_T = the terminal-to-terminal conversion loss,

P_i = the incident millimeter-wave signal power and

ΔP_D = the change in the detected X-band power due to the presence of the millimeter-wave signal.

4.2.2 Dependence of the Reflected Power on the Millimeter-Wave Signal. The change in the detected power was given by Eq. 3.23 and can be written as

$$\Delta P_D = - \frac{4\alpha\beta_o}{(1 + \beta_o)^2} \left[\frac{1 + x}{\left(1 + \frac{x}{1 + \beta_o}\right)^2} - 1 \right] P_{ox} \quad , \tag{4.2}$$

where all the quantities have been defined earlier. For small values of x which is essentially the case here, Eq. 4.2 reduces to

$$\Delta P_D = 4\alpha P_{ox} \left[\frac{\beta_o(1 - \beta_o)}{(1 + \beta_o)^3} \right] x \quad . \tag{4.3}$$

Equation 4.3 can be used to study the downconversion scheme if the dependence of x on P_i is known. Since $x = F(\Delta\sigma/\sigma_o)$, a study of the change in the material conductivity as a function of the

millimeter-wave signal is necessary. For the time being any change in the material dielectric constant resulting in the cavity resonance frequency shift is neglected.

The material conductivity in the absence of the signal to be detected can be written as

$$\sigma_o = e\left[\mu_{co}n + (N_I - n)\mu_{io}\right] , \tag{4.4}$$

where n is the concentration of the carriers that are thermally excited to the conduction band in the absence of the millimeter-wave signal and the remaining quantities were defined earlier. The general form of the conductivity in the presence of the signal can be written as follows:

$$\sigma = \left[\mu_c(n + n_s) + \mu_i(N_I - n - n_s)\right] e , \tag{4.5}$$

where n_s = the density of the carriers excited from the impurity band to the conduction band as a result of photoconductive transitions and is given by[62]

$$n_s = \frac{\gamma P_{im}\tau}{hf_i V_s}\, u(hf_i - \Delta E) , \tag{4.6}$$

where γ = the conversion efficiency,

f_i = the signal frequency,

τ = the carrier lifetime,

P_{im} = the millimeter-wave power absorbed by the sample and

$$u(hf_i - \Delta E) = \begin{cases} 0 & \text{if } hf_i \leq \Delta E \\ 1 & \text{if } hf_i > \Delta E \end{cases} .$$

The change in the material's conductivity due to the incident signal can be obtained by combining Eqs. 4.4 and 4.5 and is given by

$$\Delta\sigma = e\left[n(\mu_c - \mu_{co}) + n_s(\mu_c - \mu_i) + (N_I - n)(\mu_i - \mu_{io})\right] , \qquad (4.7)$$

where the subscript zero indicates quantities in the absence of the signal. Three cases are of interest. They are:

1. The impurity and conduction bands totally overlap; in this case $n_s = 0$ and $n = N_I$ and the detection scheme operates on the principle of free-carrier absorption. The detector performance is well represented by this case in the absence of a magnetic field.

2. The charge carriers are strongly bound to the impurity band and the familiar band picture of a semiconductor prevails. This implies that $n = 0$ and the detector operates in a photoconductive mode. It has been shown earlier that freeze-out of carriers can be achieved in the presence of a strong magnetic field. However donor levels in n-type InSb were shown to exist at energies of 1.8×10^{-2} and 6.7×10^{-4} eV

below the conduction band[63] which correspond to activation frequencies of 4352 and 162 GHz, respectively. Both are above the frequency range of the available signal sources and therefore a discussion of this case will not be presented here. This mode of operation might prove very useful as a narrow-band tunable detector.

3. There is a partial overlap between the impurity and the conduction bands. This case will be discussed later when the magnetic field effects are considered. Equation 4.7 is applicable in this case.

Since no ionization energy for n-InSb has been observed in the absence of a magnetic field,[64] the change in the material conductivity as a result of irradiating the sample must be due to a change in the mobility, since the carrier concentration remains essentially constant. The change in the material conductivity as a result of the millimeter-wave signal in the presence of the microwave bias is shown in Appendix A to be given by the following equation:

$$\Delta\sigma = K_m P_i \quad . \tag{4.8}$$

The proportionality factor K_m is given by

$$K_m = \frac{\gamma K \sigma_o \tau}{ncV_s(K\sigma_o + G + Y)(1 + j\omega_m\tau)} \left[\frac{d\sigma(T_e)}{dT_e} \right] , \tag{4.9}$$

where

$$\tau = \left[\frac{1}{\tau_e} - \frac{\gamma K(G + Y)P_i}{ncV_s(K\sigma_o + G + Y)^2} \frac{d\sigma(T_e)}{dT_e} \right]^{-1} ,$$

τ_e = the energy relaxation time,

c = the electron specific heat,

γ = the conversion efficiency of the incident millimeter-wave signal,

T_e = the electron temperature

and the remainder of the terms were defined earlier.

The parameters τ_e, c and $d\sigma(T_e)/dT_e$ can be obtained by studying the temperature dependence of the material conductivity and the detector response time as a function of the temperature at approximately liquid helium temperature. However for the purpose of studying the detection scheme it is adequate to determine experimentally the dependence of the conductivity on the millimeter-wave signal in the presence of the microwave saturation bias signal (the microwave signal power which results in the highest sensitivity for the detector). The millimeter-wave signal level is very small compared to the microwave bias signal and can be considered as a small perturbation. Thus the conductivity can be written as

$$\sigma(P_x + P_{im}) = \sigma(P_x) + K'_m P_{im} , \qquad (4.10)$$

where $\sigma(P_x + P_{im})$ and $\sigma(P_x)$ are the material conductivity in the presence and absence of the millimeter-wave signal, respectively. P_{im} = the millimeter-wave power absorbed by the sample and K'_m is given by

$$K'_m = \left.\frac{d\sigma}{dP}\right|_{P = P_x} . \tag{4.11}$$

In the absence of any mismatch or attenuation loss at the millimeter-wave port $P_i = P_{im}$. Neglecting any mismatch loss the value of x can be obtained from Eq. 4.10, and when substituted into Eq. 4.3 gives the following expression for the change in the detected power as a result of applying the millimeter-wave signal

$$\Delta P_D = \frac{4\alpha K'_m F}{\sigma_o}\left[\frac{\beta_o(1-\beta_o)}{(1+\beta_o)^3}\right] P_{ox} P_{im} . \tag{4.12}$$

Substituting the value of F as given by Eq. 3.67, Eq. 4.12 can be written as

$$\Delta P_D = \frac{4\alpha K K'_m}{(K\sigma_o + G_o)}\left[\frac{\beta_o(1-\beta_o)}{(1+\beta_o)^3}\right] P_{ox} P_{im} , \tag{4.13}$$

where all the terms have been defined earlier.

Equation 4.13 contains the basic information concerning the conversion loss. A thorough investigation of this equation is necessary for optimizing the detector performance. The optimization can be achieved through a proper choice of the bulk material and the circuit both at the microwave and the millimeter-wave frequencies.

4.2.3 External Circuit Effects. The conversion loss as a result of the downconversion process follows directly from Eq. 4.13 and is given by

$$L_D = \frac{4\alpha K K'_m}{(K\sigma_o + G_o)} \left[\frac{\beta_o(1 - \beta_o)}{(1 + \beta_o)^3} \right] P_{ox} \quad , \tag{4.14}$$

where L_D = the conversion loss resulting from the downconversion process.

It is clear from Eq. 4.14 that the coupling factor in the absence of the signal to be detected plays an important role toward minimizing the conversion loss. Figure 4.2 shows the dependence of the conversion loss on the X-band coupling factor β_o in the absence of the millimeter-wave signal. The curve exhibits two peaks at $\beta_o = (2 - \sqrt{3})$ and $(2 + \sqrt{3})$ and shows minima at $\beta_o = 0$, 1 and ∞. Since the signal to be detected causes an increase in the material conductivity, according to the discussion presented earlier in Chapter III the cavity should be under-coupled and $(2 - \sqrt{3})$ will be the optimum coupling factor.

In addition to optimizing the coupling factor at the bias frequency the insertion and coupling losses at the input and output terminals should be kept at a minimum. The effect of these losses is to add extra contributions to the conversion loss.

The contribution to the conversion loss at the input terminal results from the fact that not all the incident power is being absorbed by the bulk material. The power absorbed by the material at the millimeter-wave frequency can be expressed as

$$P_{im} = \alpha_m \left(\frac{a_m}{1 + a_m} \right) (1 - \Gamma_i^2) P_i \quad ,$$

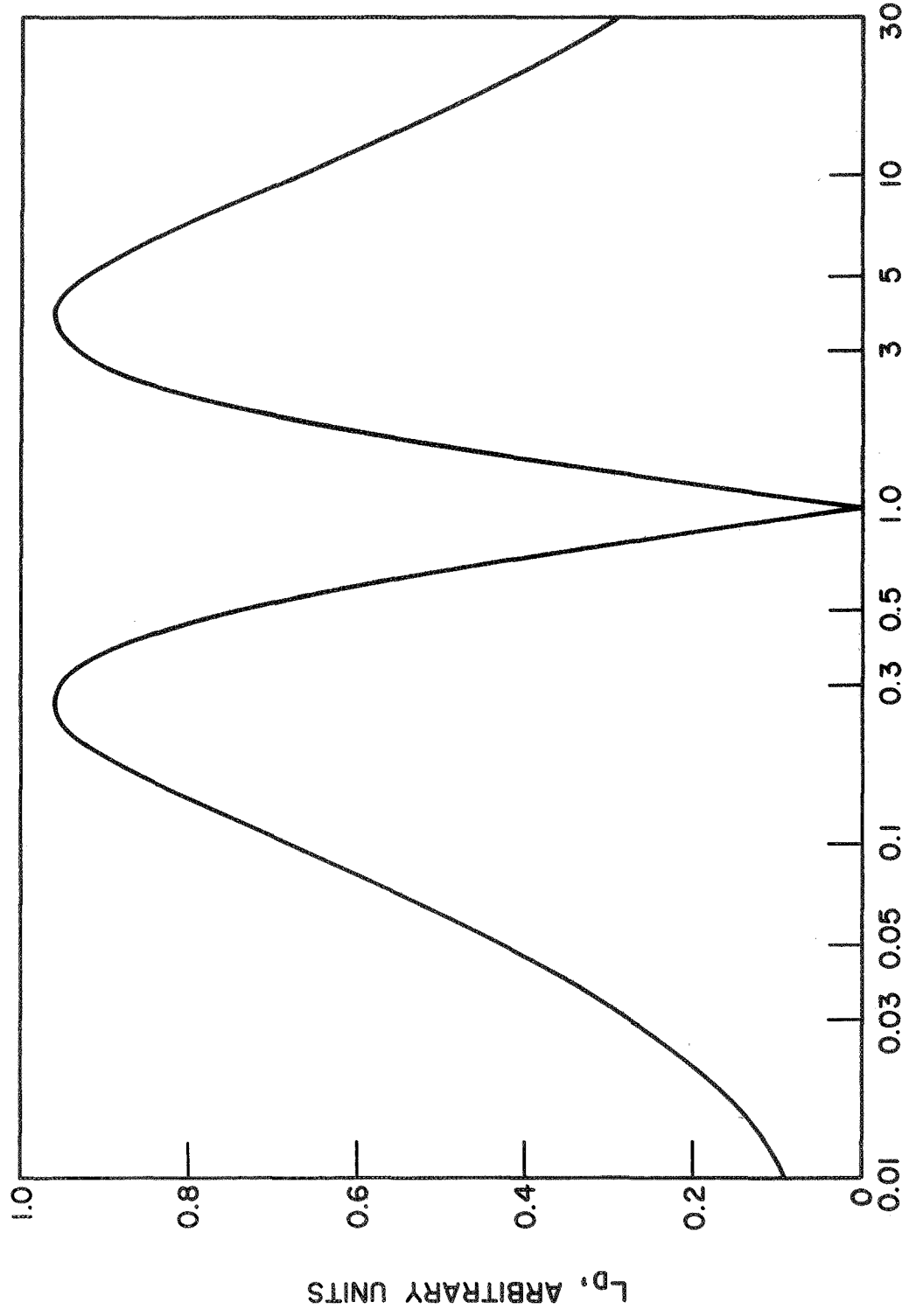

FIG. 4.2 DEPENDENCE OF THE CONVERSION LOSS ON THE X-BAND COUPLING FACTOR β_o.

where α_m = the line attenuation at the millimeter-wave frequency,

Γ_i = the reflection coefficient at the input terminal,

a_m = $K\sigma/G$ where G is the cavity conductance at the millimeter-wave frequency and

P_i = the incident signal level to be detected.

The conversion loss L_i due to mismatch and insertion loss at the input terminal is therefore given by

$$L_i = \frac{P_{im}}{P_i} = \alpha_m \left(\frac{a_m}{1 + a_m} \right) (1 - \Gamma_i^2) \quad . \tag{4.15}$$

In order to optimize L_i, α_m should equal one and Γ_i should be as small as possible, which means that the reflected power and the line loss should be kept as low as possible. On the other hand a_m should be as large as possible, which means that the signal power dissipated by the cavity walls should be very small compared to the power absorbed by the sample. A plot of L_i as a function of Γ_i for different values of a_m is shown in Fig. 4.3 assuming $\alpha_m = 1$ (lossless line).

Before concluding this section the effect of output mismatch and insertion loss on the conversion efficiency should be considered. The contribution is due to mismatch loss at the circulator input and output ports and insertion loss between the circulator ports. The output mismatch loss can be expressed as

$$L_{ox} = \frac{P_{ox}}{P_{ix}} \cdot \frac{P_D}{P_{rx}} \quad , \tag{4.16}$$

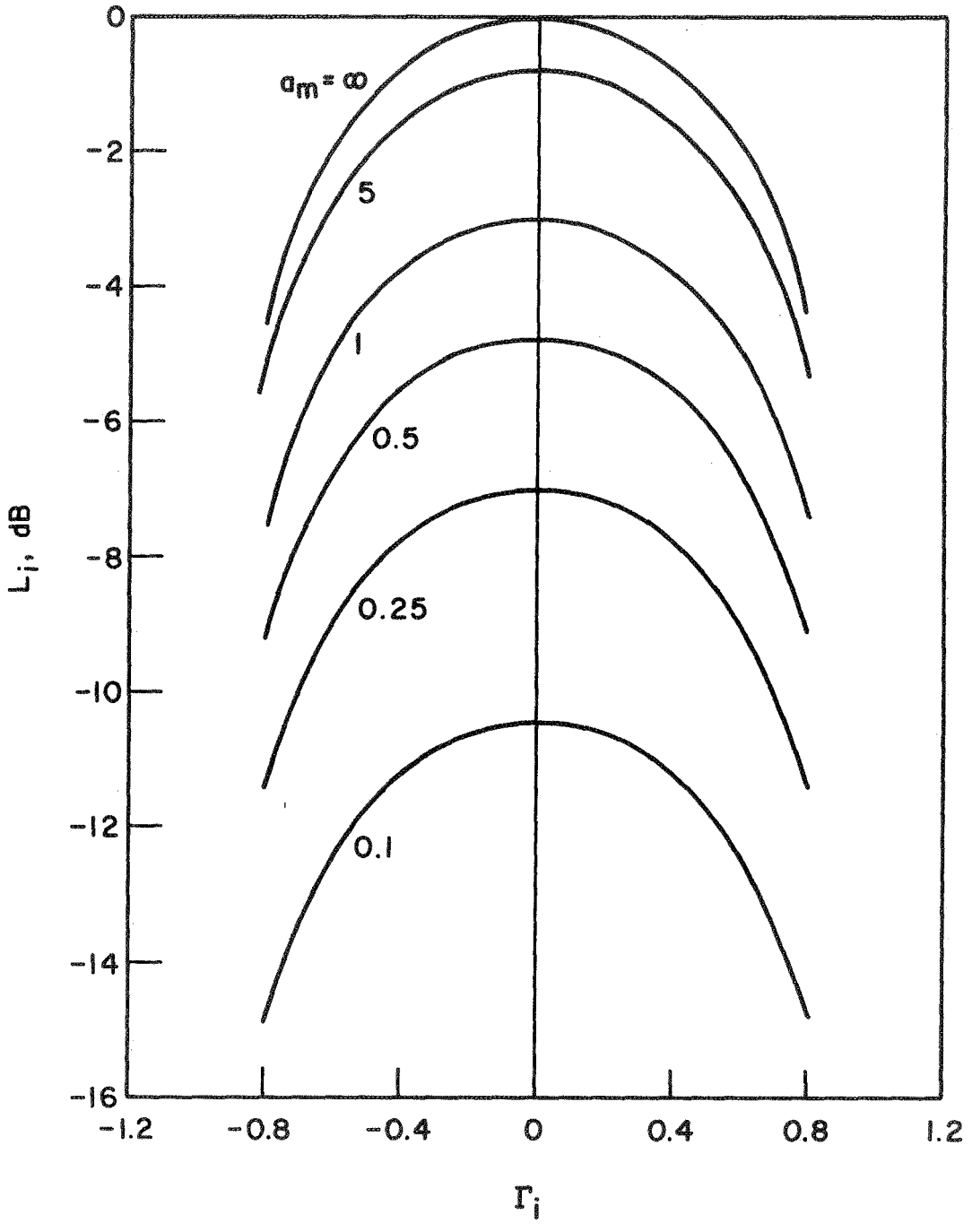

FIG. 4.3 DEPENDENCE OF L_i ON THE VOLTAGE REFLECTION COEFFICIENT Γ_i FOR SEVERAL VALUES OF a_m.

where P_{ox} = the available power at circulator port No. 2,

P_{ix} = the local oscillator power at the microwave frequency,

P_{rx} = the reflected power from the cavity and

P_D = the detected power at the microwave frequency.

Referring to Fig. 3.1 (P_{ox}/P_{ix}) and (P_D/P_{rx}) can be written as

$$\frac{P_{ox}}{P_{ix}} = \alpha(1 - \Gamma_{ix}^2)\alpha_{12} \tag{4.17}$$

and

$$\frac{P_D}{P_{rx}} = (1 - \Gamma_{ox}^2)\ \alpha_{23}\ , \tag{4.18}$$

where Γ_{ix} and Γ_{ox} are the voltage reflection coefficients at circulator port Nos. 1 and 3, respectively, and α_{ij} = the circulator insertion loss between ports i and j. Substituting Eqs. 4.17 and 4.18 into Eq. 4.16 the output mismatch loss L_{ox} can be expressed as

$$L_{ox} = \alpha\alpha_{12}\alpha_{23}(1 - \Gamma_{ix}^2)(1 - \Gamma_{ox}^2)\ . \tag{4.19}$$

It is clear from Eq. 4.19 that in order to minimize this conversion loss the circulator should be perfectly matched to both the local oscillator source and the microwave detector. In addition, the insertion loss due to the circulator and the transmission line connecting the cavity to the circulator should be kept at their lowest possible values.

4.2.4 Saturation Effects. Equation 4.13 shows that the change in the detected power is proportional to the microwave bias signal level; this relation will hold if the material conductivity is proportional to the microwave bias. However it has been shown in Chapter II that this holds only for small signal levels and as the bias power is increased the material conductivity changes at a lower rate and finally becomes independent of the bias level as shown in Fig. 2.28. In order to account for this effect, a term L_s representing the saturation loss at the microwave frequency should be added to the expression for the change in the detected power. The experimental results for the dependence of the insertion loss on the microwave bias level are shown in Fig. 4.4. The experimental results were found to fit the following equation

$$L_s = \frac{P_{ix}/P_s}{1 + P_{ix}/P_s} , \qquad (4.20)$$

where P_s is the power level at which the conversion loss drops by 3 dB. The function $(P_{ix}/P_s)/(1 + P_{ix}/P_s)$ is plotted in Fig. 4.4 for comparison. Equation 4.20 shows that for optimum detector performance $P_{ix} \gg P_s$.

The concept of electron temperature can be utilized to explain the saturation phenomena at the microwave frequency. Since at 4.2°K the scattering mechanism is dominated by ionized impurity scattering, the electron temperature will increase above that of the lattice if $\tau_e \gg \tau_{ee}$, where τ_e is energy relaxation time and τ_{ee} is the effective time of electron-electron collision redistributing the energy among the system of electrons. The increase in the carrier temperature results in a corresponding increase in their mobility. Studies made on the dependence of τ_e on

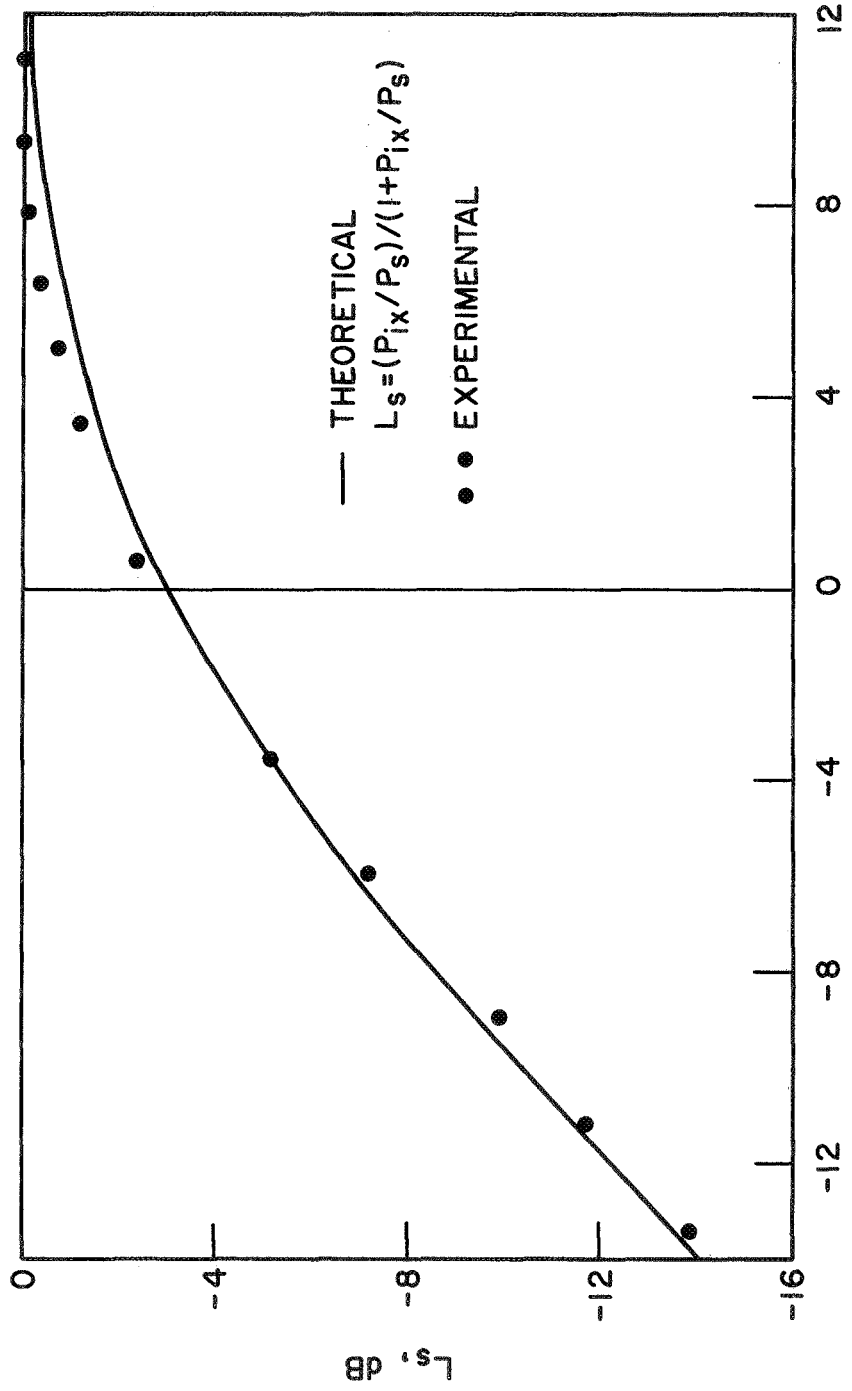

FIG. 4.4 L_s AS A FUNCTION OF P_{ix}/P_s.

temperature by Whalen and Westgate[65] show that τ_e is essentially independent of temperature up to about 14°K, and above that temperature τ_e decreases considerably with increasing temperature. Therefore as the incident microwave signal level increases the electron temperature will increase above 4.2°K until it reaches a value of about 14°K where the optical phonon scattering becomes appreciable. As a result τ_e starts to decrease causing the carrier temperature to increase at a lower rate; finally, as the inequality $\tau_e \gg \tau_{ee}$ becomes invalid the carrier temperature saturates and the material conductivity becomes independent of the microwave power level.

4.2.5 The Terminal-to-Terminal Conversion Loss. The contribution of the external circuit can be combined with the downconversion and saturation loss to give the terminal-to-terminal conversion loss L_T which can be expressed as

$$L_T = L_D L_i L_{ox} L_s \quad . \tag{4.21}$$

Substituting from Eqs. 4.14, 4.15, 4.19 and 4.20 into Eq. 4.21 the terminal-to-terminal conversion loss becomes

$$L_T = \frac{4\alpha^2 \alpha_m \alpha_{12} \alpha_{23} KK'_m}{K\sigma_o \left(1 + \frac{G_o}{K\sigma_o}\right)} \left(\frac{a_m}{1 + a_m}\right)\left(\frac{\beta_o(1 - \beta_o)}{(1 + \beta_o)^3}\right)$$

$$\cdot (1 - \Gamma_{ix}^2)(1 - \Gamma_i^2)(1 - \Gamma_{ox}^2)\left(\frac{P_{ix}/P_s}{1 + P_{ix}/P_s}\right) P_s \quad . \tag{4.22}$$

This is the basic equation describing the detector performance, it includes all the external circuit effects and the material parameters. The external circuit effects have been discussed earlier and can be improved. However the material parameters have the most important effect; they will set the limits regarding the detector performance.

The most important material parameters affecting the detector performance are σ_o, τ_e, K and K'_m. The effect of τ_e will be discussed later when the response time of the detector is considered. The dependence of L_T on σ_o and K'_m can be seen from Eq. 4.22. A low value of σ_o and high values of K'_m and K are required for improved detector performance. This means that very high purity compensated samples with a large value of $(d\sigma_o/dP_{ix})$ are required for application in this scheme. In addition the cavity losses should be kept as low as possible such that $(G_o/K\sigma_o) \ll 1$. This can be achieved by highly polishing and electroplating the interior cavity walls and choosing K as high as possible.

In order to investigate the theoretical limit on the conversion loss the ideal case of no mismatch or insertion loss at the input or output terminal is considered. It is also assumed that the optimum coupling factor β_o is used and the microwave bias signal is much greater than the saturation signal level. With these assumptions, Eq. 4.22 reduces to

$$(L_T)_{matched} = \frac{0.384KK'_m}{K\sigma_o\left(1 + \frac{G_o}{K\sigma_o}\right)} \left(\frac{K\sigma/G}{\frac{K\sigma}{G} + 1}\right) P_s \quad , \tag{4.23}$$

where $(L_T)_{matched}$ = the insertion loss with a matched and lossless circuit.

It is seen from Eq. 4.23 that the saturation microwave signal level and the sample dimensions are important factors in determining the theoretical limit on the detection scheme. Since the saturation signal level is proportional to the volume of the material, Eq. 4.23 can be written in the following form:

$$(L_T)_{matched} = R \frac{K(K\sigma)V_s}{(G_o + K\sigma_o)(G + K\sigma)} , \tag{4.24}$$

where R is a proportionality factor and V_s is the material volume. Assuming the area of the sample to be limited by the area under the central post of the cavity and its thickness to be t, Eq. 4.24 can be written as

$$(L_T)_{matched} = R \frac{A^3 t}{(tG_o + A\sigma_o)(tG + A\sigma)} . \tag{4.25}$$

The optimum thickness can be found by differentiating the right-hand side of Eq. 4.25 with respect to t and equating the result to zero which yields

$$t_{op} = A \sqrt{\frac{\sigma\sigma_o}{GG_o}} , \tag{4.26}$$

where t_{op} is the optimum thickness and the remaining quantities have been defined earlier. Equation 4.26 is valid provided $t_{op} \leq \ell$, where ℓ is the spacing between the central post and the bottom of the cavity as shown in Fig. 3.12. Figure 4.5 shows the dependence of $(L_T)_{matched}$ on A/t for different values of σ/G. The value of σ/G for these plots

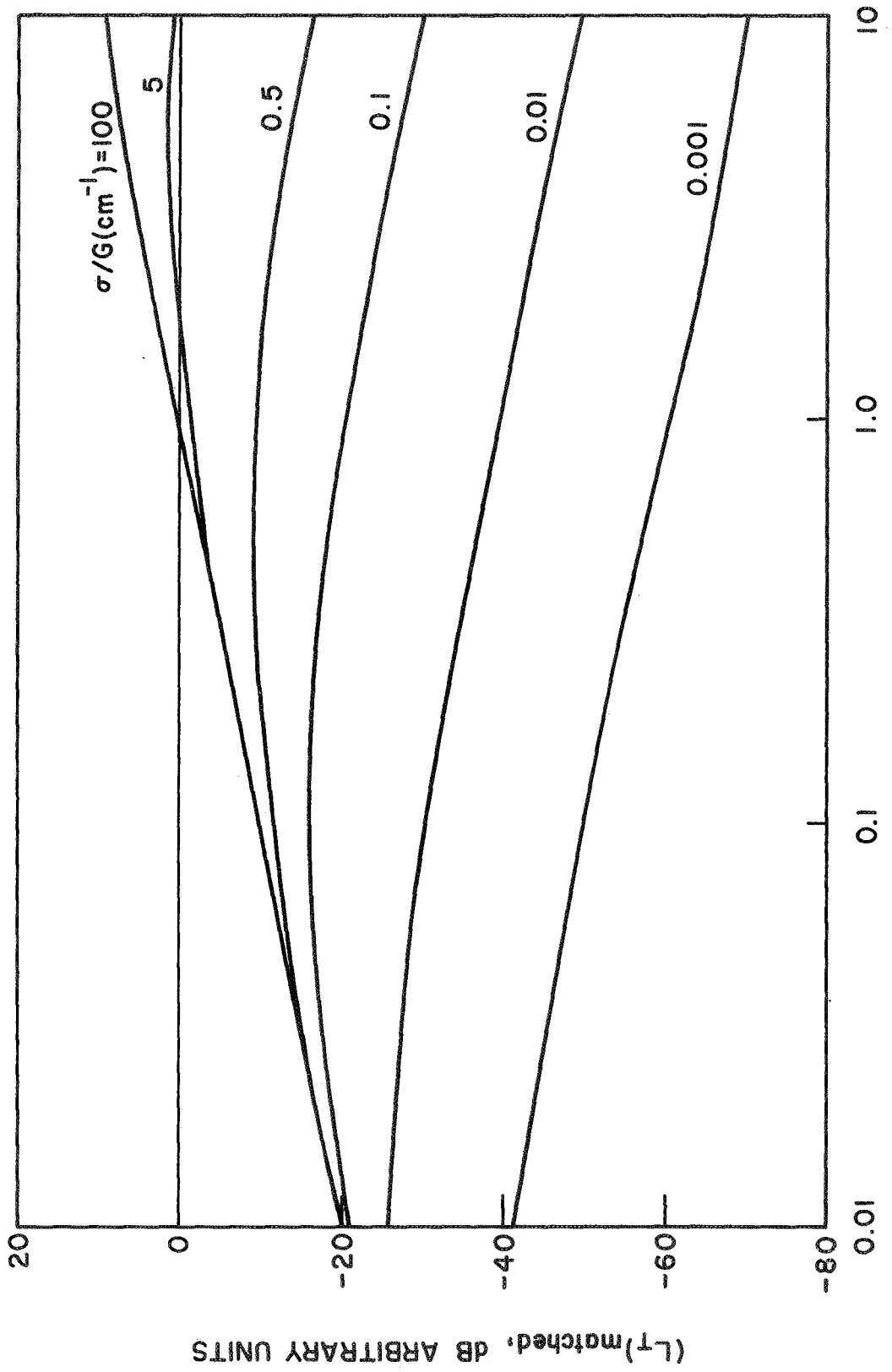

FIG. 4.5 $(L_T)_{MATCHED}$ VS. A/t FOR SEVERAL VALUES OF σ/G.

was assumed independent of the frequency ($\sigma_o/G_o = \sigma/G$) and the scale for $(L_s)_{matched}$ is arbitrary.

4.3 Estimation of the Response Time

The detector response time is a measure of its ability to respond to modulated signals at sufficiently rapid rates. The maximum modulation bandwidth is the factor that sets the limit on the response time of the detector. The modulation bandwidth should not be confused with the useful bandwidth which is the frequency range over which the input signal can be tuned without appreciable deterioration in the output.

The speed of response of dc-biased and heterodyne detectors using bulk InSb is limited by the external circuit parameters. In the case of dc-biased bulk semiconductor detectors the response time is limited by the RC time constant of the circuit, most of which is due to the input capacitance of the following amplifier together with the stray and lead capacitances. On the other hand, the response time of bulk mixers is limited by the mixer circuit and the IF of the system. In the case of microwave-biased detectors the time constant is limited by the carrier energy relaxation time τ_e provided the bandwidth of the input millimeter-wave cavity does not degrade this time constant. This requirement is satisfied if $B_m > f_m$, where B_m is the input millimeter-wave cavity bandwidth and f_m is the maximum modulation bandwidth, which is readily realizable at values of $B_m \geq 20$ MHz. It is seen from the previous discussion that with microwave-biased detectors, the full potential of the bulk material can be utilized for achieving a high speed of response.

The response time of the detector is derived in Appendix A and is given by

$$\tau = \left[\frac{1}{\tau_e} - \frac{\gamma K(G + Y)P_i}{ncV_s(K\sigma_o + G + Y)^2} \frac{d\sigma(T_e)}{dT_e} \right]^{-1} , \tag{4.27}$$

where all the parameters have been defined earlier. Assuming the system of conduction electrons to have a degenerate Fermi-Dirac distribution, the electron specific heat c can be calculated[66,67] and when substituted into Eq. 4.27 yields

$$\tau = \left[\frac{1}{\tau_e} - \frac{0.68\gamma K(G + Y)P_i}{V_s(K\sigma_o + G + Y)^2} \frac{d\sigma(T_e)}{dT_e} \right]^{-1} , \tag{4.28}$$

where P_i is the incident millimeter-wave power in mW. In order to examine the effect of the material parameters on τ, Eq. 4.28 is written in the following form:

$$\tau = \tau_e \left[1 - \frac{\tau_e}{\tau_1} \right]^{-1} , \tag{4.29}$$

where

$$\frac{\tau_1}{\tau_e} = \frac{V_s(K\sigma_o + G + Y)^2}{0.68\gamma K(G + Y)} \frac{1}{\left(\frac{d\sigma}{dT} \right) P_i \tau_e} . \tag{4.30}$$

It is seen from Eq. 4.29 that the detector response time τ approaches τ_e if $\tau_1/\tau_e \gg 1$. Assuming $\gamma = 1$, Eq. 4.30 can be expressed, in terms of the measurable quantities, as follows:

$$\frac{\tau_1}{\tau_e} = \frac{V_s}{0.68\gamma K} \frac{K\sigma_o(1+\beta_o)\beta_{oo}\left(1+\frac{G+Y}{K\sigma_o}\right)}{\beta_o(1+\beta_{oo})\left(\frac{d\sigma}{dT}\right)P_i} \frac{1}{\tau_e} \quad . \tag{4.31}$$

Values of $1/\tau_e$ and $d\sigma/dT$ for InSb samples of interest were found to be of the order of 5×10^6 s^{-1} and 3 mho $m^{-1}{}^{\circ}K^{-1}$ respectively at liquid helium temperature. Substituting these values in Eq. 4.31 yields a value of τ_1/τ_e which is greater than 3 for input signals less than 1 mW with typical samples and assuming optimum coupling. It is seen from Fig. 4.6 that for such values of τ_1/τ_e the response time is essentially equal to τ_e.

4.3.1 Trade Offs Between Conversion Loss and Response Time. This section discusses qualitatively the nature of the trade offs between the response time and the conversion loss of the detector. At a fixed temperature τ_e is constant and sets the limit on the response time. It has been shown that this limit can be achieved at any signal level below 1 mW. However as the signal level increases, it is seen from Eq. 4.30 that the value of τ_1/τ_e will decrease causing the response time to increase. It is seen from Eq. 4.31 that in order to achieve a high speed of response with large signals either σ_o should be increased or $d\sigma/dT$ should be decreased. Both effects will degrade the conversion loss as discussed earlier. This kind of trade off does not degrade the quality of the detector performance since in all practical applications the signal to be detected is very small.

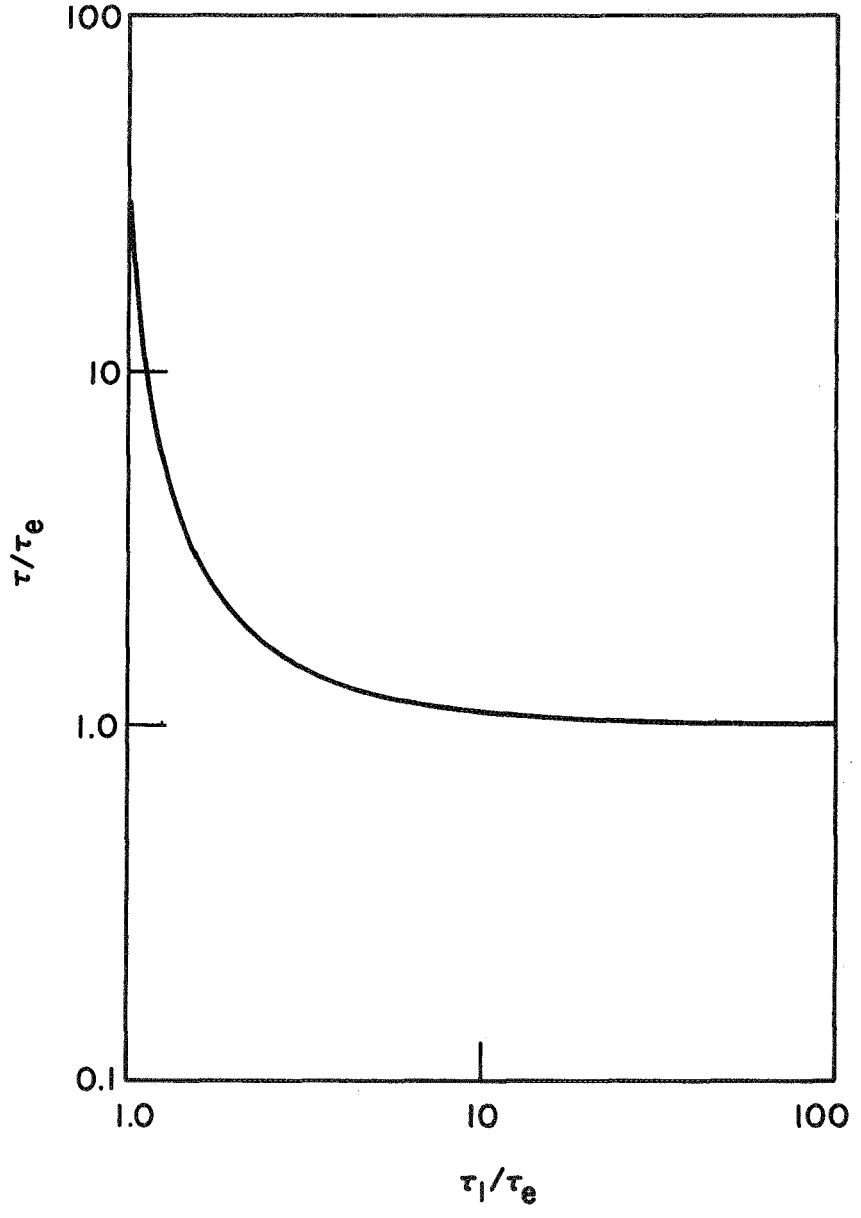

FIG. 4.6 RESPONSE TIME VS. τ_1/τ_e.

Another trade off deals with the detector performance as a function of the temperature. The carrier relaxation time τ_e decreases considerably as the temperature is increased beyond 14°K[65] which results in a faster speed of response. However as the carrier effective temperature is increased K_m and K_m' decrease considerably resulting in a degradation of the conversion loss. It should be kept in mind that despite the trade offs it is the carrier relaxation time that sets the limit to the speed of response.

4.4 The Noise Equivalent Power (NEP)

4.4.1 Introduction. The NEP is the measure of the detection capability of the detector. In order to develop an expression for the NEP an investigation of the minimum detectable power and the origin of noise within the detection scheme is necessary. Four sources of noise are present in the detection system; namely, fluctuation in the background radiation, fluctuation in the incident signal, noise as a result of the downconversion process and the noise contribution from the postdetection system.

In this section expressions for the minimum detectable power are derived. These expressions together with the noise sources can be utilized to determine the NEP. The results will be compared to the ideal case where the only noise source is the background radiation fluctuation.

4.4.2 Minimum Detectable Power $(MDP)_{mm}$. The criterion for determining the smallest observable signal can be understood by examining the basic mechanism of operation of the detection system. The reflected microwave power from the cavity is separated from the incident one in the circulator and applied to the crystal detector. The modulation on

the millimeter-wave signal appears as modulation on the reflected microwave signal and the problem essentially becomes that of detecting a small change on top of a large-signal level. It has been shown that[8,68] in order to keep the signal larger than the noise the following inequality must be satisfied

$$\Delta P_r \geq 2\sqrt{P_n P_r} \quad , \tag{4.32}$$

where ΔP_r = the change in the reflected microwave power,

P_r = the reflected microwave power and

P_n = the noise power in the output line.

It should be noted that Eq. 4.32 is based on the assumption that $P_r \gg P_n$ and that the equality sign sets the threshold for detection, i.e.,

$$(\Delta P_r)_{min} = 2\sqrt{P_n P_r} \quad , \tag{4.33}$$

where $(\Delta P_r)_{min}$ = the minimum detectable change in the reflected power.

The change in the reflected power reaching the conventional detector was shown to be

$$\delta P_r = \frac{4\alpha K K'_m}{(K\sigma_o + G_o)} \left(\frac{\beta_o(1 - \beta_o)}{(1 + \beta_o)^3} \right) \frac{P_{ix}/P_s}{(1 + P_{ix}/P_s)} L_i L_{ox} P_s P_i \quad , \tag{4.34}$$

while the reflected microwave power can be written as

$$P_r = \frac{4\alpha \beta_o^2}{(1 + \beta_o)^2} L_{ox} P_{ix} \quad . \tag{4.35}$$

The minimum detectable power can be obtained by substituting Eqs. 4.34 and 4.35 into Eq. 4.33 and arranging terms and is given by

$$(MDP)_{mm} = \frac{\sigma_o(1 + G_o/K\sigma_o)}{\sqrt{\alpha}\, K'_m L_i \sqrt{L_{ox}}} \left(\frac{(1 + \beta_o)^2}{1 - \beta_o} \right) \left(\frac{1 + P_{ix}/P_s}{(P_{ix}/P_s)P_s} \right) \sqrt{P_n P_{ix}} \quad . \tag{4.36}$$

It is clear that the $(MDP)_{mm}$ can be minimized for $P_{ix} = P_s$. On the other hand its dependence on β_o is shown in Fig. 4.7. It is seen from this figure that the best results are achieved with undercoupled cavities whose coupling factor β_o is less than 0.6. Therefore a coupling factor of $(2 - \sqrt{3})$ is well recommended.

For perfectly matched and lossless input and output circuits, Eq. 3.36 reduces to the following form

$$(MDP_M)_{mm} = \frac{\sigma_o(1 + G_o/K\sigma_o)}{K'_m} \left(\frac{(1 + \beta_o)^2}{1 - \beta_o} \right) \left(\frac{1 + P_{ix}/P_s}{(P_{ix}/P_s)P_s} \right) \sqrt{P_n P_{ix}} \quad . \tag{4.37}$$

This equation will be used to check the theoretical limits on the NEP of the detection system.

4.4.3 The Downconverter Noise Contribution (P_{nD}). This is the inherent noise in the detection system and is independent of the external circuit effects. Noise sources of this nature include the noise generated in the bulk material, background radiation fluctuation and the local oscillator noise.

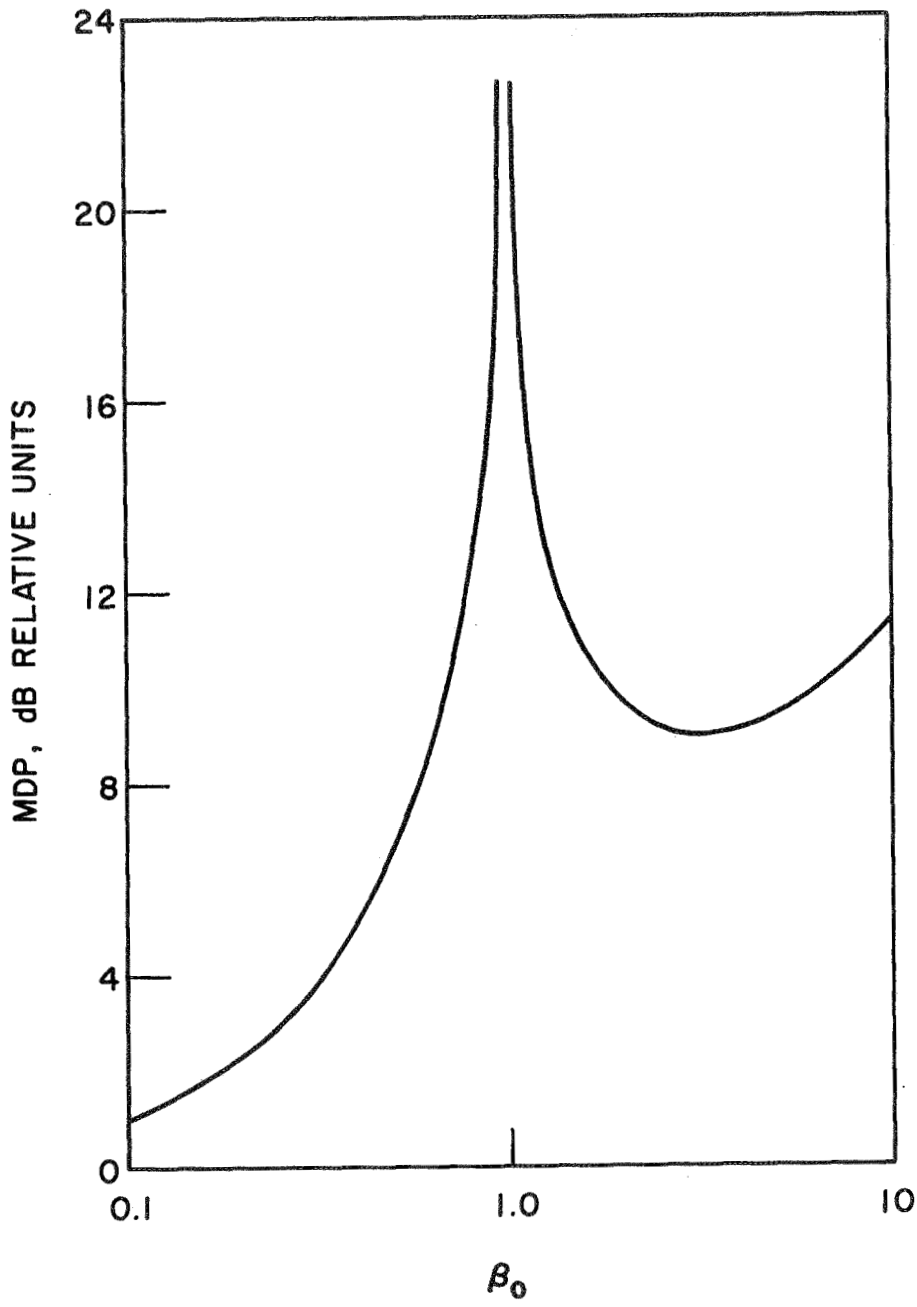

FIG. 4.7 DEPENDENCE OF THE MDP ON β_o.

The principal noise sources in a semiconductor material are current noise, generation-recombination noise and thermal noise. Current noise has been associated with the nonohmic contacts and surface conditions of the material. It will exist only in the presence of dc current through the material. Therefore the current noise in a contactless microwave-biased sample is zero.

Generation-recombination noise is due to modulation of the material conductivity as a result of the instantaneous random fluctuation of the free-carrier density. The performance of most photoconductive detectors is essentially generation-recombination noise limited. However, this is not the case for microwave-biased InSb detectors for the following reasons. First, the mechanism of generation-recombination noise depends on the presence of carriers bound to the impurity band (or valence band) which are being excited to the conduction band. The absence of any ionization energy for InSb indicates that all the carriers are in the conduction band. Therefore carrier density fluctuation is negligible. Second, the noise power is proportional to the average current in the sample. Third, the microwave bias effectively increases the photoconductive lifetime of the carriers which reduces the contribution of the generation-recombination noise.

The previous discussion shows that the only noise source in InSb microwave-biased samples is the thermal noise. To find the output noise power of the downconverter two noise sources will be added to the equivalent circuit of Fig. 3.2. The resulting circuit is shown in Fig. 4.8. The noise currents generated by the cavity and the material are given by

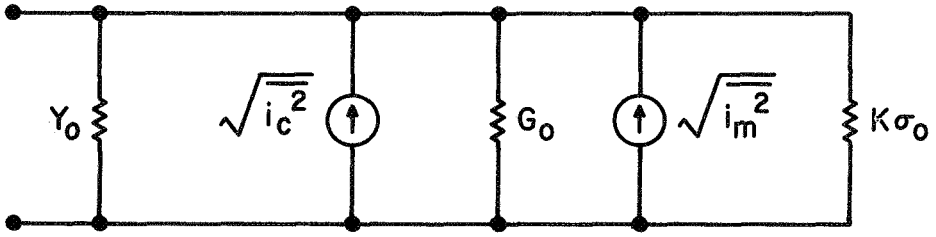

FIG. 4.8 MODIFIED CAVITY EQUIVALENT CIRCUIT INCLUDING THERMAL NOISE.

$$\sqrt{\overline{i_c^2}} = \sqrt{4kT_o G_o B_x} \tag{4.38}$$

and

$$\sqrt{\overline{i_m^2}} = \sqrt{4kT_e K\sigma_o B_x} \quad , \tag{4.39}$$

where $\sqrt{\overline{i_c^2}}$ and $\sqrt{\overline{i_m^2}}$ = the rms of the noise current of the cavity and the material, respectively, and

B_x = the bandwidth of the output circuit.

The noise power delivered to the output will be given by

$$P_{nT} = \frac{4kB_x(G_o T_o + K\sigma_o T_e)Y_o}{(Y_o + G_o + K\sigma_o)^2} \quad . \tag{4.40}$$

The equivalent noise temperature of the cavity and the bulk material T_D follows directly from Eq. 4.40 and is given by

$$T_D = \frac{4Y_o(G_o T_o + K\sigma_o T_e)}{(Y_o + G_o + K\sigma_o)^2} \quad . \tag{4.41}$$

The second noise source in the downconversion process is due to the background radiation fluctuation. It was shown that the noise power due to the background radiation fluctuation is an incoherent energy detector with no long-wave cutoff is given by[8]

$$P_{nb} = \pi \sqrt{\frac{B_x}{3h}} (kT)^{3/2} \quad , \tag{4.42}$$

where P_{nb} is the noise power due to the background radiation fluctuation and T is the background temperature which is assumed to be much higher than the detector temperature. The ratio of the thermal to the background radiation fluctuation noise is

$$\frac{P_{nT}}{P_{nb}} = \sqrt{\frac{3hB_x}{\pi^2 k}} \frac{T_D}{(T)^{3/2}} \quad . \tag{4.43}$$

To check whether the thermal noise or the background radiation fluctuation dominates, it is assumed that $T_D = T_e$ which simplifies Eq. 4.43 to the following form:

$$\frac{P_{nT}}{P_{nb}} = \sqrt{\frac{3hB_x}{\pi^2 k}} \frac{4\beta_o}{(1+\beta_o)^2} \frac{T_e}{(T)^{3/2}} \quad . \tag{4.44}$$

Figure 4.9 is a plot of P_{nT}/P_{nb} vs. T for $T_e = 10°K$. It is clear from this figure that $P_{nb} \gg P_{nT}$ for all practical cases.

The third noise source in the downconverter is due to the local oscillator. Noise in the local oscillator is a result of the random fluctuation of the amplitude and frequency of its output signal. The noise power reaching the postdetection system due to random amplitude fluctuations can be obtained using Eq. 4.35 and is given by

$$P_{nam} = \frac{4\alpha \beta_o^2 L_{ox}}{(1+\beta_o)^2} n_{am} P_{ix} \quad , \tag{4.45}$$

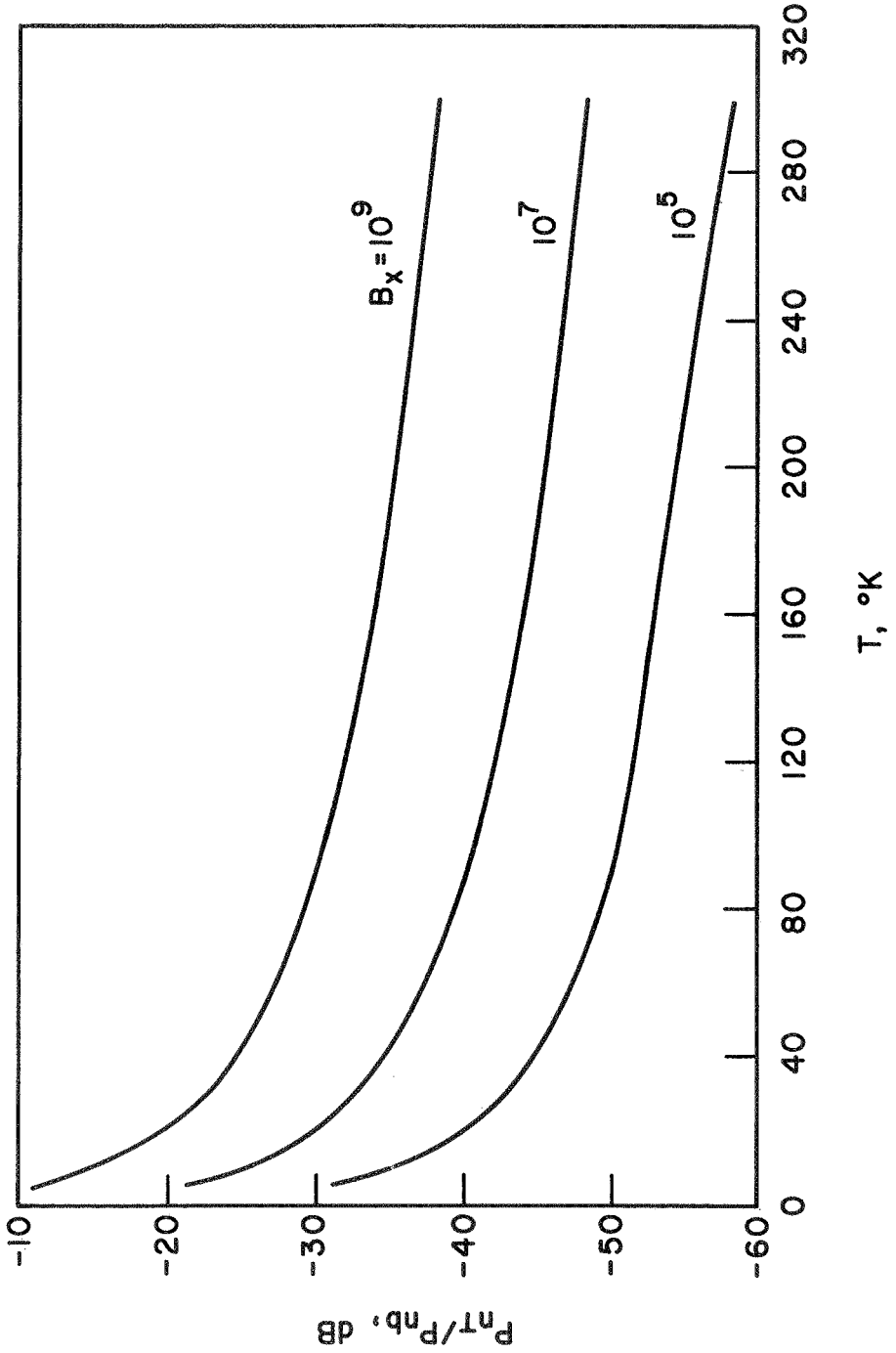

FIG. 4.9 P_{nt}/P_{nb} VS. BACKGROUND RADIATION TEMPERATURE FOR DIFFERENT OUTPUT CIRCUIT BANDWIDTHS. (T_e = 10°K)

where n_{am} is the noise-to-signal power ratio at the output of the local oscillator. Similarly the random deviation in the input frequency will contribute to the noise power reaching the postdetection system. This is a direct result of the FM to AM conversion of the cavity frequency response. The output power due to the local oscillator frequency random fluctuation is

$$P_{nfm} = \frac{4\alpha Q_{ox}^2 \Gamma_{ox}}{(1+\beta_o)^2} \overline{\Delta f_{rms}^2} P_{ix} \quad , \tag{4.46}$$

where Q_{ox} = the unloaded Q of the cavity at the local oscillator frequency and

Δf_{rms} = the rms frequency deviation and is given by[69]

$$\Delta f_{rms} = f_n \sqrt{\frac{P_{sB}}{P_{ix}}} \quad , \tag{4.47}$$

where P_{sB} = the double sideband FM power and

f_n = the frequency deviation from the cavity resonance frequency.

Equations 4.45 and 4.46 can therefore be combined to give the local oscillator noise contribution as

$$P_{n\ell o} = \frac{4\alpha\Gamma_{ox}}{(1+\beta_o)^2} \left[\beta_o^2 n_{am} + Q_{ox}^2 \overline{\Delta f_{rms}^2}\right] P_{ix} \quad , \tag{4.48}$$

where $P_{n\ell o}$ = the local oscillator noise power at the output terminal.

It is seen from Eq. 4.46 that the FM noise can be reduced by reducing the cavity Q.

4.4.4 Noise in the Postdetection System. In addition to the internal noise generated in the downconversion process there is the external noise generated in the postdetection system or the demodulator. The postdetection system used in conjunction with the detection scheme is shown in Fig. 4.10. Noise in the postdetection system is due to the crystal detector noise and the video amplifier noise. The noise power generated in a point contact diode is given by[70]

$$P_{nc} = kT \left(1 + \frac{K_d P_d^2}{f}\right) B_x \quad , \tag{4.49}$$

where K_d = a constant,

P_d = the power incident on the diode and

f = the video frequency.

On the other hand the noise power generated in the video amplifier is

$$P_{na} = kT_a B_x \quad , \tag{4.50}$$

where T_a = the effective amplifier noise temperature.

4.4.5 NEP and Signal-to-Noise Ratio of the Detection System. The results of the previous sections will now be utilized to determine the NEP and S/N ratio of the detection system. It is assumed that the crystal detector obeys a square law. The change in the detector output voltage due to a change δP_r in the reflected power is given by

$$\Delta V_o = g S_d \delta P_{rx} \quad , \tag{4.51}$$

FIG. 4.10 POSTDETECTION SYSTEM.

where g = the gain of the video amplifier and

S_d = the detector responsivity in V/W.

The detected signal as a result of the incident millimeter-wave power can be obtained by substituting Eq. 4.34 into Eq. 4.51 and is given by

$$V_s = \frac{4\alpha K K'_m}{(K\sigma_o + G_o)} gS_d \left(\frac{\beta_o(1 - \beta_o)}{(1 + \beta_o)^3} \right) \left(\frac{P_{ix}/P_s}{1 + P_{ix}/P_s} \right) P_s L_i L_{ox} P_i \quad . \quad (4.52)$$

The noise power at the input of the crystal detector can be obtained by combining Eqs. 4.40, 4.42 and 4.48 and is given by

$$P_{nD} = kT_D B_x + \pi \sqrt{\frac{B_x}{3h}} (kT)^{3/2} + \frac{4\alpha\Gamma_{ox}}{(1 + \beta_o)^2} \left(\beta_o^2 n_{am} + Q_{ox}^2 \overline{\Delta f_{rms}^2} \right) P_{ix} \quad , \quad (4.53)$$

where P_{nD} = the noise power at the input of the crystal detector. The noise voltage V_n at the output of the video amplifier can be expressed as

$$V_n = \left[\left(2gS_d \sqrt{P_{nD} P_r} \right)^2 + \overline{V_{nc}^2} + \overline{V_{na}^2} \right]^{1/2} \quad , \quad (4.54)$$

where $\overline{V_{nc}^2}$ and $\overline{V_{na}^2}$ are the mean square noise of the crystal detector and the amplifier, respectively, and are given by

$$\overline{V_{nc}^2} = 4g^2 kTR_v B_x \left(1 + \frac{K_d P_d^2}{f} \right) \quad (4.55)$$

and

$$\overline{V_{na}^2} = 4g^2 \, kTR_a B_x \quad , \tag{4.56}$$

where R_v = the video resistance of the diode and

R_a = the equivalent noise resistance of the video amplifier.

From Eqs. 4.53 through 4.56 the rms noise voltage in the output is

$$V_n = 2g \left\{ S_d^2 \frac{4\alpha\beta_o^2 \Gamma_{ox} P_{ix}}{(1+\beta_o)^2} \left[kT_D B_x + \pi \sqrt{\frac{B_x}{3h}} (kT)^{3/2} + \frac{4\alpha\Gamma_{ox}}{(1+\beta_o)^2} \right.\right.$$

$$\left. \cdot \left(\beta_o^2 n_{am} + Q_{ox}^2 \overline{\Delta f_{rms}^2} \right) P_{ix} \right] + kTR_a B_x + kTR_v B_x$$

$$\left. \cdot \left[1 + (K_d/f) \left(\frac{\alpha\Gamma_{ox}\beta_o^2}{(1+\beta_o)^2} P_{ix} \right)^2 \right] \right\}^{1/2} \quad . \tag{4.57}$$

The signal-to-noise ratio follows directly from Eqs. 4.57 and 4.52 and is given by

$$\frac{S}{N} = \frac{V_s}{V_n} \quad . \tag{4.58}$$

On the other hand the $(NEP)_{mm}$ can be obtained by equating V_n to V_s which yields

$$(NEP)_{mm} = \frac{\sigma_o \left(1 + \frac{G_o}{K\sigma_o} \right) (1+\beta_o)^3}{4\alpha K'_m g S_d \beta_o (1-\beta_o) L_i L_{ox}} \frac{(1 + P_{ix}/P_s)}{P_s (P_{ix}/P_s)} V_n \quad . \tag{4.59}$$

As indicated earlier, the $(NEP)_{mm}$ when normalized to 1 Hz bandwidth is a good measure of the detecting ability of the detection system. The normalized $(NEP_{NM})_{mm}$ with a perfectly matched circuit is given by

$$(NEP_{NM})_{mm} = \frac{\sigma_o(1 + G_o/K\sigma_o)(1 + \beta_o)^2(1 + P_{ix}/P_s)}{2K_m'(1 - \beta_o)} \left[\frac{kT_D + \pi\sqrt{k^3T^3/h}}{P_{ix}} + \frac{\beta_o^2 n_{am} + Q_{ox}^2 \overline{\Delta f_{rms}^2}}{(1 + \beta_o)^2} + \frac{kT\left\{R_a + R_v\left[1 + (K_d/f)^2\left(\frac{\beta_o}{1 + \beta_o}\right)^4 P_{ix}^2\right]\right\}}{[S_d P_{ix}\beta_o/(1 + \beta_o)]^2} \right]^{1/2} \tag{4.60}$$

It is worthwhile to investigate the dependence of the NEP on the microwave bias level and the background temperature. Equation 4.60 is plotted in Fig. 4.11 for different values of T using the parameter values listed in Table 4.1. It is seen from Fig. 4.11 that there exists an optimum bias level at which the $(NEP)_{mm}$ is minimum. A study of the contribution of the different noise sources at this bias level indicates that the background radiation fluctuation is the limiting factor concerning the detector performance. However, the background radiation fluctuation noise contribution can be cut down considerably by incorporating appropriate filters with the detection system. Figure 4.12 describes the detector $(NEP_M)_{mm}$ when the background radiation fluctuation noise contribution is neglected. In this case the crystal detector shot noise will set the limit on the detection system performance.

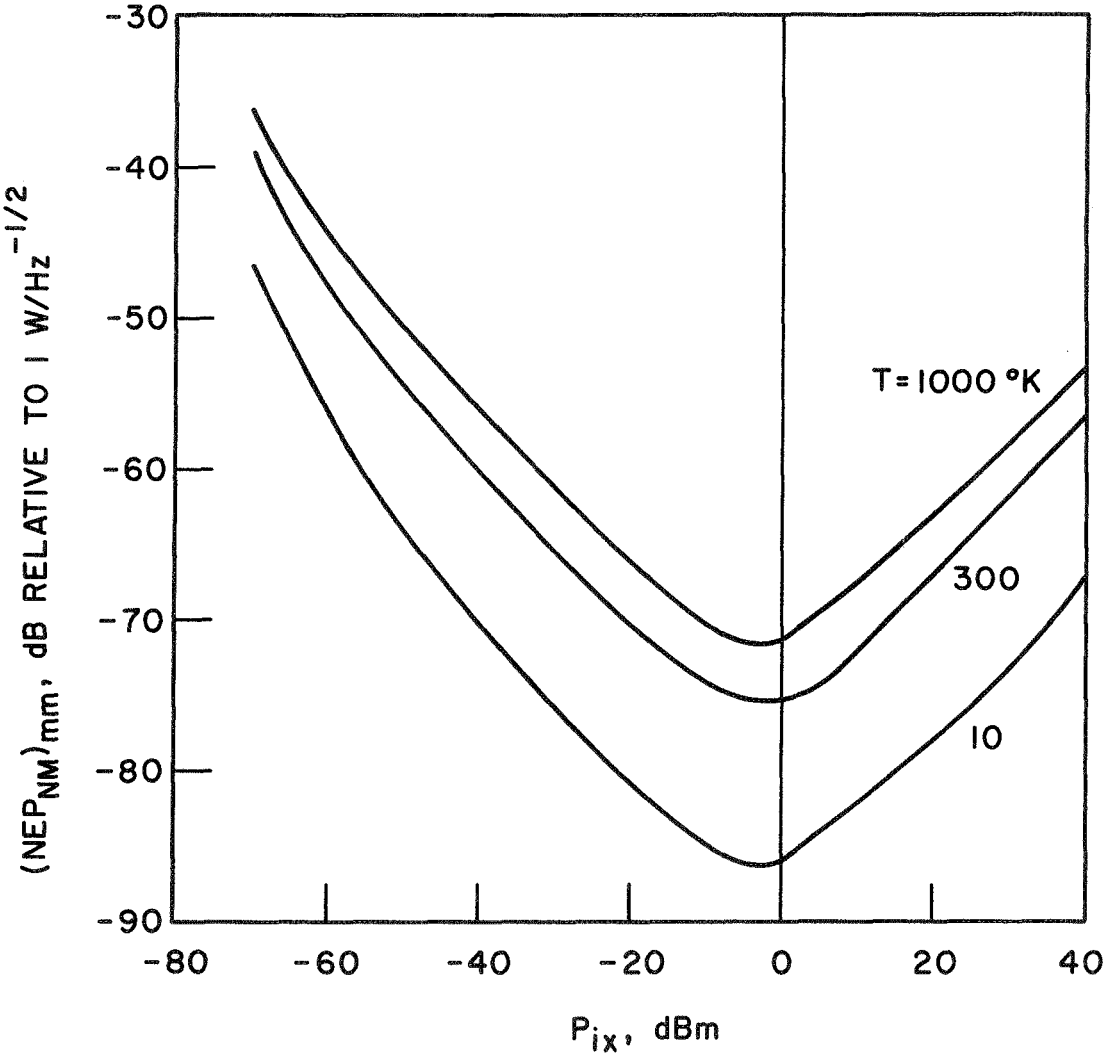

FIG. 4.11 $(NEP_{NM})_{mm}$ VS. P_{ix} FOR DIFFERENT VALUES OF BACKGROUND TEMPERATURE.

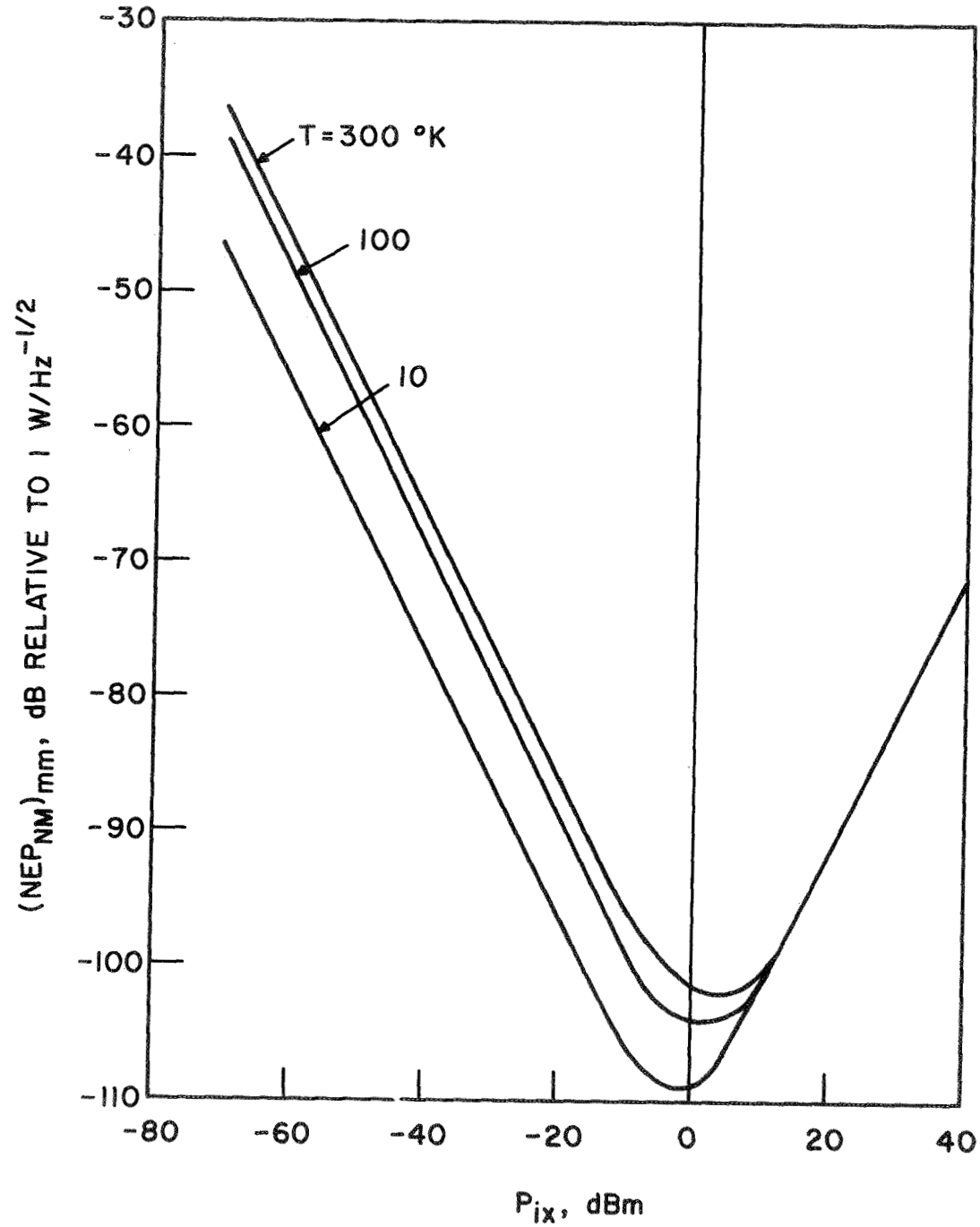

FIG. 4.12 $(NEP_{NM})_{mm}$ IN THE ABSENCE OF BACKGROUND RADIATION FLUCTUATION NOISE.

Table 4.1

Parameters Used in Figs. 4.11 and 4.12

$\overline{\Delta f^2_{rms}} = 0.001\ Hz^2$	$K'_m/\sigma_o = 1250$
$P_s = 0.5\ mW$	$T_D = 10°K$
$R_a = 1000\ \Omega$	$\beta_o = 2 - \sqrt{3}$
$R_v = 10{,}000\ \Omega$	$K\sigma_o/G_o = 1$
$S_d = 2 \times 10^3\ V/W$	$n_{am} = 10^{-15}$
$Q_{ox} = 500$	$K_d = 6 \times 10^{14}$

4.5 Summary

In this chapter the physical properties describing the detection scheme were described. The factor (K'_m/σ_o) plays an important role in reducing the $(NEP)_{mm}$ and the conversion loss. The conversion loss is minimum if $P_{ix} \gg P_s$. The response time is limited by the carrier relaxation time which is of the order of 10^{-7} s. The $(NEP)_{mm}$ is limited by the video detection system at the microwave output. Table 4.2 summarizes the theoretical results of the detector parameters using the experimentally obtained value for (K'_m/σ_o) and a 1N23 as the video detector. It should be emphasized that values listed in Table 4.2 correspond to the material and the circuit used and do not represent the theoretical limit of the detector performance.

Table 4.2

Summary of the Theoretical Values

of Detector Parameters*

$(L_T)^{**}_{matched}$	$\simeq$	6 dB
$(NEP_{NM})_{mm}$ using 1N23 crystal detector	=	-74.25 dBm per unit bandwidth
(NEP_{NM}) using an ideal video receiver	=	-89.7 dBm per unit bandwidth
Response time	$\cong$	10^{-7} s

---

* Using the available sample and the circuit shown in Fig. 5.2.

** $(L_T)_{matched}$ depends on P_s which is a function of the size of the sample used.

CHAPTER V. EXPERIMENTAL INVESTIGATION OF THE DETECTION SCHEME

5.1 Introduction

This chapter deals with the experimental evaluation of the detection scheme. The detector was tested at some chosen frequencies in the range of 35 to 150 GHz. The test frequencies were chosen according to the availability of signal sources and test components. The experimental results will be presented and compared to the theoretical analyses of Chapters III and IV. In the first section the experimental setup is described along with a discussion of the measurement system. The experimental results on the conversion loss and the noise equivalent power will be presented next and compared to the theoretical predictions. One section will deal with the measurement of the response time and a qualitative comparison to the theoretical predictions. The last section is devoted to the investigation of the detector's properties as a function of the magnetic field.

5.2 Experimental Setup

5.2.1 Downconverter Circuit. The circuit used for the detection scheme is illustrated in Figs. 5.1. The high-purity InSb sample with dimensions of 4 x 2 x 1 mm is placed under the central post of the reentrant cavity. The cavity must be simultaneously resonant at the microwave bias frequency and the frequency of the millimeter-wave signal to be detected which insures a greater interaction between the signal and the material. The resonance frequencies of the cavity are essentially

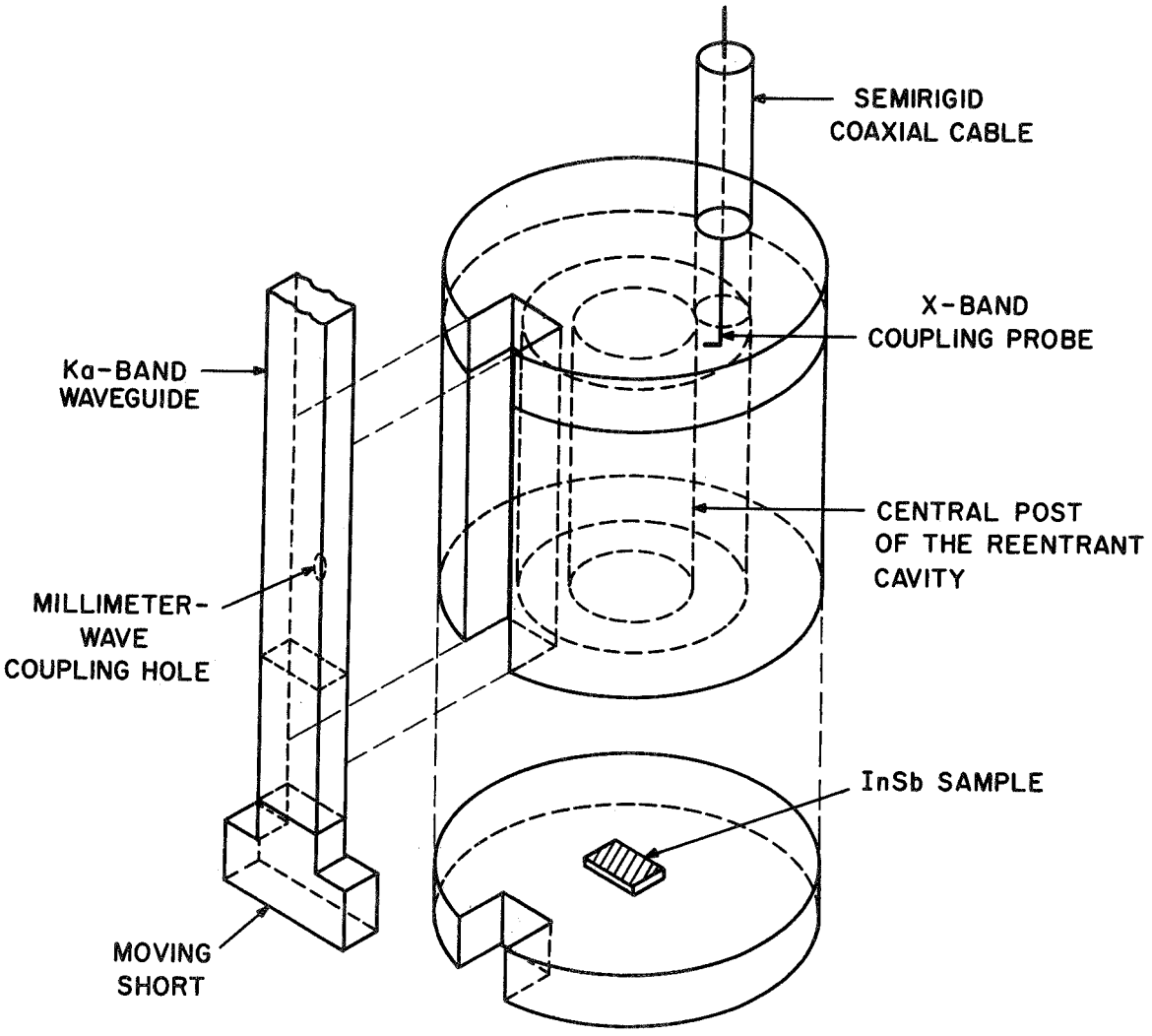

(a) DOWNCONVERTER CAVITY ASSEMBLY

FIG. 5.1a SCHEMATIC OF THE DETECTION SYSTEM.

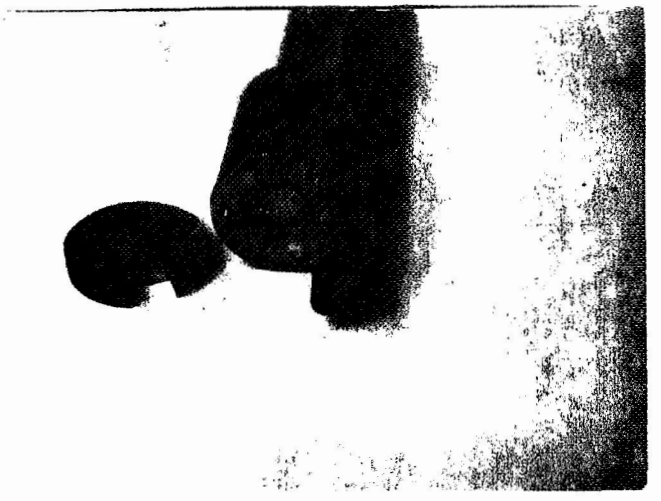

(b) PHOTOGRAPH OF THE DOWNCONVERTER CAVITY ASSEMBLY

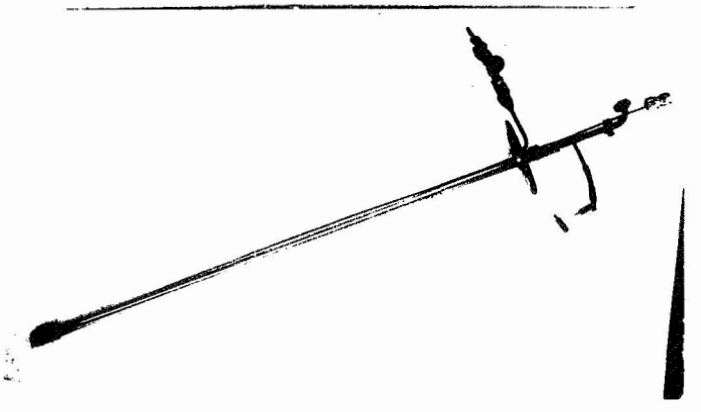

(c) PHOTOGRAPH OF THE DOWNCONVERTER CIRCUIT ASSEMBLY

FIG. 5.1b-c PHOTOGRAPHS OF THE DETECTION SYSTEM.

determined by its physical dimensions due to the fact that the sample volume is very small compared to that of the cavity and its dielectric constant is not too high ($\epsilon_r = 16$).[1] The cavity dimensions were chosen to make it resonant at an X-band frequency at one of the lower-order modes. Many higher-order modes will exist providing resonance frequencies in the millimeter- and submillimeter-wave region.

The microwave bias signal is coupled to the cavity by a semirigid coaxial cable (Amphenol No. 412-668) and the coupling factor can be adjusted by changing the orientation of the coupling probe with respect to the flux lines within the cavity. This can be done by providing means to rotate the coaxial line. On the other hand the millimeter-wave signal was coupled to the cavity by a long piece of a Ka-band waveguide through an iris. A moving short at the end of the waveguide has been provided to adjust the millimeter-wave cavity coupling factor. It was possible to obtain any desired coupling factor at the microwave frequency by rotating the coaxial line. However the problem was rather severe at the millimeter-wave frequencies because the moving short used to freeze in its place once the cavity system was cooled down. The measurements had to be done at the available modes, most of which were poorly coupled. It is felt, however, that this problem can be resolved.

5.2.2 Measurement Circuit. Figure 5.2 shows a block diagram of the experimental setup used to investigate the detection scheme. The circuit consists of two parts, the input section at the millimeter-wave frequency to be tested and the output section at the microwave bias frequency. The output circuit is essentially the same as that discussed in Section 3.2. The input circuit provided means to monitor the incident

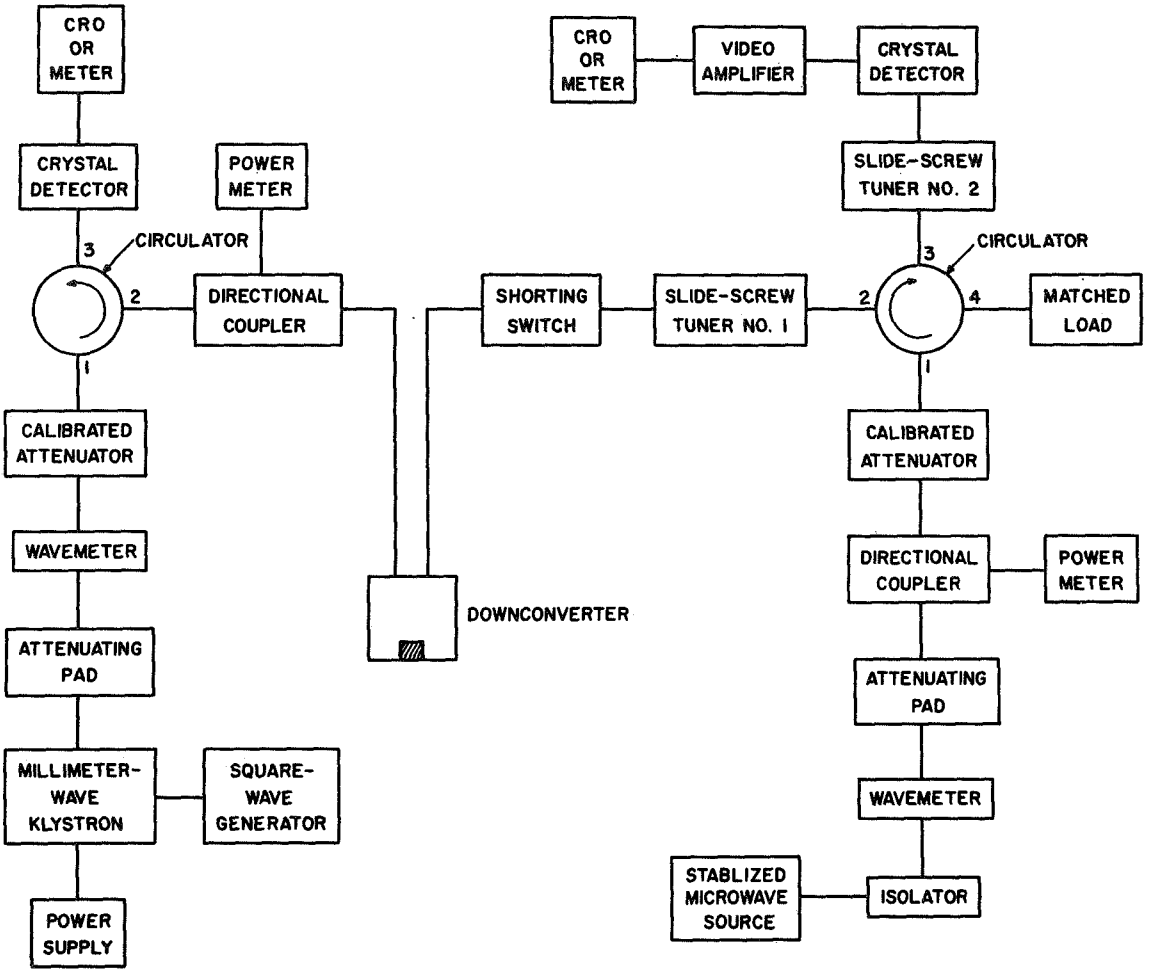

FIG. 5.2 BLOCK DIAGRAM OF THE EXPERIMENTAL SETUP TO TEST THE DETECTION SCHEME.

and reflected millimeter-wave signals. The details of this circuit varied according to the available components at the test frequency and a typical circuit is shown in Fig. 5.2. The circuit parameters were measured at each frequency and typical values for such parameters are given in Table 5.1.

Table 5.1

Typical Values of Circuit Parameters at the Test Frequencies*

Operating Frequency (GHz)	Line Loss (dB)	β_o	Q_L	Cavity 3 dB Bandwidth (MHz)	Line VSWR
8.526	1.2	0.579	255	33	1.1
34.56	4	0.43	425	80	1.5
80.02	4	0.72	600	110	1.45
148.82	7	**	**	**	1.26

* T = 4.2°K.

** Not measured.

5.2.3 Measurement Procedure. The first step in the operation of the device is to stabilize the microwave source to one of the cavity modes. The coupling factor to the cavity is then adjusted to the desired value. The next step is to locate a cavity resonance in the vicinity of the millimeter-wave frequency of the signal to be detected and to tune the millimeter-wave klystron to the resonance frequency of the cavity. Square-wave modulation is applied to the millimeter-wave klystron in such a way that the klystron is turned on and off and the change in the

reflected microwave signal as a result of the incident signal is observed. Care should be exercised to make sure that the cavity system is in thermal equilibrium with the liquid helium bath during the course of the measurements. Enough time should be allowed after transferring the liquid helium for the system to reach thermal equilibrium. In addition, the liquid helium level should be checked regularly.

5.3 Conversion Loss Measurement

5.3.1 Saturation Loss at the Microwave Frequency. It was shown in Chapter IV that the conversion loss is minimized if $P_{ix} \gg P_s$. The saturation effects at the microwave frequency were studied by monitoring δP_D vs. P_{ix}. The microwave source was stabilized at the cavity resonance frequency whose value is 8.576 GHz. The millimeter-wave signal was square-wave modulated at 1000 Hz and its level was maintained constant. The experiment was performed at three millimeter-wave frequencies whose values are 34.56, 80.02 and 148.82 GHz. The experimental results are illustrated in Figs. 5.3 through 5.5 for the signal frequencies of 34.56, 80.02 and 148.82 GHz, respectively. It is seen from these plots that the dependence of the detector performance on the microwave bias level is in good agreement with Eq. 4.20. The experimentally measured values of P_s varied slightly for the three cases considered. It is anticipated that P_s is a function of the sample volume and the microwave cavity coupling factor. However the discrepancy in the values of P_s for the three cases considered could be due to a slight deviation between the cavity resonance frequency and the microwave signal frequency.

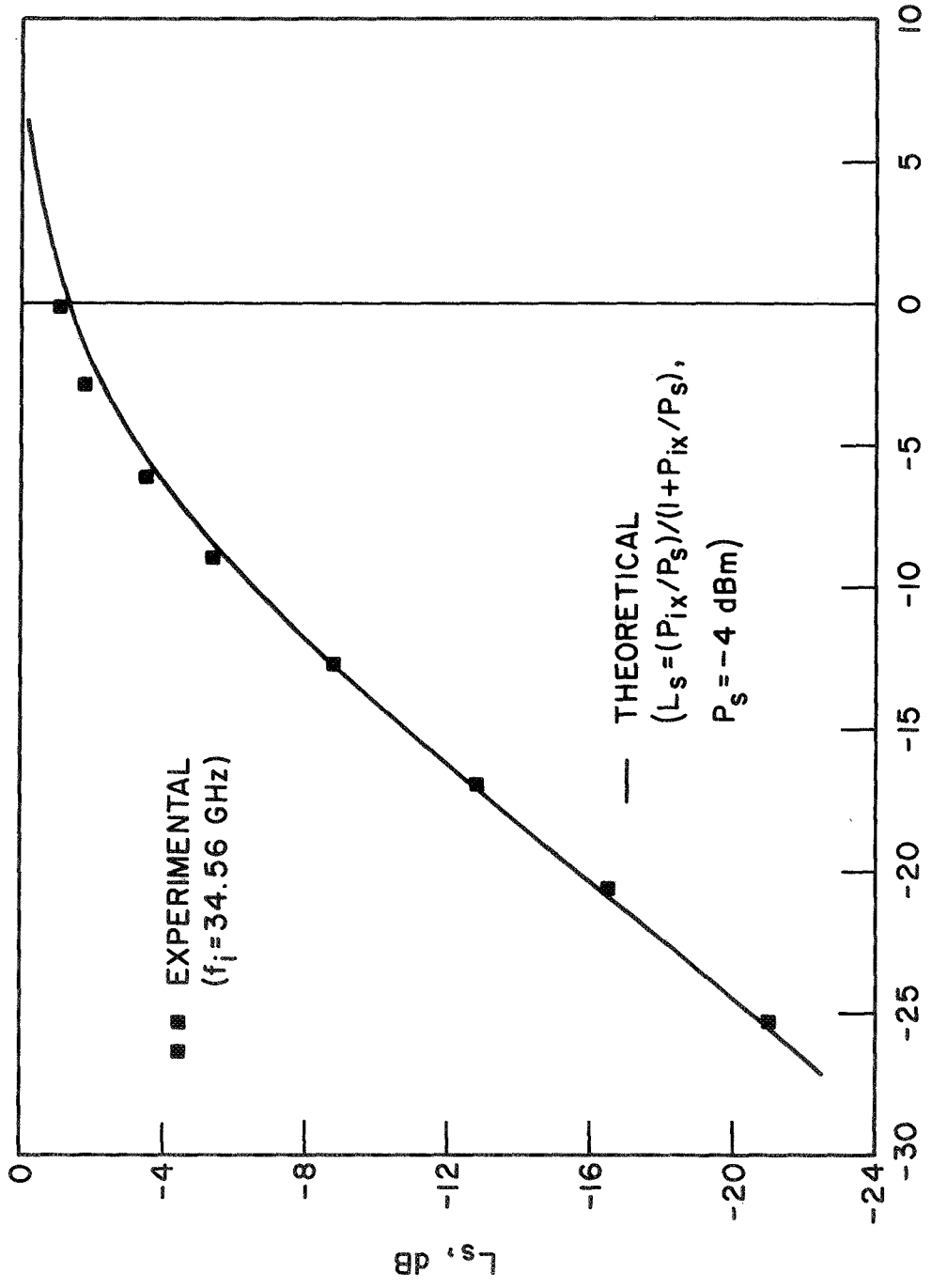

FIG. 5.3 SATURATION LOSS VS. P_{ix}. (f_i = 34.56 GHz, f_x = 8.576 GHz)

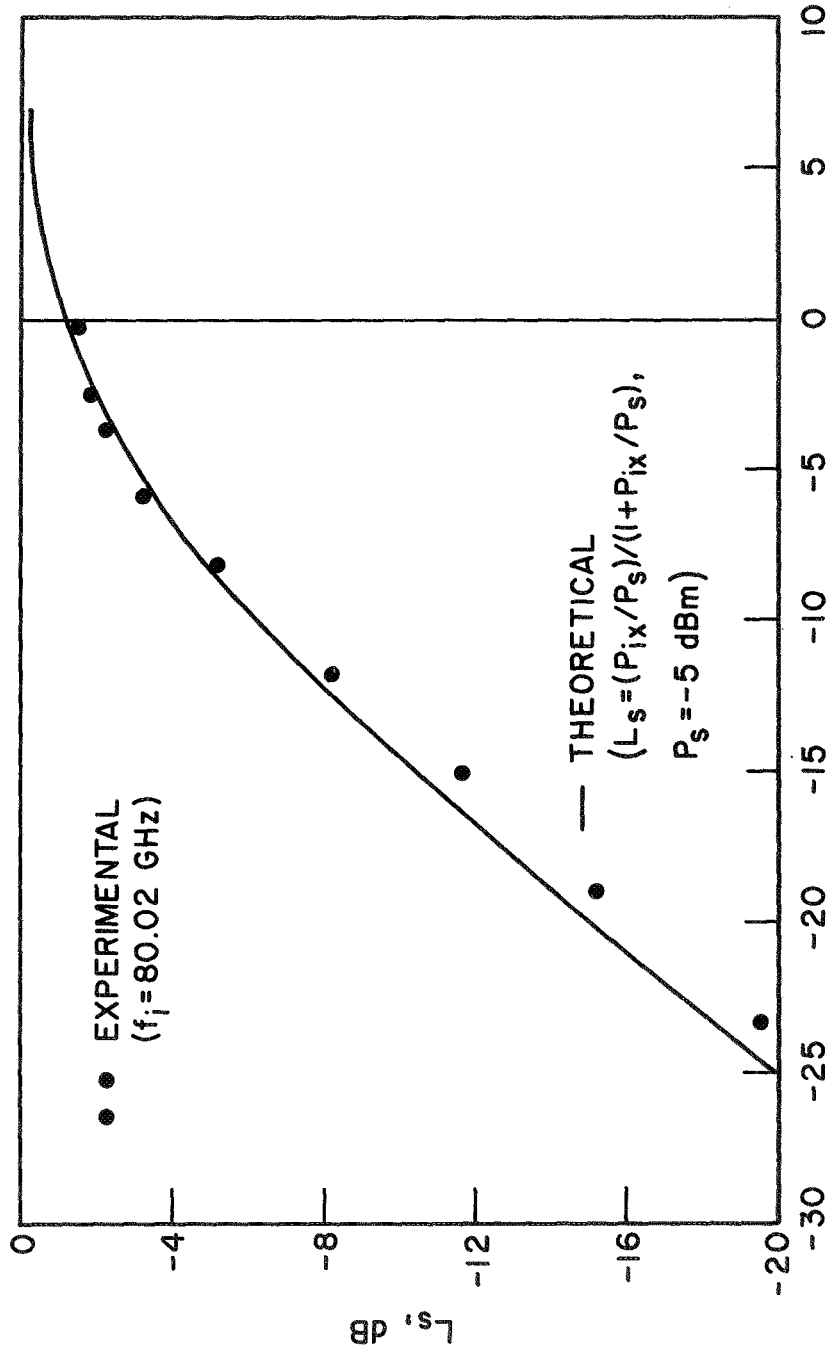

FIG. 5.4 SATURATION LOSS VS. P_{ix}. (f_i = 80.02 GHz, f_x = 8.576 GHz)

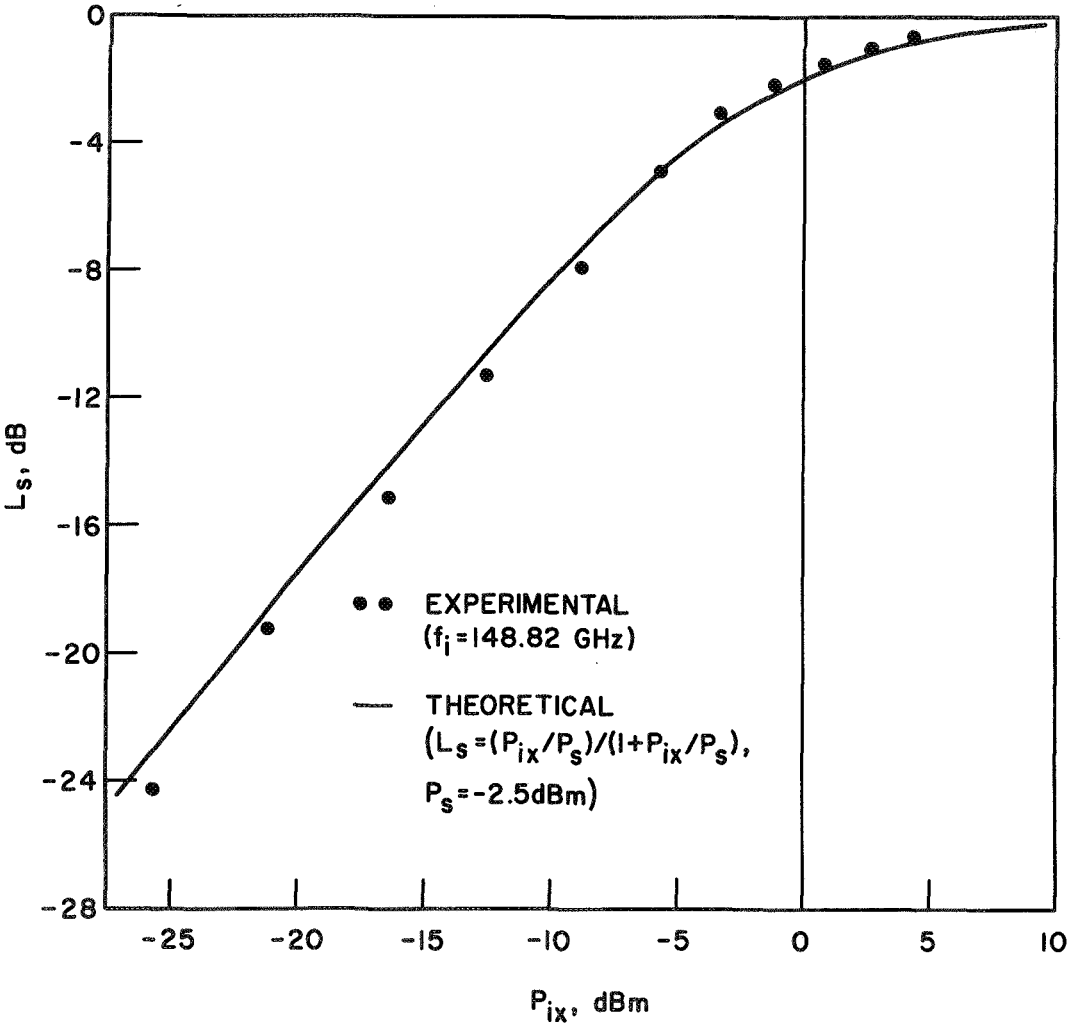

FIG. 5.5 SATURATION LOSS VS. P_{ix}. (f_i = 148.82 GHz, f_x = 8.576 GHz)

5.3.2 Input Frequency Deviation Loss L_{if}. The dependence of the detector performance on the input frequency is very important in determining the usable input bandwidth.

Deviation of the signal frequency from the millimeter-wave cavity resonance frequency will cause a decrease in the power absorbed by the sample. This results in an effective increase in the conversion loss. The input frequency deviation loss L_{if} can be measured by monitoring the terminal-to-terminal conversion loss vs. the frequency of the input signal. On the other hand the effective input tunable bandwidth is defined as the bandwidth at which the detector response drops by 3 dB compared to that at the resonance frequency of the millimeter-wave cavity.

It is clear that the input circuit sets the limit to the detector input bandwidth. Therefore L_{if} equals the power absorbed by the cavity at the signal frequency to that at the cavity resonance frequency and is given by

$$L_{if} = \frac{1}{1 + (2\delta_i Q_{Li})^2}, \qquad (5.1)$$

where $\delta_i = (f_i - f_{io})/f_{io}$,

Q_{Li} = the loaded Q of the millimeter-wave cavity and

f_{io} = the resonance frequency of the millimeter-wave cavity.

Figure 5.6 illustrates a typical experimental result for the input frequency deviation loss vs. the signal frequency deviation from the cavity resonance frequency. A plot of Eq. 5.1 with $Q_{Li} = 425$ is included

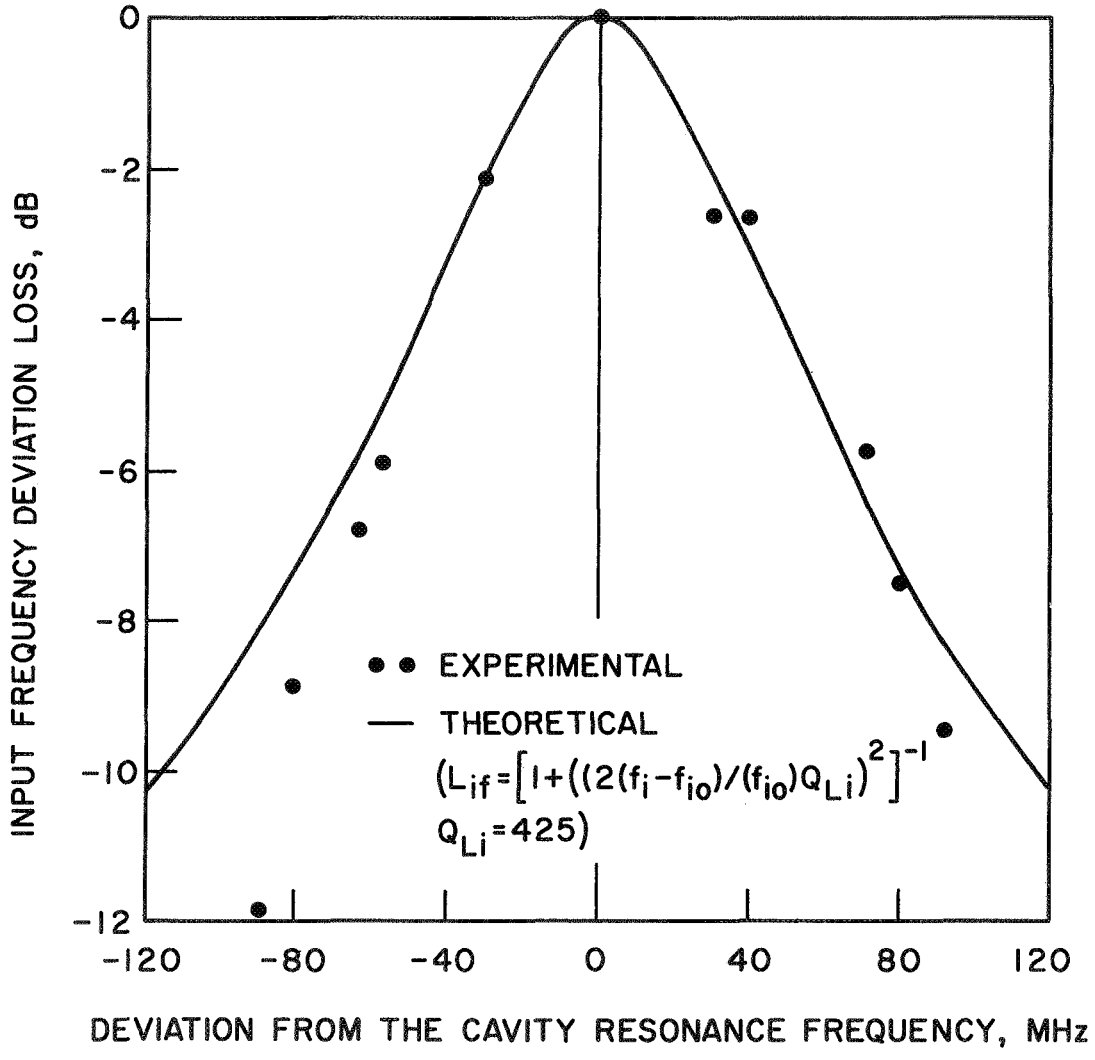

FIG. 5.6 L_{if} VS. $(f_i - f_{io})$. $(f_{io} = 34.56$ GHz)

in Fig. 5.6 for comparison. It is seen from this figure that the tunable bandwidth of the detector is about 80 MHz at the operating point under consideration (f_{io} = 34.56 GHz).

5.3.3 Terminal-to-Terminal Conversion Loss L_T. Equation 4.1 together with the circuit shown in Fig. 5.2 were used to measure L_T. Calibrated thermistors were used to monitor the input millimeter-wave signal for frequencies in the Ka- and E-bands. On the other hand the nominal sensitivity of an FXR Z224S crystal detector was used to get an estimate of the incident power level at frequencies on the order of 150 GHz. The operating conditions were adjusted to allow a terminal-to-terminal conversion loss as low as possible. The millimeter-wave signal was modulated at 1000 Hz and the microwave bias level was approximately 1 mW.

The experimental results for L_T together with the input and output mismatch losses are shown in Table 5.2. The ideal overall conversion loss was used as the basis for comparing the experimental and theoretical results. The ideal device conversion loss is defined as the device conversion loss if $P_{ix} \gg P_s$ and both the input and output circuits are ideal (perfectly matched and lossless). The expression for the ideal device conversion loss follows directly from Eq. 4.22 and is given by

$$L_D = \frac{4(K_m'/\sigma_o)}{(1 + G_o/K\sigma_o)} \left(\frac{\beta_o(1 - \beta_o)}{(1 + \beta_o)^3} \right) P_s \quad , \tag{5.2}$$

where L_{ov} is the device conversion loss and the rest of the quantities have been defined earlier. It should be noted that L_D sets the

Table 5.2

The Detection Scheme Conversion Loss

Signal Frequency (GHz)	P_{ix} (dBm)	Minimum Measured Terminal-to-Terminal Conversion Loss (dB)	Measured Input Conversion Loss (dB)	Measured Output Line Loss (dB)	Saturation Loss (dB)	Circuit Loss (dB)	Device Conversion Loss L_D (dB)	Theoretical Minimum Device Conversion Loss (dB)
34.56	0	21.5	8	1.2	1	10.2	11.3	6.8
80.02	0	11.5	3	1.2	1.2	5.4	6.1	7.8
148.82	3	18*	9*	1.2	0.8	11	7	5.3

* Within ±2 dB uncertainties (using Z224S nominal sensitivity values).

ultimate performance of the detector concerning the conversion loss. The value of (K_m'/σ_o) obtained from Fig. 2.27 together with the measured value of $G_o/K\sigma_o$ and P_s were used to calculate the values of L_{ov} given in the last column of Table 5.2. The discrepancy in the values listed in the last column is due to the fact that the measured values of P_s differed with frequency. On the other hand, the experimental values of L_D were obtained by subtracting the circuit losses from the measured values of the terminal-to-terminal conversion loss.

The dependence of the terminal-to-terminal conversion loss on the input signal level was also measured. A typical result is shown in Fig. 5.7. It is seen from this figure that the terminal-to-terminal conversion loss is essentially independent of the signal level to be detected. This proves that K_m' is independent of the signal level.

5.4 The Response Time

The response time was measured by using a square-wave modulation to switch the millimeter-wave klystron on and off and by observing the detected signal. Oscillograms displaying typical responses of the detector are shown in Fig. 5.8. No noticeable drop in the detector performance was observed up to modulation frequencies as high as 300 kHz. This corresponds to the maximum rate at which the millimeter-wave klystron could be modulated. In-line solid-state modulators could not be used for measuring the detector response time since the best commercially available modulator has a rise time of 0.2 ms for frequencies in the millimeter-wave range. It is seen from the previous discussion that the

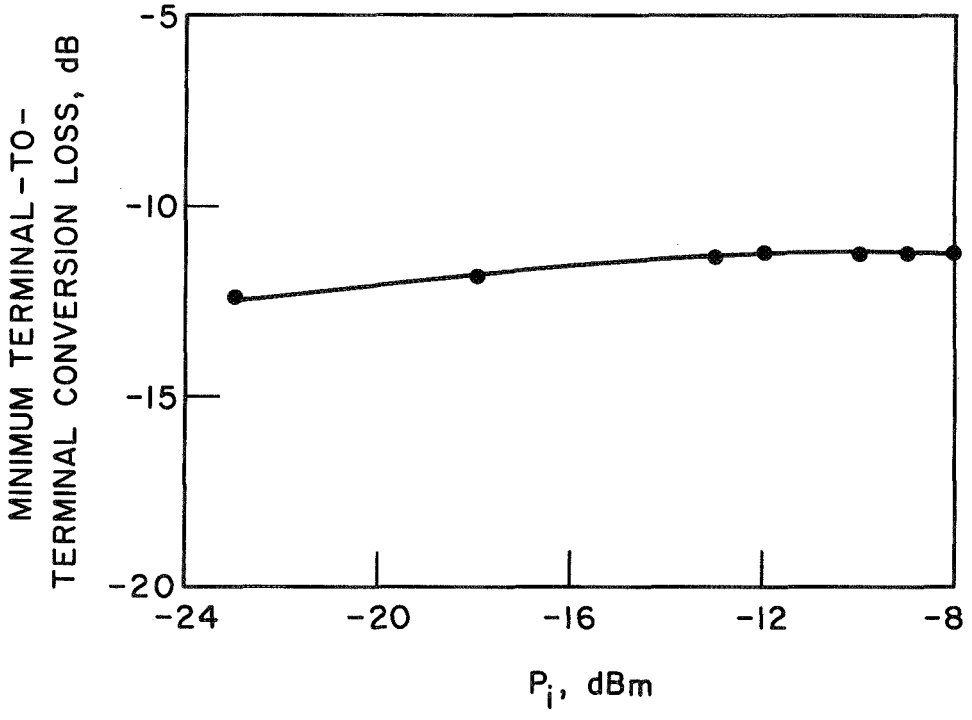

FIG. 5.7 DEPENDENCE OF THE TERMINAL-TO-TERMINAL CONVERSION LOSS ON THE INPUT SIGNAL LEVEL. (f_i = 80.02 GHz, P_{ix} = 1 mW)

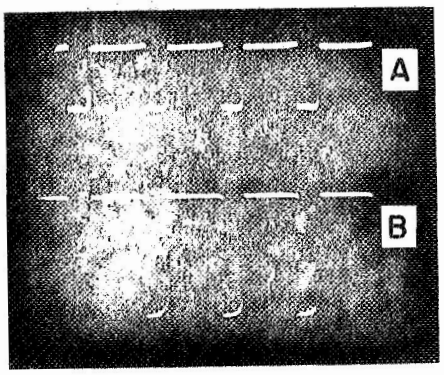

(a) $f_i = 34.56$ GHz, $f_m = 25$ kHz

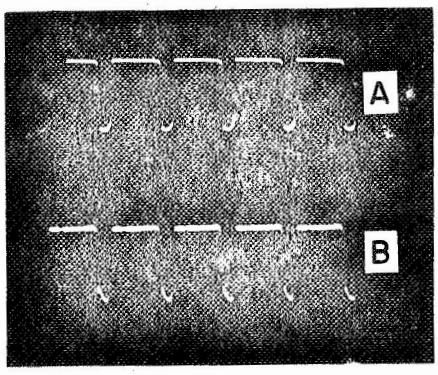

(b) $f_i = 80.02$ GHz, $f_m = 25$ kHz

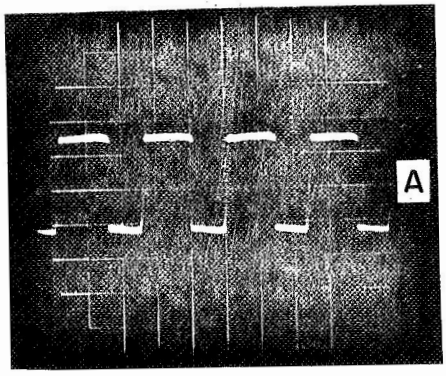

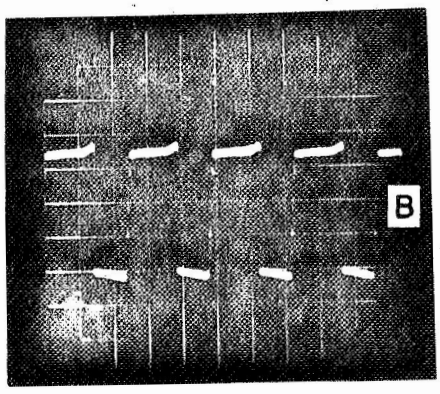

(c) $f_i = 148.82$ GHz, $f_m = 1$ kHz

FIG. 5.8 TYPICAL DETECTOR RESPONSE. A. DETECTED SIGNAL. B. INCIDENT SIGNAL.

detector response time could not be measured directly due to the lack of test components at the millimeter-wave frequencies. It is also seen that the response time is much less than 3×10^{-6} s. This result agrees with the predictions of Chapter IV, where it was shown that the response time is limited by the carrier energy relaxation time whose value is approximately 10^{-7} s. The detector's ability to respond to a fast modulation rate was compared to a 1N53 crystal mounted in a waveguide. Figure 5.9 shows the result of such a comparison at a modulation frequency of 250 kHz. It is seen from this figure that the suggested scheme considerably outperforms crystal detectors (point-contact diodes) concerning the speed of response.

5.5 The Noise Equivalent Power $(NEP)_{mm}$

The noise equivalent power was estimated by measuring the power input to the detector which gives rise to a mean-square output equal to the mean-square value of the output noise. The signal was square-wave modulated at 1000 Hz and the concept of tangential sensitivity has been adopted. The tangential sensitivity, as defined for a square-wave modulated signal, is defined as the signal level which results in an output where the top of the noise at the base line is at the same level as the bottom of the noise or the square-wave modulation. The criterion for the tangential sensitivity is easily understood from the oscillogram shown in Fig. 5.10. The experiment was performed at 34.56 and 80.02 GHz, it was not carried out at 150 GHz due to the lack of equipment to measure the absolute signal level in this frequency range. Figures 5.11 and 5.12 show the experimental results of the $(NEP_N)_{mm}$ vs. P_{ix} for the input

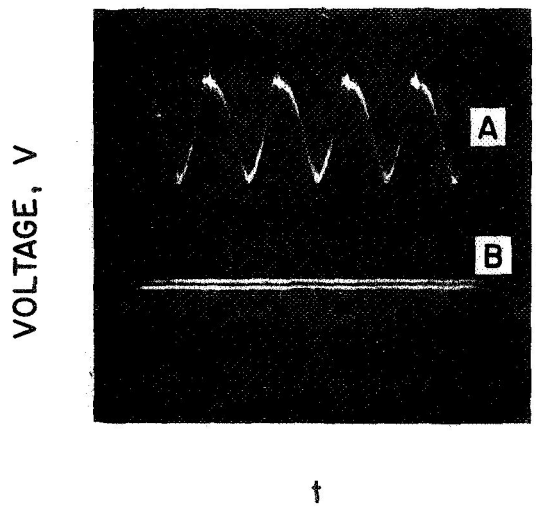

A. OUTPUT OF THE PRESENT SCHEME

B. OUTPUT OF IN53 CRYSTAL IN A WAVEGUIDE

FIG. 5.9 COMPARISON OF THE DETECTOR RESPONSE WITH A 1N53 CRYSTAL MOUNTED IN A WAVEGUIDE. (f_i = 80.02 GHz, f_m = 250 kHz)

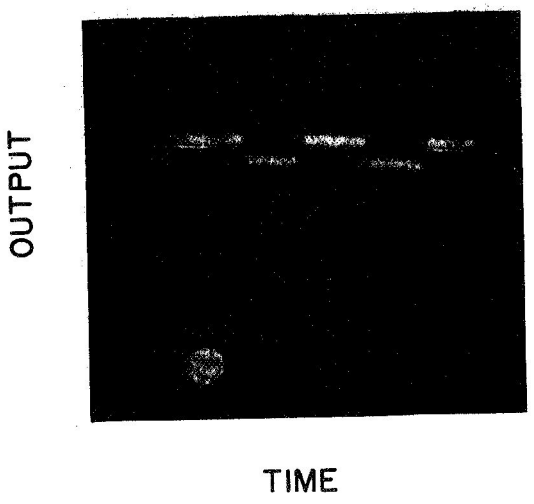

FIG. 5.10 CRITERION FOR EQUAL SIGNAL AND NOISE.

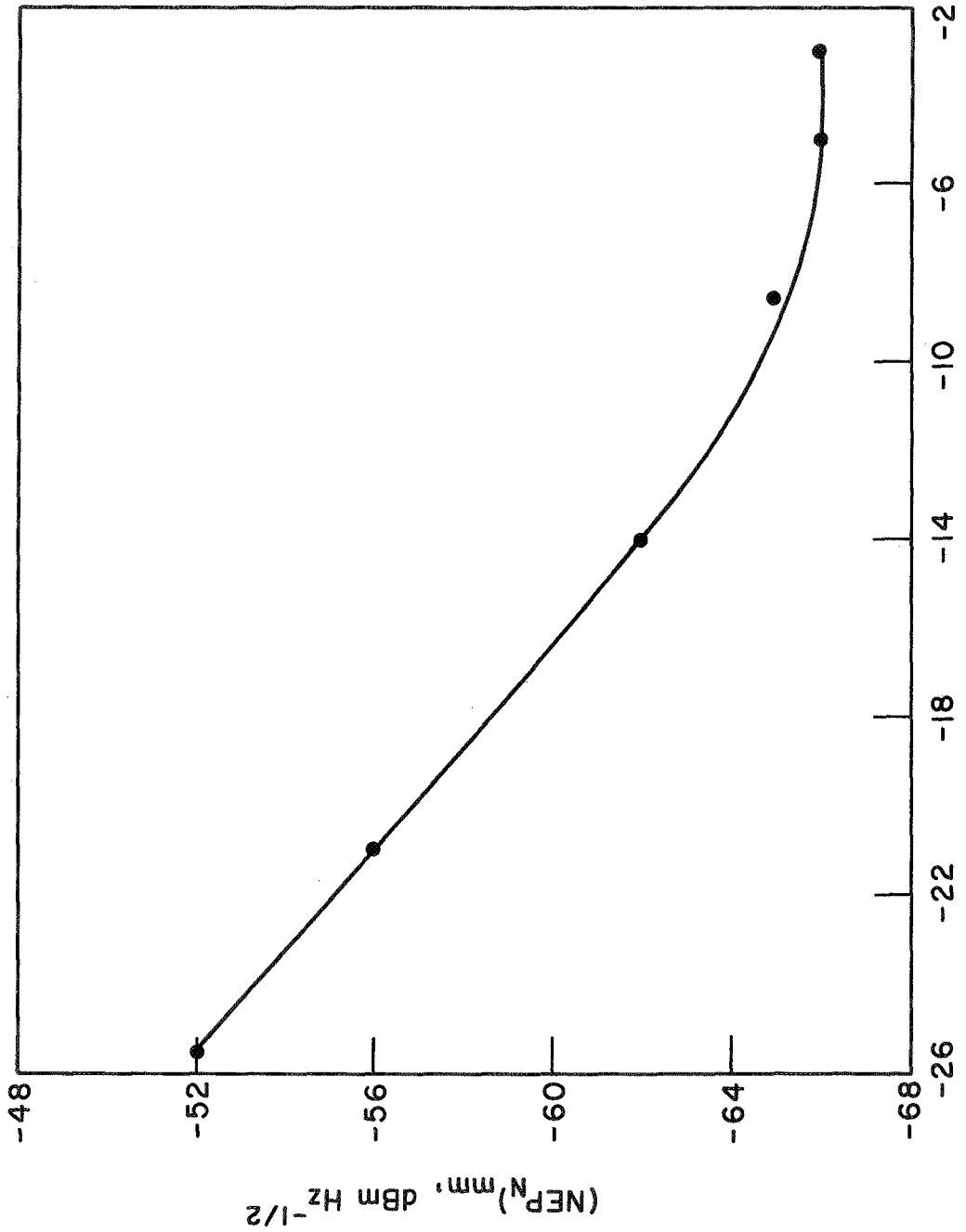

FIG. 5.11 $(NEP)_{min}$ NORMALIZED TO UNIT BANDWIDTH VS. P_{ix}. (f_i = 20.02 GHz)

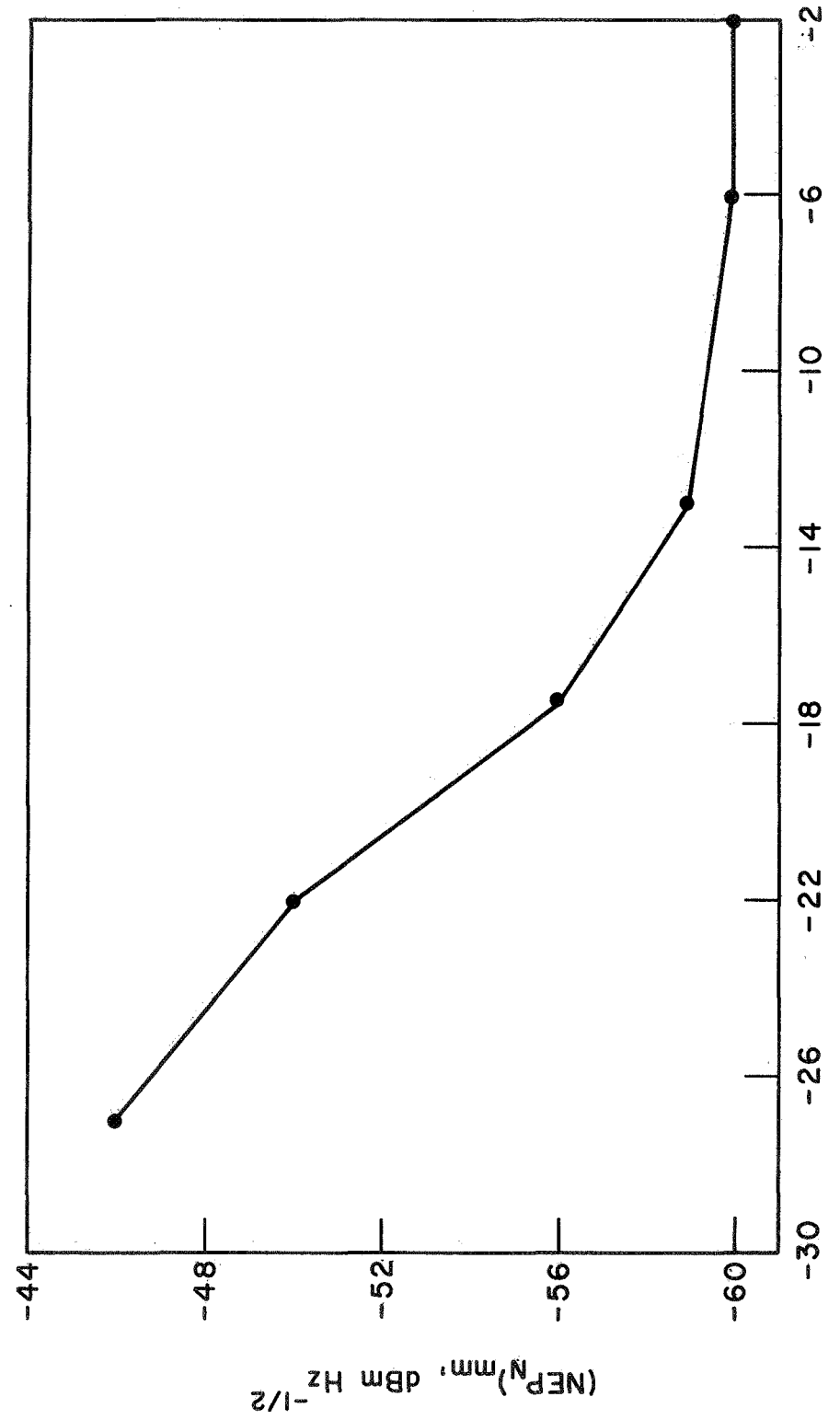

FIG. 5.12 $(NEP)_{min}$ NORMALIZED TO A UNIT BANDWIDTH VS. P_{ix}. (f_i = 34.56 GHz)

frequencies of 80.02 and 34.56 GHz, respectively, where $(NEP_N)_{mm}$ is the $(NEP)_{mm}$ normalized to a unit bandwidth. It should be noted that $(NEP_N)_{mm}$ and $(NEP)_{mm}$ are related to the following equation

$$(NEP_N)_{mm} = (NEP)_{mm}(B_x)^{-1/2} \quad , \tag{5.5}$$

where B_x is the bandwidth of the video amplifier. It is seen from Figs. 5.11 and 5.12 that the minimum measured values of $(NEP_N)_{mm}$ at 80.02 and 34.56 GHz are 2.5×10^{-10} and 10^{-9} W, respectively. It should be emphasized that these numbers are obtained from the measured terminal values, i.e., the conversion losses have not been accounted for.

It should be kept in mind that Figs. 5.11 and 5.12 were obtained using the circuit shown in Fig. 5.2. Therefore, in order to check the ultimate noise performance of the detection scheme the circuit losses must be taken into consideration. The normalized noise equivalent power with both input and output circuits perfectly matched $(NEP_{NM})_{mm}$ will set the limit of the ultimate noise performance of the scheme. The $(NEP_{NM})_{mm}$ can be obtained experimentally by subtracting the circuit losses given in Table 5.2 from the measured values of $(NEP_N)_{mm}$. The dependence of $(NEP_{NM})_{mm}$ on P_{ix} is shown in Fig. 5.13. It is seen from this figure that the experimental results agree favorably with Eq. 4.60. In addition, analysis of the contribution of the different noise sources shows that the video detector sets the limit to the detector noise performance. It is expected that $(NEP_N)_{mm}$ could be lowered by at least 10 dB by improving the video detection system. A summary of the $(NEP)_{mm}$ results is shown in Table 5.3. The numbers in the last column were obtained on

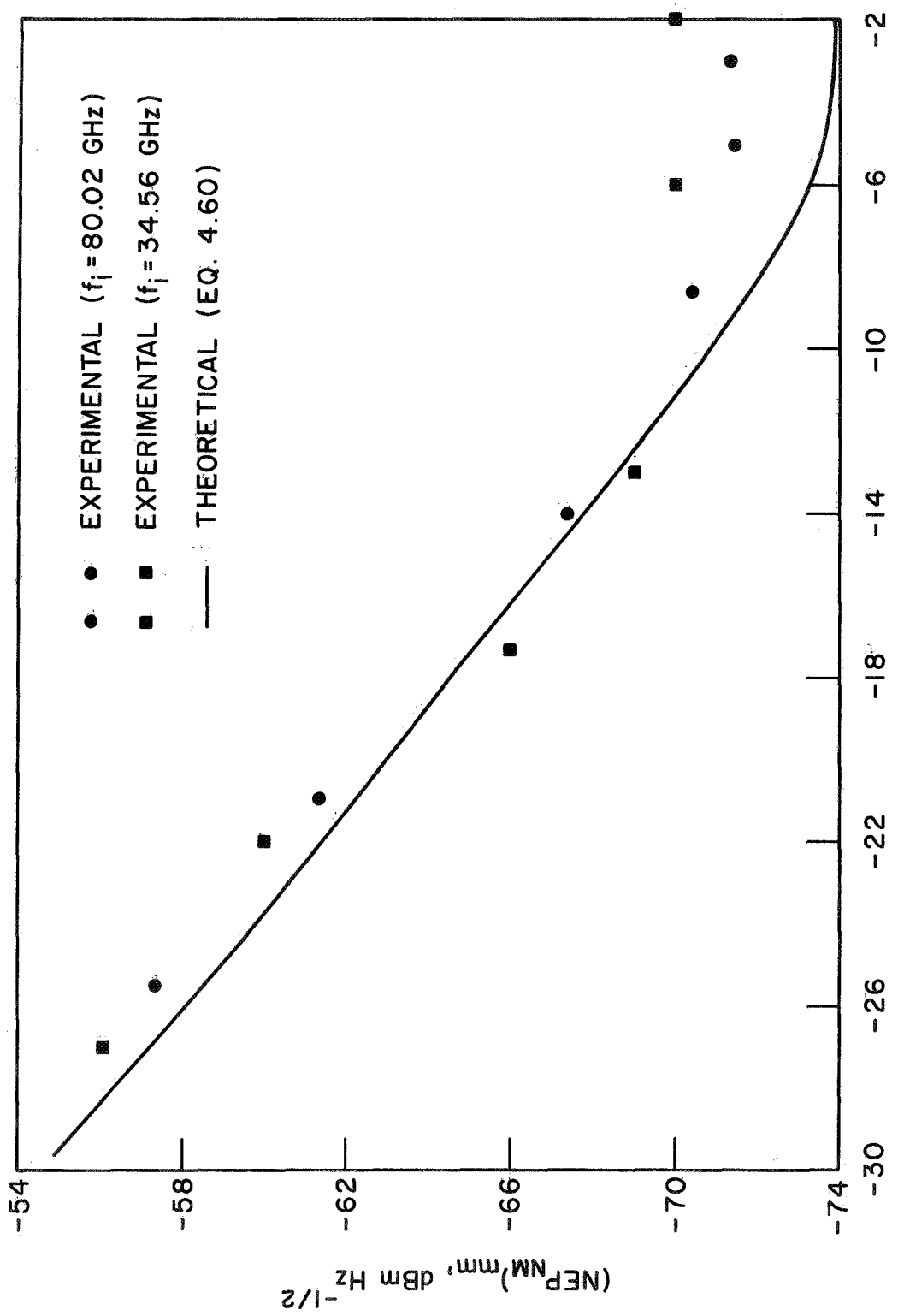

FIG. 5.13 $(NEP_{NM})_{mm}$ vs. P_{ix}.

the assumption of an ideal noisefree video detector. In this case the noise limit of the detection scheme is determined by the AM and FM noise of the microwave source.

Table 5.3

A Summary of the Minimum Values of $(NEP)_{mm}$

Signal Frequency (GHz)	Experimental $(NEP_N)_{mm}$ (dBm)	Experimental* $(NEP_{NM})_{mm}$ (dBm)	Theoretical** $(NEP_{NM})_{mm}$ (dBm)	Theoretical† $(NEP_{NM})_{mm}$ (dBm)
34.53	-60	-70.2	-74.25	-89.7
80.02	-66	-71.4	-74.25	-89.7
148.82	-58††	-69††	-74.25	-89.7

* Using the values of circuit losses listed in Table 5.2.

** Using Eq. 4.60 together with the constants listed in Table 4.1.

† Assuming an ideal noiseless video detector.

†† Accuracy is based on the nominal sensitivity of the Z224S crystal.

5.6 The Dynamic Range

The dynamic range is defined here as the ratio of the maximum to the minimum detectable signal level. This is important whenever the modulation index of the signal varies considerably. In addition, the dynamic range is indicative of the ability of the detector to stand instantaneous signal overloads. Therefore the dynamic range is an important factor when designing protective circuits for detectors with burnout limitations.

The lower limit of the dynamic range is determined by $(NEP)_{mm}$. On the other hand, the upper limit is determined by burnout limitation or saturation of the detection scheme. It is clear that there is no burnout limit on bulk InSb microwave-biased detectors. Saturation effects of the detection scheme were investigated by studying the dependence of the detector's response on the millimeter-wave signal level. Figure 5.14 illustrates the experimental results of the detector's response vs. P_i. It is seen from the figure that the detector saturates at an input signal of 10 dBm. Therefore the dynamic range of the detector is approximately 85 dB. It is worth mentioning that point-contact diodes have a typical dynamic range of 55 dB. In addition, these detectors have a burnout level of -25 dBm.

5.7 Magnetic Field Effects

5.7.1 Introduction. The dependence of the detector performance on magnetic field will be presented in this section. Application of the magnetic field results in quantizing the energy levels in the conduction band. The charge carriers in the conduction band will reside in the first Landau level in the absence of millimeter-wave radiation. The energy of the Landau levels above the bottom of the conduction band is given by[71]

$$\mathcal{E}_n = \hbar\omega_c(n + 1/2) \pm \frac{1}{2}\mu_B g^* H \quad , \tag{5.4}$$

where g^* = the g-factor which = -52 for InSb,

μ_B = the Bohr magneton and n is an integer (n = 0,1,2,...).

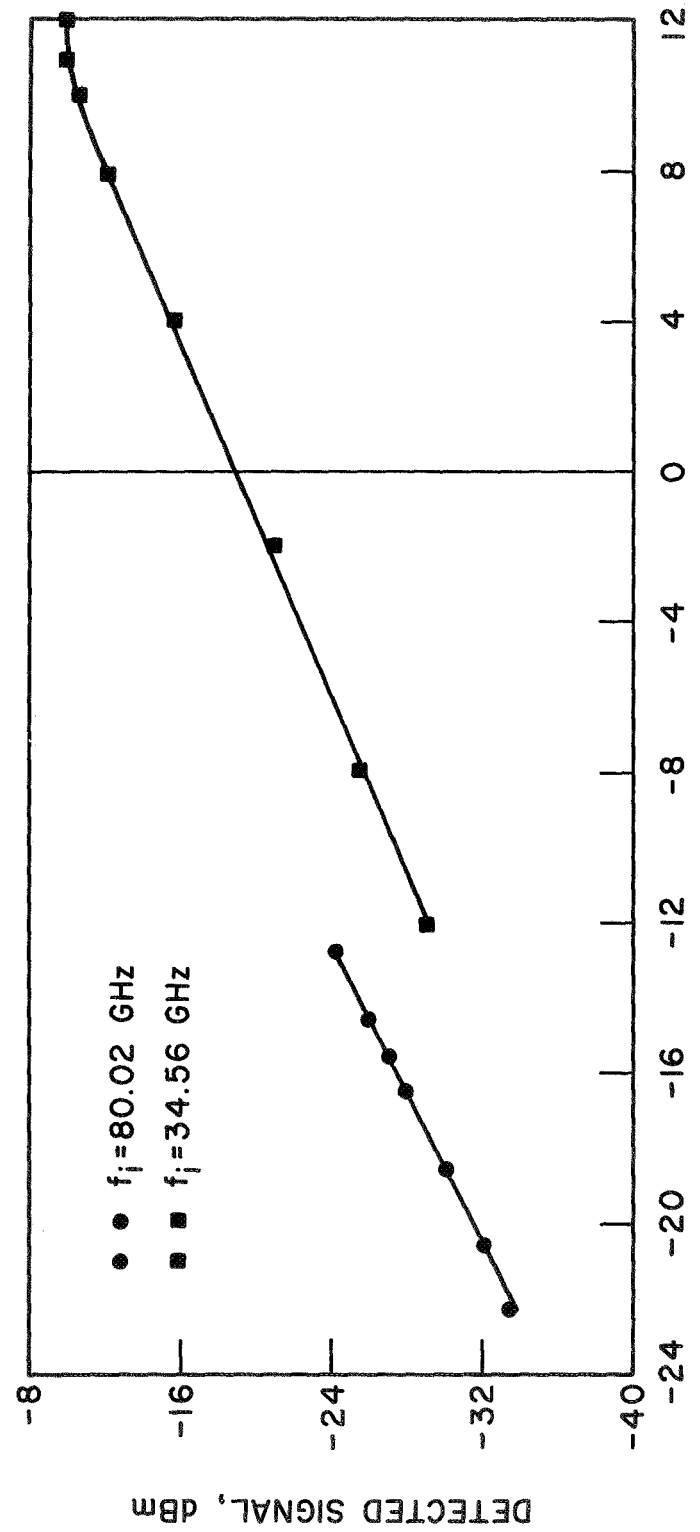

Fig. 5.14 DETECTOR RESPONSE VS. P_i.

Moreover, as the magnetic field is increased fewer carriers will remain in the conduction band. This will reduce the overlap between the impurity and the conduction bands and finally splits them completely for fields greater than the freeze-out magnetic field.

Conductivity change and signal detection could be the result of free-carrier absorption resulting in a change of the carrier mobility, transitions between the different Landau levels or transitions between the impurity and conduction bands. The hot-electron effect becomes inefficient as the magnetic field is increased since fewer carriers become available in the conduction band. As a result the performance of the device as a wideband detector deteriorates at very high magnetic fields. On the other hand, transitions between Landau levels or from the impurity to the conduction band could result in a narrow-band tunable detector. These transitions become effective for high magnetic fields (above 3 to 4 kG) where most of the carriers will be residing in the impurity band. It has been shown[71] that the most probable transition is between the two lowest levels associated with two consecutive Landau levels. Figure 5.15 shows the activation frequencies for such transitions as a function of B. Transitions between Landau levels become significant for fields greater than the freeze-out magnetic field. Therefore this effect can be observed for frequencies above approximately 400 GHz. Transitions between the impurity and conduction bands occur at frequencies in the vicinity of 160 and 4350 GHz at high values of the

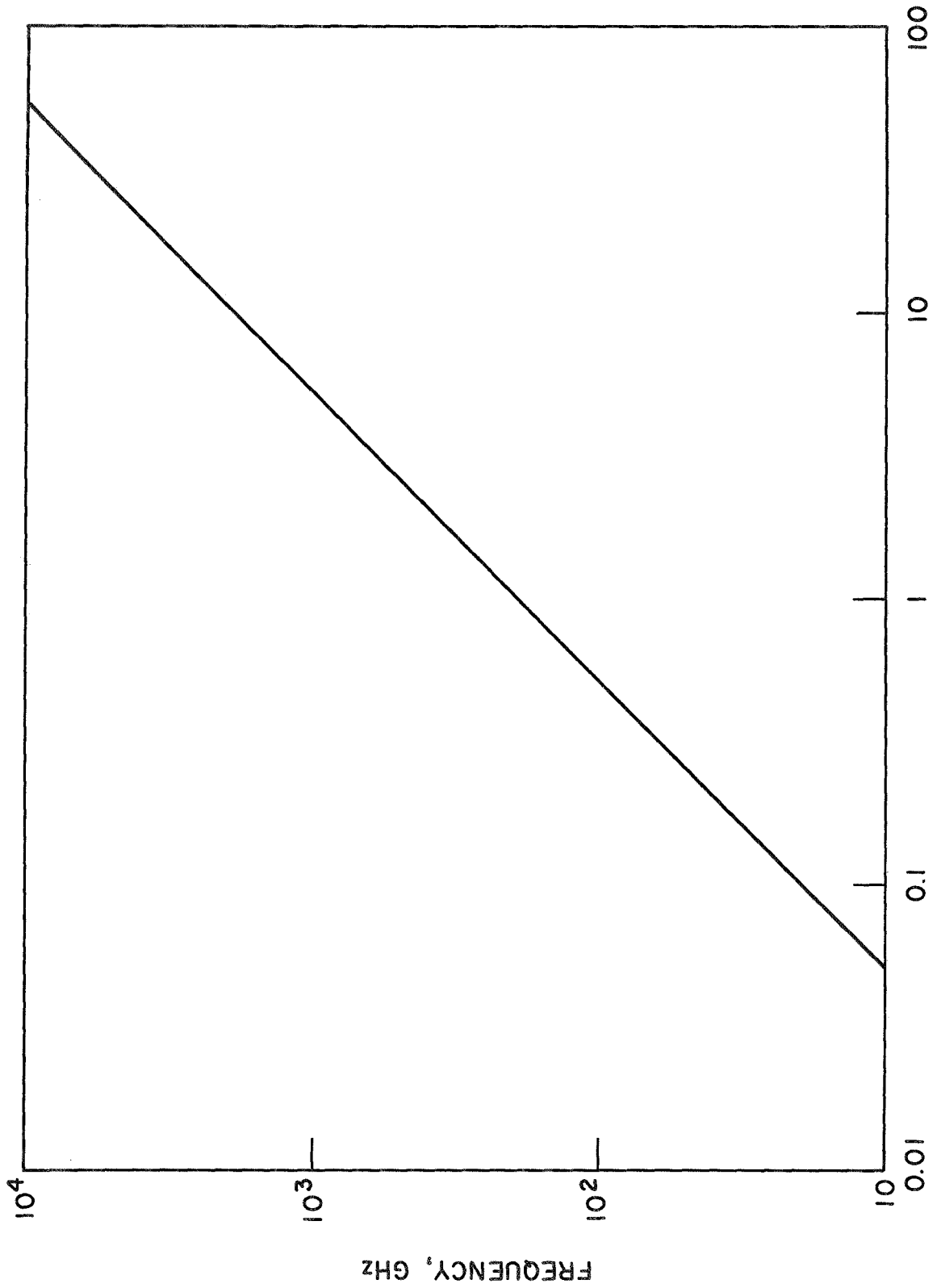

FIG. 5.15 ACTIVATION FREQUENCY FOR TRANSITIONS BETWEEN TWO CONSECUTIVE LANDAU LEVELS VS. B FOR InSb.

magnetic field (3 to 4 kG). However, broadband transitions are possible at magnetic field values less than B_F where there is a partial overlap between the impurity and conduction bands. These transitions tend to increase the conductivity and thus will add to the hot-electron effect.

5.7.2 Dependence of the Detector Response on Magnetic Field. The concept of the magnetic field conversion loss L_B will be used to discuss the detector performance as a function of the applied magnetic field. L_B is defined as the ratio of the detected signal in the presence of the magnetic field to that without a magnetic field when all the other parameters are held fixed. Using Eq. 4.7, L_B could be written as

$$L_B = \frac{n(\mu_c - \mu_{co}) + n_s\mu_c}{n_{co}(\mu_c - \mu_{co})} \quad , \tag{5.5}$$

where all the parameters have been defined earlier. It is worth noting that μ_c depends on the signal level, n is a function of the magnetic field and its value decreases with B, while n_s is given by Eq. 4.6.

Figure 5.16 illustrates the typical dependence of L_B on B for a Ka-band signal and various microwave bias levels. It is seen from this figure that the detector response deteriorates with magnetic field as a result of the drop in the value of n (number of carriers contributing to the hot-electron effect). It is also seen that the contribution of the electronic transitions between the

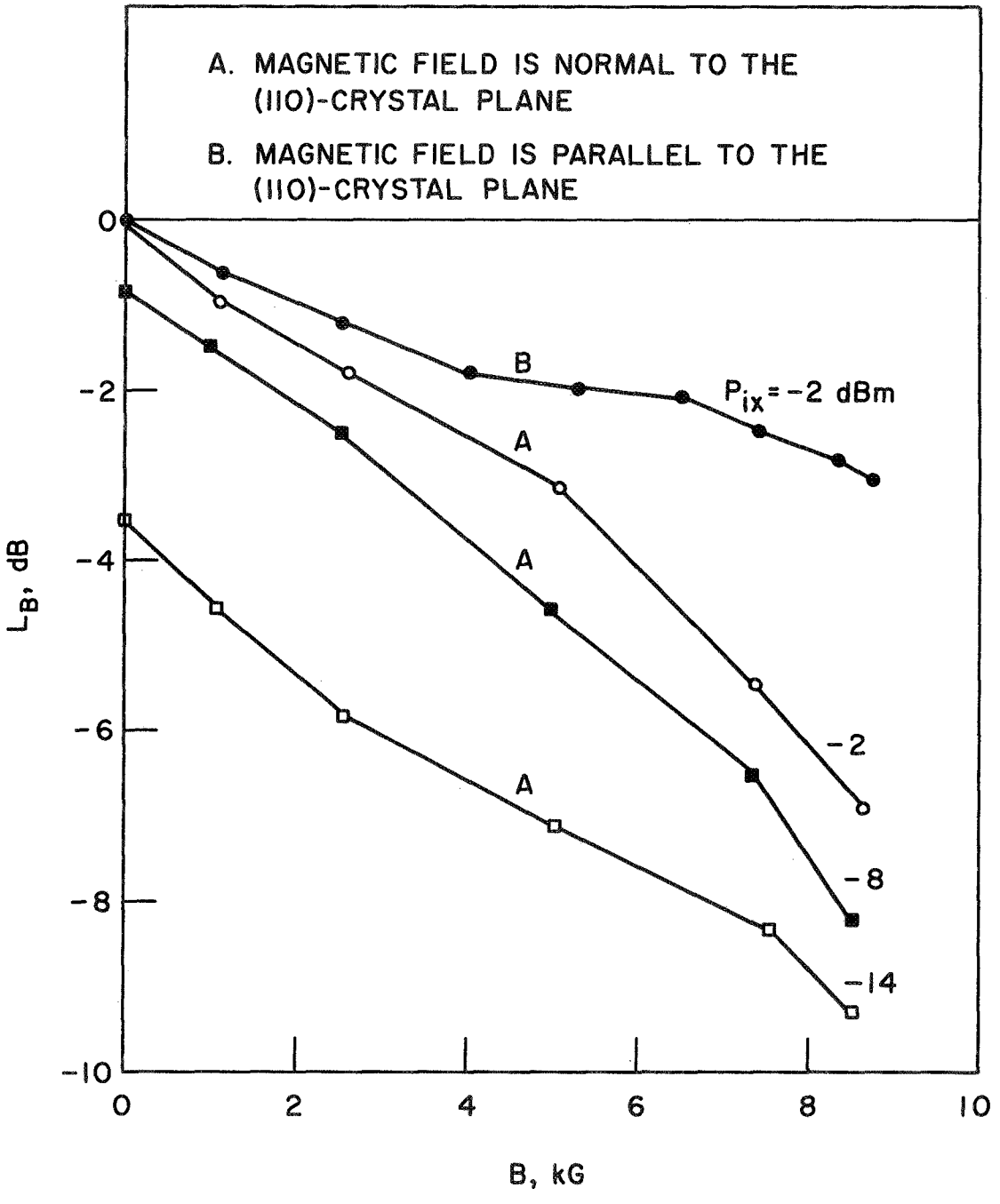

FIG. 5.16 L_B VS. B. (f_i = 34.56 GHz)

impurity and conduction bands is negligible and the free-carrier absorption is the dominant process in this frequency range.

Figures 5.17 and 5.18 display L_B vs. B for frequencies in the E- and G-bands. It is seen that L_B first increases with B, reaches a maximum and then starts decreasing again. This behavior is consistent with the discussion presented in the previous section. The improvement in the detector response at low magnetic fields is due to the electronic transitions from the impurity to the conduction band. The contribution of these transitions to the detection process will increase as the magnetic field is increased above zero since more carriers become available in the impurity band. Electronic transitions dominate over free-carrier absorption for values of L_B greater than 0 dB. However, as the magnetic field is increased further, energy bands will be formed and the energy gap associated with them will increase with magnetic field.[33] The electronic transitions will drop to zero when $hf_i < \Delta E$ causing the detector response to deteriorate with increasing magnetic field as a result of the inefficiency of the free-carrier absorption. It is also seen from Figs. 5.16 and 5.17 that the detector response is less sensitive to magnetic field when B is parallel to the (110)-crystal plane.

5.7.3 Dependence of the Conversion Loss, Response Time and $(NEP)_{mm}$ on the Magnetic Field. Figure 5.19 illustrates the dependence of the detector bandwidth on magnetic field. It is seen from this figure that the detector's bandwidth is reduced by about 25 percent as the magnetic field is increased from 0 to 1.2 kG. Therefore

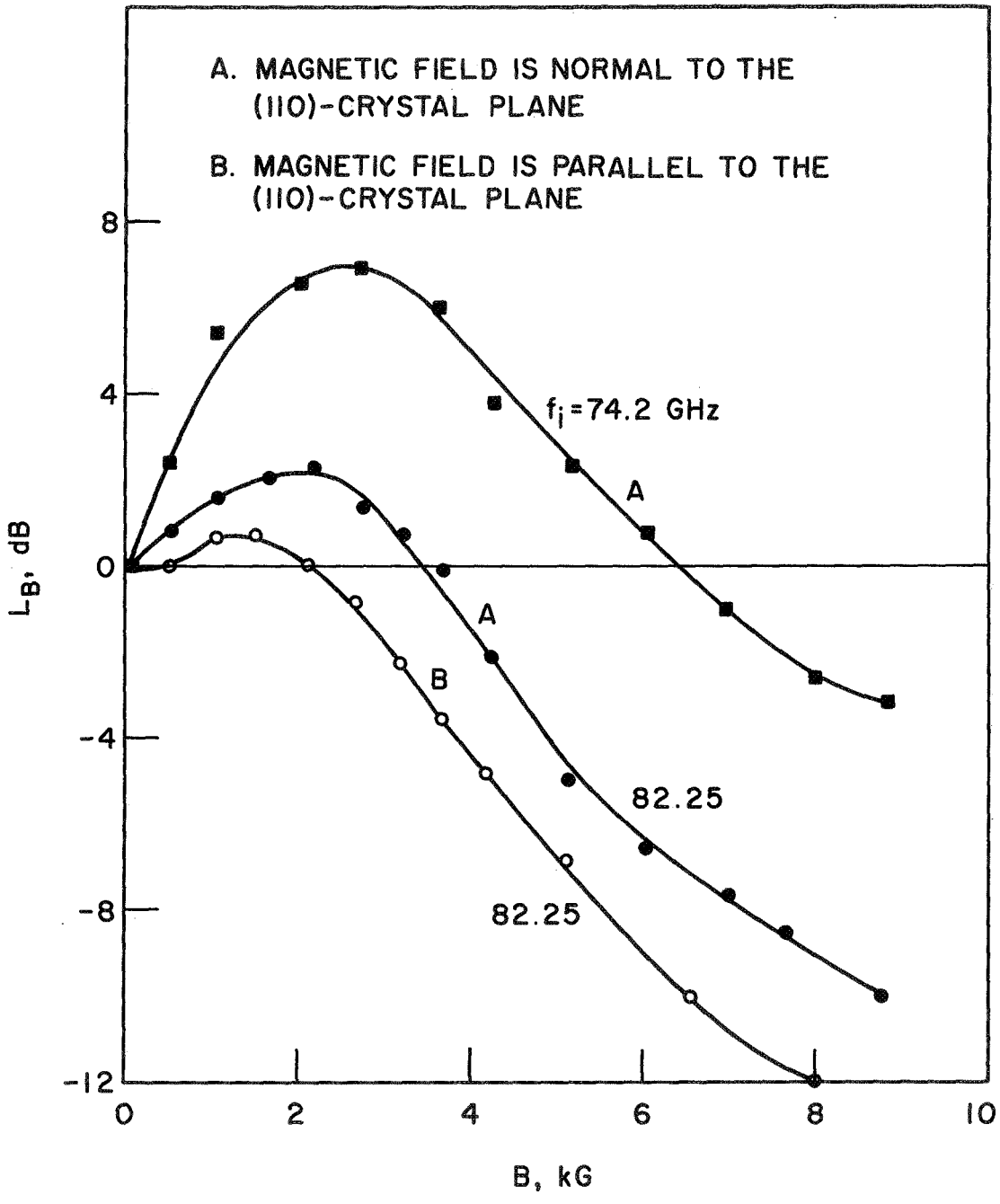

FIG. 5.17 L_B VS. B. (f_i = 82.25, 74.2 GHz)

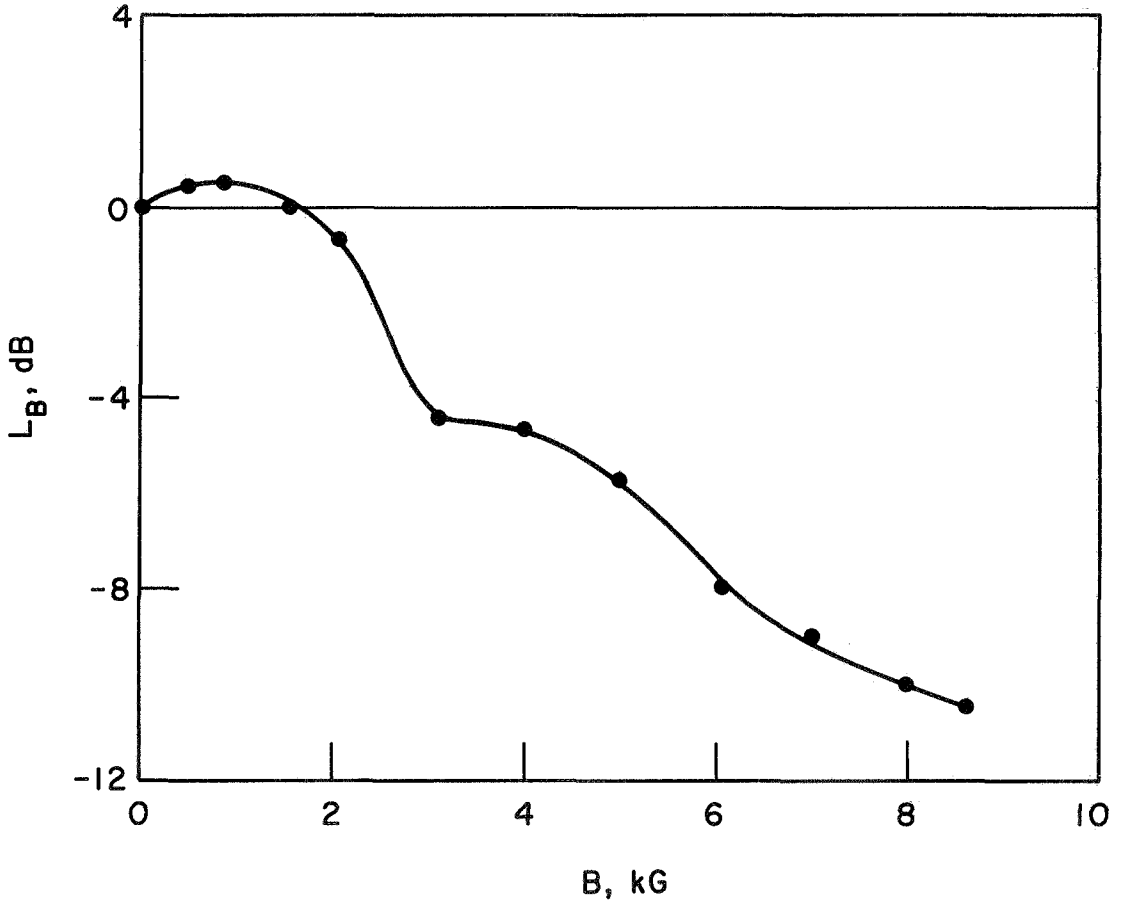

FIG. 5.18 L_B VS. B. (f_i = 148.8 GHz)

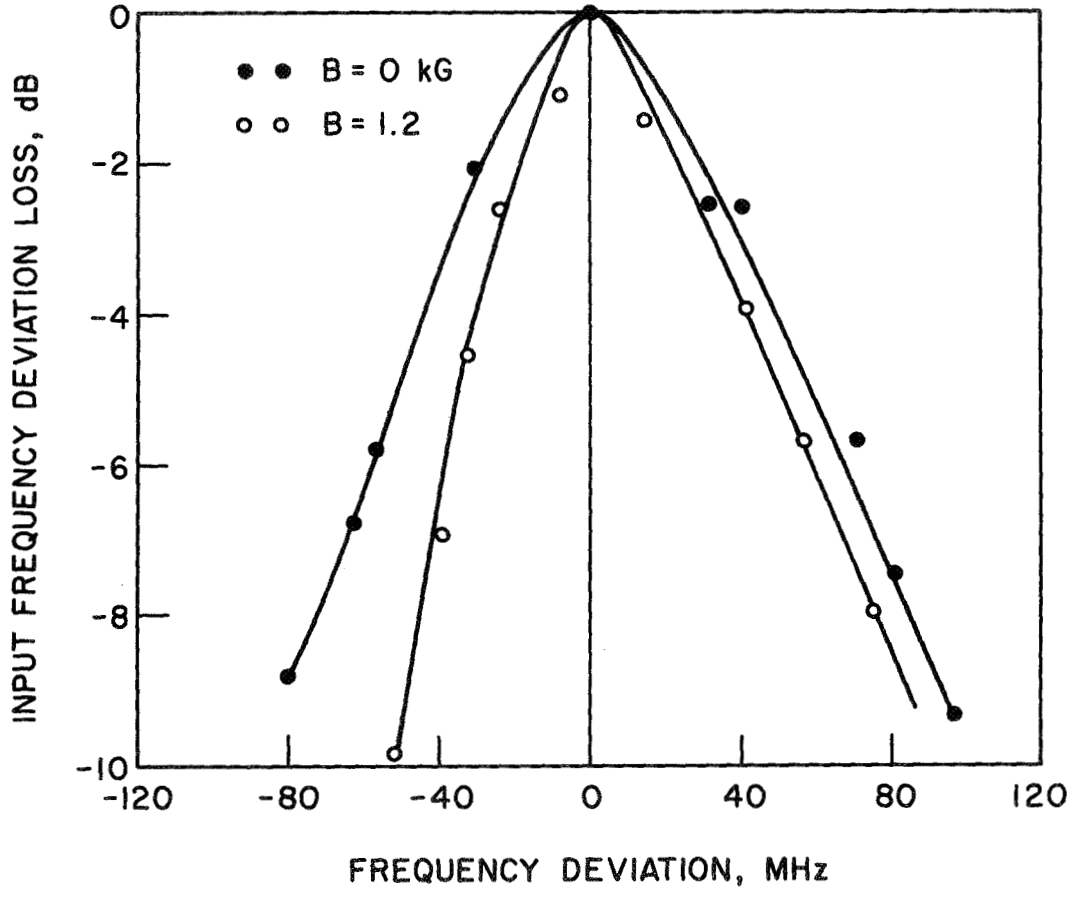

FIG. 5.19 EFFECT OF B ON L_{if}. (f_i = 35.46 GHz)

magnetic fields can be used to improve the selectivity of such a class of detectors.

The terminal-to-terminal conversion loss was found to depend strongly on the level of the millimeter-wave signal in the presence of a magnetic field. This is in contrast with the case where the magnetic field is zero. Figure 5.20 illustrates the experimental results for the dependence of L_{TN} on P_i for several values of the magnetic field. L_{TN} is the terminal-to-terminal conversion loss normalized to the minimum value measured at the designated value of the magnetic field. It is seen from this figure that the hot-electron effect is the mechanism responsible for the signal detection in the absence of the magnetic field ($n_s = 0$). In this case all the charge carriers are essentially in the conduction band irrespective of the signal level to be detected. On the other hand the dependence of the terminal-to-terminal conversion loss on P_i in the presence of magnetic fields proves that both the electronic transitions between the impurity and the conduction bands together with the hot-electron effect are responsible for the detection mechanism. The number of carriers in the impurity band increases with the magnetic field and the percentage of these carriers excited to the conduction band will depend on the signal level as indicated by Eq. 4.6.

The experimental results for the dependence of the response time on magnetic field is shown in Fig. 5.21. The millimeter-wave klystron was modulated at 50 kHz and the detected signal was observed as the magnetic field was varied between 0 and 8 kG. It is

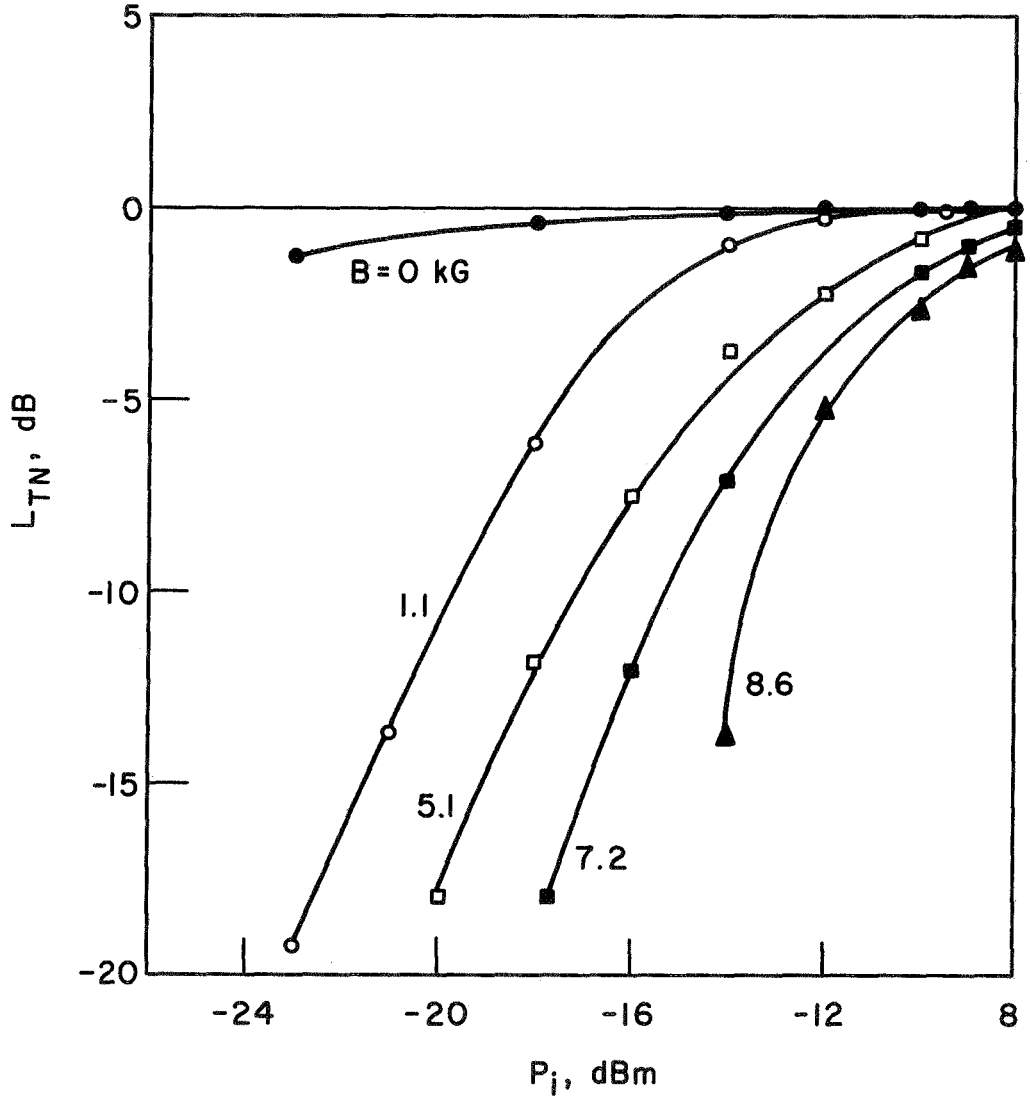

FIG. 5.20 NORMALIZED TERMINAL-TO-TERMINAL CONVERSION LOSS VS. P_i FOR DIFFERENT VALUES OF B. (f_i = 80.8 GHz)

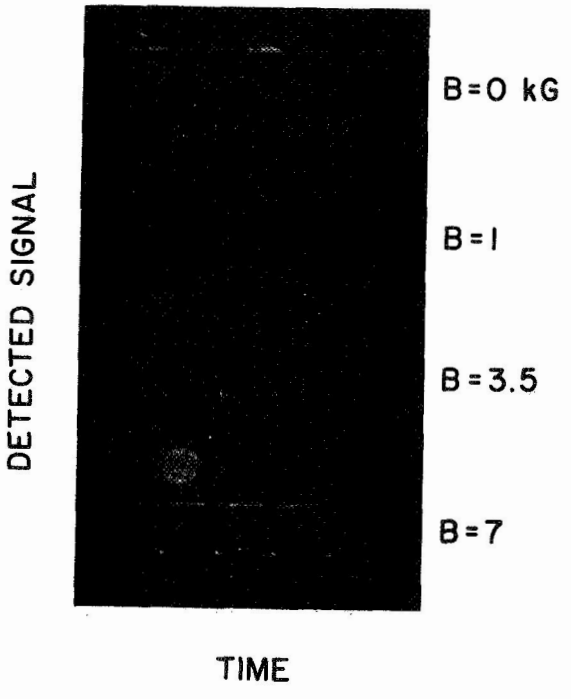

FIG. 5.21 EFFECT OF THE MAGNETIC FIELD ON THE RESPONSE TIME. (f_i = 35.73 GHz, f_m = 50 kHz)

seen from the oscillograms shown in Fig. 5.21 that the response time is essentially independent of the magnetic field. The same experiment was carried out at a modulation frequency of 200 kHz. In this case the detected signal was monitored using an rms vacuum tube voltmeter. No change in the detected signal was observed as the magnetic field was varied between zero and 8.6 kG.

Figure 5.22 shows the experimental results for the dependence of $(MDP)_{mm}$ on B. The $(MDP)_{mm}$ is less sensitive for the magnetic field when it is oriented parallel to the (110)-crystal plane. However the $(MDP)_{mm}$ increased by 10 dB as the magnetic field was increased from zero to 8 kG. This means that $(NEP)_{mm}$ increases as a result of applying the magnetic field.

5.8 Summary

The device was operated successfully at frequencies in the Ka-, E- and G-bands. The agreement between the theoretical and experimental results is quite favorable. The best results achieved so far with the given material are listed in Table 5.4. The results listed in this table can be improved by proper material choice.

Table 5.4

The Best Performance Achieved with the Device

L_T (with no magnetic field)	=	11.5 dB
L_T (with B = 2.5 kG)	=	4.5 dB
$(NEP_{NM})_{mm}$ (with no magnetic field)	=	-66 dBm per unit bandwidth
$(NEP_{NM})_{mm}$ (with B = 2.5 kG)	=	-69.5 dBm per unit bandwidth

The device performance was compared with available crystal detectors for these frequencies. The responsivity of the device is

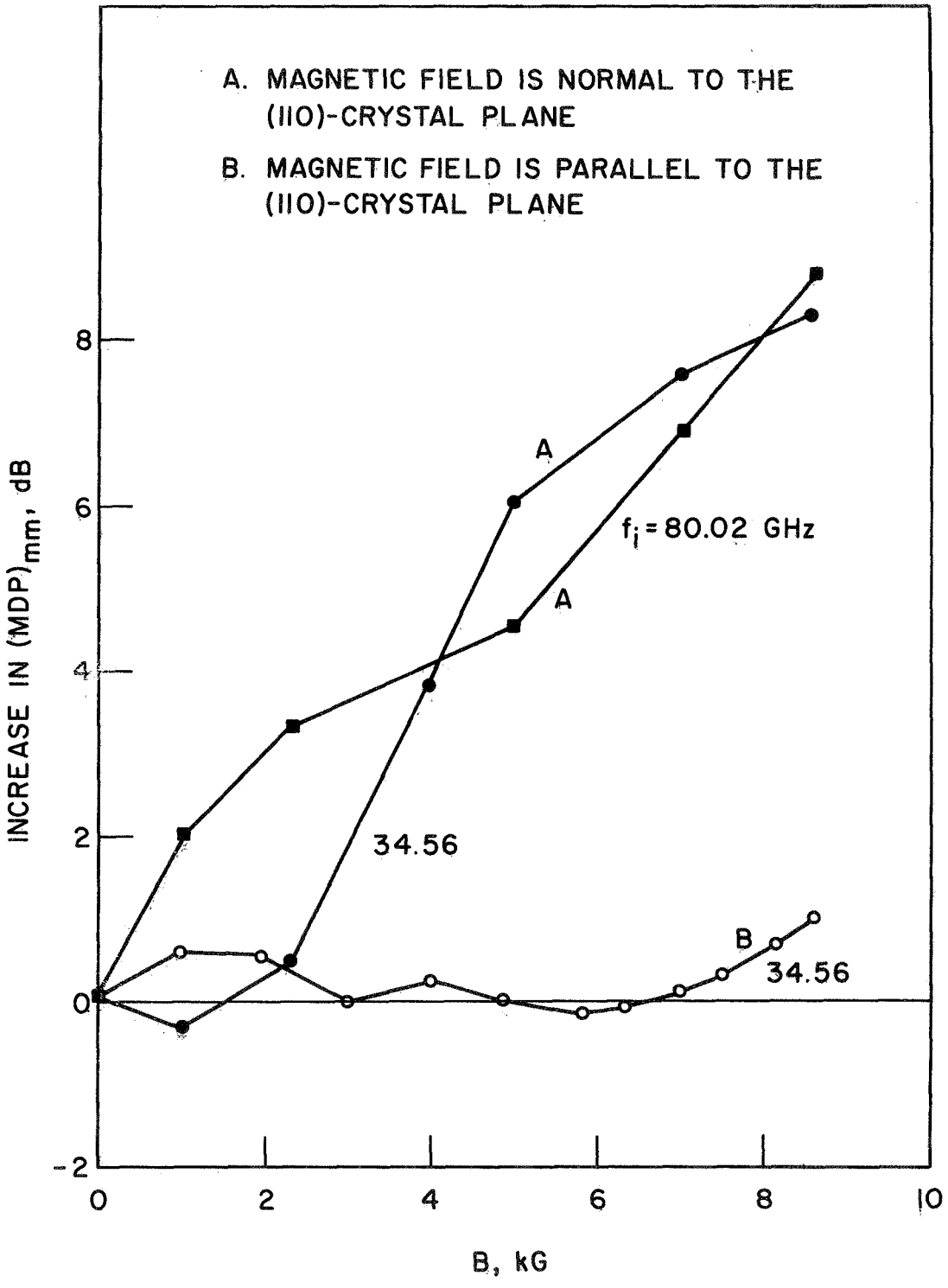

FIG. 5.22 DEPENDENCE OF $(MDP)_{mm}$ ON B. (f_i = 34.56, 80.02 GHz)

at least 50 times better than a Z224S crystal mounted in a G-band waveguide at 150 GHz. In addition the $(NEP)_{mm}$ was found to be at least 10 dB lower than that achieved with the Z224S crystal. In addition the device was found to excel over point-contact crystal detectors mounted in a waveguide over all the frequencies tested.

CHAPTER VI. SUMMARY, CONCLUSIONS AND SUGGESTIONS FOR FURTHER STUDY

6.1 Summary and Conclusions

The purpose of this study was to investigate bulk semiconductor material properties and to study their potential for application as millimeter- and submillimeter-wave detectors. The feasibility of bulk InSb as a microwave-biased detector for the millimeter- and submillimeter-wave range has been experimentally demonstrated. An NEP of 6.8×10^{-11} W per unit bandwidth with 11.5 dB conversion loss has been measured using the circuit described earlier. The device competes favorably with existing detectors for this frequency range. A comparison between the device performance and the existing schemes is illustrated in Fig. 6.1. It should be emphasized that there is still room for improvement through better circuit design and proper material choice.

The scheme offers a fast, wideband, highly sensitive and rugged detector with very low conversion loss. It excels over bulk mixers by eliminating the need for a local oscillator at the millimeter-wave frequency and over Putley detectors (dc-biased) with regard to the speed of response and the elimination of flicker noise. A comparison between this scheme and millimeter-wave diodes shows that the former is free from burnout limitations and is a lot easier to fabricate. An extremely fine contact area makes it very difficult to manufacture millimeter-wave diodes and imposes severe burnout limitations on them. The only inconvenience in using this detector is the requirement for cooling to a cryogenic

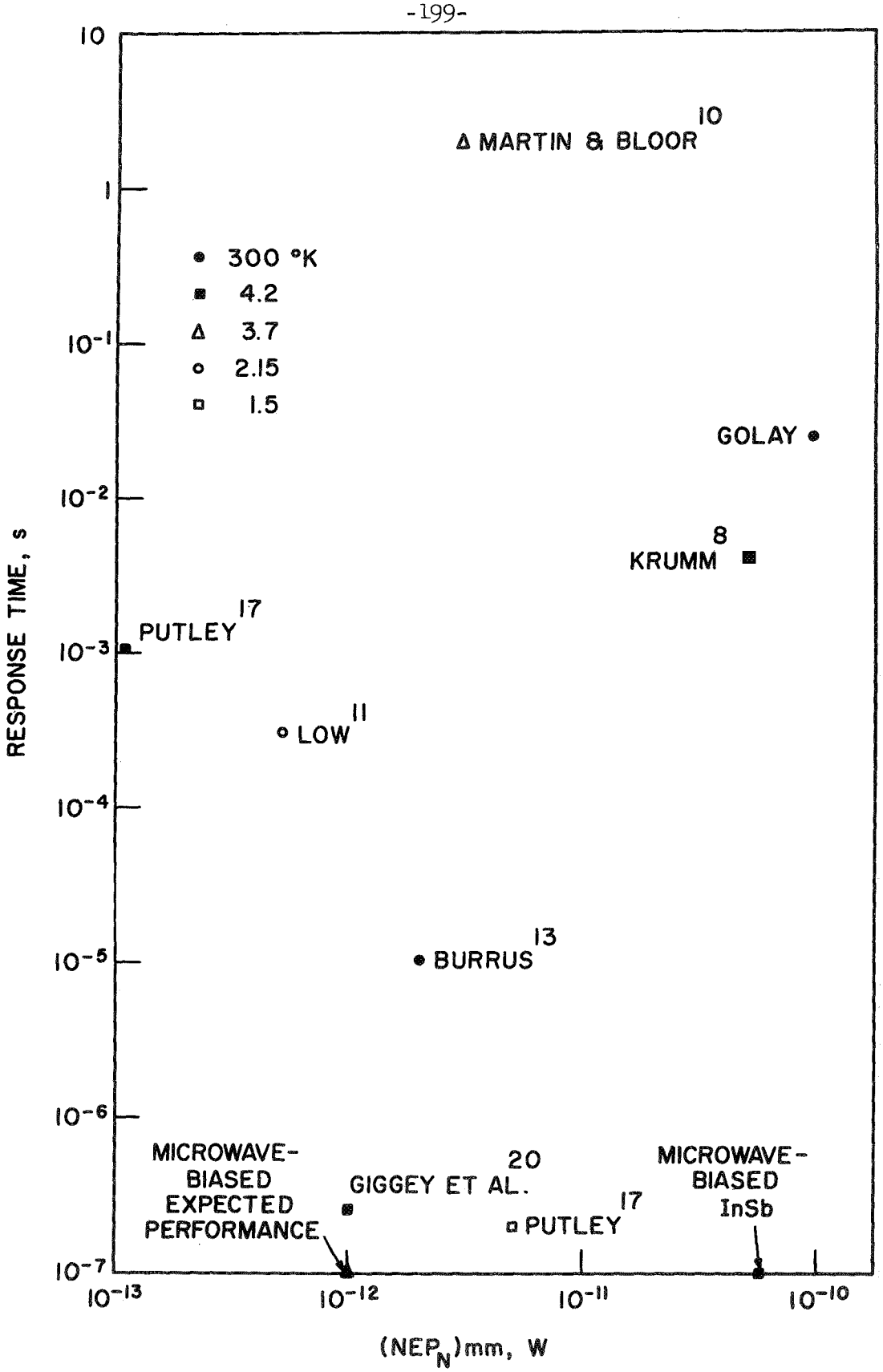

FIG. 6.1 COMPARISON BETWEEN THE PRESENT SCHEME AND EXISTING MILLIMETER-WAVE DETECTORS.

temperature. However this has become quite feasible recently through the development of closed refrigeration systems.

In order to determine the characteristics of the detection scheme a detailed and thorough evaluation of the microwave properties of bulk semiconductors in the presence of a dc magnetic field has been conducted with special emphasis on InSb. A two-band conduction model was used for this purpose. In the analysis a hydrogenic model was utilized; the impurity ions were assumed to be arranged on a uniform lattice and the carriers were assumed to have a Maxwellian distribution. An expression for the magnetic field required to freeze out the carriers in the impurity band was derived. Cavity perturbation techniques using an equivalent circuit approach were utilized to compare the theoretical and experimental results. The method was found to be very sensitive and highly versatile. In addition the good agreement between theory and experiment justifies the case of the equivalent circuit approach.

The conductivity of InSb proved to be independent of the microwave signal level for temperatures above 77°K. This proves that the hot-electron effect is negligible over this temperature range. In addition the scattering mechanism was found to be dominated by acoustic and optical modes above 77°K. However, the hot-electron effect was found to be pronounced at liquid helium temperature and is the process responsible for the broadband detection mechanism.

An equivalent circuit approach was utilized to derive the expressions describing the physical properties of the detection scheme. An expression for the conversion loss was obtained and its dependence on the circuit losses was given. It was found that the conversion loss

is minimum when P_{ix} is much greater than P_s which depends on the size of the sample. The effect of the cavity coupling factor was discussed and its optimum value was obtained. The NEP was derived using the tangential sensitivity concept. The factor K_m' which is proportional to $d\sigma_o/dP$ and is inversely proportional to σ_o plays an important role toward the ultimate performance of the downconverter. Its value was measured experimentally at liquid helium temperature by studying the dependence of the conductivity on the microwave signal level. A large value for K_m' results in a lower value for NEP and the conversion loss. This shows that high-purity compensated samples are best suited for the detection scheme. The NEP was found to be limited by the postdetection system and can be reduced by at least 10 dB by improving the video detector. The expression for the detector response time was derived by studying the energy balance equation within the sample. The response time is limited by the carrier relaxation time and is independent of the circuit parameters and the signal level to be detected for all practical purposes.

The detection scheme was tested at frequencies in the range of 35 to 150 GHz. The agreement between the theoretical and experimental results is excellent in most cases. The response time was too fast to be measured directly with the available millimeter-wave test equipment. The theoretical results show that the response time is of the order of 10^{-7} s. The tunable bandwidth of the detector was found to be limited by the input cavity and of the order of 100 MHz with the circuit under test.

A minor improvement in the detector performance at E- and G-bands was observed on applying a small magnetic field (0-3 kG). However the performance was degraded at higher magnetic fields. This indicates the presence of broadband transitions from the impurity to the conduction band as a result of the incident radiation. It also shows that the hot-electron effect becomes inefficient at high magnetic fields as a result of the reduction in the number of carriers available in the conduction band.

6.2 Suggestions for Future Work

The feasibility of microwave-biased bulk semiconductor detectors for the millimeter- and submillimeter-wave detector has been demonstrated. However the ultimate performance of this class of detectors has not been realized. The choice of material plays an important role toward that end. One problem which requires future investigation is to study the effect of the net carrier concentration along with the degree of compensation within the sample on the detector performance. This requires both a theoretical and experimental study of the factor K_m' and its dependence on these parameters. A high value for K_m' is desirable toward a lower NEP and conversion loss.

Another problem of interest is to study the temperature dependence of the detector performance. This requires accurate and reliable means for temperature control and measurement in the vicinity of liquid helium temperature. The knowledge of $d\sigma/dT$ as a function of the temperature and the signal level will also prove useful toward understanding the hot-electron effect at high frequencies.

A third problem of interest is the investigation of the detector response as a function of the signal frequency and that of the microwave bias. This problem can be readily carried out if the means to measure the absolute value of the millimeter-wave power and to change the coupling factor at the input cavity are accessible.

The problem of reducing NEP should also be given some consideration. It was shown that the limitation on the detector noise performance is imposed by the postdetection system. Studies to reduce the noise contribution in this system could lead to a reduction of as much as 10 dB in NEP.

Finally, a challenging problem is to measure the response time and check its dependence on the various parameters. This can be done indirectly by operating the system in a heterodyne arrangement and measuring the response as a function of IF. In addition the feasibility of using the device as a narrow-band tunable detector is very important and should be investigated.

APPENDIX A. FUNCTIONAL DEPENDENCE OF THE CONDUCTIVITY ON THE MILLIMETER-WAVE SIGNAL AMPLITUDE IN THE PRESENCE OF THE MICROWAVE BIAS

In order to establish the dependence of the conductivity on the incident millimeter-wave signal at liquid helium temperature, the concept of electron temperature will be used. This concept is applicable since it was shown[64] that the scattering mechanism is dominated by ionized impurity scattering. In the absence of any radiation the electrons in the conduction band are in thermal equilibrium with the lattice whose temperature is T_o. When the material is irradiated the average electron temperature of the free carriers will increase above the lattice temperature due to the fact that the rate at which the energy is redistributed among the free carriers is much lower than the rate of transfer of energy from the electrons to the lattice.[48] The average electron temperature T_e can be written as

$$T_e = T_o + T_x + T_i \quad , \tag{A.1}$$

where T_o = the lattice temperature and is assumed to be independent of the signal,

T_x = the increase in the electron temperature due to the microwave bias and

T_i = the increase of the electron temperature as a result of the millimeter-wave signal.

T_i can be obtained by making a Taylor series expansion of the energy balance equation,[48,72] which can be written as

$$\frac{d\bar{\mathcal{E}}(T_e)}{dt} = \frac{P_f(t)}{nV_s} - P(T_e,T_o) \quad , \tag{A.2}$$

where $\bar{\mathcal{E}}$ = the average energy of the electron,

P_f = the average rate at which power is absorbed by the sample,

P = the average rate at which an electron loses energy to the lattice and

n = the number of free carriers per unit volume.

Referring to Fig. 3.2 P_f can be written as

$$P_f(t) = \frac{\gamma_o K\sigma_o}{K\sigma_o + G_o + Y_o} P_{ix}(t) + \frac{\gamma K\sigma}{K\sigma + G + Y} P_i(t) \quad , \tag{A.3}$$

where γ_o and γ are the conversion efficiencies of the microwave and millimeter-wave signal, respectively; G_o and Y_o are the cavity and line conductance at the microwave frequency and G and Y are the corresponding quantities at the millimeter-wave frequency.

Substituting Eq. A.3 into Eq. A.2, expanding into a Taylor series about the point $(T_o + T_x)$ and keeping only the first-order terms yields

$$\frac{d\bar{\mathcal{E}}(T_e)}{dT_e}\frac{dT_e}{dt} = \frac{1}{nV_s}\left[P_{ix}\frac{\gamma_o K\sigma_o}{K\sigma_o + G_o + Y_o} + \frac{\gamma K(G+Y)}{(K\sigma_o + G + Y)^2}\frac{\partial\sigma}{\partial T_e}P_i T_i + \frac{\gamma K\sigma_o}{K\sigma_o + G + Y}P_i\right] - P(T_o,T_o+T_x) - \frac{dP(T_o,T_e)}{dT_e}T_i \quad , \tag{A.4}$$

where the values of the derivatives are taken at $T_e = T_o + T_x$. In the absence of the millimeter signal $T_i = 0$, Eq. A.4 reduces to the following form:

$$nV_s c \frac{dT_x}{dt} = -nV_s P(T_o, T_o + T_x) + \frac{\gamma_o K\sigma_o}{K\sigma_o + G_o + Y_o} P_{ix} \quad , \tag{A.5}$$

where $c = d\bar{\mathcal{E}}(T_e)/dT_e$ is the electron specific heat.

On substituting Eq. A.5 into Eq. A.4 the following relation results:

$$nV_s c \frac{dT_i}{dt} = \frac{\gamma K\sigma_o P_i}{K\sigma_o + G + Y} + \frac{\gamma K(G + Y)P_i}{(K\sigma_o + G + Y)^2} \frac{d\sigma}{dT_e} T_i - nV_s \frac{dP(T_o, T_e)}{dT_e} T_i \quad . \tag{A.6}$$

Assuming $T_i = \mathrm{Re}(T_{io} e^{j\omega_m t})$, where ω_m is the modulation frequency of the incident millimeter-wave signal and substituting into Eq. A.6 yiel

$$T_i = \frac{\gamma K\sigma_o}{K\sigma_o + G + Y} \left[nV_s \frac{dP(T_e, T_o)}{dT_e} - \frac{\gamma K(G + Y)P_i}{(K\sigma_o + G + Y)^2} \frac{d\sigma}{dT_e} + jn\omega_m V_s c \right]^{-1} P_i \tag{A.7}$$

which can be simplified to the following form:

$$T_i = \frac{\gamma K\sigma_o \tau}{ncV_s(K\sigma_o + G + Y)(1 + j\omega_m \tau)} P_i \quad , \tag{A.8}$$

where

$$\tau = \left[\frac{1}{c} \frac{dP(T_e, T_o)}{dT_e} - \frac{\gamma K(G + Y)P_i}{ncV_s(K\sigma_o + G + Y)^2} \frac{d\sigma}{dT_e} \right]^{-1} \quad . \tag{A.9}$$

It was shown by Kogan[48] that

$$\frac{1}{\tau_e} = \frac{1}{c} \frac{dP(T_e,T_o)}{dT_e} \quad , \tag{A.10}$$

where τ_e = the energy relaxation time of the carriers. Therefore τ can be related to the energy relaxation time τ_e of the carriers as follows

$$\tau = \left[\frac{1}{\tau_e} - \frac{\gamma K(G + Y)P_i}{ncV_s(K\sigma_o + G + Y)^2} \frac{d\sigma(T_e)}{dT_e} \right]^{-1} \quad . \tag{A.11}$$

Once the value of T_i is known it becomes a straightforward process to derive the dependence of the conductivity on the incident millimeter-wave power. Expanding the conductivity in a Taylor series and retaining only first-order terms results in

$$\sigma(T_o + T_x + T_i) = \sigma(T_o + T_x) + \frac{d\sigma(T_e)}{dT_e} T_i \quad , \tag{A.12}$$

where the derivative is calculated at $T = T_o + T_x$. Substituting Eq. A.8 into Eq. A.12, the change in the conductivity as a result of the incident millimeter-wave signal can be obtained and is given by

$$\Delta\sigma = K_m P_i \quad , \tag{A.13}$$

where

$$K_m = \frac{\gamma K\sigma_o \tau}{ncV_s(K\sigma_o + G + Y)(1 + j\omega\tau)} \frac{d\sigma}{dT} \quad . \tag{A.14}$$

LIST OF REFERENCES

1. Coates, R. J., "Solar Observations at Millimeter Wavelengths," Proc. IEEE, vol. 54, No. 4, pp. 471-477, April 1966.

2. Meyer, J. W., "Radar Astronomy at Millimeter and Submillimeter Wavelengths," Proc. IEEE, vol. 54, No. 4, pp. 484-492, April 1966.

3. King, D. D., "Long Waves or Short--Perspective on the Millimeter Region," IEEE Spectrum, vol. 2, No. 5, pp. 64-68, May 1965.

4. Dees, J. W., "Detection and Harmonic Generation in the Submillimeter Wavelength Region," Microwave J., vol. 9, No. 9, pp. 48-55, September 1966.

5. Jones, R. C., "Performance of Detectors for Visible and Infrared Radiation," Advances in Electronics, Martin, L. (Ed.), Academic Press, Inc., New York, vol. 5, pp. 1-95, 1953.

6. Jones, R. C., "Phenomenological Description of the Response and Detecting Ability of Radiation Detectors," Proc. IRE, vol. 47, No. 9, pp. 1495-1502, September 1959.

7. Putley, E. H., "The Detection of Sub-mm Radiation," Proc. IEEE, vol. 51, No. 11, pp. 1412-1423, November 1963.

8. Krumm, C. F., "Millimeter- and Submillimeter-Wave Detection by Paramagnetic Materials," Tech. Report No. 116, Contract No. NGL 23-005-183, Electron Physics Laboratory, The University of Michigan, Ann Arbor, April 1970.

9. McLean, T. P. and Putley, E. H., "The Performance of Ideal Receivers of Optical, Infrared and Radio Frequency Radiation," Royal Radar Establishment J., No. 52, pp. 5-43, April 1965.

10. Martin, D. H. and Bloor, D., "The Application of Superconductivity to the Detection of Radiant Energy," Cryogenics, vol. 1, pp. 157-165, March 1961.

11. Low, F. J., "Low Temperature Germanium Bolometers," J. Opt. Soc. Am., vol. 51, No. 11, pp. 1300-1304, November 1961.

12. Jones, C. E., Jr., Hilton, A. R., Damrel, J. B., Jr. and Helms, C. C., "The Cooled Germanium Bolometer as a Far Infrared Detector," Appl. Optics, vol. 4, No. 6, pp. 683-685, June 1965.

13. Burrus, C. A., Jr., "Millimeter-Wave Point-Contact and Junction Diodes," Proc. IEEE, vol. 54, No. 4, pp. 575-587, April 1966.

14. Bauer, R. T., Cohn, M., Cotton, J. M., Jr. and Packard, R. F., "Millimeter-Wave Semiconductor Diode Detectors, Mixers, and Frequency Amplifiers," Proc. IEEE, vol. 54, No. 4, pp. 595-605, April 1966.

15. Krumm, C. F. and Haddad, G. I., "Millimeter- and Submillimeter-Wave Detection by Paramagnetic Materials," Presented at the 1969 IEEE G-MTT Int. Microwave Symposium, Dallas, Texas, May 1969.

16. Rollin, B. V., "Detection of Millimeter- and Submillimeter-Wave Radiation by Free-Carrier Absorption in a Semiconductor," Proc. Phys. Soc. (London), vol. 77, Part 5, No. 497, pp. 1102-1105, May 1961.

17. Putley, E. H., "Indium Antimonide Submillimeter Photoconductive Detectors," Appl. Optics, vol. 4, No. 6, pp. 649-656, June 1965.

18. Putley, E. H., "The Ultimate Sensitivity of Submillimeter-Wave Detectors," Infrared Phys., vol. 4, No. 1, pp. 1-8, March 1964.

19. Kinch, M. A. and Rollin, B. V., "Detection of Millimeter- and Submillimeter-Wave Radiation by Free-Carrier Absorption in Semiconductors," Brit. J. Appl. Phys., vol. 14, No. 9, pp. 672-676, September 1963.

20. Giggey, G. F., Debye, P. P. and Bratt, P. R., "Photoelectric Millimeter-Wave Detectors," Final Report, Contract No. AF30(602)-3015, Raytheon Co., Infrared and Optical Research Lab., Waltham, Mass., 1964.

21. Arams, F., Allen, C., Peyton, B. and Sard, E., "Millimeter Mixing and Detection in Bulk InSb," Proc. IEEE, vol. 54, No. 4, pp. 612-622, April 1966.

22. Whalen, J. J. and Westgate, C. R., "Bulk InSb Mixers for the Submillimeter-Wave Region," Presented at the Symposium on Submillimeter Waves, Brooklyn, N. Y., March 31-April 2, 1970.

23. Sommers, H. S., Jr., "Demodulation of Low-Level Broad-Band Optical Signals with Semiconductors," Proc. IEEE, vol. 51, No. 1, pp. 140-148, January 1963.

24. Sommers, H. S., Jr. and Teutsch, W. B., "Demodulation of Low-Level Broad-Band Optical Signals with Semiconductors: Part II--Analysis of the Photoconductive Detector," Proc. IEEE, vol. 52, No. 2, pp. 144-153, February 1964.

25. Sommers, H. S., Jr. and Gatchell, E. K., "Demodulation of Low-Level Broad-Band Optical Signals with Semiconductors Part III: Experimental Study of the Photoconductive Detector," Proc. IEEE, vol. 54, No. 11, pp. 1553-1568, November 1966.

26. Paranjape, V. V. and De Alba, E., "Decrease of Electron Temperature by Electric Fields," Proc. Phys. Soc. (London), vol. 85, Part 5, No. 547, pp. 945-953, 1965.

27. Rose, A., Concepts in Photoconductivity and Allied Problems, Interscience Publishers, New York, 1963.

28. Sladek, R. J., "Effective Mass of Electrons in Indium Arsenide and Indium Antimonide," Phys. Rev., vol. 105, No. 2, pp. 460-464, January 1957.

29. Putley, E. H., "Impurity Photoconductivity in N-type InSb," J. Phys. Chem. Solids, vol. 22, pp. 241-247, December 1961.

30. Danilychev, V. A. and Lebedev, P. N., "Ionization of Donor Atoms in n-InSb by a Microwave Electric Field," JETP Letters, vol. 2, No. 10, pp. 300-302, November 15, 1965.

31. Conwell, E. M., "Impurity Band Conduction in Germanium and Silicon," Phys. Rev., vol. 103, No. 1, pp. 51-61, July 1, 1956.

32. Hung, C. S. "Theory of Resistivity and Hall Effect at Very Low Temperatures," Phys. Rev. (Correspondence), vol. 79, No. 4, pp. 727-728, August 15, 1950.

33. Yafet, Y., Keyes, R. W. and Adams, E. N., "Hydrogen Atom in Strong Magnetic Field," J. Phys. Chem. Solids, vol. 1, No. 3, pp. 137-142, November 1956.

34. Keyes, R. W. and Sladek, R. J., "Effect of a Magnetic Field on Donor Impurity Levels in InSb," J. Phys. Chem. Solids, vol. 1, No. 3, pp. 143-145, November 1956.

35. Sladek, R. J., "Magnetically Induced Banding in n-InSb," J. Phys. Chem. Solids, vol. 5, No. 3, pp. 157-170, May 1958.

36. Brown, M.A.C.S. and Kimmit, M. F., "Far-Infrared Resonant Photoconductivity in Indium Antimonide," Infrared Phys., vol. 5, No. 2, pp. 93-97, June 1965.

37. Apel, J. R., Poehler, T. O. and Westgate, C. R., "Quantum Effects in Electron Cyclotron Resonance in InSb," Appl. Phys. Letters, vol. 14, No. 5, pp. 161-163, 1 March 1969.

38. Putley, E. H., Semiconductors and Semimetals, Beer, A. C. and Willardson, R. K. (Eds.), Academic Press Inc., New York, vol. 1, 1966.

39. Goodman, C.H.L., "Ionic Covalent Bonding in Crystal," Nature, vol. 187, No. 4737, pp. 590-591, August 1960.

40. Mooser, E. and Pearson, W. B., "The Ionic Character of Chemical Bonds," Nature, vol. 190, No. 4774, pp. 406-408, April 1961.

41. Cochran, W., "Effective Ionic Charge in Crystals," Nature, vol. 191, No. 4783, pp. 60-61, July 1961.

42. Hass, M. and Henvis, B. W., "Infrared Lattice Reflection Spectra of III-V Compound Semiconductors," J. Phys. Chem. Solids, vol. 23, pp. 1099-1104, August 1962.

43. Born, M. and Huang, K., Dynamical Theory of Crystal Lattices, Oxford University Press, London, Eng., 1954.

44. Attard, A. E. and Azaroff, L. V., "Electron Density Distribution in Indium Antimonide," J. Appl. Phys., vol. 34, No. 4, Part 1, pp. 774-776, April 1963.

45. Hilsum, C., "Some Key Features of III-V Compounds," Semiconductors and Semimetals, Beer, A. C. and Willardson, R. K. (Eds.), Academic Press, Inc., New York, vol. 1, pp. 3-18, 1966.

46. Sucher, M., "Measurement of Q," Handbook of Microwave Measurements, Sucher, M. and Fox, J. (Eds.), Polytechnic Press of Polytechnic Institute of Brooklyn, Brooklyn, N. Y., vol. II, pp. 417-494, 1963.

47. Johnson, E. J. and Dickey, D. H., "Infrared Cyclotron Resonance and Related Experiments in the Conduction Band of InSb," Phys. Rev. B, vol. 1, No. 6, pp. 2676-2692, March 15, 1970.

48. Kogan, Sh. M., "A Photoconductivity Theory Based on Variations of Carrier Mobility," Soviet Phys.--Solid State, vol. 4, No. 7, pp. 1386-1389, January 1963.

49. Stern, F., "Calculation of Optical Absorption in III-V Semiconductors," Proc. Int. Conf. Semiconductor Physics, Prague, Czechoslovakia, pp. 363-365, 1961.

50. Bagguley, D. M., Robinson, M. L. and Strabling, R. A., "Cyclotron Resonance in p-Type InSb at Millimeter-Wavelength," Phys. Letters, vol. 6, No. 2, pp. 143-145, September 1963.

51. Champlin, K. S., Holm, J. D. and Glover, G. H., "Electrodeless Determination of Semiconductor Conductivity from TE_{01}°-Mode Reflectivity," J. Appl. Phys., vol. 38, No. 1, pp. 96-98, January 1967.

52. D'Altroy, F. A. and Fan, H. Y., "Microwave Transmission in P-Type Germanium," Phys. Rev., vol. 94, No. 5, pp. 1415-1416, June 1, 1954.

53. Jacobs, H., Brand, F. A., Meindl, J. D., Weitz, S. and Benjamin, R., "New Microwave Technique in the Measurement of Semiconductor Phenomenon," IRE Int. Convention Record, New York, vol. 10, Part 3, pp. 30-42, March 1962.

54. Datta, A. N. and Nag, B. R., "Techniques for the Measurement of Complex Microwave Conductivity and the Associated Errors," IEEE Trans. on Microwave Theory and Techniques, vol. MTT-18, No. 3, pp. 162-166, March 1970.

55. Champlin, K. S. and Glover, G. H., "'Gap Effect' in Measurement of Large Permittivities," IEEE Trans. on Microwave Theory and Techniques (Correspondence), vol. MTT-14, No. 8, pp. 397-398, August 1966.

56. Holm, J. D., "Microwave Conductivity of Silicon and Germanium," Ph.D. Thesis, The University of Minnesota, 1967.

57. Casimir, H.R.G., "On the Theory of Electromagnetic Waves in Resonant Cavities," Phillips Research Reports, vol. 6, 1951.

58. Altschuler, H. M., "Dielectric Constant," Handbook of Microwave Measurements, Sucher, M. and Fox, J. (Eds.), Polytechnic Press of Polytechnic Institute of Brooklyn, Brooklyn, N. Y., vol. II, pp. 495-590, 1963.

59. De Groot, S. R. and Mazur, P., "Extension of Onsager's Theory of Reciprocal Relations," Phys. Rev., vol. 94, No. 2, pp. 218-226, April 15, 1954.

60. Montgomery, C. G., Techniques of Microwave Measurements, McGraw-Hill Book Co., Inc., New York, vol. 11, No. 1, pp. 384-386, 1947.

61. Hindert, P., "Thermal Expansion of Copper and Its Important Industrial Alloys," Scientific paper of NBS No. 410, March 1921.

62. Stom, J. L. and Hartwig, W. H., "A Unique Laser Detector Utilizing the Photodielectric Effect in Cooled Semiconductors," Tech. Report No. 39, Laboratories for Electronics and Related Science Research, University of Texas, Austin, September 1967.

63. Ismailov, I. M., Nasledov, D. N., Smetannikova, Yu. S. and Felitsiant, V. R., "Donor Levels in n-InSb and Their Ionization Electric Field," Phys. Stata. Sol., vol. 36, No. 2, pp. 747-754, December 1969.

64. Putley, E. H., "Electrical Conduction in n-Type InSb Between 2°K and 300°K," Proc. Phys. Soc. (London), vol. 73, Part 2, No. 470, pp. 280-290, February 1958.

65. Whalen, J. J. and Westgate, C. R., "Temperature Dependence of the Energy Relaxation Time in n-InSb," Appl. Phys. Letters, vol. 15, No. 9, pp. 292-297, 1 November 1969.

66. McKelvey, J. P., Solid State and Semiconductor Physics, Harper and Row Publishers, New York, 1966.

67. Tolman, R. C., The Principles of Statistical Mechanics, Oxford University Press, London, Eng., 1938.

68. Townes, C. H. and Geschwind, S., "Limiting Sensitivity of a Microwave Spectrometer," J. Appl. Phys. (Correspondence), vol. 19, No. 8, pp. 795-796, August 1948.

69. Ondria, J. G., "A Microwave System for Measurements of AM and FM Noise Spectra," IEEE Trans. on Microwave Theory and Techniques, vol. MTT-16, No. 9, pp. 767-781, September 1968.

70. Robinson, F.N.H., Noise in Electrical Circuits, Oxford University Press, London, Eng., 1962.

71. Hasegawa, H. and Howard, R. E., "Optical Absorption Spectrum of Hydrogenic Atoms in a Strong Magnetic Field," J. Phys. Chem. Solids, vol. 21, No. 3/4, pp. 179-198, December 1961.

72. Whalen, J. J. and Westgate, C. R., "Temperature Dependence of the Conversion Loss and Response Time of InSb Mixers," IEEE Trans. on Electron Devices, vol. ED-17, No. 4, pp. 310-319, April 1970.

LIST OF SYMBOLS

a_m	Ratio of the sample to the cavity conductance.
B	Magnetic field intensity.
B_F	Freeze-out magnetic flux density.
B_{Fh}	Magnetic field at which 90 percent of the carriers are in the conduction band.
B_x	Video bandwidth.
b	Defined by Eq. 2.37.
C_{eff}	Effective capacitance of the cavity.
c	Electron specific heat.
$\underline{D}$	Electric displacement vector.
d_1	Sample length.
d_2	Sample width.
$\underline{E}$	Electric field intensity.
$\mathcal{E}$	Average energy of the carriers.
e	Electronic charge.
e^*	Effective charge ratio.
F	Defined in Eq. 3.73.
f	Resonance frequency of the cavity.
f_o	Resonance frequency of the cavity with no perturbation.
f_i	Signal frequency.
G_o	Empty cavity conductance.
G_{eff}	Effective conductance of the cavity system.
g	Gain of the video amplifier.

H	Magnetic field intensity.
h	Planck's constant.
J	Current density.
j	$\sqrt{-1}$.
K	Sample's geometrical factor, defined by Eq. 3.72.
K_1	Constant = $d_1 d_2/t$.
K_m	Sample conversion factor defined by Eq. 4.9.
K'_m	Sample conversion factor defined by Eq. 4.11.
k	Boltzmann's constant.
L_{ox}	Output circuit conversion loss.
L_D	Downconverter conversion loss.
L_i	Input circuit conversion loss.
L_s	Saturation conversion loss.
L_T	Terminal-to-terminal conversion loss.
$(L_T)_{matched}$	Terminal-to-terminal conversion loss with matched circuits.
$(MDP)_{mm}$	Minimum detectable millimeter-wave power.
$(MDP_M)_{mm}$	Minimum detectable power with matched input and output circuits.
m	Electronic mass.
m^*	Carrier effective mass.
N_b	Carrier concentration required for band formation.
N_c	Carrier concentration resulting in total overlap between the impurity and conduction bands.
N_I	Net impurity concentration.
n_c	Carrier density in the conduction band.
n_i	Carrier density in the impurity band.

n_s	Density of carriers excited by photoconductive transitions.
P_o	Power available from the source.
P_c	Power absorbed by the cavity.
P_D	Detected power.
P_i	Incident millimeter-wave power.
P_n	Noise power in the output line.
P_{nam}	AM modulation noise power.
P_{nb}	Background radiation fluctuation noise power.
P_{nD}	Noise power at the input of the crystal detector.
P_{nlo}	Local oscillator noise power.
P_r	Reflected power from the cavity.
P_s	Saturation microwave power.
Q_L	Loaded Q of the cavity.
Q_{Lo}	Loaded Q of the cavity with no perturbation.
Q_U	Unloaded Q of the cavity.
Q_{Uo}	Unloaded Q of the cavity with no perturbation.
q	Charge of the carriers.
R	Factor given by Eq. 4.24.
r_c	Cyclotron radius.
r_n	nth-orbital radius.
r_s	Occupancy radius.
S_d	Crystal detector responsivity.
T	Temperature.
T_D	Equivalent noise temperature of the downconverter.
T_e	Effective carrier temperature.

t	Time, and sample thickness.
t_{op}	Optimum sample thickness.
V_n	Output noise voltage.
V_s	Sample volume.
v	Average particle velocity.
x	Defined by Eq. 3.23.
Y_o	Line conductance.
Y_{ani}	Contribution to Y_m due to the anisotropy of the sample.
Y_m	Conductance of the material.
α	Microwave line attenuation.
α_{ij}	Circulator insertion loss between Ports i and j.
α_m	Millimeter line attenuation.
α_T	Coefficient of thermal expansion of the cavity material.
β	Cavity coupling factor.
β_o	Cavity coupling factor with no perturbation.
β_{oo}	Empty cavity coupling factor.
β_{op}	Optimum coupling factor.
Γ_{ox}	Output reflection coefficient.
Γ_i	Input reflection coefficient.
ΔE	Energy gap of the material.
Δf	Cavity resonance frequency shift.
Δf_e	Resonance frequency shift due to cavity thermal expansion.
Δf_N	Cavity normalized resonance frequency shift (Eq. 3.62).
Δf_{rms}	rms frequency deviation of the local oscillator.
ΔP_d	Change in the detected power.

$\Delta\epsilon$	Change in the material dielectric constant.
$\Delta\sigma$	Change in the material conductivity.
ϵ	Dielectric constant = $\kappa_o \epsilon_r$.
ϵ_ℓ	Lattice dielectric constant.
ϵ_r	Relative dielectric constant.
η	Cavity filling factor.
κ_o	Permittivity of free space.
μ	Mobility.
μ_c	Mobility of carriers in the conduction band.
μ_i	Mobility of carriers in the impurity band.
$\underline{\underline{\sigma}}$	Conductivity tensor.
σ_o	Conductivity of the sample with no perturbation.
σ_c	Complex conductivity.
τ	Response time.
τ_c	Energy relaxation time of the carrier in the conduction band.
τ_e	Energy relaxation time.
τ_{ee}	Effective time for electron-electron collision.
τ_i	Carrier relaxation time in the impurity band.
Ω	Complex resonance frequency of the cavity system.
ω	Real angular frequency = $2\pi f$.
ω_c	Cyclotron frequency.